EVALUATION AND APPLICATION OF NEW NANOPOROUS MATERIALS FOR ACID GAS SEPARATIONS

A Thesis
Presented to
The Academic Faculty

by

Joshua Allen Thompson

In Partial Fulfillment
of the Requirements for the Degree
Doctor of Philosophy in the
School of Chemical & Biomolecular Engineering

Georgia Institute of Technology
August 2013

EVALUATION AND APPLICATION OF NEW NANOPOROUS MATERIALS FOR ACID GAS SEPARATIONS

Approved by:

Dr. Christopher W. Jones, Co-Advisor
School of Chemical & Biomolecular Engineering
Georgia Institute of Technology

Dr. Sankar Nair, Co-Advisor
School of Chemical & Biomolecular Engineering
Georgia Institute of Technology

Dr. William J. Koros
School of Chemical & Biomolecular Engineering
Georgia Institute of Technology

Dr. David S. Sholl
School of Chemical & Biomolecular Engineering
Georgia Institute of Technology

Dr. Sven Behrens
School of Chemical & Biomolecular Engineering
Georgia Institute of Technology

Dr. Angus P. Wilkinson
School of Chemistry and Biochemistry
Georgia Institute of Technology

Date Approved: May 8, 2013

If you want to have good ideas, you must have many ideas. Most of them will be wrong, and what you have to learn is which ones to throw away.

-Linus Pauling

To my wife, Sarah, and my mother, Sharon

ACKNOWLEDGEMENTS

The contents of this thesis would not exist without the many people who have been a part of this experience. I would like to first acknowledge and thank my advisors: Drs. Christopher W. Jones and Sankar Nair. They have provided a lot of guidance over the years towards completing my degree. In addition, they have offered tremendous criticism and help when I have needed it most, especially as a novice engineer and scientist. Without them, I would not be the same person or engineer or scientist that I am today, and I am grateful for the opportunity to have worked with them over the years. I would next like to give special acknowledgement and thanks to Dr. William J. Koros. Dr. Koros has not only provided funding for this thesis through the KAUST collaborative research project, but has also lent me great knowledge on membranes and their applications when I have needed it, and without his group and their expertise, many parts of this thesis would have never been done. I also want to thank the rest of my committee: Dr. David S. Sholl; Dr. Sven Behrens; and Dr. Angus Wilkinson. They have offered great feedback over the years and have been very helpful when I have needed their expertise.

I want to thank the Jones and Nair group members for being such great people. They have always offered consultation and advice when I have needed it in regards to not just science, but also many of the issues we all face as graduate students and young engineers and scientists. I would like to specially thank Dr. Nicholas Brunelli for all the NMR work that these pages contain and the many useful conversations we have had over the years. In addition, I also want to thank Drs. Justin Vaughn and Ryan Lively for their

help and expertise over the years, concerning membranes and adsorbents. I want to also thank Megan Lydon for being another great resource to talk and commiserate with as a fellow “Bunger-Henry”-ite. Lastly, I wish to thank Karena Chapman at Argonne National Laboratory for her contributions to this thesis. She was able to perform the pair distribution function analysis presented in Chapter 4, and as a result, made the conclusions in that work much stronger.

Finally, the most important people I want to thank are my wife, Sarah, and my mom, Sharon. Sarah has been with me on every single part of this journey through graduate school and has been my ultimate source for support. Without her being in my life, I am unsure if I would have been able to finish graduate school, and I am excited to start the rest of my life with her as my wife. My mom has always been a great supporter for me, and she has helped me financially and emotionally through the hard times. If not for her, I probably never would have attended college or graduate school in the first place. I hope I continue to make her proud throughout the years.

TABLE OF CONTENTS

LIST OF TABLES

LIST OF FIGURES

SUMMARY

Distillation and absorption columns offer significant energy demands for future development in the petrochemical and fine chemical industries. Membranes and adsorbents are attractive alternatives to these classical separation units due to lower operating cost and easy device fabrication; however, membranes possess an upper limit in separation performance that results in a trade-off between selectivity (purity) and permeability (productivity) for the target gas product, and adsorbents require the need to be water-resistant to natural gas streams in order to withstand typical gas compositions. Composite membranes, or mixed-matrix membranes, are an appealing alternative to pure polymeric membrane materials by use of a molecular sieve "filler" phase which has higher separation performance than the pure polymer. In this thesis, the structure-property-processing relationships for a new class of molecular sieves known as zeolitic imidazolate frameworks (ZIFs) are investigated for their use as the filler phase in composite membranes or as adsorbents. These materials show robust chemical and thermal stability and are a promising class of molecular sieves for acid gas (CO_2/CH_4) separations.

The synthesis of mixed-linker ZIFs is first investigated. It is shown that the organic linker composition in these materials is controllable without changing the crystal structure or significantly altering the thermal decomposition properties. There are observable changes in the adsorption properties, determined by N_2 physisorption, that depend on the overall linker composition. The results suggest the proposed synthesis

route facilitates a tunable process to control either the adsorption or diffusion properties depending on the linker composition. The structure-property-processing relationship for a specific ZIF, ZIF-8, is then investigated to determine the proper processing conditions necessary for fabricating defect-free composite membranes. The effect of ultrasonication shows an unexpected coarsening of ZIF-8 nanoparticles that grow with increased sonication time, but the structural integrity is shown to be maintained after sonication by using X-ray diffraction, Pair Distribution Function analysis, and N_2 physisorption. The permeation properties of composite membranes revealed that intense ultrasonication is necessary to fabricate defect-free membranes for CO_2/CH_4 gas separations. Finally, the separation properties of mixed-linker ZIFs is investigated by using adsorption studies of CO_2 and CH_4 and using composite membranes with differing linker compositions. Adsorption properties of mixed-linker ZIFs reveal that these materials possess tunable surface properties, and a selectivity enhancement of six fold over ZIF-8 is observed with mixed-linker ZIFs without changing the crystal structure. Gas permeation studies of composite membranes reveal that the separation properties of mixed-linker ZIFs are different from their parent frameworks. By proper selection of mixed-linker ZIFs, there is an overall improvement of separation properties in the composite membranes when compared to ZIF-8.

CHAPTER 1

Introduction

1.1 Natural Gas Use in the United States

During early development in the oil and gas industry, there was little need or infrastructure for natural gas products that would result during depressurization of oil wells. Often, if the gas was not needed in the immediate area of the oil well, it would be flared instead of captured or processed. With the increase in infrastructure and piping, natural gas has become a vital component for heating and electricity in the United States. In some cases, this gas can also be used as fuel for vehicles or as a feedstock in making chemicals.

With the use of shale sand hydraulic fracturing (fracking) to produce both gas and oil, the projected natural gas production is predicted to grow.[1] The U.S. Energy Information Administration predicts shale sources will increase the United States production by 29% over the next 25 years (Figure 1.1). This expected growth means that reducing costs elsewhere (separations, transport, etc.) will help increase demand for natural gas to be used as a fuel or electricity source and also provide less greenhouse gas pollution than coal or gasoline. In addition, developing more modular separation units will aid the development of natural gas use in nations outside the U.S. that may not have the same well-developed infrastructure.

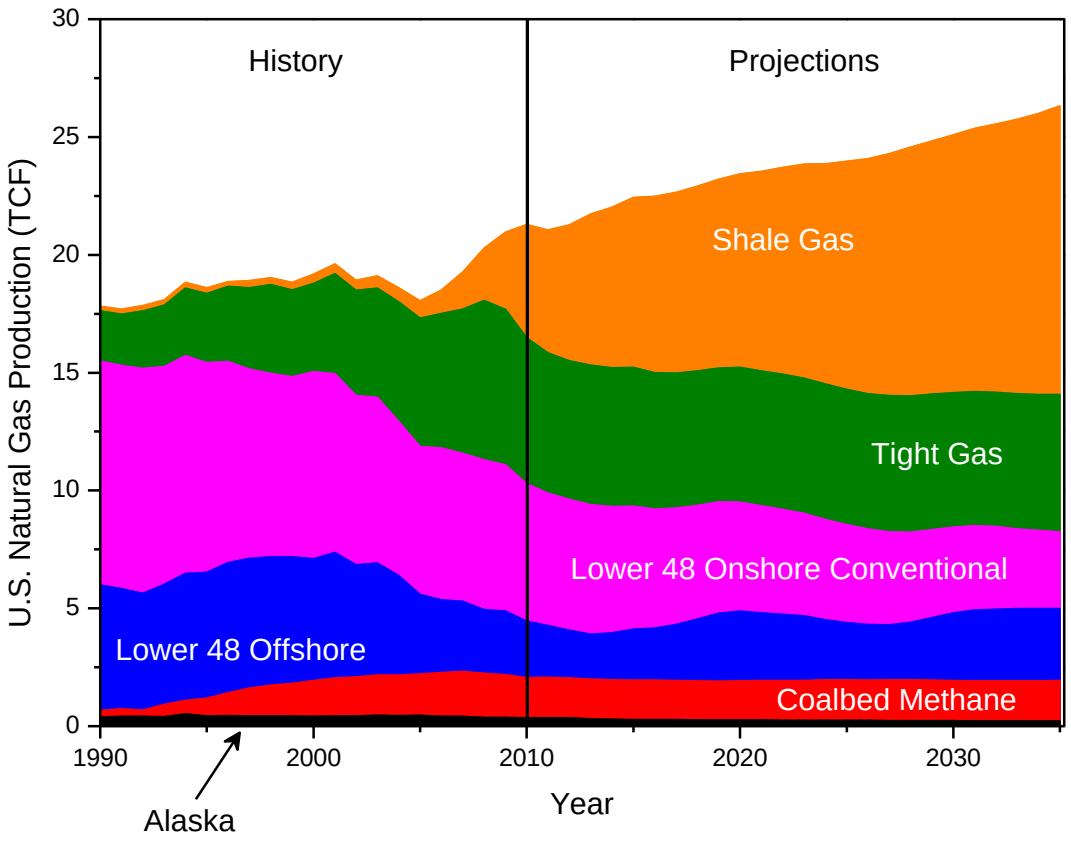

Figure 1.1. United States natural gas projections (in trillion cubic feet) from the EIA. With shale gas, there is an expected growth of nearly 30% in total gas production.[1]

1.2 Industrial Separations of Acid Gases

Raw natural gas when pulled from a wellhead contains many different components. Table 1.1 provides a summary of the typical components and concentration ranges.[2] Of these components, the two largest fractions other than CH_4 are higher-chain hydrocarbons (C_2s-C_4s) and acid gases (CO_2 and H_2S). C_2-C_4 fractions require energy-intensive separations, using cryogenic distillation columns, in order to produce pure products used in chemical feedstocks. Acid gases are typically converted to elemental

sulfur (H_2S), and then the "tail gas" is incinerated to further clean the acid gas stream before emission to the atmosphere.[2]

Acid gas is normally separated using an aqueous amine solution, just before the natural gas is dehydrated (Figure 1.2).[3] The amine solution (*e.g.*, piperazine, monoethanolamine) is typically loaded in an absorber tower that strips the acid gases from the natural gas stream. Then, the saturated solution is pumped to a regeneration column, where heating up the solutions at low pressures lowers the solubility of the captured gas where it is removed for further processing. Although this process can have high separation efficiency, it requires the use of significant amounts of process water, is energy-intensive, and must be done at a refinery or processing site rather than the wellhead, which acid gases can corrode pipelines with higher concentrations (>8 mol%).[3] Therefore, more energy-efficient and modular separation technologies should be considered for removing and purifying acid gases.

Table 1.1. Typical components and composition of raw natural gas in the United States and U.S. pipeline specifications for commercial natural gas used for heating.[2,3]

Component	Composition Range (mol %)	U.S. Pipeline Specifications (mol%)
CH_4	70-90%	
C_2s – C_4s	0-20%	
CO_2	0-10%	< 2%
H_2S	0-5%	< 4 ppm
N_2	0-5%	< 4%
H_2O	vapor	< 120 ppm

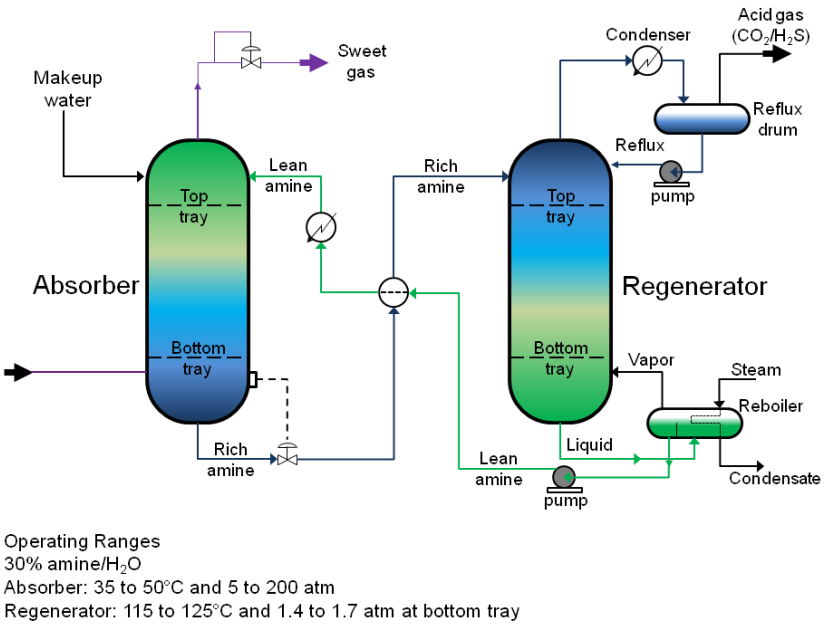

Figure 1.2. Process diagram of an aqueous amine absorber used to remove acid gases from natural gas stream.

1.3 Gas Separations with Membrane Technology

Membrane-based separations provide several advantages over aqueous amine absorption for separating acid gases. Because the separation is driven by pressure and concentration gradients between the feed and the permeate sides, the operating cost for energy is much less if the number of modules is minimized.[3] Additionally, membranes can be designed with a hollow-fiber architecture, which has very high surface area-to-volume ratios, making it a smaller, and therefore, more portable, separation unit than typical absorption- or adsorption-based units.

Membranes are typically judged by several physical properties when dealing with natural gas separations: permeability, the intrinsic flux of a gas through a membrane material; selectivity, the ratio of permeability values for a gas pair; and plasticization

resistance, the amount of swelling that occurs when a gas is exposed to a membrane material. Advances in membrane technology have led to some adoption in different industries, including some use in the purification of natural gas and also nitrogen separation from air.[4]

1.3.1 Polymeric-based Membranes

Polymer membranes have been in development for more than 30 years and have found uses not only in gas separations, but also in reverse-osmosis and pervaporation separations. Polymer membranes are typically dense and operate by a solution-diffusion mechanism.[4] They can be categorized into two types of materials: glassy and rubbery. Glassy polymers operate below the glass transition temperature (T_g) and separate small molecules based on diffusion selectivity due to tight polymer chain packing. Rubbery polymers operate above T_g and separate based on sorption selectivity and generally have much higher permeability and lower selectivity than glassy polymers.

An advantage of using polymer membranes is the easy scale-up that can be used by a hollow-fiber or spiral-wound module design. Typical fabrication conditions will produce membranes with thin selective skin layers (~200 nm) and high packing volumes in a membrane module (10,000 $m^2 \cdot m^{-3}$).[5] However, in the early 1990s, a trend showed that there is an inherent trade-off in polymer membrane separation performance; as the permeability of a gas increases, the expected selectivity for a gas pair will decrease, and vice versa.[6] This behavior has been known as the "Upper Bound" of polymer membrane performance and is shown in Figure 1.3.[7] This relationship was found to be consistent

with the differences in molecular sizes for a given gas pair, meaning that the diffusion selectivity based on the polymer chain packing governs the trade-off in membrane performance.[6]

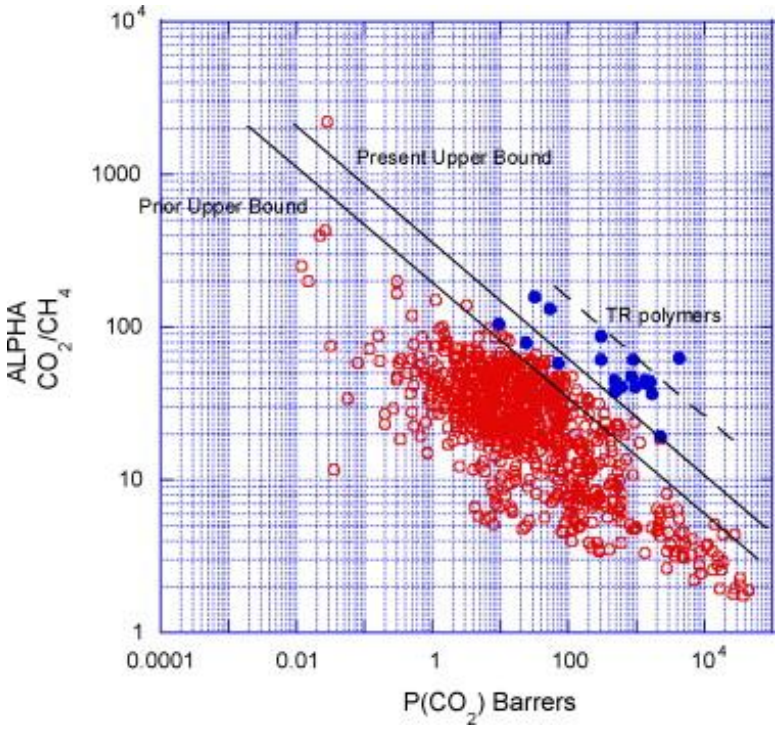

Figure 1.3. Robeson plot showing the upper bound relationship between CO_2 and CH_4. Discounting thermally-rearranged polymers shows very little shift in the upper bound after 17 years of research activity.[7]

1.3.2 Inorganic-based Membranes

There has been a number of other membrane technologies developed for gas separations using inorganic materials. These membranes can also operate by a solution-diffusion mechanism (dense Pd membranes),[8] but also can operate by a molecular-sieving mechanism. Molecular sieve membranes are porous materials that are formed with a skin layer of either zeolite, metal-organic framework (MOF), or a mesoporous material.[9–11]

Molecular sieves are able to operate above the upper bound because they are not limited by chain packing. Instead, these materials can separate gas molecules based entirely on size; therefore, if a material has a pore size smaller than a gas molecule in a separation, very high selectivity can be obtained.[12]

While, in theory, molecular sieves have the capability of exceeding polymer membrane performance, there are several problems in the fabrication and processing of these membranes. Cracks and grain-boundary defects are common problems associated with forming defect-free zeolite membranes.[13] MOF membranes can also suffer from grain-boundary defects, but also have poor adhesion with other inorganic supports that are commonly used in zeolite membrane synthesis and require extra processing steps.[14] However, there have been developments more recently to address these issues; for instance, a MOF membrane has been grown successfully on a porous hollow fiber polymer support without any additional processing steps other than coating the fiber with the MOF seeds.[15]

1.3.3 Mixed-Matrix Membranes

Mixed-matrix, or composite, membranes theoretically combine the advantages of both polymers (*e.g.*, processibility) and molecular sieves (*e.g.*, performance based on sieving).[16,17] Historically, zeolites have been used as the molecular sieve "filler" material in these composite membranes. Due to the purely inorganic surface of zeolites, there is poor adhesion between the filler and the polymer matrix. This causes defects known as "sieve-in-a-cage" morphology, where gaps form between the zeolite and the polymer

creating unselective transport between the two phases. There are several other defects that have been shown to occur, and Figure 1.4 shows the general behavior for each of these known defects and has been discussed elsewhere.[18,19]

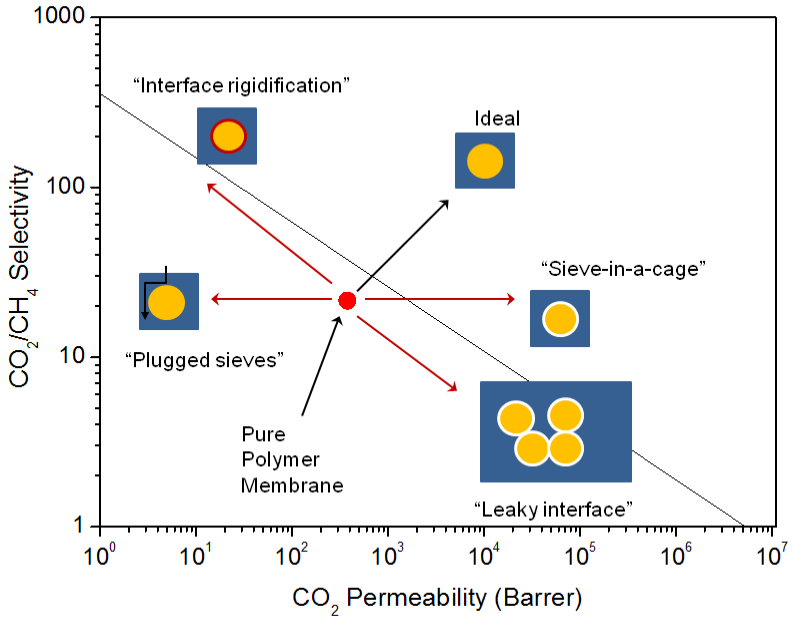

Figure 1.4. Typical defects found during mixed-matrix membrane formation and the performance trends based on these defects.

To address the issue of poor adhesion, there have been several strategies to improve polymer and zeolite interaction by functionalizing the surface of the zeolite. The most successful of these is to deposit inorganic nanostructures on the zeolite surface by different techniques.[20–23] This strategy helps adhesion by roughening the surface and promoting polymer chain entanglement along the surface of the zeolite.[24] Some other strategies have been to react surface silanols of the zeolite with silane coupling agents that contain organic functional groups which interact or covalently bond with the polymer

chain; however, this has shown to cause "interface rigidification"-type defects in the composite membrane performance.[25] Lastly, it is possible to grow mesoporous-microporous zeolite hybrids.[26] The mesopores in these materials are large enough to allow the polymer chains to actually enter and become entangled in the mesoporous regime; however, it is unclear what effect the mesopores have on the composite membrane performance.[27]

The other filler materials that can be considered are metal-organic framework materials. These materials are composed of metal centers and linked together by organic molecules, which together forms a continuous, porous network.[28,29] There have been some studies showing that these materials do not have the same adhesion problems that zeolites do in a polymer matrix.[30–32] However, there have not been any studies showing what processing and fabrication can do to these materials, which may be important since MOFs tend to be less thermally and chemically stable than zeolites.

1.4 Nanoporous Materials

1.4.1 Zeolites

Zeolites are classified as aluminosilicate materials with a microporous crystal structure (pore size < 2 nm).[33,34] Composed of a tetrahedral arrangement of Si and Al (T-atoms) connected by O-bridges, these materials form pores ranging from 6 T-atoms in the ring up to 18 T-atoms. Figure 1.5 shows the range of pore size and crystal structures available for zeolite materials. Besides Si and Al, there can also be a different number of arrangements of T-atoms for inorganic molecules sieves: Si only, Si-Ge, Al-P, and Si-Al-

P. If the molecular sieve is composed of Si-Al or Si-Al-P, there is a net negative charge in the framework, and this is balanced by a cation, such as Na^+ or Ca^{2+}. The framework composition (Si/Al ratio, framework cations, etc.) is often derived from the synthetic route taken and any post-synthesis treatment steps used for activating the zeolite.

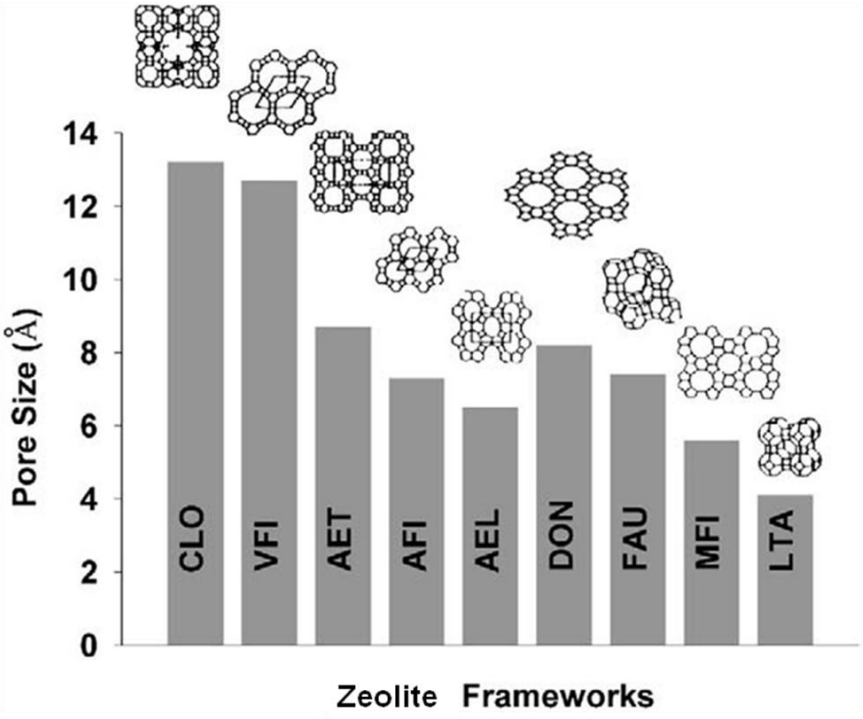

Figure 1.5. Range of zeolite structures and pore sizes.[35]

Zeolites have been traditionally used as adsorbents, ion exchange resins and catalysts.[36] While zeolites have been used primarily in pressure swing adsorption separation processes (*e.g.*, air separations), there has been an increase in research activity using these materials as membranes.[13,37] However, there have been very limited studies on the types of zeolites used in mixed-matrix membranes (IZA database zeolite code): MFI, CHA, and LTA. There are several small-pore (8 T-atom rings or less) that have promising application for CO_2/CH_4 separations.[21–23,38] Specifically, zeolites RHO and

DDR have pore sizes within the range required for molecular sieving of CO_2/CH_4 gas mixtures (see Figure 1.6).[39–41] Zeolite DDR has already shown promise for membrane separations of CO_2/CH_4; several studies have grown DDR on supports of alumina and stainless steel with selectivity as high as 150.[42,43] Zeolite RHO has only been studied as an adsorbent; its pore window has shown some flexibility as a result of CO_2 adsorption and little to no adsorption of CH_4 in the material.[44] Considering that surface functionalization methods have been used for different zeolite structures already (MFI and LTA), it is likely these same methods will work for both RHO and DDR. What effect these methods will have on the separation properties once the zeolite is embedded in the polymer matrix will provide insight into the breadth these functionalization methods could provide for making different composites.

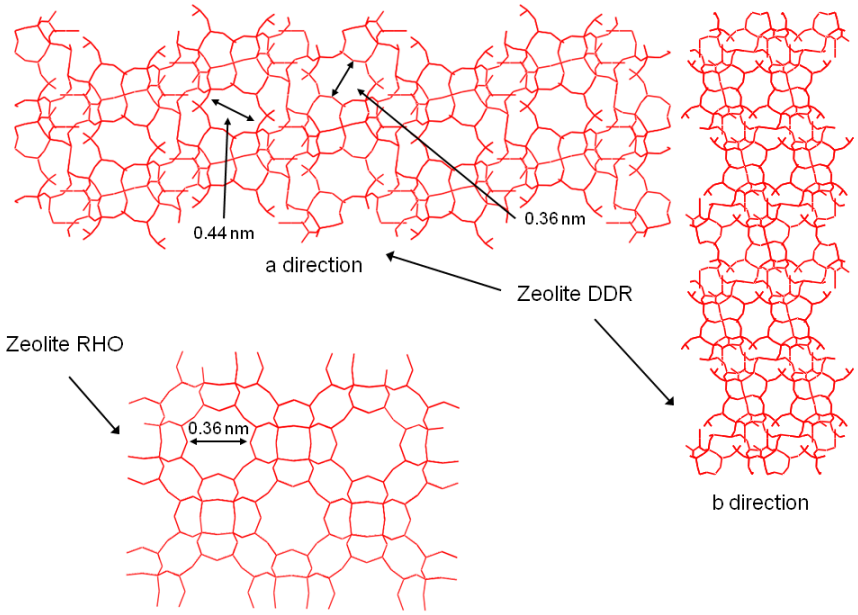

Figure 1.6. Wireframe structures of zeolites DDR and RHO showing small-pore windows capable of molecular sieving CO_2/CH_4.

1.4.2 Metal-Organic Frameworks

Metal-organic frameworks (MOFs) are classified as coordination polymers composed of a transition metal center linked together by some organic molecule that forms a continuous, porous framework.[28] These materials were previously difficult in activating to take advantage of the highly porous networks, but advances have provided a range of materials with different transition metal centers and organic linkers with many different functional groups. Typically, MOFs are synthesized under solvothermal or hydrothermal conditions, but more recently, research activity has shown these materials can be made at room temperature.[45,46]

A subclass of MOFs named zeolitic imidazolate frameworks (ZIFs) are made of zinc (or sometimes cobalt) metals connected by imidazolate linkers, and these materials form zeolite-like structures and topologies analogous to zeolites (SOD, LTA, RHO).[29,47,48] These materials have been shown to easily form under facile conditions and are robust to a number of solvents and even concentrated aqueous alkaline solutions.[48] Of this subclass, ZIF-8 (structure shown in Figure 1.7) has been studied extensively for a number of applications and is one of the few MOFs produced commercially. Some ZIF structures have been formed by only having certain organic linker combinations and ratios in the reaction solution.[49] It is not well understood if the adsorption and separation properties of ZIFs are greatly affected by changing these linker ratios but keeping the same crystal structure.

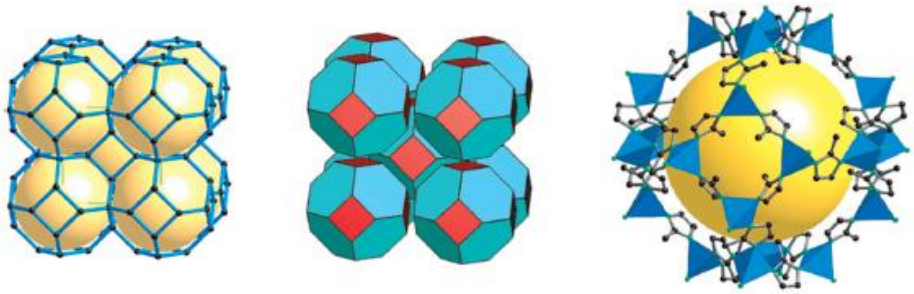

Figure 1.7. Unit cell and topology of ZIF-8 crystal structure.[48]

Like zeolites, MOFs can also be used for adsorption and membrane applications. There have been a number of studies more recently, showing that continuous MOF membrane layers can be grown on supports using similar techniques for zeolite membrane fabrication.[10,50] Additionally, some studies have shown that MOFs easily adhere with polymers in mixed-matrix membrane fabrication.[30] However, the fabrication process has so far not been studied to understand if there are any effects on the MOF separation properties during membrane formation. This is important to understand since often the pure MOF membrane studies do not agree with the mixed-matrix membrane studies in terms of separation performance.

1.5 Research Objectives and Strategy

The focus of this thesis is to examine nanoporous materials for the application of natural gas purification by using both adsorption and mixed-matrix membranes as means for evaluating separation performance of CO_2 and CH_4. In addition, it is important to also study the effects that membrane processing has on MOF materials in order to help in evaluating mixed-matrix membrane separation performance.

1. *Develop a synthetic method for mixed-linker ZIFs that have tunable pore sizes and surface functionality to tune CO_2/CH_4 separations*

Discussed in Section 1.4.2, ZIFs with controlled amounts of certain linkers precipitate a distinct crystal structure, but it is unclear if partial substitution of a linker (*e.g.*, substitution of 2-methylimidazole in forming ZIF-8) would affect the properties of the ZIF without changing its crystal structure. By rational development of a synthetic procedure to alter the linker composition, ZIFs could have pore sizes tuned for a particular gas separation. In addition, introduction of certain functional groups could also allow tuning of the surface properties of the material; this would have effects on the adsorption selectivity, which plays a role in the overall selectivity of a gas pair for both adsorption and membrane applications.

Chapter 3 will show that using a synthetic technique mixed-linker ZIFs can be formed by using linkers from already known ZIF structures (ZIF-7, ZIF-8 and ZIF-90) and also from linkers that do not form any known ZIF structures (*e.g.*, 2-aminobenzimidazole). Using different characterization techniques, it will be shown that this technique produces varying degrees of control on the composition of these ZIFs depending on synthesis conditions and molar ratios of reagents. In addition, the composition of linkers will also show the effects on crystal structure, thermal degradation behavior, and surface area properties.

2. *Study the effects high-intensity ultrasonication has on MOF materials during mixed-matrix membrane fabrication*

Because MOFs have only been recently used in mixed-matrix membranes, the effect of processing conditions on MOF crystal structure and separation performance is not well understood. Ultrasonication is used regularly when preparing dense-film composite membranes. Because the mechanism creates localized areas of high temperature in the solution, this may severely alter the framework crystallinity and composition of a MOF material if not robust enough. ZIF-8 has shown to be very stable in alkaline solutions, but there is no understanding of its behavior when subjected to sonication. Therefore, using a robust MOF can help provide insight in changes to the crystal structure and any other material properties when ultrasonication is used for membrane fabrication.

In Chapter 4, two different sonication techniques are used for dispersing ZIF-8 nanoparticles in a mixed-matrix membrane to show the effects of gas separation performance properties. Structural characterization techniques are used on ZIF-8 nanoparticles subjected to high-intensity sonication to understand changes in the crystal structure and chemical environment that result from this fabrication technique. Also, dynamic light scattering is used to show any changes in particle size distribution as a result of ultrasonication, and microscopy is used to see any effects on particle morphology and to confirm light scattering results.

3. *Study the changes in gas adsorption properties and selectivity of mixed-linker ZIFs for CO_2 and CH_4*

Adsorption studies help elucidate information about an adsorbent's surface properties and can also be used to predict adsorption selectivity of gas mixtures. ZIF-8 has shown to have very low CO_2/CH_4 selectivity in comparison to other adsorbents and synthesizing mixed-linker ZIFs may improve the selectivity for this gas pair. In addition, knowing the adsorption properties of a material before testing its separation performance in a mixed-matrix membrane can help in understanding any changes in the overall selectivity when a filler material is added to a membrane.

In Chapter 5, several mixed-linker ZIFs are chosen to explore the changes in gas adsorption properties for CO_2 and CH_4 using a custom built adsorption apparatus. In addition, some of these samples are also reacted with ethylenediamine to produce a functionalized material that also changes the adsorption properties. Measurements are done at different temperatures to obtain heats of adsorption values, and ideal adsorbed solution theory and breakthrough simulations of a fixed bed adsorber column are used to predict the adsorption selectivity and performance of these materials in mixtures of CO_2/CH_4.

4. *Demonstrate mixed-linker ZIFs can improve separation performance of commercially-available polymer membranes for CO_2/CH_4 separations and develop structural-property relationships of mixed-linker ZIFs for gas separation performance*

Commercial polymer membranes have well-understood gas separation performance and plasticization behavior. By incorporating mixed-linker ZIFs to form mixed-matrix membranes, the effect on gas separation performance from these mixed-linker ZIFs can be well-understood. In addition, composite membrane models can help predict the permeability and selectivity of a mixed-linker ZIF based on the composite membrane experimental results. With knowing the adsorption properties, diffusion properties can be predicted from these models, giving a comprehensive understanding of the gas separation properties of mixed-linker ZIFs.

Chapter 6 shows the study of using mixed-linker ZIFs in a commercially-available polyimide. The changes in separation performance with changing linker composition are explored for a series of these ZIFs embedded in a polymeric matrix. Using the time-lag method, both the permeability and diffusivity changes of each membrane are examined to find the relative changes originating from linker substitution in the ZIF-8 structure. In addition, mixed gas permeation is used to assess ZIF-containing composite membranes under more realistic concentrations of CO_2 in the gas feed. Hollow fiber membrane simulations are used to evaluate the performance of membranes containing mixed-linker ZIFs with mixed gas permeation results.

1.6 References

(1) Annual Energy Outlook 2011. *Energy Information Administration* DOE/EIA–0383(2011).

(2) Overview of Natural Gas www.naturalgas.org (accessed Oct 19, 2012).

(3) Baker, R. W.; Lokhandwala, K. *Ind. Eng. Chem. Res.* **2008**, *47*, 2109–2121.

(4) Koros, W. J.; Fleming, G. K. *J. Membr. Sci.* **1993**, *83*, 1–80.

(5) Koros, W. J.; Lively, R. P. *AIChE J.* **2012**, *58*, 2624–2633.

(6) Robeson, L. *J. Membr. Sci.* **1991**, *62*, 165–185.

(7) Robeson, L. M. *J. Membr. Sci.* **2008**, *320*, 390–400.

(8) Yun, S.; Oyama, S. T. *Journal of Membrane Science* **2011**, *375*, 28–45.

(9) Li, S.; Falconer, J. L.; Noble, R. D. *J. Membr. Sci.* **2004**, *241*, 121–135.

(10) Venna, S. R.; Carreon, M. A. *J. Am. Chem. Soc.* **2010**, *132*, 76–8.

(11) Jang, K.-S.; Kim, H.-J.; Johnson, J. R.; Kim, W.; Koros, W. J.; Jones, C. W.; Nair, S. *Chem. Mater.* **2011**, *23*, 3025–3028.

(12) Haldoupis, E.; Nair, S.; Sholl, D. S. *J. Am. Chem. Soc.* **2012**, *134*, 4313–4323.

(13) Caro, J.; Noack, M. *Micropor. Mesopor. Mater.* **2008**, *115*, 215–233.

(14) Huang, A.; Dou, W.; Caro, J. *J. Am. Chem. Soc.* **2010**, *132*, 15562–15564.

(15) Brown, A. J.; Johnson, J. R.; Lydon, M. E.; Koros, W. J.; Jones, C. W.; Nair, S. *Angew. Chem. Int. Ed.* **2012**, *51*, 10615–10618.

(16) Zimmerman, C. M.; Singh, A.; Koros, W. J. *J. Membr. Sci.* **1997**, *137*, 145–154.

(17) Mahajan, R.; Koros, W. J. *Ind. Eng. Chem. Res.* **2000**, *39*, 2692–2696.

(18) Moore, T. T.; Mahajan, R.; Vu, D. Q.; Koros, W. J. *AIChE J.* **2004**, *50*, 311–321.

(19) Moore, T. T.; Koros, W. J. *J. Mol. Struct.* **2005**, *739*, 87–98.

(20) Shu, S.; Husain, S.; Koros, W. J. *Chem. Mater.* **2007**, *19*, 4000–4006.

(21) Bae, T.-H.; Liu, J.; Lee, J. S.; Koros, W. J.; Jones, C. W.; Nair, S. *J. Am. Chem. Soc.* **2009**, *131*, 14662–14663.

(22) Bae, T.-H.; Liu, J.; Thompson, J. A.; Koros, W. J.; Jones, C. W.; Nair, S. *Micropor. Mesopor. Mater.* **2011**, *139*, 120–129.

(23) Lydon, M. E.; Unocic, K. A.; Bae, T.-H.; Jones, C. W.; Nair, S. *J. Phys. Chem. C* **2012**, *116*, 9636–9645.

(24) Husain, S.; Koros, W. J. *J. Phys. Chem. C* **2007**, *111*, 652–657.

(25) Jiang, L. Y.; Chung, T. S.; Kulprathipanja, S. *AIChE J.* **2006**, *52*, 2898–2908.

(26) Zhang, Y.; Balkus, K. J.; Musselman, I. H.; Ferraris, J. P. *J. Membr. Sci.* **2008**, *325*, 28–39.

(27) Zornoza, B.; Irusta, S.; Téllez, C.; Coronas, J. *Langmuir* **2009**, *25*, 5903–5909.

(28) Eddaoudi, M.; Moler, D. B.; Li, H.; Chen, B.; Reineke, T. M.; O'Keeffe, M.; Yaghi, O. M. *Acc. Chem. Res.* **2001**, *34*, 319–330.

(29) Phan, A.; Doonan, C. J.; Uribe-Romo, F. J.; Knobler, C. B.; O'Keeffe, M.; Yaghi, O. M.; O'Keeffe, M. *Acc. Chem. Res.* **2010**, *43*, 58–67.

(30) Ordoñez, M. J. C.; Balkus Jr., K. J.; Ferraris, J. P.; Musselman, I. H. *J. Membr. Sci.* **2010**, *361*, 28–37.

(31) Adams, R.; Carson, C.; Ward, J.; Tannenbaum, R.; Koros, W. *Micropor. Mesopor. Mater.* **2010**, *131*, 13–20.

(32) Bae, T.-H.; Lee, J. S.; Qiu, W.; Koros, W. J.; Jones, C. W.; Nair, S. *Angew. Chem. Int. Ed.* **2010**, *49*, 9863–9866.

(33) Cundy, C. S.; Cox, P. A. *Chem. Rev.* **2003**, *103*, 663–702.

(34) Cundy, C. S.; Cox, P. a. *Micropor. Mesopor. Mater.* **2005**, *82*, 1–78.

(35) Payra, P.; Dutta, P. K. In *Handbook of Zeolite Science and Technology*; Auerbach, S. M.; Carrado, K. A.; Dutta, P. K., Eds.; Marcel Dekker, Inc., 2003.

(36) Davis, M. E. *Nature* **2002**, *417*, 813–821.

(37) Bowen, T.; Noble, R.; Falconer, J. *J. Membr. Sci.* **2004**, *245*, 1–33.

(38) Ward, J. K.; Koros, W. J. *J. Membr. Sci.* **2011**, *377*, 75–81.

(39) Den Exter, M. J.; Jansen, J. C.; Van Bekkum, H.; Zikanova, A. *Zeolites* **1997**, *19*, 353–358.

(40) Himeno, S.; Tomita, T.; Suzuki, K.; Yoshida, S. *Micropor. Mesopor. Mater.* **2007**, *98*, 62–69.

(41) Corbin, D. R.; Abrams, L.; Jones, G. A.; Eddy, M. M.; Harrison, W. T. A.; Stucky, G. D.; Cox, D. E. *J. Am. Chem. Soc.* **1990**, *112*, 4821–4830.

(42) Van den Bergh, J.; Zhu, W.; Gascon, J.; Moulijn, J. A.; Kapteijn, F. *J. Membr. Sci.* **2008**, *316*, 35–45.

(43) Van den Bergh, J.; Mittelmeijer-Hazeleger, M.; Kapteijn, F. *J. Phys. Chem. C* **2010**, *114*, 9379–9389.

(44) Palomino, M.; Corma, A.; Jordá, J. L.; Rey, F.; Valencia, S. *Chem. Commun.* **2012**, 215–217.

(45) Wiebcke, M.; Cravillon, J.; Münzer, S.; Lohmeier, S.-J.; Feldhoff, A.; Huber, K. *Chem. Mater.* **2009**, *21*, 1410–1412.

(46) Pan, Y.; Liu, Y.; Zeng, G.; Zhao, L.; Lai, Z. *Chem. Commun.* **2011**, *47*, 2071–2073.

(47) Huang, X.-C.; Lin, Y.-Y.; Zhang, J.-P.; Chen, X.-M. *Angew. Chem. Int. Ed.* **2006**, *45*, 1557–1559.

(48) Park, K. S.; Ni, Z.; Côté, A. P.; Choi, J. Y.; Huang, R.; Uribe-Romo, F. J.; Chae, H. K.; O'Keeffe, M.; Yaghi, O. M. *Proc. Nat. Acad. Sci.* **2006**, *103*, 10186–10191.

(49) Banerjee, R.; Phan, A.; Wang, B.; Knobler, C. B.; Furukawa, H.; O'Keeffe, M.; Yaghi, O. M. *Science* **2008**, *319*, 939–943.

(50) Bux, H.; Feldhoff, A.; Cravillon, J.; Wiebcke, M.; Li, Y. S.; Caro, J. *Chem. Mater.* **2011**, *23*, 2262–2269.

CHAPTER 2

Metal-Organic Framework-Based Mixed-Matrix Membranes: A Review

2.1 Introduction

As global demand for energy rises, better process efficiency is needed for fuel and chemical production to increase the longevity of energy sources. Separation units currently require 45% of the total energy consumed in the downstream petrochemical and manufacturing industries.[1] The benefits of reducing energy consumption can already be seen from the water purification sector, and extension to other separations (*e.g.*, natural gas, olefin/paraffin) is necessary.[1] Membrane technologies may offer these lower energy requirements, and by means of fundamental research on new materials design and membrane processing methods, non-incremental improvements in efficiency may be achieved.

As mentioned in Section 1.3, membrane-based separations can offer better efficiency over more mature technologies such as absorption and adsorption for acid gas separations, but not without trade-offs. To propose new materials for acid gas separations, and other molecular separations, several issues must be considered:

1. Separation performance trade-off between productivity and purity
2. Behavior over a range of operating conditions (pressure, temperature)
3. Effects of impurities and other major components (H_2O, C_3 and higher hydrocarbons, etc.)
4. Materials cost, ageing properties, and lifetime

This Chapter aims to frame the current understanding of using metal-organic frameworks (MOFs) in mixed-matrix membranes (MMMs) for improving gas separation properties. The main issues of interest in this Chapter are: (1) the state of art for synthesizing and modifying MOF materials; (2) the gas transport properties inside MOF materials; (3) stability of MOF materials in the presence of impurities commonly found in real gas streams; and (4) the state of art for mixed-matrix membranes fabricated with MOFs. While this Chapter cannot comprehensively address all issues, relevant comments are made when appropriate. Finally, an outlook on possible directions and necessary studies for MOF-based MMMs is given.

2.2 Metal-Organic Frameworks

MOFs are organic-inorganic hybrid materials that have a metal atom coordinated to an organic linker bridging to another metal atom. These materials are typically porous and form many different structural topologies resulting in a wide variety of pore sizes.[2] Therefore, MOFs may be able to separate many different gases or liquids depending on their adsorption and transport properties. When considering these materials for gas separations, it is important to first distinguish how these separations are performed based on two very different concepts: equilibrium-based separations and kinetic-based separations. Membrane technologies often operate based on a combination of kinetic and equilibrium separations, wherein the differences in both the diffusion rates and sorption affinities of the gas pair being considered can play a role in the separation performance.

Therefore, the pore size, the topology and the surface properties of MOFs can all be expected to affect the resulting overall separation performance.

In this section, several aspects of MOFs are discussed that are important for developing materials for gas separations, specifically focusing on mixed-matrix membranes. The synthesis of MOFs is important to consider if these materials are to replace existing porous materials in mixed-matrix membranes. Typical synthesis routes are discussed, and different routes for altering, or "designing," these materials are also presented. When selecting a MOF material for gas separations, it is important to have some knowledge or estimate of its transport properties. Engineering models are presented that give an easy estimate for permeability and ideal selectivity of a gas pair, and then, known MOF properties, either determined by simulations or experiments, are provided as examples. Finally, it is also important to consider the relative stability of a MOF material for any anticipated impurities in a gas feed stream. Examples from the literature on the stability of MOFs in the presence of water and gaseous impurities are provided to give insight into the expected behavior for different classes of MOF materials.

2.2.1 Synthesis and Design of Metal-Organic Frameworks

When selecting a MOF material for replacing current filler materials in mixed-matrix membranes, not only are the crystal structure and surface properties important for consideration, but also the required reagents and steps to synthesize and "activate" (*e.g.*, remove occluded solvent molecules) the material for use in a gas separation must be understood. While these are not necessarily limiting factors in materials selection, they

will ultimately determine the research still needed to make these materials competitive to commercially-available technologies. It is also important to note that some MOFs are already commercially available, but are manufactured on small scales relative to other commercially-available porous materials.

The conventional synthesis of MOFs can be categorized by two methods: solvothermal and non-solvothermal.[2] Solvothermal synthesis represents a set of conditions that require heating solutions above the boiling point of the solvent in a sealed vessel under autogeneous pressures; non-solvothermal synthesis is performed at or below the boiling point and under atmospheric pressure. This distinction can be important in determining preliminary costs and expected properties of MOF materials for gas separations. For instance, synthesis of ZIF-8 can be done with methanol as the solvent at ambient temperatures and atmospheric pressure.[3–5] With a low boiling point solvent, there is little need for high-temperature activation of the MOF after synthesis, reducing the steps required to use this material. Other synthesis techniques for MOFs do exist, and details can be found elsewhere.[2]

Table 2.1 shows the synthesis conditions for several MOFs, including solvent, temperature, and reagent sources, and whether the MOF is commercially available. One important observation is that MOFs with less costly organic linkers (ZIF-8, HKUST-1, MIL-53) are already commercially available, while the others are not. Developing synthetic routes to produce these linkers by a more cost effective route may result in rapid commercial development of other MOFs. Another important note is that few MOFs have been scaled up to large batches.[2] While this may be relatively easy to perform for

non-solvothermally synthesized materials, MOFs made under solvothermal conditions would require very expensive reactors to replicate the same conditions due to the required autogeneous pressures generated during synthesis.

Table 2.1. Synthesis requirements for several common MOFs.

MOF Code	Solvent[a]	Temperature (°C)	Linker[b]	Metal	Commercial?
MOF-5[6]	DEF	130	H_2BDC	Zn^{2+}	N
MOF-74[7]	DMF/EtOH/H_2O	125	H_2DOBDC	Mg^{2+}	N
HKUST-1[8]	DMSO/MeOH	RT	H_3BTC	Cu^{2+}	Y (BASF)
MIL-53[9]	H_2O	220	H_2BDC	Al^{3+}	Y (BASF)
ZIF-8[5]	MeOH	RT	2-MeIM	Zn^{2+}	Y (BASF)
ZIF-20[10]	DMF	65	Pur	Zn^{2+}	N

[a]DEF – diethylformamide, DMF – dimethylformamide, EtOH – ethanol, DMSO – dimethylsulfoxide, MeOH – methanol; [b]H_2BDC – benzenedicarboxylic acid, H_2DOBDC – 2,5-dihydroxyl-benzenedicarboxylic acid, H_3BTC – benzenetricarboxylic acid, 2-MeIM – 2-methylimidazole, Pur – purine

Another aspect of the synthesis of MOF materials is making crystallites suitable for membrane fabrication. Typically, solvothermal synthesis techniques can result in very large crystallites (>100 μm) that are too large for MMM applications. To avoid using solvothermal conditions, a technique has been developed that dissolves the reagents in a solvent, and then a "non-solvent" is added to force the crystal to precipitate by rapid solubility change of the nuclei.[8,11] This may be referred to as non-solvent induced crystallization (NSIC). As shown in Figure 2.1, Bae et al. synthesized ZIF-90 particles using this technique and showed that using different non-solvents resulted in different

crystallite sizes. Other characterization methods revealed that the non-solvents used also affected the textual properties of ZIF-90 based on N_2 physisorption and the gas separation performance in MMMs.[11]

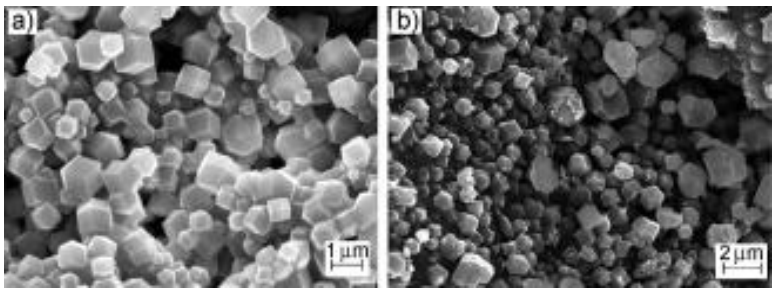

Figure 2.1. Using NSIC technique, ZIF-90 was synthesized, and different particle sizes were obtained depending on the non-solvent used.[11]

The "designable" aspect of MOFs makes them very appealing for developing materials tailored to different gas separation applications. There are a variety of means to design MOFs for different applications, and reviews and studies can be found elsewhere.[12–15] Pertaining to kinetic separations, there are specific methods for tuning pore sizes and surface properties by either postsynthetic modification (PSM) or mixed-linker synthesis.[12,16–18] PSM allows the introduction of a pendant organic functional group to interact with a specific gas in the pores of the MOF. This technique has been used to successfully graft alkylamines to open-metal center MOFs to increase affinity for CO_2, therefore enhancing the adsorption selectivity.[7,19] Mixed-linker synthesis techniques have been explored less than PSM, possibly due to the difficulty in controlling the crystal phases formed during synthesis. Shown in Figure 2.2, Zhang et al. were able to synthesize mixed-linker MOF materials containing imidazolate and triazolate bridging linkers that formed the same crystal structure.[16] Using linkers that form different crystal

structures may require more rigorous synthesis design approaches to form single crystal phases, but could result in tuning pore sizes and surface properties to a greater extent.

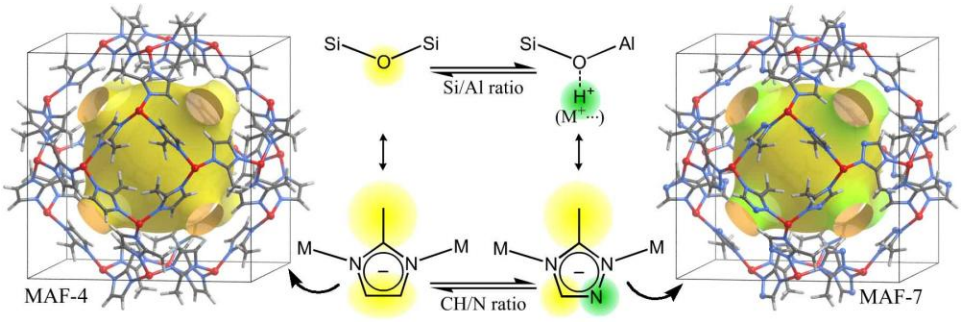

Figure 2.2. Using similar bridging linkers, MOFs with varying linker composition can be synthesized to tune surface properties.[16]

2.2.2 Adsorption and Transport Properties

In selecting a MOF or any porous material to separate a gas pair, it is important to understand the likely adsorption and transport properties. Detailed transport models can relate the expected permeability and selectivity in a microporous material to its adsorption and diffusion properties. The flux of a pure gas or gas mixture through a membrane is defined as:

$$N_i = -D_i \nabla q \tag{2.1}$$

where N_i is the flux of component i in the MOF, D_i is the diffusivity, and ∇q is the concentration gradient. If q can be defined by an adsorption isotherm model (*e.g.*, the Langmuir isotherm in Equation 2.2), the flux equation becomes:

$$N_i = -D_i \nabla \left(\frac{q_{sat,i} b_i p_i}{1 + b_i p_i} \right) \tag{2.2}$$

where $q_{sat,i}$ is the saturation capacity of the MOF, b_i is the affinity constant, and p_i is the partial pressure of gas. If the flux is assumed to occur linearly over a fixed length, l, with a negligible pressure drop, Equation 2.2 is simplified to:

$$N_i = D_i \frac{q_{sat,i}}{l} \ln \left(\frac{1 + b_i p_{i,f}}{1 + b_i p_{i,p}} \right) \tag{2.3}$$

where f represents the feed side and p is the permeate side. Because the permeability of a material is normalized by the pressure gradient and the length, the flux is related to permeability, P_i, by:

$$N_i = P_i \frac{\left(p_{i,f} - p_{i,p} \right)}{l} \tag{2.4}$$

and the diffusion and adsorption properties are related to the intrinsic permeability by the following relationship:

$$P_i = \frac{D_i q_{sat,i}}{\left(p_{i,f} - p_{i,p} \right)} \ln \left(\frac{1 + b_i p_{i,f}}{1 + b_i p_{i,p}} \right) \tag{2.5}$$

This equation represents the permeability of a single component gas through any nanoporous material described by the Langmuir isotherm for its adsorption properties. In order to estimate mixed gas permeation, Maxwell-Stefan equations must be used.[20] To obtain the ideal permselectivity of a nanoporous material, the ratios of two permeability values can be taken:

$$\alpha_{i/j} = \frac{P_i}{P_j} \tag{2.6}$$

Because the permeability is dependent on both the adsorption and the diffusion properties, it is important to evaluate both when selecting a material; however, for molecular sieve materials, diffusion selectivity plays a major role in the overall permselectivity.[21]

The adsorption properties of many MOF materials have been studied and characterized, and there are several reviews focusing on the gas separation properties by adsorption.[22–26] When comparing adsorption properties and selectivity of gas pairs for MOF materials, it is important to consider commercially available adsorbents as references. Henry's law selectivities of BPL carbon at 303 K have been reported to be 2.5, 7.5, and 11.1 for CO_2 relative to CH_4, CO, and N_2, respectively.[27] Table 2.2 compares the predicted ideal selectivity from Henry's constants of several ZIFs with BPL carbon. The overall trend shown in Table 2.2 is that ZIFs with very polar functional groups on the bridging organic linker (*e.g.*, ZIF-78) lead to higher Henry's constant selectivities when compared to a non-polar linker (*e.g.*, ZIF-8).

Table 2.2. Ideal selectivity predicted from Henry's constants at 303 K for CO_2/CH_4 and CO_2/N_2 gas pairs and the limiting pore diameter of each adsorbent.

Sample	Henry's Law Ideal Selectivity		Limiting Pore Diameter (nm)
	CO_2/CH_4	CO_2/N_2	
BPL Carbon[27]	2.5	11	2-3
ZIF-8[28]	1.8	5.1	0.34
ZIF-78[29]	45	50	0.38
ZIF-82[29]	32	35	0.81
ZIF-95[30]	4.3	18	0.38
ZIF-100[30]	5.9	25	0.34

As mentioned above, both adsorption and diffusion may play an important role in the observed gas pair selectivity. When selecting a filler material for a MMM, it is important to select a material with the correct pore size range. In addition, knowing the diffusion properties of a MOF material *a priori* to using it in a MMM is very useful so the filler and polymer matrix can be properly matched in terms of permeability values. Molecular simulations have played a crucial role in evaluating MOFs for different gas pairs. Keskin et al. performed simulations on both $Cu_3(BTC)_2$ and MOF-5, examining the diffusion and adsorption behavior with the gas pairs CO_2/H_2, CH_4/H_2, and CO_2/CH_4.[31] Although $Cu_3(BTC)_2$ showed favorable adsorption selectivity for CH_4/H_2, diffusion selectivity favored the smaller H_2 molecules, giving an overall low molecular separation selectivity. In addition, the authors also showed that CO_2/CH_4 separation in $Cu_3(BTC)_2$ membranes was determined almost entirely by adsorption selectivity due to a diffusion

selectivity close to 1. Therefore, it is critical to properly select a material that would have a pore size small enough to give diffusion selectivity.

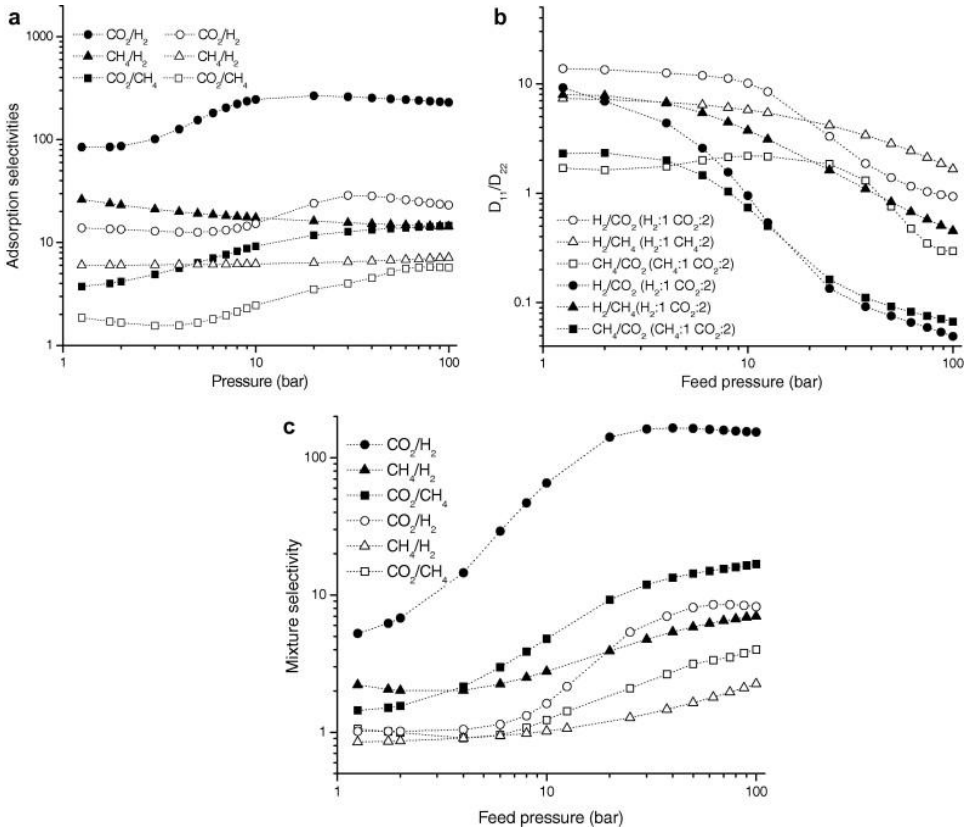

Figure 2.3. (**a**) Adsorption selectivity, (**b**) diffusion selectivity, and (**c**) mixture selectivity of gas pair mixtures in $Cu_3(BTC)_2$ (closed symbols) and MOF-5 (open symbols).[31]

However, unlike many zeolite materials wherein a precipitous drop in diffusion rates can be expected once the gas molecule size approaches the crystal pore diameter,[32] MOF materials can have greater inherent lattice flexibility associated with the linkers bound to the metal centers when compared with purely inorganic molecular sieves. If a MOF has this flexibility, its nominal pore size may not be an accurate assessment of its potential separation performance for a target gas pair.[33] ZIF-8 has been shown to undergo "gate-opening" upon adsorption of N_2 molecules at 77 K.[34] At a certain threshold

pressure (P_{GO}), the organic linkers bridging the Zn^{2+} metal centers rotate to allow more gas molecules to adsorb into the crystal. The consequence of this rotation is a larger effective diameter than what is predicted from the crystal structure of ZIF-8. Zhang et al. studied the diffusion coefficients of ZIF-8 for a wide range of gases (H_2 up to iso-C_4H_{10}).[35] The authors found that instead of molecular sieving occurring at the crystallographic pore size (0.34 nm) ZIF-8 actually shows a drop in diffusivity at 0.4 nm, indicating that gate-opening can severely alter the separation performance. As a result, the predicted CO_2/CH_4 performance is very low compared to other nanoporous materials.[21] Therefore, when selecting a MOF material to use for membrane applications, it is important to consider if there is any evidence of flexibility and if there are adverse consequences concerning diffusion selectivity as a result of flexibility properties.

2.2.3 Stability of MOF Materials

Although most inorganic, porous materials (*e.g.* zeolites) have shown robust thermal and chemical stability, use of metal-organic frameworks for large scale separations has received skepticism due to the poor stability of some MOFs in the presence of water and various impurities. Table 1.1 showed that there can be a significant concentration of both H_2S and H_2O, and in flue gas streams, impurities, such as SO_x and NO_x, can also be present. It has already been shown that zeolites with low silicon-to-alumina ratios can be adversely affected by the presence of water when considering transport and adsorption properties;[36] therefore, studying the effects of these impurities in MOFs, which are considered to be less stable, is important in moving towards their use in industrial applications.

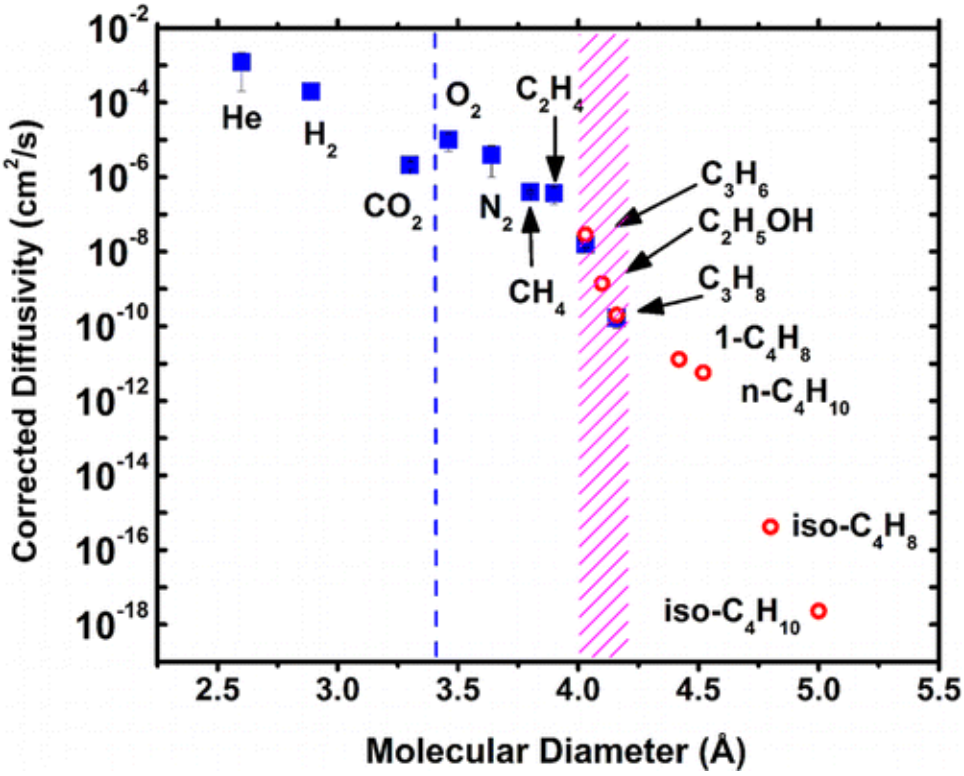

Figure 2.4. Corrected diffusivities of gases in ZIF-8, showing molecular sieving occurring at higher pore size than expected from crystallographic data.[35] The dashed blue line represents the limiting pore diameter of ZIF-8 determined from X-ray crystallography, and the shaded red area is the effective molecular sieving diameter based on the diffusion data.

When considering the water stability of a MOF material, it is important to consider two aspects: (1) the coordination of the metal atoms to the organic linkers (*e.g.*, open metal center or coordinatively-saturated metal center); and (2) the bond strength between the metal and the organic linker.[37] A common technique for testing water stability has been to boil powder MOF samples in water, and sometimes exposure to water vapor, followed by analyzing with X-ray diffraction (XRD) to confirm that the crystal structure is maintained.[38,39] ZIF-8 has been shown to exhibit excellent crystal structure stability in boiling water, as well as various solvents and alkaline solutions;

however, the authors did not examine its porosity after exposure to these solutions.[38] As pointed out by Schoenecker et al., only examining the XRD patterns of MOF materials fails to take into account changes in adsorption and diffusion properties.[40] Using other characterization techniques, changes in adsorption properties or metal coordination environments can be confirmed. For example, Mg-MOF-74 is synthesized in water, which remains bound to the Mg^{2+} sites following synthesis. Schoenecker et al. showed that although Mg-MOF-74 maintained its crystal structure after exposure to 90% relative humidity (RH) of water vapor, the material exhibited 83% loss of surface area even after reactivation, suggesting that Mg-MOF-74 may not be useful in gas streams containing high concentrations of water vapor.[40] Other researchers have suggested that Mg-MOF-74 undergoes disordered rearrangement of coordinated Mg^{2+} metal centers upon dehydration of the material after exposure to water, and the original coordination symmetry of Mg^{2+} can only be obtained reversibly after exposure to 100% RH water.[41] This disordered rearrangement in coordination may explain the drastic changes in adsorption properties that were observed by Schoenecker et al.

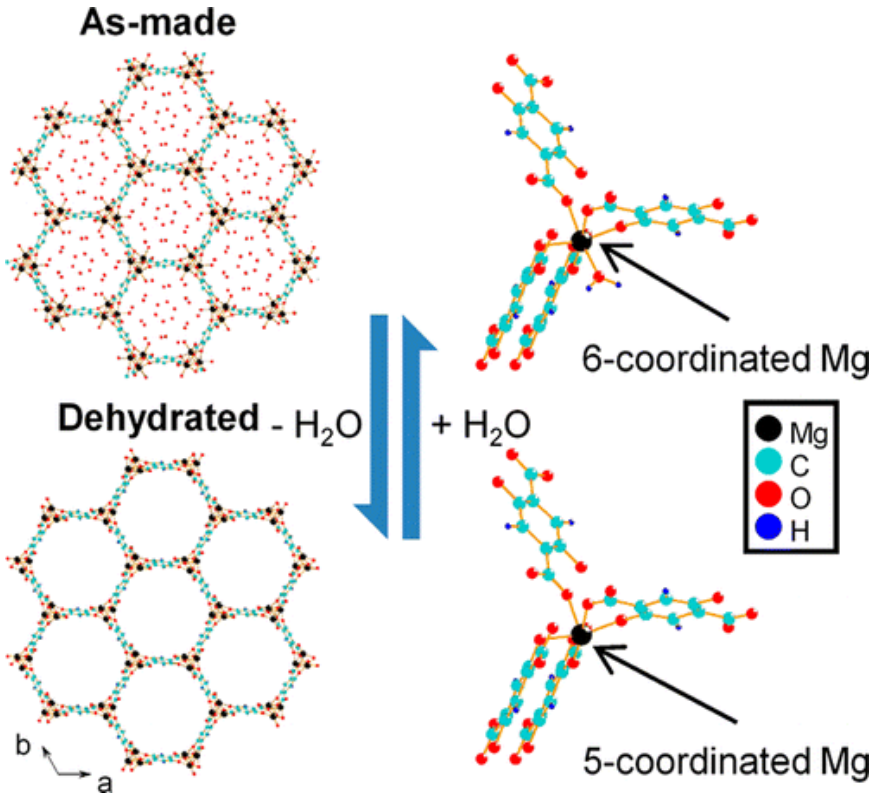

Figure 2.5. Upon dehydration of Mg-MOF-74, Mg^{2+} metal center undergoes a coordinative rearrangement that is near irreversible and may change the overall adsorption properties.[40,41]

Although some classes of MOFs have inherent water stability (*e.g.*, UiO-66, ZIF-8), several strategies have been developed for generally improving water stability in MOFs.[42–45] One common method is to develop syntheses that produce isostructural MOF materials with different organic functional groups or metal centers. Jasuja et al. found that using polar functional groups (-Br, -NO_2, -OH, etc.) had no effect on the water stability when exposed to water vapor at 90% RH; however, non-polar, alkyl- or phenyl-type functional groups produced materials with much higher stability, as determined by BET analysis.[42] Kang et al. examined the chemical stability of the isostructural M-BDC (or M-MIL [Material of Institut Lavoisier]) series of MOFs, examining both surface area and XRD patterns after exposure to basic, acidic, and neutral H_2O solutions.[44] In general,

the trend found for stable MOFs with differing metal centers was Cr- > Al- > V-BDC, where V-BDC showed complete loss of crystallinity and surface area. The authors concluded that the stability was derived from inertness or lack of lability of the metal centers, which is the tendency of the organic linkers to be released and to rebind rapidly in an aqueous solution. Bond strength was not considered the common factor between these materials due to average bond strength following V-O > Al-O > Cr-O, and coordination environment was ruled out because all of the M-BDC materials form the same isostructural binding network. Therefore, if the metal center is highly labile and submerged in a solvent, the degree of stability may be lessened, but the authors of this study did not conclude whether this same trend was observed for water vapor as well.

When examining MOF stability in the presence of gaseous impurities (*e.g.*, SO_x, NO_x, H_2S), many of the same characterization techniques (XRD, BET) can be used, as well as cyclic studies to understand if degradation is caused immediately or over many cycles of use. Several MOFs have been studied by both experiments and simulations to understand the effects of impurities on adsorption properties, typically in the context of CO_2 separations.[46–51] Of the MIL class of MOF materials,[46] isostructural M-BDC (V, Al, Cr, Fe) materials showed no degradation of methane adsorption after exposure to H_2S, except for Fe-BDC, suggesting that H_2S only physically adsorbs on V-, Al-, and Cr-BDC materials; however, MIL-100(Cr) showed degradation of the quantity of methane adsorbed after exposure to H_2S at 303 K (Figure 2.6). BET analysis showed 14% loss of surface area compared to the material before exposure. MIL-101, isostructural to MIL-100, showed no change in methane adsorption properties before and after exposure to

H_2S and maintained the same BET surface area. These results suggest that both the metal center and organic linker can play a crucial role in the stability of the MOF material when exposed to various impurities; however, no hypothesis was offered to help narrow the cause for degradation in some MIL-type materials, and not others.

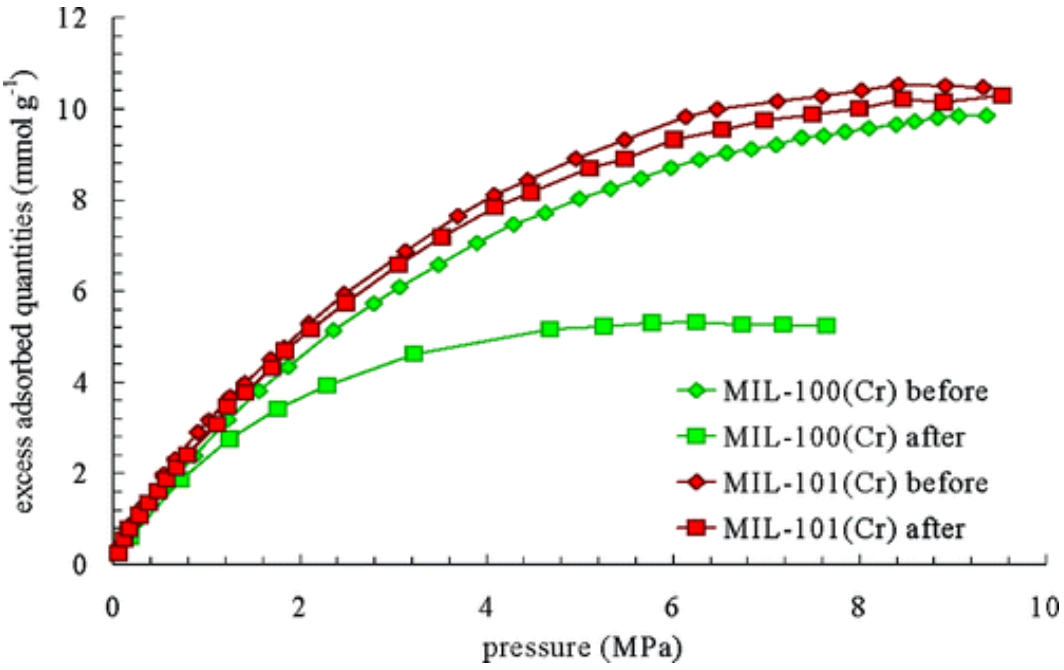

Figure 2.6. Methane adsorption properties of MIL-100(Cr) and MIL-101(Cr) before and after exposure to H_2S at 303 K.[46]

2.3 Metal-Organic Framework-Based Mixed-Matrix Membranes

As discussed in Chapter 1, membrane-based gas separations provide a promising route to lower energy requirements and to improve process efficiency, but due to limitations in materials, polymeric membranes have inherent limitations in membrane performance when considering permeability and selectivity. Although several advanced membrane technologies exist that could replace pure polymeric membranes (*e.g.*, carbon molecular sieves), mixed-matrix membranes provide a theoretically easy route due to the

same processibility and fabrication requirements as polymeric-based membranes, but with higher potential membrane performance due to the filler, in this case, MOF or zeolite, materials.

2.3.1 Mixed-Matrix Membrane Fabrication

Like zeolite-based mixed-matrix membranes, it is expected that MOF-based MMM materials require the same preparation steps for fabricating dense film and hollow fiber membranes. In general, the first step required is to prepare a dispersion of the MOF in the polymer casting solution. To properly disperse MOFs or zeolites in a solution on a lab scale, ultrasonication is widely used; however, there have been examples of using high-shear rate stirring and other preparative methods for fabricating membranes containing filler materials with different morphologies.[52,53] Poor particle dispersion in solvents is one of several important challenges for successful membrane formation.[54,55] Typically, poor dispersion leads to aggregation and results in defective membrane performance. It is important to point out that increasing the particle loading in MMMs normally results in poorer dispersion due to more likely particle aggregation as the volume fraction of particles increases in the solvent.[52]

Additives to the solution can typically alleviate dispersion problems for membrane fabrication if the additive is able to absorb to the surface of the particle and prevent aggregation from occurring. These additives may include dilute polymer dope solutions, surfactants, coupling agents and ionic liquids.[56–59] However, with the latter three additives, there may be significant effects to the gas permeation properties,

sometimes resulting in lower expected permeability values. Therefore, the best solution may be to use a dilute polymeric solution that is ultimately a part of the polymer matrix in the composite membrane.[60,61] By doing so, no new components are introduced to the composite membrane system, and separation performance is then more likely enhanced by the filler material and not a tertiary phase. However, there has been some work done to show that tertiary phases may enhance the MMM properties if chosen properly.[58]

Once proper dispersion has been achieved, the polymer is added to obtain the desired ratios of the two phases. A dense film is obtained by either pouring the mixed-matrix membrane solution into a Petri dish or pouring the solution across a glass or Teflon plate and pulling a uniform casing knife over the membrane solution. Because solvents used for membrane preparation typically have low boiling points (< 333 K), it may be necessary to use a controlled environment to prevent rapid evaporation and air bubble formation in the MMM.[62] Many research groups have used glove bags to form an atmosphere containing the polymer dope solvent, and this slows the effective evaporation rate. Ultimately, scanning electron microscopy (SEM) can easily determine if the resulting membrane formed without significant defects by analyzing cross sections of the dense film membranes. The last step is to remove any remaining solvent before permeation testing. This is done by thermal annealing under vacuum with a temperature high enough to remove the solvent. Figure 2.7 shows a generalized procedure of the different fabrication steps.[63]

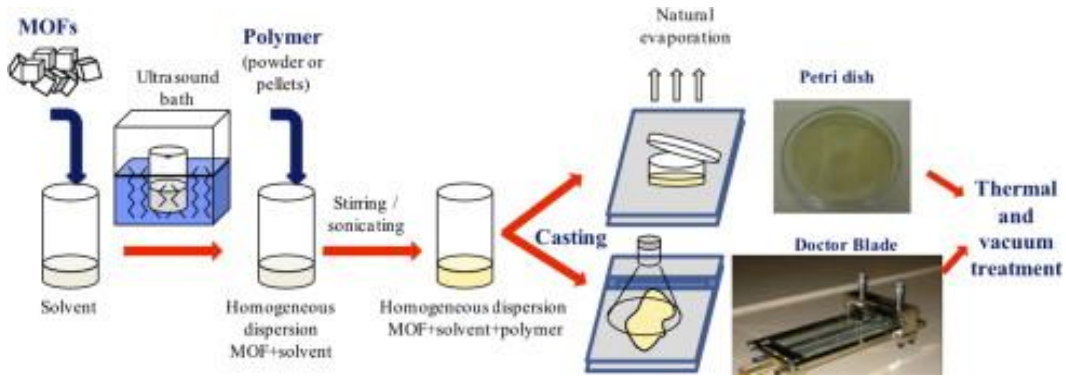

Figure 2.7. Generalized procedure for the fabrication of mixed-matrix membranes in the form of flat films.[63]

As discussed in Section 1.3.3, membrane fabrication can result in a number of different permeability behaviors depending on the membrane morphology and particle dispersion in the polymer matrix. If poor dispersion results from the fabrication step, expected behavior will be either a "sieve-in-a-cage" or "leaky-interface" morphology.[54,64] While these are easy to see in a microscope, other defects may not be immediately obvious. Because MOFs may contain organic functional groups, it is possible for MOF surfaces to react with the surrounding polymer matrix depending on the organic functionality. This is analogous to the case of silylation of zeolite surfaces to create good adhesion with the polymer matrix, and the resulting composite may have a "rigidified" interface.[59,65,66] Therefore, when selecting both a MOF material and the surrounding polymer matrix, it is important to consider adverse reactions of functional groups between these two materials.

2.3.2 Performance of MOF-based Mixed-Matrix Membranes

Because there are many factors controlling the effective transport properties of gases in MMMs, it may not always be obvious why a particular membrane combination

may show improved selectivity.[54,55] When reporting new membrane data, it is necessary to consider as many factors as possible: dispersion, polymer chain adhesion and rigidification, MOF flexibility, MOF transport properties, etc. As a consequence, it may be difficult to properly interpret all membrane data in the literature. The subsequent review of MMM performance from the literature was chosen based on the following: (1) the transport properties of $Cu_3(BTC)_2$ have already been explored by simulations and discussed in Section 2.2.2, providing a basis to compare MMM data; (2) ZIF materials are to be explored in the remaining Chapters of this thesis and are of interest for using in different gas separation applications; and (3) interesting trends in membrane performance that depend on organic functionality in MOFs embedded in MMMs, which will be relevant in later discussion in this thesis.

Mixed-matrix membranes containing $Cu_3(BTC)_2$ were some of the first composite membranes containing MOF materials to be explored. As pointed out in Section 2.2.2, it was expected that MMMs containing $Cu_3(BTC)_2$ will likely not provide any apparent CO_2/CH_4 separation improvements based on the transport properties. One of the first examples[67] using $Cu_3(BTC)_2$ used poly(dimethylsiloxane) (PDMS) and poly(ethersulfone) (PSF) as the polymer matrix, and as expected, there was either no perceived trend in the change in selectivity for the gases explored (H_2, N_2, O_2, CO_2, CH_4) or an overall drop in the permselectivity for PDMS. However, PSF MMMs did show an initial increase in selectivity at 5 wt% loading of $Cu_3(BTC)_2$, and then a significant drop at 10 wt%. This implies that there may be an optimal loading for $Cu_3(BTC)_2$ in glassy polymers to achieve a greater selectivity, but the enhancement of selectivity cannot be

simply explained as being due to inclusion of $Cu_3(BTC)_2$ because Figure 2.3 shows there is a lower permselectivity expected for CO_2/CH_4 for $Cu_3(BTC)_2$ ($\alpha \sim 10$) compared to pure PSF ($\alpha \sim 18$).

Other MMMs containing $Cu_3(BTC)_2$ have shown different trends depending on the polymer matrix used. Zornoza et al.[68] used mixed combinations of filler materials and with a 16 wt% $Cu_3(BTC)_2$/PSF membrane, showed similar behavior to a previous study, where the permselectivity for H_2/CH_4 decreased with the addition of $Cu_3(BTC)_2$. However, when authors have used polyimides (*e.g.*, Matrimid® 5128) as the polymer matrix, most MMMs exhibited an enhancement in permselectivity CO_2-based separations.[69–72] For example, Basu et al.[70,71] have shown in two studies that using $Cu_3(BTC)_2$ with Matrimid® 5128 as the polymer an increase in the selectivity for CO_2/CH_4 separations was observed, even in mixed-gas permeation experiments. In addition, a patent by Liu *et al.*[69] also claimed either maintenance or improvement in permselectivity when using a 30 wt% $Cu_3(BTC)_2$/Matrimid MMM. Although it may be that polyimides have a different interaction with $Cu_3(BTC)_2$ than other polymer matrices, Basu et al.[70] showed there to be no change in the glass transition temperature (T_g) of the polymer, suggesting that the polymer structure was not greatly influenced by the presence of the MOF. Therefore, it may be necessary to perform further investigation of the polymer structure and the influence of $Cu_3(BTC)_2$ using different characterization techniques besides examining T_g.

As discussed in Section 2.2.2, ZIF-8 exhibited an adsorbate-induced framework deformation termed "gate-opening", and this had the consequence of lower than expected separation performance for gases like CO_2/CH_4. It is important to know if this "gate-opening" phenomenon occurs when using ZIF-8 inside a polymer matrix. Although there have been several studies examining the membrane performance of ZIF-8 MMMs, most permeability trends did not show consistent performance as the weight loading is changed for CO_2/CH_4 separations.[52,73] For example, Ordoñez et al.[52] explored the separation performance at different weight loadings for ZIF-8 embedded in Matrimid® 5128. Although there was no overall trend in the separation performance for the MMMs as the weight loading is increased, at 60 wt% ZIF-8 in Matrimid®, the permeability for all gases examined was significantly lower than the pure polymer, and the selectivity of H_2/CH_4 was much higher compared to Matrimid®. This observation implied that as the weight loading for these MMMs was increased there was actually some polymer rigidification that lowers the effective permeability of all gases and enhanced the permselectivity.

Similarly, Song et al.[73] did not observe any consistent trend in the change of the permselectivity for increasing the ZIF-8 weight loading using Matrimid® 5128 as the polymer matrix. However, they were able to show an overall significant increase in the permeability for CO_2. It may be that preparation of the composite membranes was inconsistent from sample to sample, creating this inconsistent trend in selectivity. Díaz et al.[74] used a different polymer matrix than Matrimid® 5128, poly(1,4-phenylene ether-ether sulfone) (PPEES), in their study of ZIF-8 based MMMs. As the weight loading was increased, they observed poorer dispersion of ZIF-8 in the polymer matrix. As such, the

permselectivity for H_2/CH_4 for composite membranes increased at 10 wt% ZIF-8, but then an overall decrease in selectivity was observed as the weight loading was further increased. Dai et al.[56] also observed an enhancement in selectivity when looking at CO_2/N_2 separations using Ultem 1000, a polyimide, as the polymer matrix. Using dense film and hollow fiber membranes, the authors observed a significant improvement in permselectivity at 13 wt% ZIF-8 loading; however, weight loadings beyond this were not explored.

Besides ZIF-8 and $Cu_3(BTC)_2$ as MOF filler materials, there have been several studies using other MOFs, including MIL- and UiO-class materials. In these studies, the authors have normally sought to understand the influence of amine functional groups on the separation performance of different MMMs. Using NH_2-MIL-53 as a filler material, both Zornoza et al.[75] and Chen et al.[76] observed significant enhancement in permselectivity for CO_2/CH_4, with Zornoza observing a permselectivity over 100 for CO_2/CH_4 using a 25 wt% NH_2-MIL-53/PSF membrane. In both studies, the authors observed a precipitous drop in permselectivity at the maximum loading studied. This suggested that poor dispersion again plays a crucial role on the observed membrane performance for MOF-based MMMs. Nik et al.[77] examined different MOF fillers with and without primary amines, while maintaining the same crystal structure. The authors found very little improvement when comparing functionalized and normal MOF fillers at the same weight loading. This was best explained by an adsorption study with NH_2-MIL-53 that showed the influence of primary aromatic amine groups in the MOF is not necessarily the cause for improved CO_2/CH_4 adsorption selectivity, but is instead caused

by changes in the crystal structure with inclusion of the $-NH_2$ group.[78] Considering all of the MOF filler materials examined have aromatic organic linkers similar to NH_2-MIL-53, this may be a likely explanation for little improvement observed for $-NH_2$ functionalized MOFs in composite membranes.

Overall, the general trends of MMM performance data represented in the literature have shown an inconsistent picture for using MOF materials in MMMs. In general, all MOF materials incorporated in MMMs showed high permeability enhancement, unless a highly permeable polymer was used. However, permselectivity for MMMs did not show consistent changes with increasing weight loading, and different studies yielded different results. Indeed, there may need to be a uniform methodology for membrane fabrication and preparation to properly compare membrane performance between different studies. In addition, influences and studies on different fabrication methods (sonication methods, casting solvent, etc.) may yield more useful information on how to properly prepare MOF-based MMMs. A promising aspect of using MOFs in MMMs is the lack of extra processing steps required to provide better adhesion with the polymer matrix, compared to zeolite and other inorganic materials, but the general trends and membrane performance must be more closely scrutinized to draw any useful conclusions from the membrane data.

2.3.3 Mixed-Matrix Membrane Permeation Models

Currently, there exist several different models for predicting composite membrane permeation based on the permeation properties of the polymer and filler and the volume

fraction of the filler material. These models are typically adapted from thermal or electrical conductivity models because permeation is analogous to thermal and electrical conduction in composites.[79] A model often used is the Maxwell model:[80]

$$P_{eff} = P_m \left(\frac{1 + 2\phi \frac{(\lambda_d - 1)}{(\lambda_d + 2)}}{1 - \phi \frac{(\lambda_d - 1)}{(\lambda_d + 2)}} \right) \tag{2.7}$$

where P is the permeability, ϕ is the filler volume fraction, λ_d is the ratio of filler permeability to polymer (P_d / P_m) and subscripts *eff*, *m*, and *d* stand for effective, polymer, and filler phases, respectively. This model assumes a spherical filler phase and is often accurate only at low volume fraction loadings. The Bruggeman model has an improved derivation based on a differential effective medium approach, but has the same limitations concerning the accuracy at higher volume fractions.[81] The Lewis-Nielsen model[82] was originally developed to describe the elastic moduli in composite materials but has been adapted to describe the permeability:

$$P_{eff} = P_m \left[\frac{1 + 2\phi \frac{(\lambda_d - 1)}{(\lambda_d + 2)}}{1 - \psi\phi \frac{(\lambda_d - 1)}{(\lambda_d + 2)}} \right] \tag{2.8}$$

where

$$\psi = 1 + \left(\frac{1 - \phi_{\max}}{\phi_{\max}^2} \right) \phi \tag{2.9}$$

where $\phi_{\max}$ is the theoretical maximum loading for the filler phase and is normally assumed to be 0.64.

All of the above models assume only two phases: the polymer and the filler. In some cases (especially with zeolites), there may be a ternary phase that represents defects, or even an ionic liquid, at the interface.[83] In this case, models are typically solved by assuming two different modes: (1) a mode in which the bulk filler phase is surrounded by an "interphase" with properties different from the polymer or filler; and (2) a mode for the whole membrane where the "interphase" and the filler are lumped together by:

$$\phi_t = \frac{\phi}{\phi + \phi_I} \tag{2.10}$$

where *I* represents the "interphase" ternary volume fraction. This method has been applied successfully for zeolites, but because MOFs typically show good adhesion to a polymer matrix, this method is normally not used for MOF-based MMMs.

Because the above models assume spherical morphology of the filler phase and anisotropic transport, several models have been developed to describe different particle morphologies and mass transport in filler materials.[84–87] Kang et al.[86] have developed a

model for describing transport of nanotubular filler materials and expected membrane performance based on average orientation of nanotube alignment. Although these studies have shown it is possible to derive models for transport while taking into account non-spherical morphologies or more complicated transport mechanisms, in general, the Maxwell model has been the preferred model for predicting filler transport properties based on experimental MMM permeation data. However, this model may not be accurate depending on the membrane system.[79]

2.4 Conclusions

The MOF-based MMM literature is rapidly growing, but several important questions of interest remain. In general, because MOFs have lower chemical and thermal stability than zeolites or other inorganic materials, the influence on different membrane preparation techniques must be studied if any meaningful correlations are to be developed for the materials currently studied. In addition, more careful selection of MOF materials used as fillers needs to be employed. Currently, several MOFs have been used that have very large pore sizes (*e.g.*, $Cu_3(BTC)_2$) that will not be capable of molecular sieving small gases using membrane technology. Since the goal of fabricating MOF/polymer MMMs is to enhance the membrane separation performance, close attention to its crystal structure must be observed in order to properly pick compatible materials with the current suite of polymers that are available for gas permeation membranes.

2.5 References

(1) Koros, W. J.; Lively, R. P. *AIChE J.* **2012**, *58*, 2624–2633.

(2) Stock, N.; Biswas, S. *Chem. Rev.* **2012**, *112*, 933–969.

(3) Wiebcke, M.; Cravillon, J.; Münzer, S.; Lohmeier, S.-J.; Feldhoff, A.; Huber, K. *Chem. Mater.* **2009**, *21*, 1410–1412.

(4) Cravillon, J.; Nayuk, R.; Springer, S.; Feldhoff, A.; Huber, K.; Wiebcke, M. *Chem. Mater.* **2011**, *23*, 2130–2141.

(5) Venna, S. R.; Jasinski, J. B.; Carreon, M. A. *J. Am. Chem. Soc.* **2010**, *132*, 18030–18033.

(6) Mueller, U.; Schubert, M.; Teich, F.; Puetter, H.; Schierle-Arndt, K.; Pastré, J. *J. Mater. Chem.* **2006**, *16*, 626–636.

(7) Choi, S.; Watanabe, T.; Bae, T.-H.; Sholl, D. S.; Jones, C. W. *J. Phys. Chem. Lett.* **2012**, *3*, 1136–1141.

(8) Zhuang, J.-L.; Ceglarek, D.; Pethuraj, S.; Terfort, A. *Adv. Func. Mater.* **2011**, *21*, 1442–1447.

(9) Remy, T.; Ma, L.; Maes, M.; De Vos, D. E.; Baron, G. V.; Denayer, J. F. M. *Ind. Eng. Chem. Res.* **2012**, *51*, 14824–14833.

(10) Hayashi, H.; Côté, A.; Furukawa, H.; O'keeffe, M.; Yaghi, O. *Nature Mater.* **2007**, *6*, 501–506.

(11) Bae, T.-H.; Lee, J. S.; Qiu, W.; Koros, W. J.; Jones, C. W.; Nair, S. *Angew. Chem. Int. Ed.* **2010**, *49*, 9863–9866.

(12) Wang, Z.; Cohen, S. M. *Chem. Soc. Rev.* **2009**, *38*, 1315–1329.

(13) Tanabe, K. K.; Cohen, S. M. *Chem. Soc. Rev.* **2011**, *40*, 498–519.

(14) Kim, M.; Cahill, J. F.; Su, Y.; Prather, K. A.; Cohen, S. M. *Chem. Sci.* **2012**, *3*, 126–130.

(15) Kim, M.; Cahill, J. F.; Fei, H.; Prather, K. A.; Cohen, S. M. *J. Am. Chem. Soc.* **2012**, *134*, 18082–18088.

(16) Zhang, J.-P.; Zhu, A.-X.; Lin, R.-B.; Qi, X.-L.; Chen, X.-M. *Adv. Mater.* **2011**, *23*, 1268–1271.

(17) Ma, B.-Q.; Mulfort, K. L.; Hupp, J. T. *Inorg. Chem.* **2005**, *44*, 4912–4914.

(18) Bae, Y.; Mulfort, K. L.; Frost, H.; Ryan, P.; Punnathanam, S.; Broadbelt, L. J.; Hupp, J. T.; Snurr, R. Q. *Langmuir* **2008**, *24*, 8592–8598.

(19) McDonald, T. M.; Lee, W. R.; Mason, J. A.; Wiers, B. M.; Hong, C. S.; Long, J. R. *J. Am. Chem. Soc.* **2012**, *134*, 7056–7065.

(20) Van den Bergh, J.; Zhu, W.; Gascon, J.; Moulijn, J. A.; Kapteijn, F. *J. Membr. Sci.* **2008**, *316*, 35–45.

(21) Jee, S. E.; Sholl, D. S. *J. Am. Chem. Soc.* **2009**, *131*, 7896–904.

(22) Keskin, S.; Van Heest, T. M.; Sholl, D. S. *ChemSusChem* **2010**, *3*, 879–891.

(23) Bae, Y.-S.; Snurr, R. Q. *Angew. Chem. Int. Ed.* **2011**, *50*, 11586–11596.

(24) Sumida, K.; Rogow, D. L.; Mason, J. A.; McDonald, T. M.; Bloch, E. D.; Herm, Z. R.; Bae, T.-H.; Long, J. R. *Chem. Rev.* **2012**, *112*, 724–781.

(25) Li, J.-R.; Kuppler, R. J.; Zhou, H.-C. *Chem. Soc. Rev.* **2009**, *38*, 1477–1504.

(26) Li, J.-R.; Sculley, J.; Zhou, H.-C. *Chem. Rev.* **2012**, *112*, 869–932.

(27) Sircar, S.; Golden, T. C.; Rao, M. B. *Carbon* **1996**, *34*, 1–12.

(28) Pérez-Pellitero, J.; Amrouche, H.; Siperstein, F. R.; Pirngruber, G.; Nieto-Draghi, C.; Chaplais, G.; Simon-Masseron, A.; Bazer-Bachi, D.; Peralta, D.; Bats, N. *Chem. Eur. J.* **2010**, *16*, 1560–1571.

(29) Banerjee, R.; Furukawa, H.; Britt, D.; Knobler, C.; Keeffe, M. O.; Yaghi, O. M.; O'Keeffe, M. *J. Am. Chem. Soc.* **2009**, *131*, 3875–3877.

(30) Wang, B.; Côté, A. P.; Furukawa, H.; O'Keeffe, M.; Yaghi, O. M. *Nature* **2008**, *453*, 207–211.

(31) Keskin, S.; Liu, J.; Johnson, J. K.; Sholl, D. S. *Micropor. Mesopor. Mater.* **2009**, *125*, 101–106.

(32) Ruthven, D. M. *Principles of Adsorption and Adsorption Processes*; John Wiley & Sons, Inc., 1984.

(33) Bux, H.; Chmelik, C.; Van Baten, J. M.; Krishna, R.; Caro, J. *Adv. Mater.* **2010**, *22*, 4741–4743.

(34) Fairen-Jimenez, D.; Moggach, S. A.; Wharmby, M. T.; Wright, P. A.; Parsons, S.; Düren, T. *J. Am. Chem. Soc.* **2011**, *133*, 8900–8902.

(35) Zhang, C.; Lively, R. P.; Zhang, K.; Johnson, J. R.; Karvan, O.; Koros, W. J. *J. Phys. Chem. Lett.* **2012**, *3*, 2130–2134.

(36) Ruthven, D. M. *Micropor. Mesopor. Mater.* **2012**, *162*, 69–79.

(37) Low, J. J.; Benin, A. I.; Jakubczak, P.; Abrahamian, J. F.; Faheem, S. A.; Willis, R. R. *J. Am. Chem. Soc.* **2009**, *131*, 15834–15842.

(38) Park, K. S.; Ni, Z.; Côté, A. P.; Choi, J. Y.; Huang, R.; Uribe-Romo, F. J.; Chae, H. K.; O'Keeffe, M.; Yaghi, O. M. *Proc. Nat. Acad. Sci.* **2006**, *103*, 10186–10191.

(39) Greathouse, J. A.; Allendorf, M. D. *J. Am. Chem. Soc.* **2006**, *128*, 10678–10679.

(40) Schoenecker, P. M.; Carson, C. G.; Jasuja, H.; Flemming, C. J. J.; Walton, K. S. *Ind. Eng. Chem. Res.* **2012**, *51*, 6513–6519.

(41) Xu, J.; Terskikh, V. V; Huang, Y. *J. Phys. Chem. Lett.* **2013**, *4*, 7–11.

(42) Jasuja, H.; Huang, Y.-G.; Walton, K. S. *Langmuir* **2012**, *28*, 16874–16880.

(43) Jasuja, H.; Zang, J.; Sholl, D. S.; Walton, K. S. *J. Phys. Chem. C* **2012**, *116*, 23526–23532.

(44) Kang, I. J.; Khan, N. A.; Haque, E.; Jhung, S. H. *Chem. Eur. J.* **2011**, *17*, 6437–6442.

(45) Taylor, J. M.; Vaidhyanathan, R.; Iremonger, S. S.; Shimizu, G. K. H. *J. Am. Chem. Soc.* **2012**, *134*, 14338–14340.

(46) Hamon, L.; Serre, C.; Devic, T.; Loiseau, T.; Millange, F.; Férey, G.; De Weireld, G. *J. Am. Chem. Soc.* **2009**, *131*, 8775–8777.

(47) Petit, C.; Mendoza, B.; Bandosz, T. J. *ChemPhysChem* **2010**, *11*, 3678–3684.

(48) Petit, C.; Levasseur, B.; Mendoza, B.; Bandosz, T. J. *Micropor. Mesopor. Mater.* **2012**, *154*, 107–112.

(49) Ding, L.; Yazaydin, A. Ö. *J. Phys. Chem. C* **2012**, *116*, 22987–22991.

(50) Thallapally, P. K.; Motkuri, R. K.; Fernandez, C. A.; McGrail, B. P.; Behrooz, G. S. *Inorg. Chem.* **2010**, *49*, 4909–4915.

(51) Ebrahim, A. M.; Levasseur, B.; Bandosz, T. J. *Langmuir* **2013**, *29*, 168–174.

(52) Ordoñez, M. J. C.; Balkus Jr., K. J.; Ferraris, J. P.; Musselman, I. H. *J. Membr. Sci.* **2010**, *361*, 28–37.

(53) Johnson, J. R.; Koros, W. J. *J. Taiwan Inst. Chem. Eng.* **2009**, *40*, 268–275.

(54) Mahajan, R.; Burns, R.; Schaeffer, M.; Koros, W. J. *J. Appl. Polym. Sci.* **2002**, *86*, 881–890.

(55) Mahajan, R.; Koros, W. J. *Ind. Eng. Chem. Res.* **2000**, *39*, 2692–2696.

(56) Dai, Y.; Johnson, J. R.; Karvan, O.; Sholl, D. S.; Koros, W. J. *J. Membr. Sci.* **2012**, *401-402*, 76–82.

(57) Noble, R. D. *J. Membr. Sci.* **2011**, *378*, 393–397.

(58) Hudiono, Y. C.; Carlisle, T. K.; Bara, J. E.; Zhang, Y.; Gin, D. L.; Noble, R. D. *J. Membr. Sci.* **2010**, *350*, 117–123.

(59) Li, Y.; Guan, H.; Chung, T.; Kulprathipanja, S. *J. Membr. Sci.* **2006**, *275*, 17–28.

(60) Vu, D. Q.; Koros, W. J.; Miller, S. J. *J. Membr. Sci.* **2003**, *211*, 311–334.

(61) Vu, D. Q.; Koros, W. J.; Miller, S. J. *J. Membr. Sci.* **2003**, *211*, 335–348.

(62) Adams, R.; Carson, C.; Ward, J.; Tannenbaum, R.; Koros, W. *Micropor. Mesopor. Mater.* **2010**, *131*, 13–20.

(63) Zornoza, B.; Tellez, C.; Coronas, J.; Gascon, J.; Kapteijn, F. *Micropor. Mesopor. Mater.* **2013**, *166*, 67–78.

(64) Chung, T.-S.; Jiang, L. Y.; Li, Y.; Kulprathipanja, S. *Prog. Polym. Sci.* **2007**, *32*, 483–507.

(65) Husain, S.; Koros, W. J. *J. Membr. Sci.* **2007**, *288*, 195–207.

(66) Hillock, A. M. W.; Miller, S. J.; Koros, W. J. *J. Membr. Sci.* **2008**, *314*, 193–199.

(67) Car, A.; Stropnik, C.; Peinemann, K.-V. *Desalination* **2006**, *200*, 424–426.

(68) Zornoza, B.; Seoane, B.; Zamaro, J. M.; Téllez, C.; Coronas, J. *ChemPhysChem* **2011**, *12*, 2781–2785.

(69) Liu, C.; McCulloch, B.; Wilson, S. T.; Benin, A. I.; Schott, M. E. U.S. Patent 7,637,983, **2009**.

(70) Basu, S.; Cano-Odena, A.; Vankelecom, I. F. J. *J. Membr. Sci.* **2010**, *362*, 478–487.

(71) Basu, S.; Cano-Odena, A.; Vankelecom, I. F. J. *Sep. Purif. Technol.* **2011**, *81*, 31–40.

(72) Hu, J.; Cai, H.; Ren, H.; Wei, Y.; Xu, Z.; Liu, H.; Hu, Y. *Ind. Eng. Chem. Res.* **2010**, *49*, 12605–12612.

(73) Song, Q.; Nataraj, S. K.; Roussenova, M. V.; Tan, J. C.; Hughes, D. J.; Li, W.; Bourgoin, P.; Alam, M. A.; Cheetham, A. K.; Al-Muhtaseb, S. A.; Sivaniah, E. *Energy Environ. Sci.* **2012**, *5*, 8359–8369.

(74) Díaz, K.; López-González, M.; Del Castillo, L. F.; Riande, E. *J. Membr. Sci.* **2011**, *383*, 206–213.

(75) Zornoza, B.; Martinez-Joaristi, A.; Serra-Crespo, P.; Tellez, C.; Coronas, J.; Gascon, J.; Kapteijn, F. *Chem. Commun.* **2011**, *47*, 9522–9524.

(76) Chen, X. Y.; Vinh-Thang, H.; Rodrigue, D.; Kaliaguine, S. *Ind. Eng. Chem. Res.* **2012**, *51*, 6895–6906.

(77) Nik, O. G.; Chen, X. Y.; Kaliaguine, S. *J. Membr. Sci.* **2012**, *413-414*, 48–61.

(78) Stavitski, E.; Pidko, E. A.; Couck, S.; Remy, T.; Hensen, E. J. M.; Weckhuysen, B. M.; Denayer, J.; Gascon, J.; Kapteijn, F. *Langmuir* **2011**, *27*, 3970–3976.

(79) Hashemifard, S. A.; Ismail, A. F.; Matsuura, T. *J. Membr. Sci.* **2010**, *347*, 53–61.

(80) Maxwell, J. C. *A Treatise on Electricity and Magnetism*; Dover Publications: New York, 1954.

(81) Bruggeman, D. A. G. *Ann. Phys.* **1935**, *24*, 636–679.

(82) Lewis, T. B.; Nielsen, L. E. *J. Appl. Polym. Sci.* **1970**, *14*, 1449–1471.

(83) Moore, T. T.; Mahajan, R.; Vu, D. Q.; Koros, W. J. *AIChE J.* **2004**, *50*, 311–321.

(84) Sheffel, J. A.; Tsapatsis, M. *J. Membr. Sci.* **2007**, *295*, 50–70.

(85) Sheffel, J. A.; Tsapatsis, M. *J. Membr. Sci.* **2009**, *326*, 595–607.

(86) Kang, D.-Y.; Jones, C. W.; Nair, S. *J. Membr. Sci.* **2011**, *381*, 50–63.

(87) Marand, E.; Surapathi, A. *J. Membr. Sci.* **2012**, *415-416*, 871–877.

CHAPTER 3

Synthesis and Characterization of Mixed-Linker Zeolitic Imidazolate Frameworks

3.1 Introduction

Recent studies have shown that zeolitic imidazolate frameworks (ZIFs) exhibit a "gate-opening" phenomenon:[1–3] as they interact with adsorbing molecules, they undergo structural changes during adsorption, thereby allowing more adsorbate molecules into the framework. Because the organic linker components in the framework rotate to allow the above phenomena, the nature of the organic linker has significant implications on the selection and behavior of appropriate ZIF materials for specific applications. For instance, ZIF-8 has a crystallographic pore aperture of 0.34 nm as determined by X-ray diffraction; however, there is increasing evidence that the as-made material separates gases considerably larger than its pore aperture (*e.g.*, C_3H_6/C_3H_8) more efficiently than gases closer to its crystallographically determined pore size (CO_2/CH_4).[4–6]

In general, it is possible to tune the properties of MOFs for specific applications using methods such as chemical or structural modifications. One approach for chemically modifying a MOF is to use a linker that has a pendant functional group for postsynthetic modification. For example, ZIF-90, an aldehyde-containing ZIF, can be modified using $NaBH_4$ as a reducing agent to generate alcohol groups.[7] Another approach to modification is to use organic linkers that can change the structural characteristics of the

material. MIL-53 exhibits a flexible framework,[8] but modification of the terephthalic acid linker to include an amino functional group improves the separation performance for CO_2 by changing the structural properties of the material.[9–11] Another recent approach to modification is the use of a triazolate linker in which a C-H moiety of the imidazole is replaced by a nitrogen atom for the synthesis of a ZIF-8-like material, thereby allowing crystallization of a hybrid material that does not disturb the crystal structure of the original material.[12] However, in the case of using mixed linkers, determining appropriate linker combinations *a priori* is not always straightforward. It has been shown[13–15] that the use of linkers with bulky substituents produces new ZIF frameworks with enhanced CO_2 adsorption properties by preventing crystallization of ZIF topologies with smaller unit cells and network cages; however, this discovery came from using high-throughput synthesis techniques. Similarly, the pore size of a MOF can be tuned by increasing the length of bridging organic linkers. A series of mixed-linker Zn-based MOFs were transformed from a nonporous material to one with relatively high surface area and porosity by increasing the length of bridging dicarboxylic or bipyridyl linkers.[16]

In this Chapter, a novel structural modification approach is explored for tuning the properties of ZIF materials. In particular, hybrid, or mixed-linker, ZIFs containing a combination of different ligands in differing relative quantities are synthesized. The synthesis of hybrid ZIF materials that crystallize in a single crystal structure is demonstrated for a number of different combinations of linkers. Furthermore, in comparison to the triazolate linker,[12] which replaces a C-H moiety of the original Me-IM linker with an N atom, several bulky benzimidazole-type linkers are used during

synthesis of hybrid ZIFs that create an additional steric complexity when trying to crystallize these materials. High-resolution nitrogen physisorption isotherms are used to track the gate-opening phenomenon, which has become increasingly more important to consider in understanding guest-host interactions in MOF materials. This synthetic approach is a facile route whereby chemically and thermally robust ZIFs (*e.g.* ZIF-8) can be subjected to continuous and tunable alterations in chemical functionality or microporosity by *in situ* incorporation of different imidazole linkers. Continuous control over composition is possible, as shown by solution ^{1}H NMR spectroscopy. Characterization by X-ray diffraction and nitrogen physisorption demonstrates formation of a set of crystalline ZIF structures that exhibit adsorption properties different from their parent frameworks.

3.2 Experimental Methods

3.2.1 Materials

Sodium formate (99%, $NaCO_2H$), 2-methylimidazole (99%, 2-MeIM), $Zn(NO_3)_2 \cdot 6H_2O$ (99%) and benzimidazole (99%, Bz-IM) were obtained from Sigma-Aldrich. Methanol (MeOH), dimethylformamide (DMF), carboxaldehyde-2-imidazole (99%, OHC-IM), and 2-aminobenzimidazole (97%, 2-amBzIM) were obtained from Alfa Aesar. All materials were used without any further purification.

3.2.2 Synthesis of ZIF-8-90 Hybrids

A solution of 20 mmol $NaCO_2H$, (20-*x*) mmol 2-MeIM (ZIF-8 linker) and *x* mmol OHC-IM (ZIF-90 linker) in 50 mL MeOH was prepared. The value *x* varied between 0-20 to alter the ratio of OHC-IM:2-MeIM in solution. In order to fully dissolve the OHC-IM ligand, the solution was heated to 323 K until it became clear. A separate solution was prepared with 5 mmol $Zn(NO_3)_2 \cdot 6H_2O$ and 50 mL deionized H_2O. After the MeOH solution cooled to room temperature, the Zn salt solution was poured into the IM solution and allowed to stir at room temperature for 1 hr. The resulting milky solution was centrifuged at 10,000 rpm for 5 min, and the precipitate was redispersed in 45 mL MeOH and washed three times. The powder was dried in an oven at 358 K.

3.2.3 Synthesis of ZIF-7-8 Hybrids

A solution of 20 mmol $NaCO_2H$, (20-*x*) mmol 2-MeIM and *x* mmol of Bz-IM (ZIF-7 linker) in 50 mL MeOH was prepared. Like the ZIF-8-90 hybrids, the value *x* was changed to alter the Bz-IM:2-MeIM ratio. A separate solution was prepared with 5 mmol $Zn(NO_3)_2 \cdot 6H_2O$ and 50 mL DMF. The Zn salt solution was poured into the IM solution and allowed to stir at room temperature. Times for crystal formation varied between 1-48 hrs. The resulting suspension was centrifuged at 10,000 rpm for 10 min, and the precipitate was redispersed in 45 mL MeOH. The product was washed three times and then recovered by vacuum filtration and dried in an oven at 358 K.

3.2.4 Synthesis of ZIF-8-ambz Hybrids

A solution was prepared with (20-*x*) mmol 2-MeIM, *x* mmol 2-amBzIM, and 5 mmol $NaCO_2H$ in 50 mL deionized H_2O. The value *x* was varied between 0-10 to change the ratio of 2-MeIM:2-amBzIM in solution. To fully dissolve the 2-amBzIM, the solution was heated to 343 K for at least 2 hrs in a round bottom flask until the solution turned clear. A separate solution containing 5 mmol $Zn(NO_3)_2 \cdot 6H_2O$ in 50 mL DMF was also prepared. After the imidazole solution cooled to room temperature, the Zn salt solution was added and allowed to stir for 1 hr. The solution was then centrifuged at 10,000 rpm for 5 min, and the precipitate was washed with MeOH. This washing was repeated three times, and then the precipitate was recovered by vacuum filtration and dried in an oven at 358 K. The yield of product was approximately 20-25% based on Zn.

3.2.5 Characterization Methods

Powder X-ray diffraction (XRD) was performed at room temperature on an X'Pert Pro PANalytical X-Ray Diffractometer using Cu Kα radiation of wavelength λ = 1.5406 Å. Measurements were carried out from 3.5-50° 2θ, using an X'celerator detector with low background sample holders. For unit cell volume calculations in the ZIF-8-90 system, an internal standard (α-Al_2O_3) was added to the powder samples, and the diffraction pattern was shifted appropriately (typically by about 0.1° 2θ) such that the peak positions of the internal standard were correctly reproduced. Structureless (Le Bail) refinement of the full XRD patterns (excluding the internal standard peaks) was carried out with the Expo2009 package,[17] to obtain the cubic lattice constant (*a*) and hence the unit cell volume (a^3). Thermogravimetric and decomposition analyses were performed on

a Netzsch STA-409-PG thermogravimetric analyzer (TGA) and differential scanning calorimeter (DSC). Powder samples were heated from room temperature to 1173 K with a ramp rate of 10 $K \cdot min^{-1}$ in a diluted air stream (40% air-60% nitrogen). Smoothed differential mass loss curves were analyzed to determine decomposition temperature of hybrid materials. Solution ^1H NMR measurements were performed using a Mercury Vx 400 MHz spectrometer by digesting crystals using d_4-acetic acid (CD_3CO_2D) as the solvent. To determine the fraction of imidazole linkers in the framework of each sample, the areas of each peak were normalized to either the aldehyde proton of OHC-IM (9.84 ppm) or the 2 position proton of Bz-IM (9.05 ppm) or the aromatic proton of 2-amBzIM (7.20 ppm). Particle size and morphology were examined using a JEOL 100CX transmission electron microscope (TEM) operating at 100 keV. Samples were dispersed in isopropanol and a drop of the dispersion was added to the TEM grid. Nitrogen physisorption measurements were carried out at 77 K on a Micromeritics ASAP 2020 surface area analyzer. Samples were first degassed for 18 hrs at 473 K (ZIF-8-90 hybrids) or 523 K (ZIF-7-8 and ZIF-8-ambz hybrids) to remove occluded solvent molecules (H_2O or DMF). The BET, Langmuir and t-plot micropore volume methods were used to analyze the relative surface properties of the hybrids.

3.2.6 Horváth-Kawazoe Formulation and Selection of Parameters

Horváth-Kawazoe (HK) equations[18] were used to analyze nitrogen physisorption isotherms of hybrid materials. For a single plane interacting with a gas molecule, the potential energy function follows:

$$\varepsilon(z) = \frac{N_s A_s}{2\sigma^4}\left[-\left(\frac{\sigma}{z}\right)^4 + \left(\frac{\sigma}{z}\right)^{10}\right] \tag{3.1}$$

where N_s is the molecular surface area of the adsorbent (cm^{-2}), σ is the interaction distance between the adsorbate and adsorbent at zero energy (Å), z is the separation between adsorbent and adsorbate (Å) and A_s is the dispersion constant defined as (J mol^{-1} cm^{-6} $molecule^{-1}$):

$$A_s = \frac{6mc^2\alpha_s\alpha_A}{\left(\frac{\alpha_s}{\chi_x} + \frac{\alpha_A}{\chi_A}\right)} \tag{3.2}$$

where α is the polarizability (cm^3), χ is the diamagnetic susceptibility (cm^3), m is the mass of an electron (kg) and c is the speed of light (m s^{-1}). If now the plane becomes a slit, the potential energy function then becomes:

$$\varepsilon(z) = \frac{N_s A_s}{2\sigma^4}\left[-\left(\frac{\sigma}{z}\right)^4 + \left(\frac{\sigma}{z}\right)^{10} - \left(\frac{\sigma}{L-z}\right)^4 + \left(\frac{\sigma}{L-z}\right)^{10}\right] \tag{3.3}$$

where L is the length of the slit (Å). If the length of separation, z, is defined as the average of the adsorbate and adsorbent diameters and adsorbate-adsorbate interactions are taken into account, the original HK derivation is found:[18]

$$N_{Av}\cdot\bar{\varepsilon}(z)=N_{Av}\frac{N_sA_s+N_AA_A}{\sigma^4(L-d_0)}\times\left[\frac{\sigma^4}{3(L-d_0)^3}-\frac{\sigma^{10}}{9(L-d_0)^9}-\frac{\sigma^4}{3d_0^3}+\frac{\sigma^{10}}{3d_0^9}\right] \tag{3.4}$$

where d_0 and σ are defined as:

$$d_0=\left(\frac{d_s+d_A}{2}\right) \tag{3.5}$$

$$\sigma=\left(\frac{2}{5}\right)^{\frac{1}{6}}d_0 \tag{3.6}$$

whereas N_A is the surface molecular density of adsorbate and A_A is the dispersion constant of the adsorbate:

$$A_A=\frac{3}{2}mc^2\alpha_A\chi_A \tag{3.7}$$

In the original derivation[18], the energy function is related to relative pressure by assuming Henry's law behavior in the isotherm:

$$RT\ln\left(\frac{P}{P_0}\right)=N_{Av}\cdot\bar{\varepsilon}(z) \tag{3.8}$$

thus there is a relationship between P/P_0 in the isotherm and the effective pore width (L-d_s).

Lastly, there needs to be a set of criteria placed in order to pick parameters for each material. Because the ZIFs considered in this Chapter are coordinatively-saturated, the parameters chosen should be considered as properties of the imidazoles, and it is assumed that the Zn metal center plays no role in adsorption. Therefore, polarizability and diamagnetic susceptibility can be predicted by well-known empirical equations.[19,20] The diameter of the linker is predicted by assuming a van der Waals sphere around the linker. Then, the accessible surface area of the sphere is calculated using Marvin 5.3.7, and the diameter is found from this value. The molecular surface area (N_s) of the adsorbent can be found by first calculating the density of imidazoles based on the crystal structures of ZIF-8, ZIF-90, and ZIF-7, and then assuming the entire surface is accessible, use the following equation:

$$N_s = \rho \times \frac{d_s}{6} \tag{3.9}$$

Lastly, because the set of equations derived above assume a uniform adsorbent surface, the parameters of the hybrids have been assumed to be the weighted geometric mean of its pure components, following this generic equation:

$$\bar{a} = a_1^{y_1} \cdot a_2^{y_2} \tag{3.10}$$

where a is a given parameter, y_1 is the mole fraction of component 1 and y_2 is the mole fraction of component 2. With this methodology, Table 3.1 shows the values used for the HK analysis.

Table 3.1. Parameters of adsorbents and adsorbate used for H-K analysis.

Parameters	ZIF-8 (2-MeIM)	ZIF-90 (OHC-IM)	ZIF-7 (Bz-IM)	2-amBzIM	N_2
α (cm^3) x 10^{24}	8.96	9.14	14.39	15.86	1.46
χ(cm^3) x 10^{29}	3.68	5.48	10.12	11.55	2.00
d (Å)	6.59	6.45	7.19	7.62	3.00
N (cm^{-2}) x 10^{15}	4.35	4.76	4.66	5.03	0.671

3.3 Results and Discussion

3.3.1 Crystallization

In preparing ZIF hybrids, some observations can be made about the behavior of the induction period and crystallization process. In all syntheses described here, the non-solvent induced crystallization (NSIC) technique was used.[21] By introducing a non-solvent, rapid crystallization will occur due to a drastic solubility change in the reaction solution, and there will be a significant reduction (or elimination) of the induction period that involves precursor formation and crystallite nucleation. Because ZIF-8 has been synthesized in both non-solvents used in this study, it was hypothesized that addition of $NaCO_2H$ to the reactants would increase the nucleation time due to competitive coordination with the Zn^{2+} metal center.[22–24] Furthermore, by using $NaCO_2H$ and the

linkers in equimolar amounts for the ZIF-8-90 and ZIF-7-8 hybrids, both linkers included in the framework will likely be deprotonated before addition of the Zn salt solution, thereby allowing for a more random distribution of linkers. Otherwise, deprotonation of the linker is driven by the energy of formation of the framework, and thus the ZIF with the more favorable lattice energy is more likely to crystallize in pure form rather than a phase containing a random mixture of linkers.[25]

Upon adding the Zn salt solution in the ZIF-8-90 hybrid case, the solution remained clear for 30-60 s. A crystal suspension then formed rapidly. Crystal yields were 20-25% based on the fraction of added Zn incorporated into the crystals. ZIF-7-8 hybrids behaved quite differently during crystallization. Several solvent systems were employed, but only the DMF-MeOH solvent system yielded crystalline materials over a wide range of Bz-IM:2-MeIM ratios reported here. Upon adding the Zn-DMF solution, a long induction period of 1-4 hrs was observed in the case of low Bz-IM percentages (0-10%). Thus, these reactions were all carried out for 48 hrs at room temperature. However, at 25% Bz-IM in the reactant solution, there was rapid crystal formation, and hence reactions with higher Bz-IM percentages were only carried out for 1 hr. Yields varied considerably with the percentage of Bz-IM used, with 10% Bz-IM having the lowest (~1% based on Zn) and 100% Bz-IM having the highest crystallization yield (67% yield based on Zn).

3.3.2 Composition Analysis

^{1}H NMR was used to quantify the fraction of substituting linker (Bz-IM or OHC-IM relative to 2-MeIM) in the crystals. Because the NSIC technique was used to form the hybrid materials, it can be expected that the linker with the lower solubility in the non-solvent will be incorporated in precursors to a larger extent than the other linker. Figure 3.1 shows the fraction of substituting linker used in the reactant solution versus the corresponding fraction that resulted in the framework, as determined by ^{1}H NMR. Both OHC-IM and Bz-IM are incorporated into the framework at higher fractions than they are present in solution. It has been shown that ZIF-8 crystals grow in methanol solutions at room temperature by a nucleation-limited mechanism without addition of another coordinating linker.[22,26] Considering that nucleation is further slowed by additives in the solution ($NaCO_2H$), it is likely that the OHC-IM and Bz-IM linkers are incorporated into nuclei precursors more favorably than the 2-MeIM linker due to the rapid solubility change by addition of the non-solvent during synthesis.[24] The hybrid composition can clearly be controlled; however in the case of ZIF-7-8 hybrids, a precise control of the synthesis may be necessary to reach any arbitrary linker composition.

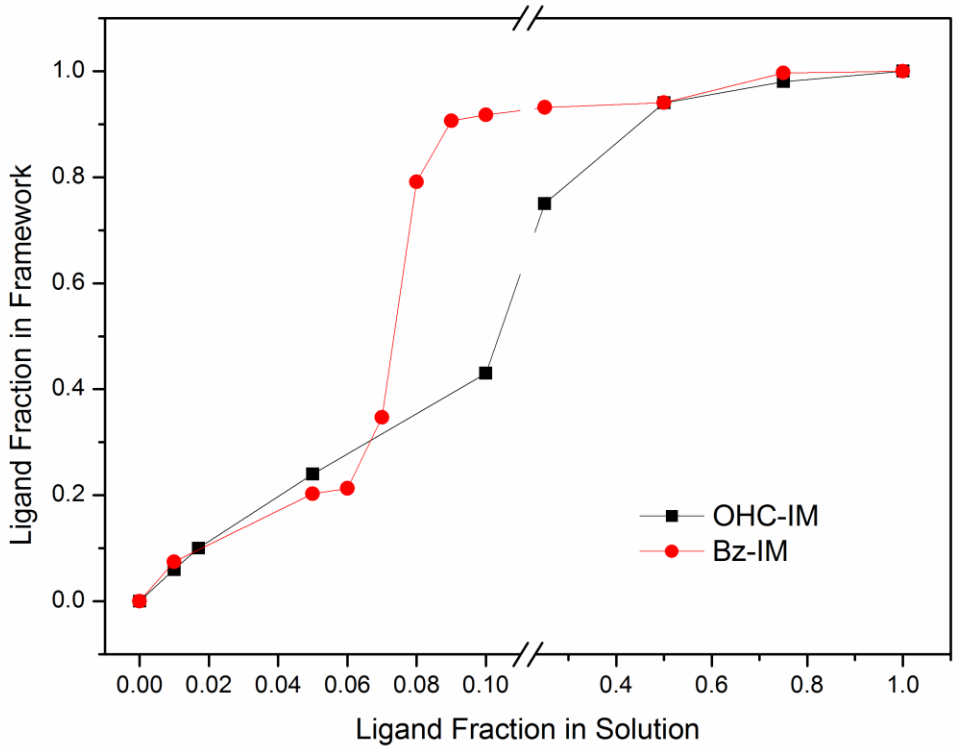

Figure 3.1. Compositional analysis of ZIF hybrid frameworks by ^{1}H NMR. Both hybrid systems show preferential inclusion of OHC-IM or Bz-IM over 2-MeIM.

3.3.3 Crystal Structure

Figures 3.2a and 3.2b show XRD patterns of the ZIF-8-90 and ZIF-7-8 hybrids, respectively. ZIF-8 and ZIF-90 have nearly identical *I-43m* cubic unit cells; structure refinement has shown that the unit cell dimension differs by 2-3%.[7,27] This makes the XRD identification of separate phases during crystallization difficult for the ZIF-8-90 hybrids. The unit cell volumes were obtained for the ZIF-8-90 hybrids using the Le Bail refinement technique.[26] To account for peak position errors when measuring powder XRD patterns, the patterns were corrected using an α-Al_2O_3 internal standard. As shown Figure 3.3, there is an overall systematic increase in the unit cell volume with increasing

OHC-IM fraction. This volume changes by 2.7% as the hybrid composition goes from pure ZIF-8 to pure ZIF-90.

Conversely to the ZIF-8-90 hybrids, ZIF-7 and ZIF-8 have considerably different crystal structures. Based on refinement, ZIF-7 has a rhombohedral *R-3* space group while ZIF-8 has the cubic *I-43m* space group.[27] Differences in XRD patterns are therefore easily discernible (Figure 3.2b). Up to 35% Bz-IM loading, the framework still maintains a cubic structure characteristic of ZIF-8, and thereafter transitions to the *R-3* space group. Between 79-92% Bz-IM, significantly disordered materials are obtained. The diffraction pattern of 79% Bz-IM, in particular, has an apparent superposition of both ZIF-8 and ZIF-7 phases; however, subsequent TEM images (Figure 3.5) show clearly that a physical two-phase mixture of ZIF-7 and ZIF-8 crystals is not apparent based on microscopy. Because these materials have considerably different crystal structures, there may be compositional ranges wherein a hybrid with a completely random distribution of linkers is unable to crystallize. Therefore, this XRD pattern may represent an intergrowth of ZIF-7 and ZIF-8 phases. However, distinguishing an intergrown material from a hybrid ZIF that has a truly random linker distribution would require a detailed microcrystallographic study (*e.g.*, with electron diffraction) and the development of suitable intergrowth models. For example, indexing of the XRD patterns for loadings of 79-92% Bz-IM was attempted; however, the number of distinct usable peaks is low with only about 10 reliable peaks present, and therefore, a reliable and unambiguous indexing was not possible to address the question of whether or not an intergrown material was formed.

No XRD patterns are shown for hybrids between loadings of 35-79% Bz-IM because of the narrow synthesis range (7-8% Bz-IM in solution) needed to obtain these materials. It is presently unclear whether hybrids in this composition range can be successfully obtained by a highly accurate adjustment of the reactant composition, or whether the materials in this range are unstable and hence transform to one of the phases obtained at lower or higher Bz-IM loadings. Further modification of the procedure could yield a material with a better range of tunability by producing more favorable crystallization conditions for the ZIF-7-8 hybrids. The XRD patterns shown, and the following TEM and nitrogen physisorption data, do not indicate the formation of a simple physical mixture of ZIF-7 and ZIF-8; instead, a single crystalline phase forms in every case. To investigate if functionality on the substituting linker plays, hybrids containing a pendant amine functional group are synthesized, and the results are discussed in Section 3.3.7.

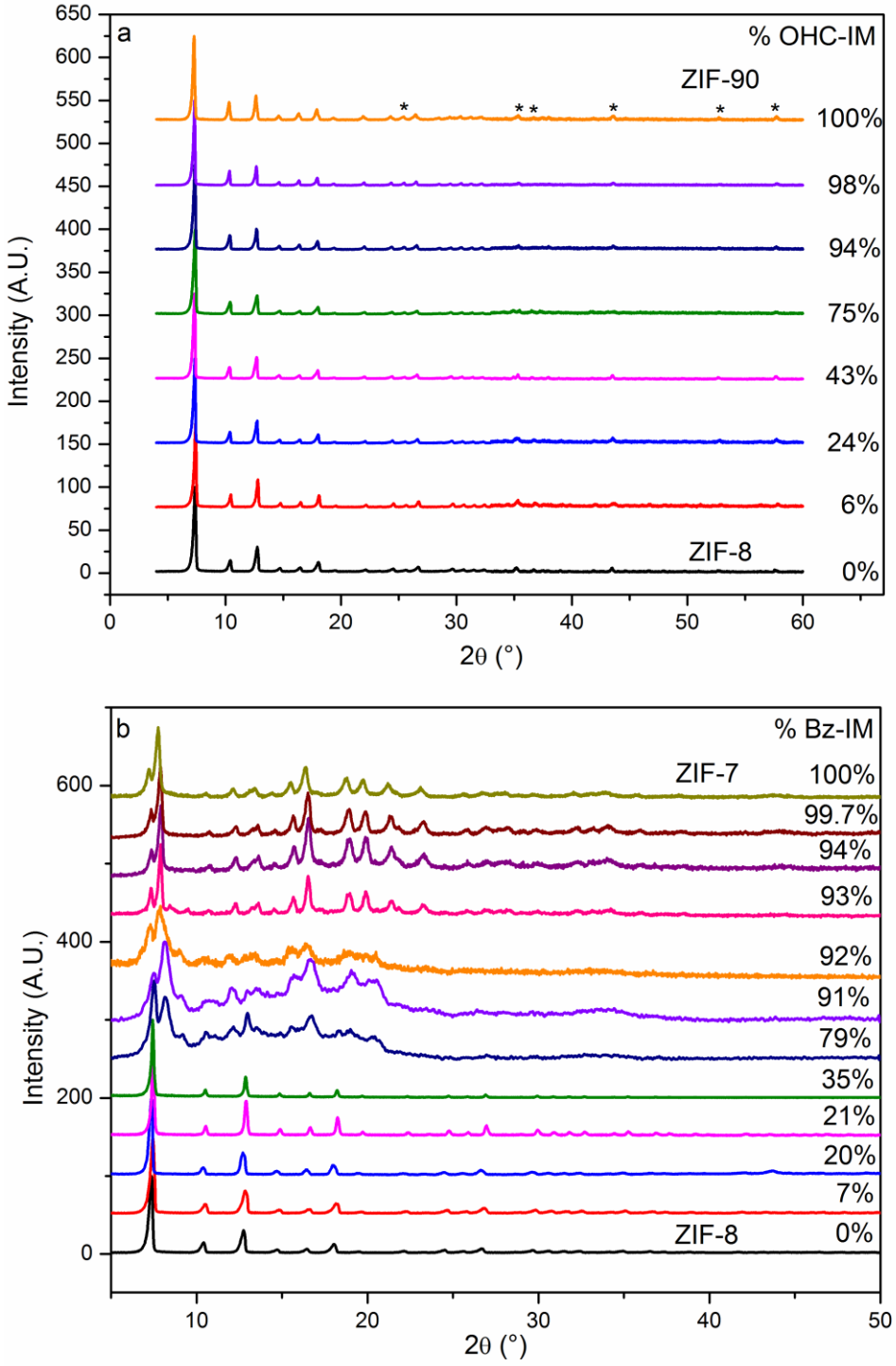

Figure 3.2. Powder XRD patterns of: (**a**) ZIF-8-90 hybrids, due to their identical space groups and very small differences in the unit cell dimensions between ZIF-8 and ZIF-90, the patterns appear almost identical but have subtle changes in peak positions and peak intensities; (**b**) ZIF-7-8 hybrids, there is a distinct shift from *I-43m* to *R-3* space group after 35% Bz-IM loading. Asterisks represent positions of α-Al_2O_3 diffraction peaks.

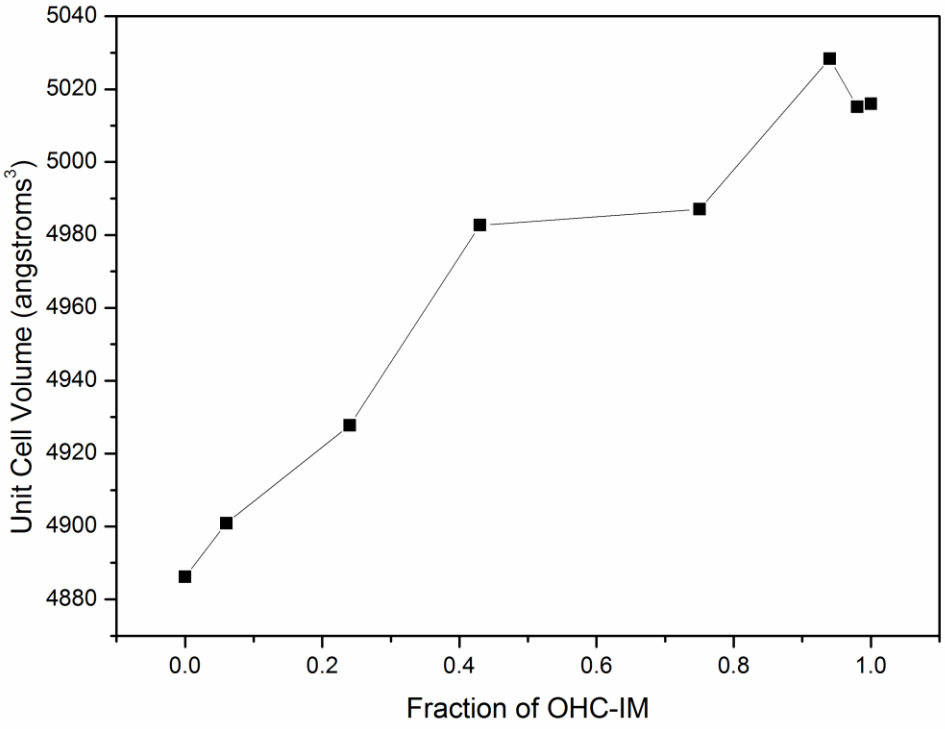

Figure 3.3. Unit cell volume of ZIF-8-90 hybrids as a function of OHC-IM obtained by Le Bail (structureless) refinement of internal-standard-corrected XRD patterns, showing an overall increase in volume with increasing fraction of OHC-IM in the framework.

3.3.4 Particle Size and Morphology

TEM was used to examine changes in particle size or morphology with the linker composition. Figure 3.4 shows TEM images of ZIF-8-90 hybrids at different OHC-IM loadings. At 0% OHC-IM (pure ZIF-8), particles show a monodisperse distribution centered at approximately 250 nm in diameter, exhibiting the typical rhombic dodecahedral morphology of ZIF-8 particles when synthesized with $NaCO_2H$.[22] As the OHC-IM loading increases, the particle size increases, growing to more than 1 μm at 24% OHC-IM. Significantly, all the TEM images showed only one particle size population, and thereby, this suggests formation of a single-phase hybrid material. If ZIF-8 and ZIF-90 had precipitated separate phases, the particle sizes would likely be

considerably different, since the pure ZIF-8 phase (Figure 3.4a) exhibits sub-micron particles while the pure ZIF-90 phase (Figure 3.4d) exhibits micron-sized particles.

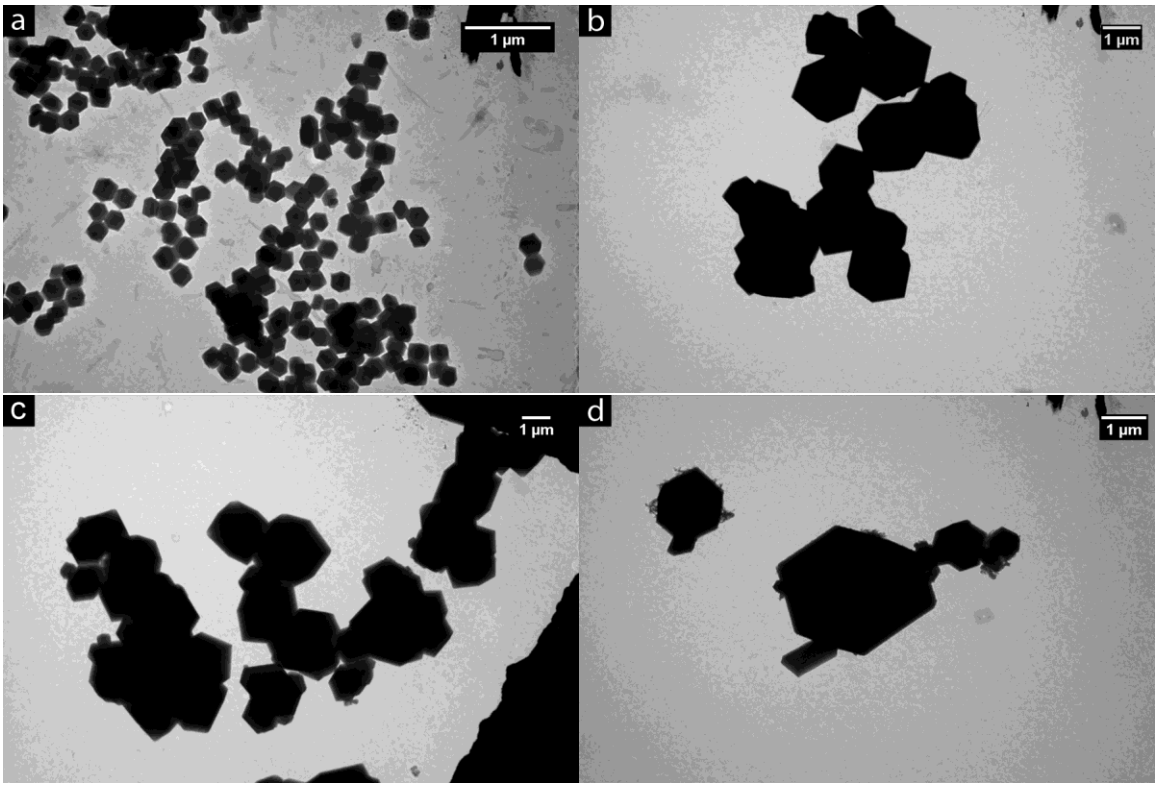

Figure 3.4. TEM images of ZIF-8-90 hybrids at (**a**) 0%; (**b**) 24%; (**c**) 43%; and (**d**) 100% OHC-IM loading.

TEM images of ZIF-7-8 hybrids are shown in Figure 3.5. The particle morphology of these materials is less well-defined than in the ZIF-8-90 hybrids, being closer to spherical in most cases than the rhombic dodecahedral morphology. This observation may support the formation of a single crystal phase different from both ZIF-7 and ZIF-8 at the intermediate loadings of Bz-IM, considering that ZIF-7 has been shown to form spherical or rod-like morphologies and ZIF-8 forms the rhombic dodecahedral morphology in the presence of an additive.[22,28] The particle size of the

disordered hybrid material determined from XRD is shown in Figure 3.5b and is considerably smaller than that of the other materials in Figure 3.5. As 2-MeIM is still the major organic linker in the solution, it may be preventing crystallization of the *R-3* phase and resulting in low crystallization yields and the disordered rhombohedral-like structure shown by XRD. Like the ZIF-8-90 hybrids, there are no different particle size populations or morphologies that indicate a physical mixture of the two phases.

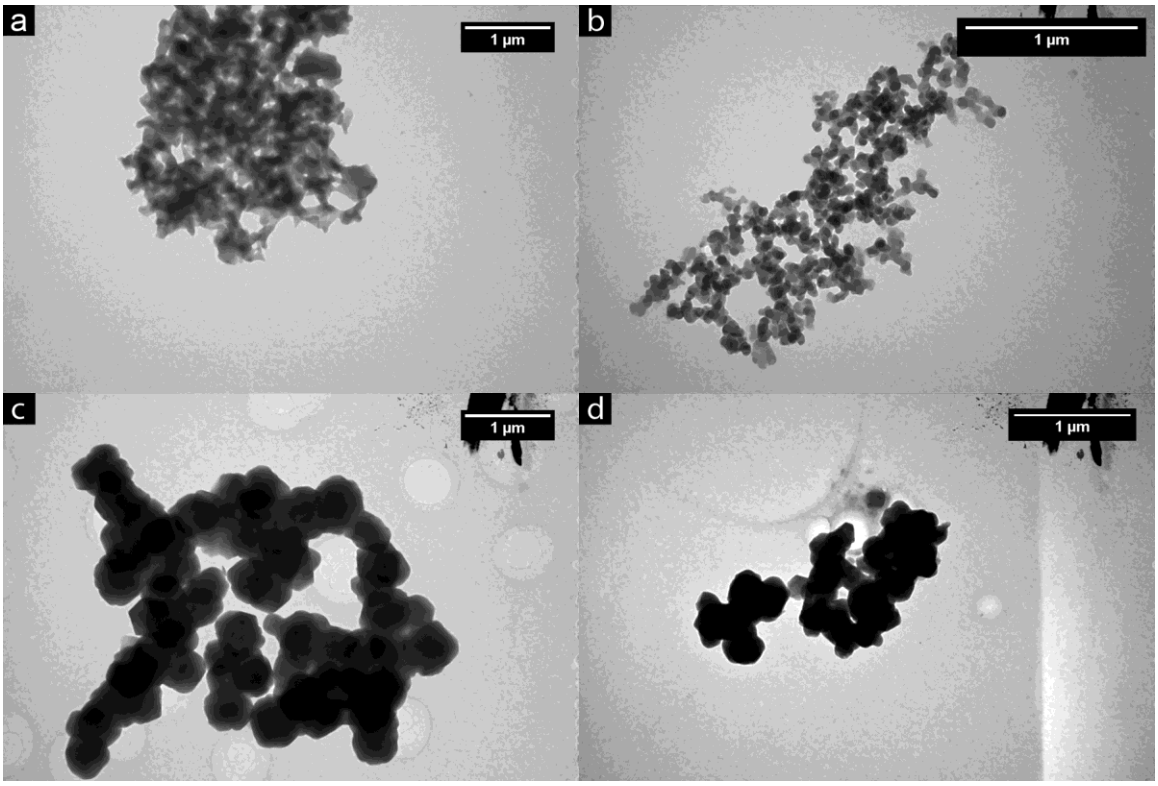

Figure 3.5. TEM images of ZIF-7-8 hybrids at (**a**) 35%; (**b**) 91%; (**c**) 94%; and (**d**) 100% Bz-IM loading.

3.3.5 Thermal Decomposition

Previous studies on thermal decomposition of ZIFs showed the existence of a wide range of decomposition temperatures that also depend on synthesis conditions.[21] Thermogravimetric analysis (TGA) was used here to elucidate stability changes in the hybrid materials. To minimize the influence of solvent mass loss, samples were first degassed under vacuum for 12 hours at either 473 K (ZIF-8-90) or 523 K (ZIF-7-8). Figures 3.6a and 3.6b show differential mass loss curves for ZIF-8-90 and ZIF-7-8, respectively. ZIF-8 (0% OHC-IM) shows the highest thermal stability for the ZIF-8-90 hybrids, with nearly no decomposition observed until 723 K. At 24% OHC-IM loading, decomposition begins closer to 673 K, and above 50% OHC-IM loading, the hybrid frameworks are thermally stable up to 573 K. Aldehydes typically oxidize easily in air, and this is the likely cause of the lower thermal stability under exposure to diluted air at elevated temperatures. On the other hand, the onset of decomposition in ZIF-7-8 hybrids remains unchanged at 673-723 K as the loading of Bz-IM changes. Materials at high loadings of Bz-IM (79-100%) are stable above 773 K. This increase in decomposition temperature of the framework may be attributed to the greater stability provided by the aryl groups of Bz-IM.

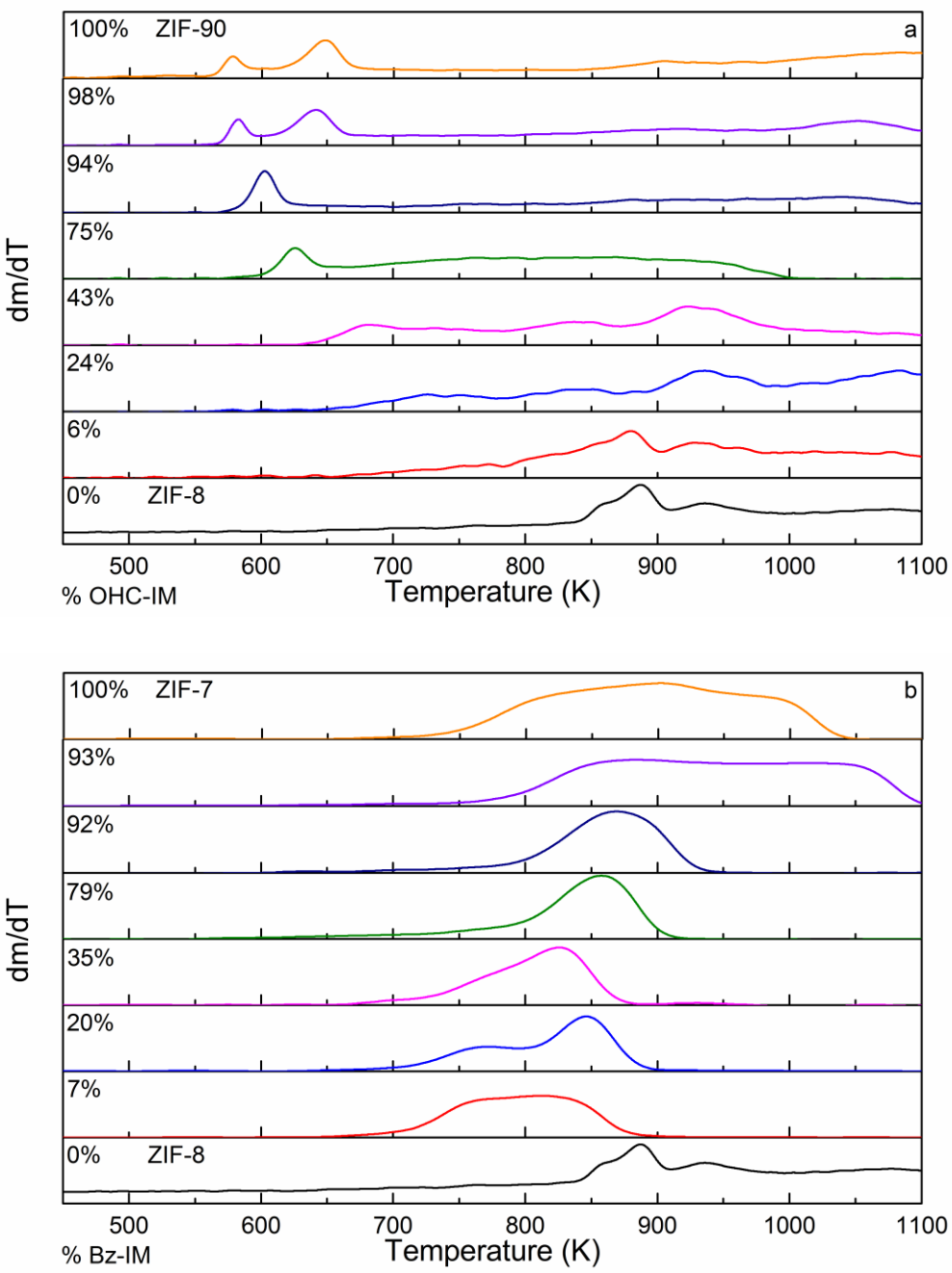

Figure 3.6. Differential mass loss curves of (**a**) ZIF-8-90 and (**b**) ZIF-7-8 hybrids as determined from thermogravimetry in a 40% air - 60% nitrogen gas stream.

3.3.6 Porosity

Figures 3.7a and 3.7b show nitrogen physisorption isotherms of ZIF-8-90 and ZIF-7-8 hybrids, respectively. Tabulated surface areas and micropore volumes are shown

in the Figures 3.8 and 3.9 for ZIF-8-90 and ZIF-7-8 hybrids, respectively. Inclusion of either OHC-IM or Bz-IM reduces the maximum quantity adsorbed in comparison to pure ZIF-8, thus decreasing the total micropore volume of the framework. It has been shown that ZIF-90 exhibits hysteresis at $P/P_0 \sim 0.4$, and this was attributed to a constriction in the micropores.[7] As the OHC-IM loading increases in the framework, the single inflection point seen in ZIF-8 at $P/P_0 \sim 5x10^{-3}$ (attributed to a gate-opening mechanism that allows more nitrogen into the micropores) turns into two inflection points as pure ZIF-90 is approached: one inflection still characteristic of the gate-opening effect at lower nitrogen activity (*e.g.*, $P/P_0 \sim 10^{-4}$) and the other attributed to constriction in the micropores at higher nitrogen activity (*e.g.*, $P/P_0 \sim 0.4$). To confirm that these inflection points and the isotherms are indeed a result of hybrid materials containing a single phase with an essentially random dispersion of linkers in the framework, a 50-50 molar physical mixture of ZIF-8 and ZIF-90 crystals was prepared. As shown in Figure 3.7a, the inflection points in the corresponding isotherm are characteristic of the parent framework materials and not of the hybrids at similar overall composition (*e.g.*, 43% OHC-IM). This is a further indication that the materials prepared with the proposed synthetic method utilizing both the NSIC technique and an additive, such as $NaCO_2H$, are single phases with different microporosity and gate-opening behavior from pure ZIF-8 or ZIF-90.

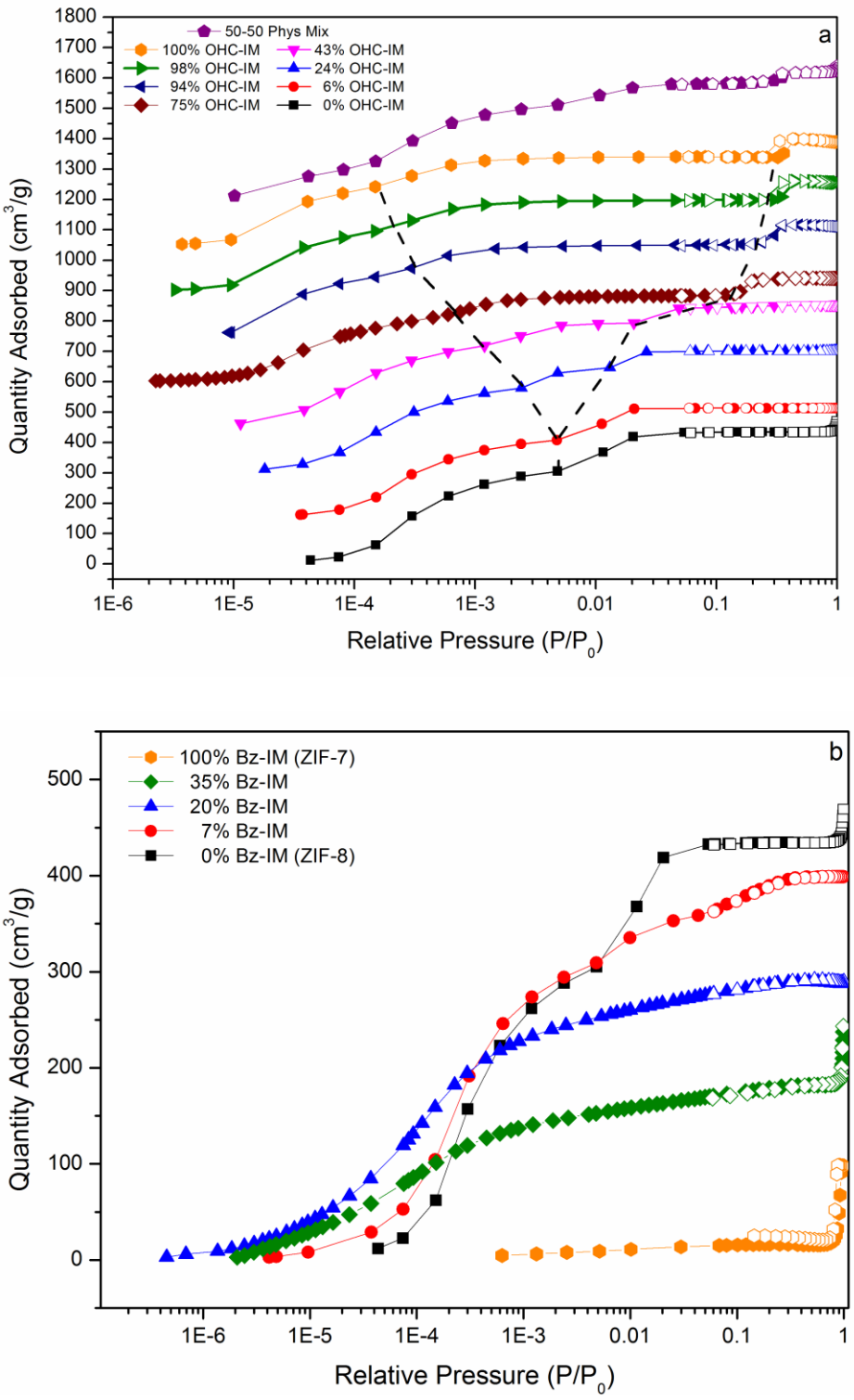

Figure 3.7. Nitrogen physisorption isotherms of (**a**) ZIF-8-90, with isotherms stacked 150 $cm^3 \cdot g^{-1}$ apart; and (**b**) ZIF-7-8 hybrids at different loadings of OHC-IM and Bz-IM, respectively.

Figure 3.7b shows physisorption isotherms of the ZIF-7-8 hybrids. As the Bz-IM loading increases, the micropore volume is severely reduced; for example, there is a 40% micropore volume reduction from pure ZIF-8 at only 20% Bz-IM loading. The inflection typical of ZIF-8 decreases and disappears as the loading increases. This indicates that the bulky Bz-IM linkers are much less amenable to rotational displacement compared to 2-MeIM. Thus, it is hypothesized that inclusion of Bz-IM in the framework reduces and even eliminates gate-opening phenomena in the hybrid ZIF materials when probed with nitrogen adsorption at cryogenic temperatures. In fact, the shape of the isotherm (Type I) with 20% Bz-IM loading is similar to the isotherm predicted for ZIF-8 by grand canonical Monte Carlo (GCMC) simulations that assume a rigid framework.[1] The progressive suppression of the gate-opening phenomena in these hybrids provides a method for tuning the average pore size and the flexibility so that the material can be adapted to specific applications (*e.g.*, separations, catalysis). Although ZIF-7 has been shown to admit condensable gases (*e.g.*, CO_2, ethane) *via* a structural change,[2,3] the pores are not accessible to nitrogen at 77 K, as shown in Figure 3.7b.

Horváth-Kawazoe analysis was used to analyze the relative pore size distributions (PSDs) of the hybrid materials. It has been shown that some assumptions of these equations are not physically accurate and therefore do not provide correct absolute values of the PSDs.[29] For example, the main pore size for both ZIF-8 and ZIF-90 predicted by the HK method are larger than the pore sizes determined crystallographically, as shown in Figure 3.10a.[7,27] However, the HK method can be reliably used for *relative* comparison of a series of structurally related materials. Figures 3.10a and 3.10b show the PSDs for

both hybrid material types. ZIF-8 (0% OHC-IM) shows two pore size distribution maxima, centered at ~0.4 nm and ~0.75 nm. The former maximum represents the limiting pore diameter of the ZIF-8 windows. Considering the gate-opening mechanism, the latter PSD maximum is interpreted as resulting from rotational displacement of linkers to allow further adsorption of nitrogen, and not due to an actual secondary pore system (*e.g.*, the SOD cages) in the framework. This interpretation is supported by the fact that while the main pore size becomes larger with increasing OHC-IM loading (the pure ZIF-90 material shows a primary pore size of ~0.5 nm), the secondary PSD is quite different from the original ZIF-8 material and hence is unlikely to originate from a secondary pore system such as the ZIF cages, which maintain essentially the same dimensions in all the ZIF-8-90 hybrids. Interestingly, the gate-opening effect is still apparent in ZIF-90, an observation not shown or explained previously. This effect in ZIF-90 occurs at a significantly lower relative pressure ($P/P_0 \sim 10^{-4}$) than typically observed for ZIF-8 ($P/P_0 \sim 5x10^{-3}$). Considering this difference, the gate-opening in ZIF-90 and in hybrids with higher OHC-IM loading can be interpreted as being more easily induced than in pure ZIF-8.

PSDs of the ZIF-7-8 hybrids are shown in Figure 3.10b. As noted before, the isotherm inflection is related to the second PSD maximum. At 7% Bz-IM loading, the intensity of the second maximum is reduced considerably, and it disappears at 20% Bz-IM. This indicates that Bz-IM groups block the rotational displacement of the imidazole linkers. The primary PSD shifts to overall smaller values, and at 20% Bz-IM, a PSD

centered at ~0.32 nm appears. This shift to smaller pore sizes indicates that Bz-IM is effectively reducing the average pore size.

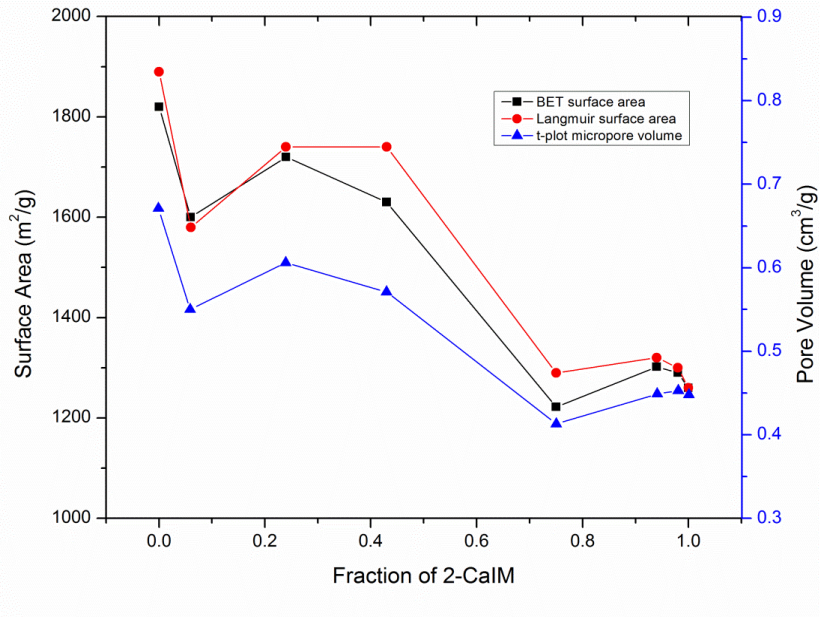

Figure 3.8. BET Surface Area, Langmuir Surface Area and t-plot Micropore Volume calculations for ZIF-8-90 Hybrids.

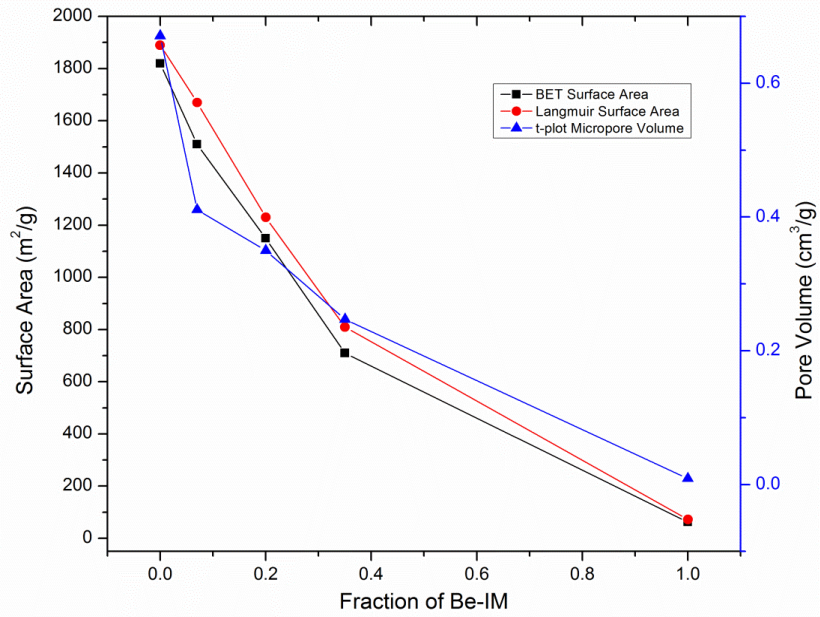

Figure 3.9. BET Surface Area, Langmuir Surface Area and t-plot Micropore Volume Calculations for ZIF-7-8 Hybrids.

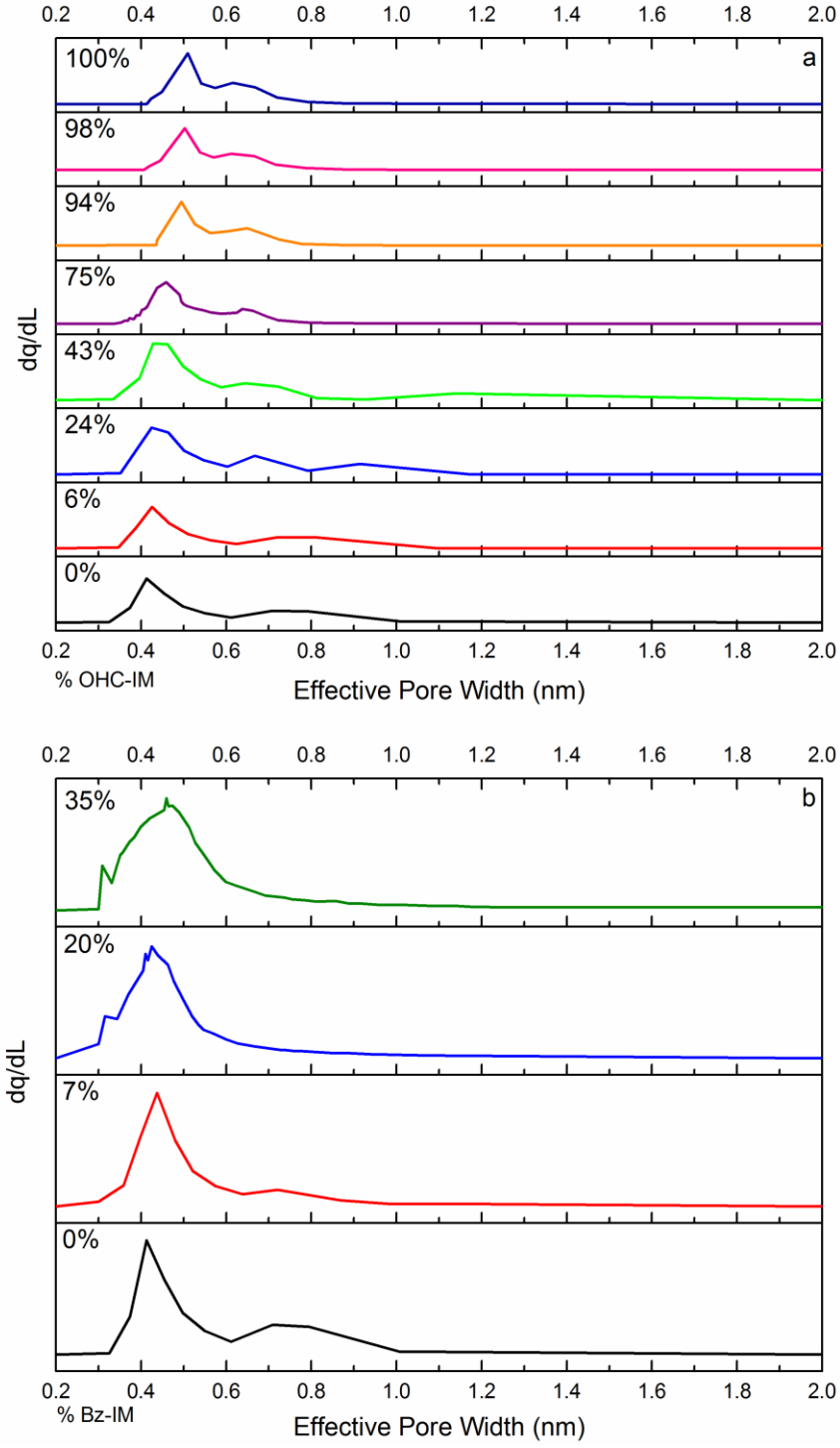

Figure 3.10. Pore size distributions determined by the HK method: (**a**) ZIF-8-90 hybrids; and (**b**) ZIF-7-8 hybrids.

3.3.7 Crystallization of ZIF-8-ambz Hybrids

As section 3.3.2 and 3.3.3 showed, it is difficult to control crystallization of a ZIF hybrid containing Bz-IM with a ZIF-8-like structure. A set of ZIF materials were prepared containing different proportions of 2-MeIM and 2-amBzIM linkers to understand if this substitution could be better controlled while maintaining a ZIF-8 crystal structure. Figure 3.11a shows the fraction of 2-amBzIM linkers included in the framework obtained from ^{1}H NMR spectra and derived from syntheses using up to 50% 2-amBzIM in the synthesis solution. In comparison to the ZIF-7-8 hybrids (Figure 3.1), the inclusion of 2-amBzIM is more controllable than Bz-IM. Because 2-amBzIM does not form any known single-linker ZIF structure, it is likely that formation of the ZIF-7 structure with Bz-IM is more thermodynamically favorable than any structure containing 2-amBzIM; therefore, the ZIFs obtained with 2-amBzIM represent a mixed-linker system with better control of linker composition while maintaining the cubic *I-43m* structure of ZIF-8 and use of a benzimidazolate-type linker. Powder XRD patterns (Figure 3.11b) of the synthesized materials show that the *I-43m* crystal structure is maintained up to high substitution fractions of 2-amBzIM. At 47% 2-amBzIM in the framework, a significant peak broadening is observed in the XRD pattern. This is either due to the formation of a crystal with a disordered distribution of the two linkers or due to a high degree of crystal strain arising from incorporation of the high fraction of 2-amBzIM in the ZIF crystal structure.

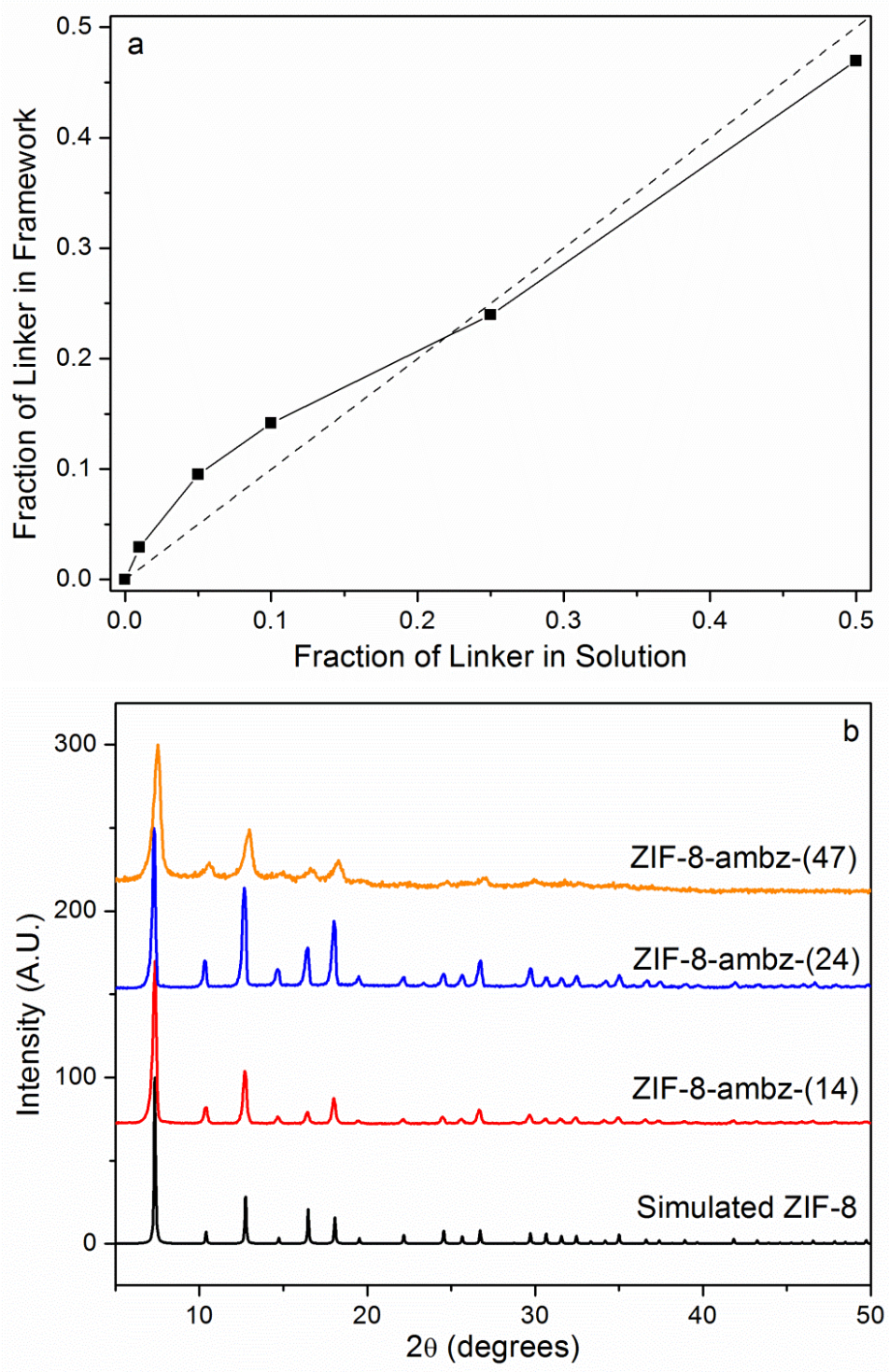

Figure 3.11. (**a**) ^{1}H NMR-based composition analysis and (**b**) powder XRD patterns of mixed-linker ZIFs prepared with 2-MeIM and 2-amBzIM linkers.

Nitrogen physisorption was used to investigate the gate-opening properties of these mixed-linker ZIFs. Figure 3.12 shows materials with modest loadings of 2-amBzIM (9.5% in the structure) have no evidence of gate-opening effects compared to ZIF-8.[1] There is a reduction in micropore volume (Table 3.2) with increasing linker substitution. Significantly, at 47% 2-amBzIM loading, there is complete loss of micropore volume and no uptake of N_2 at 77 K. To activate this material properly (Figures 3.13 and 3.14), the powder sample needed to be washed and soaked with MeOH at 323 K for 24 hrs to remove occluded solvent molecules trapped in the pores during synthesis. If degassing at 523 K was performed without this activation step, there was complete loss of crystallinity (Figure 3.13). When these samples were examined with TGA (Figure 3.14), the samples not soaked in MeOH showed mass loss before the material decomposed, whereas the samples soaked in MeOH showed no mass loss before decomposition. Based on the above observations, it is very likely that the higher 2-amBzIM substitution has significantly reduced the effective pore size and micropore volume of the ZIF material, blocking even small N_2 molecules from accessing the pores at 77 K.

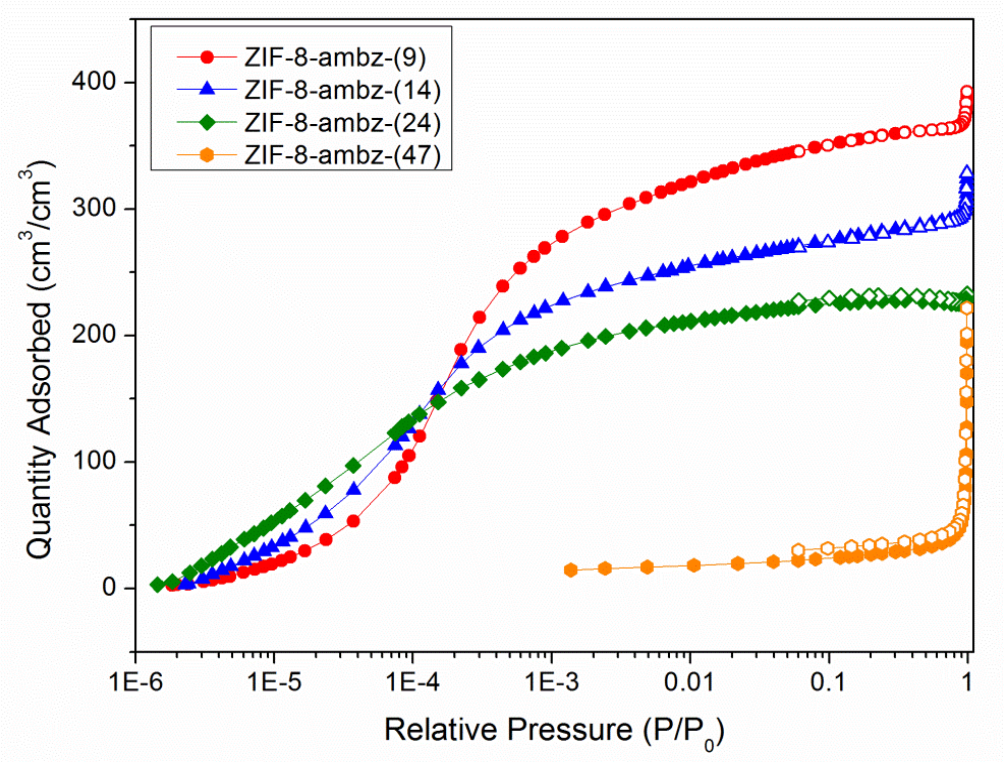

Figure 3.12. Nitrogen physisorption isotherms of mixed-linker ZIFs with 2-amBzIM, showing significant lowering of micropore volume with increasing substitution of 2-MeIM by 2-amBzIM. There is no evidence of gate-opening effects, even at modest loadings of 2-amBzIM.

Table 3.2. Linker substitution, micropore volume and BET surface area of ZIF-8-ambz hybrid materials.

Sample	Linker Substitution (mol %)	t-plot micropore volume ($cm^3 \cdot cm^{-3}$)	BET Surface Area ($m^2 \cdot cm^{-3}$)
ZIF-8-ambz-(9)	9.5	0.627	1760
ZIF-8-ambz-(14)	14	0.413	1180
ZIF-8-ambz-(24)	24	0.314	860
ZIF-8-ambz-(47)	47	0.012	60

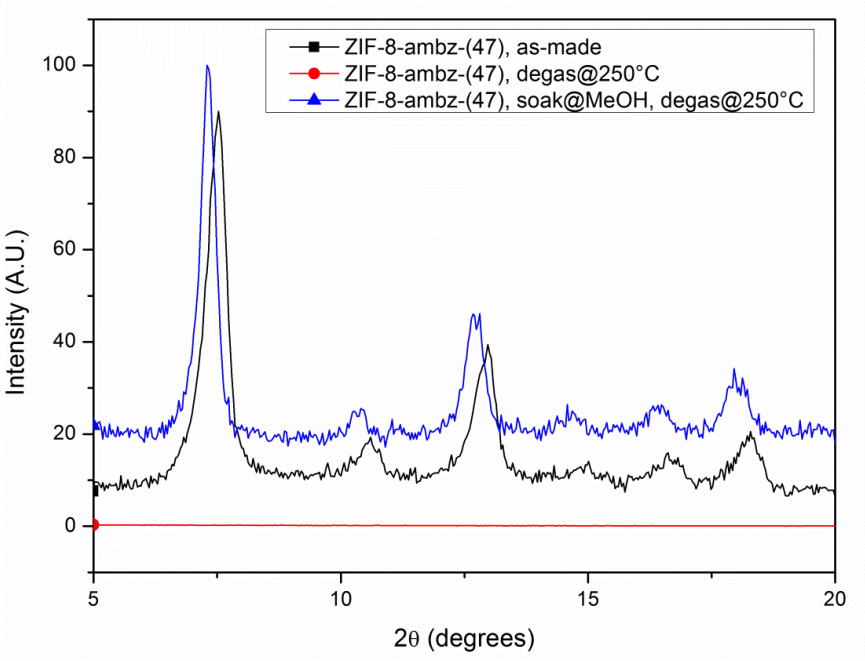

Figure 3.13. Powder XRD patterns of ZIF-8-ambz-(47) samples showing complete loss of crystal structure without proper activation steps.

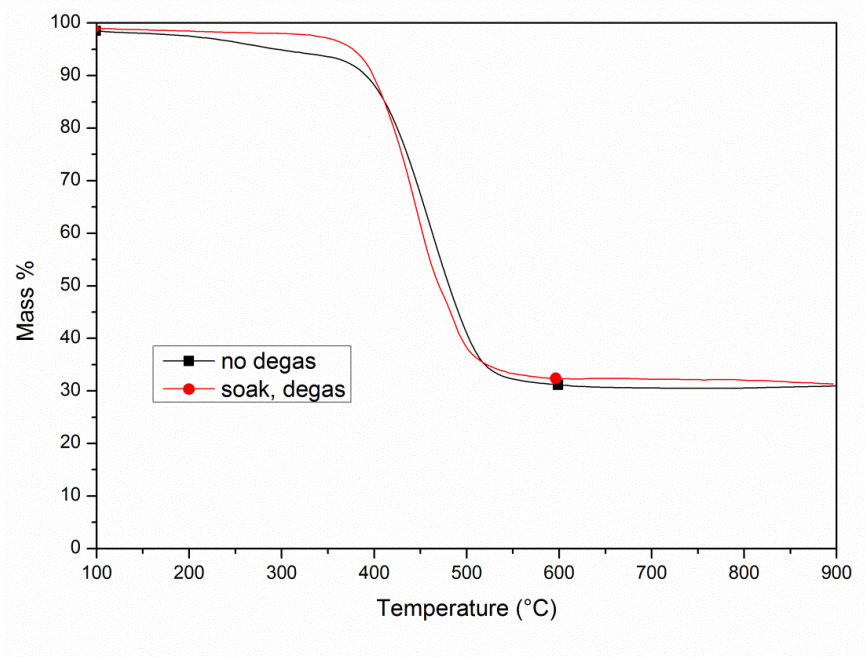

Figure 3.14. TGA mass loss curves of ZIF-8-ambz-(47), showing some retention of solvent after synthesis but removal of occluded solvents after MeOH soak at 323 K.

3.4 Conclusions

A synthetic approach for ZIF hybrid materials by *in situ* fractional linker substitution of ZIF-8 (2-MeIM linkers) has been demonstrated to produce continuously tunable framework functionality (with OHC-IM linkers) or microporosity (with Bz-IM or 2-amBzIM linkers). By inclusion of these linkers, it may be possible to control adsorption and diffusion properties for gas separations using these hybrid frameworks. In particular, nitrogen physisorption produces isotherms that have different adsorption properties than their parent frameworks. Additionally, the reduction in microporosity in the ZIF-7-8 or ZIF-8-ambz hybrids is related to the tunability of the average pore size. By changing the functionality of the substituting linker (2-amBzIM), it may be possible to produce more controllable ZIF hybrid materials. The findings in this Chapter may enable the control of gate-opening phenomena observed in the interaction of ZIF materials with molecules such as CH_4 and CO_2 and will be further explored in Chapters 5 and 6.

3.5 References

(1) Fairen-Jimenez, D.; Moggach, S. A.; Wharmby, M. T.; Wright, P. A.; Parsons, S.; Düren, T. *J. Am. Chem. Soc.* **2011**, *133*, 8900–8902.

(2) Van den Bergh, J.; Gücüyener, C.; Pidko, E. A.; Hensen, E. J. M.; Gascon, J.; Kapteijn, F. *Chem. Eur. J.* **2011**, 8832–8840.

(3) Aguado, S.; Bergeret, G.; Titus, M. P.; Moizan, V.; Nieto-Draghi, C.; Bats, N.; Farrusseng, D. *New J. Chem.* **2011**, *35*, 546–550.

(4) Bux, H.; Chmelik, C.; Van Baten, J. M.; Krishna, R.; Caro, J. *Adv. Mater.* **2010**, *22*, 4741–4743.

(5) Chmelik, C.; Voß, H.; Bux, H.; Caro, J. *Chem. Inger. Tech.* **2011**, *83*, 104–112.

(6) Zhang, C.; Dai, Y.; Johnson, J. R.; Karvan, O.; Koros, W. J. *J. Membr. Sci.* **2011**, *389*, 34–42.

(7) Morris, W.; Doonan, C. J.; Furukawa, H.; Banerjee, R.; Yaghi, O. M. *J. Am. Chem. Soc.* **2008**, *130*, 12626–12627.

(8) Serre, C.; Millange, F.; Thouvenot, C.; Nogues, M.; Louer, D.; Marsolier, G.; Ferey, G. *J. Am. Chem. Soc.* **2002**, *124*, 13519–13526.

(9) Bourrelly, S.; Llewellyn, P. L.; Serre, C.; Millange, F.; Loiseau, T.; Férey, G. *J. Am. Chem. Soc.* **2005**, *127*, 13519–13521.

(10) Couck, S.; Denayer, J. F. M.; Baron, G. V; Re, T.; Gascon, J. *J. Am. Chem. Soc.* **2009**, *131*, 6326–6327.

(11) Stavitski, E.; Pidko, E. A.; Couck, S.; Remy, T.; Hensen, E. J. M.; Weckhuysen, B. M.; Denayer, J.; Gascon, J.; Kapteijn, F. *Langmuir* **2011**, *27*, 3970–3976.

(12) Zhang, J.-P.; Zhu, A.-X.; Lin, R.-B.; Qi, X.-L.; Chen, X.-M. *Adv. Mater.* **2011**, *23*, 1268–1271.

(13) Phan, A.; Doonan, C. J.; Uribe-Romo, F. J.; Knobler, C. B.; O'Keeffe, M.; Yaghi, O. M. *Acc. Chem. Res.* **2010**, *43*, 58–67.

(14) Banerjee, R.; Phan, A.; Wang, B.; Knobler, C. B.; Furukawa, H.; O'Keeffe, M.; Yaghi, O. M. *Science* **2008**, *319*, 939–943.

(15) Banerjee, R.; Furukawa, H.; Britt, D.; Knobler, C.; O'Keeffe, M.; Yaghi, O. M. *J. Am. Chem. Soc.* **2009**, *131*, 3875–3877.

(16) Ma, B.-Q.; Mulfort, K. L.; Hupp, J. T. *Inorg. Chem.* **2005**, *44*, 4912–4914.

(17) Altomare, A.; Camalli, M.; Cuocci, C.; Giacovazzo, C.; Moliterni, A.; Rizzi, R. *J. Appl. Cryst.* **2009**, *42*, 1197–1202.

(18) Horvath, G.; Kawazoe, K. *J. Chem. Eng. Japan* **1983**, *16*, 470–475.

(19) Miller, K. J. *J. Am. Chem. Soc.* **1990**, *112*, 8533–8542.

(20) Bain, G. A.; Berry, J. F. *J. Chem. Ed.* **2008**, *85*, 1–5.

(21) Bae, T.-H.; Lee, J. S.; Qiu, W.; Koros, W. J.; Jones, C. W.; Nair, S. *Angew. Chem. Int. Ed.* **2010**, *122*, 9863–9866.

(22) Cravillon, J.; Nayuk, R.; Springer, S.; Feldhoff, A.; Huber, K.; Wiebcke, M. *Chem. Mater.* **2011**, *23*, 2130–2141.

(23) Pan, Y.; Liu, Y.; Zeng, G.; Zhao, L.; Lai, Z. *Chem. Commun.* **2011**, *47*, 2071–2073.

(24) Diring, S.; Furukawa, S.; Takashima, Y.; Tsuruoka, T.; Kitagawa, S. *Chem. Mater.* **2010**, *22*, 4531–4538.

(25) Wiebcke, M.; Cravillon, J.; Münzer, S.; Lohmeier, S.-J.; Feldhoff, A.; Huber, K. *Chem. Mater.* **2009**, *21*, 1410–1412.

(26) Venna, S. R.; Jasinski, J. B.; Carreon, M. A. *J. Am. Chem. Soc.* **2010**, *132*, 18030–18033.

(27) Park, K. S.; Ni, Z.; Côté, A. P.; Choi, J. Y.; Huang, R.; Uribe-Romo, F. J.; Chae, H. K.; O'Keeffe, M.; Yaghi, O. M. *Proc. Nat. Acad. Sci.* **2006**, *103*, 10186–10191.

(28) Li, Y.-S.; Bux, H.; Feldhoff, A.; Li, G.-L.; Yang, W.-S.; Caro, J. *Adv. Mater.* **2010**, *22*, 3322–3326.

(29) Thommes, M. In *Stud. Surf. Sci. Catal.*; van Bekkum, H.; Cejka, J.; Schuth, F.; Corma, A., Eds.; 2007; pp. 495–524.

CHAPTER 4

Processing Condition Effects on Zeolitic Imidazolate Framework Materials during Mixed-Matrix Membrane Fabrication

4.1 Introduction

A critical step in the fabrication of composite, or mixed-matrix, membranes is the dispersion of the filler particles in the polymer solution. The use of surfactants and salts can provide colloidal stability and prevent particle aggregation, but ultrasonication is widely used to disperse particles for composite membrane fabrication. While some MOFs such as ZIF-8 have shown chemical and thermal stability in various solvents, the stability of MOFs upon exposure to high-powered ultrasonication is not currently known. Indeed, it is not uncommon for sonication to generate chemical reactions due to localized high temperatures, and some MOFs such as MOF-177 have been synthesized by a sonochemical route.[1]

In this chapter, the effects of sonication on ZIF-8 nanoparticles during the fabrication of ZIF-8/Matrimid® MMMs are explored, using two distinct sonication methods. When high-intensity sonication is used for particle dispersion, there is a significant change in particle size, polydispersity, and morphology of the crystals. The results suggest that the phenomenon is a non-ideal coarsening effect induced by sonication. Dynamic light scattering measurements and electron microscopy show a distinctly bimodal particle size distribution that appears when sonication is applied to

ZIF-8 dispersions at different concentrations. The ZIF-8 nanoparticles are further characterized by examining the crystal structure of the coarsened ZIF-8 particles using XRD and pair distribution function (PDF) analysis.

It is also shown that ZIF-8/Matrimid® MMMs have different microstructures and gas permeation behavior, depending on the sonication conditions used to prepare the polymer-nanoparticle dispersions. The observed membrane morphology-permeation property relationships are shown to be wholly consistent with expected MMM behavior, as described by Maxwell models for the different membrane microstructures. A significant conclusion of this Chapter is that a systematic understanding of MOF-MMM behavior is indeed possible through detailed structure-property correlations, and careful evaluation of the effects of commonly used processing conditions is necessary in the fabrication of such membranes. Due to the systematic and consistent trends observed in the performance of the ZIF-8/Matrimid® MMMs, The permeation characteristics of the ZIF-8 crystals are reliably estimated as existing in the MMMs and show that these separation properties are indeed different from those obtained by permeation measurements with pure ZIF-8 membranes or predicted by adsorption and diffusion studies with ZIF-8 crystals or by computational predictions.

4.2 Experimental Methods

4.2.1 ZIF-8 Nanoparticle Synthesis

ZIF-8 nanoparticles were synthesized in a manner similar to a previously published procedure.[2] Two reactant solutions were prepared: 1.50 g $Zn(NO_3)_2 \cdot 6H_2O$

(Sigma-Aldrich, 99%) in 50 mL MeOH; and 1.67 g 2-methylimidazole (2-MeIM, Sigma-Aldrich, 99%) in 50 mL MeOH. The Zn salt solution was poured into the imidazole solution and stirred at room temperature for 1 hour. The resulting milky solution was centrifuged at 7,000 rpm for 5 min, and the supernatant was removed. After washing the precipitate with MeOH and sonicating in a bath to redisperse the powder product, this process was repeated three more times. The resulting powder was dried in an oven at 358 K.

4.2.2 Ultrasonication Studies

The sonication horn used for direct sonication was a FisherSci Ultrasonic Model 500 Dismembrator with an average power output of 200 W (400 W at 50% amplitude) and 20 kHz frequency. The sonication bath used for indirect sonication was a VWR Ultrasonication water bath, operating at 120 W and 40 kHz. To investigate ZIF-8 stability using direct sonication, dispersions were prepared in 20 mL borosilicate vials with constant ZIF-8 concentrations of 1.0 $g \cdot L^{-1}$ (0.025 g ZIF-8 in 5 mL tetrahydrofuran (THF)) and 20 $g \cdot L^{-1}$ (0.1 g ZIF-8 in 5 mL THF). These solutions were sonicated in 30-sec intervals and allowed to cool before sonicating again to minimize solvent evaporation. The dispersions were then filtered and washed with DI H_2O to obtain the resulting powder, which was dried in an oven at 358 K.

4.2.3 Composite Membrane Fabrication

ZIF-8/Matrimid® mixed-matrix membranes were prepared by a solution-casting technique. Matrimid® is a glassy polyimide with a hydrophobic backbone; its structure is

shown in Figure 4.1. Dried ZIF-8 particles (0.1-0.25 g) were first dispersed in 5-10 mL THF (Sigma-Aldrich, 99%) by either direct or indirect sonication. Direct sonication was done by inserting a sonication horn into the colloidal solution, and indirect sonication was done by submerging the vial containing the colloidal solution in a sonication water bath. The mixture was sonicated for 5 min. Then, 1.0 g of 10 wt% Matrimid®/THF priming solution was added. Because the ZIF and polymer are assumed to have affinity for each other, the priming step is suggested to help the ZIF dispersion by allowing the polymer to adhere to the ZIF surface, thereby providing steric stability and preventing aggregation of the nanoparticles. This primed dispersion was sonicated for another 2 min. A balance of Matrimid® powder dried in an oven at 358 K was added to obtain the desired composite membrane composition, and the dispersion was tumbled overnight. The resulting ZIF-polymer dope was placed in a glove bag, flushed with N_2, and saturated with THF. The dope was poured across a glass plate, and a film was cast manually using a 200 μm casting knife. After the solvent evaporated and the membrane vitrified, it was annealed at 523 K under vacuum for 12 hours.

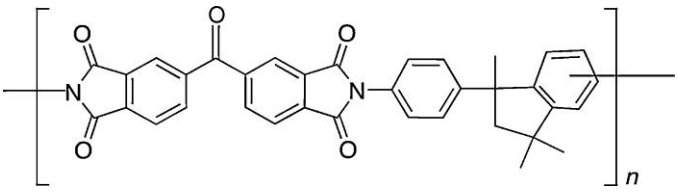

Figure 4.1. Chemical structure of Matrimid® 5128 polymer.

4.2.4 Characterization Methods

ZIF-8 particles were characterized with powder X-ray diffraction (XRD), synchrotron X-ray pair distribution function (PDF) analysis, scanning electron

microscopy (SEM), energy dispersive X-ray spectroscopy (EDX), nitrogen physisorption, Fourier transform infrared spectroscopy (FTIR), Fourier transform Raman spectroscopy (FT-Raman), and dynamic light scattering (DLS). Powder XRD measurements were done on an X'Pert Pro PANalytical X-ray Diffractometer. Experiments were carried out scanning from 4-50° 2θ, using an X'celerator detector. Total scattering data suitable for PDF analysis were collected at beamline 11-ID-B at the Advanced Photon Source at Argonne National Laboratory. High energy X-rays (58 keV, λ = 0.2128 Å) were used, in combination with a large amorphous silicon-based area detector, to collect data to high values of momentum transfer, Q_{max} = 24 Å^{-1}.[3,4] The two-dimensional images were reduced to one-dimensional scattering data within fit2d.[5] The PDFs, *G(r),* were extracted within PDFgetX2, subtracting contributions from the background and Compton scattering to the total scattering data.[6] The PDFs were smoothed by *r*-averaging over the periodicity of the termination ripples ($2\pi/Q_{max}$) to minimize the influence of these artifacts on the subsequent analysis. The measured PDFs contain local structural information as a weighted histogram of all interatomic distances within the material, regardless of crystallinity. The intensity of features in the PDF was weighted by the scattering power of both atoms in a given correlation.

SEM imaging and EDX measurements were carried out with Zeiss LEO 1530 and 1550 scanning electron microscopes. Samples were first coated with either gold or a gold-palladium mixture by sputtering under vacuum. Images were taken at 10 kV accelerating voltage, and EDX analysis was done at 20 kV. Nitrogen physisorption measurements were done with a Micromeritics ASAP 2020 surface area analyzer at 77 K.

Samples were degassed for 18 hours at 308 K. The resulting isotherms were analyzed using the BET method, the Langmuir method, and the t-plot micropore volume method. FTIR and FT-Raman measurements were done with a Bruker Vertex 80v FTIR/RAM II FT-Raman Analyzer. FTIR measurements were performed under vacuum with samples prepared in KBr pellets; FT-Raman measurements were done in open atmosphere with powders deposited in NMR tubes. Spectra were analyzed from 4000-400 cm^{-1}. DLS measurements were performed with a Protein Solutions DynaPro DLS. ZIF-8 or sonicated ZIF-8 powder was dispersed in filtered methanol with a sonication bath. The colloidal solution was then inserted into plastic cuvettes using a 5 μm syringe filter and 3 mL syringe. Autocorrelation functions were analyzed by a regularization fit method solved with a non-negative least squares algorithm to obtain particle size distributions.

ZIF-8/Matrimid® films were characterized using SEM, FTIR and differential scanning calorimetry (DSC). Samples for SEM were prepared by fracturing small portions of the film under liquid N_2 and coating with gold or a gold-palladium mixture by sputtering. FTIR samples were small portions of the film used as-is and measurements were done under vacuum. DSC measurements were done on a Netzsch STA-409-PG thermogravimetric (TGA) and differential scanning calorimeter (DSC). Samples were subjected to two heating cycles from room temperature to 623 K at a 10 $K \cdot min^{-1}$ ramp rate. Glass transition temperatures of each film were determined from the second heating cycle.

4.2.5 Gas Permeation Measurements

Permeation measurements were performed using a constant volume permeation cell described in earlier work.[7] A small area of the film was cut out, and using aluminum tape, a mask was prepared with approximately 1 cm in diameter of exposed membrane area. Film thickness was measured with a micrometer in 5-10 different locations of the masked film and varied between 50-60 μm. At least two areas of a film and two separate films were tested for each membrane reported. After insertion into the permeation cell, the film was degassed at 308 K for at least 24 hours before each permeation test. Leak tests were done before each permeation experiment, ranging from 10^{-8}-10^{-7} kPa·sec^{-1}. Subsequent permeation tests were performed after degassing both sides of the film under vacuum for 12-24 hours and testing the leak rate. Permeation experiments were performed at 308 K with 450 kPa of upstream pressure of either CO_2 or CH_4. Measurements started once upstream gas was introduced to the cell and the downstream was evacuated (<10^{-3} kPa), and permeability values were calculated after the pressure rise rate reached steady state, monitored by taking the derivative of the pressure as a function of time. The time to reach steady state varied between membranes, decreasing as the permeability of the membrane increased with loading of ZIF-8.

4.3. Results & Discussion

4.3.1. Stability of ZIF-8 Nanoparticles during Ultrasonication

Figure 4.2 shows the morphology of the as-synthesized ZIF-8 particles and the particles obtained from 1 g·L^{-1} and 20 g·L^{-1} dispersions after 10 min of direct sonication. In comparison to as-made ZIF-8 (Figure 4.2a), there is a disparity in both particle size

distribution and particle morphology in Figures 4.2b and 4.2c. In the 1 $g \cdot L^{-1}$ dispersion, the morphology of the ZIF-8 particles was largely unchanged after sonication, but a number of larger particles (>500 nm in diameter) were present. In the 20 $g \cdot L^{-1}$ dispersion, there was no longer a well-defined particle morphology; closer examination showed a number of different structures with particle size reaching over 1 μm (Figure 4.3). EDX spectra (Figures 4.4 and 4.5) revealed that these structures were considerably more oxygen-rich than as-made ZIF-8, likely due to surface defects containing hydroxyl groups that are formed upon washing with water after sonication.

To obtain quantitative insight into the SEM observations, DLS measurements were carried out over a range of sonication times, and the particle size distributions (Figure 4.6) obtained from the regularization fit were analyzed for both 1 $g \cdot L^{-1}$ and 20 $g \cdot L^{-1}$ dispersions. Plotting the PSD over time for the 1 $g \cdot L^{-1}$ dispersion, there is first a broadening of the size distribution; however, after a short amount of sonication time, the distribution becomes bimodal. This corroborates well with SEM observations that there are two different particle populations after 10 min sonication. The PSD in Figure 4.6b shows the evolution of ZIF-8 nanoparticles as a function of sonication time at 20 $g \cdot L^{-1}$ dispersion concentration. Due to an increase in volume fraction of nanoparticles, the rate of particle growth increases considerably, accounting for the much larger change in PSD from DLS.[8] To verify these changes in PSD are directly related to the ultrasonication process, ZIF-8 nanoparticles were solvothermally treated in 10 mL THF at 373 K for 24 hrs using a Parr digestion bomb. After treatment, no particle size changes were observed

by DLS. There were also no changes in the long-range crystallographic structure as observed by powder XRD (see Figures 4.7 and 4.8).

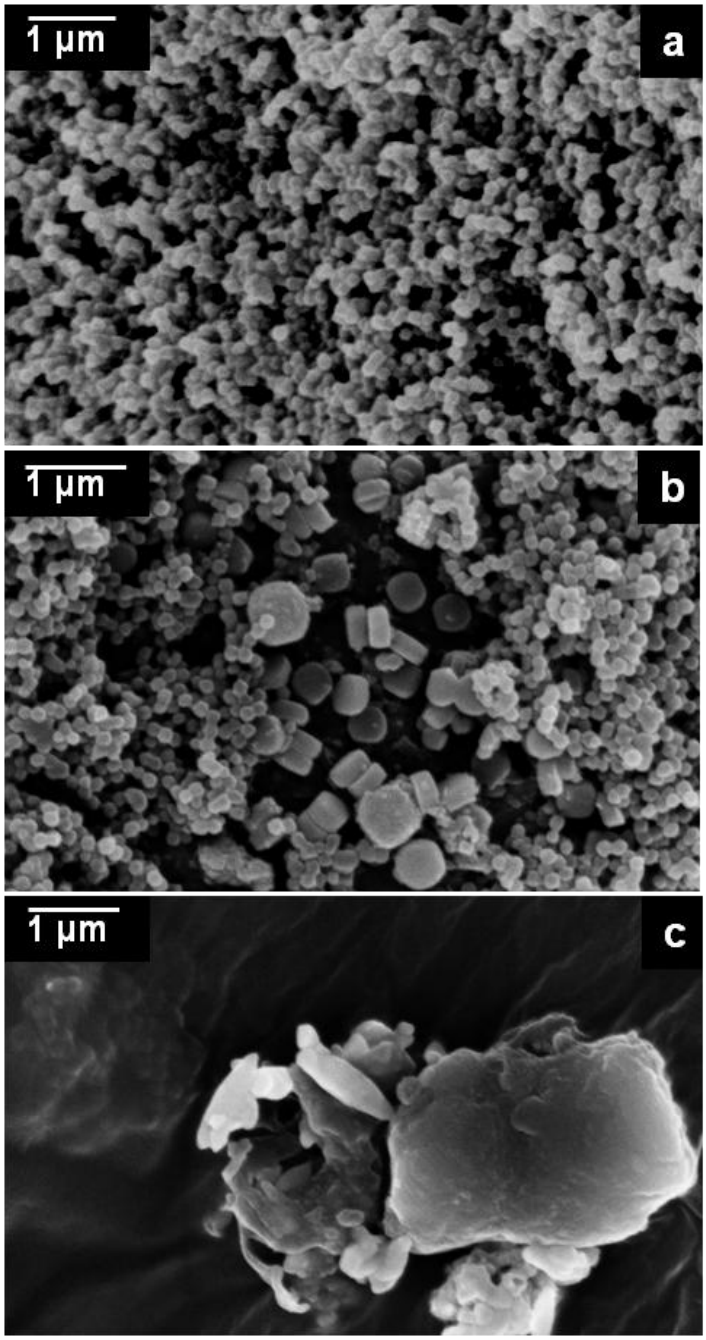

Figure 4.2. SEM images of the ZIF-8 nanoparticles showing changes in particle size, polydispersity and morphology: (**a**) as-made; (**b**) 1 $g \cdot L^{-1}$ dispersion sonicated for 10 min; (**c**) 20 $g \cdot L^{-1}$ dispersion sonicated for 10 min.

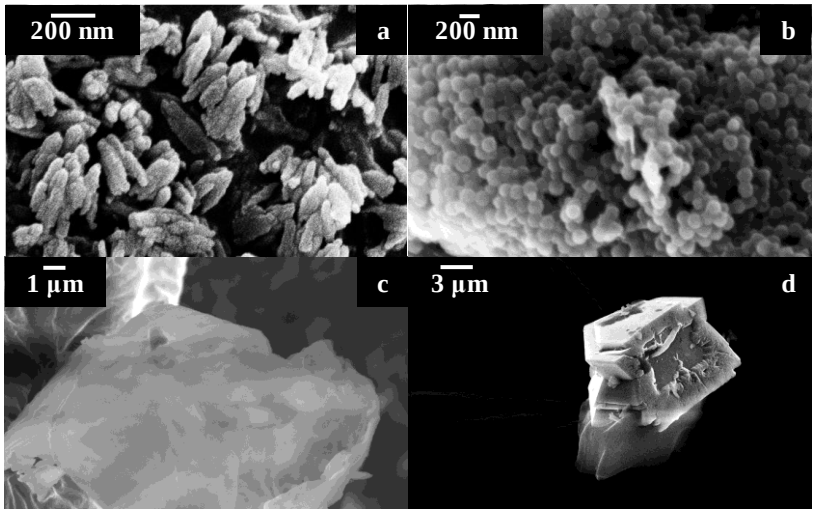

Figure 4.3. SEM images of various structures after sonicating ZIF-8 for 10 min in THF at 20 g·L^{-1} concentration.

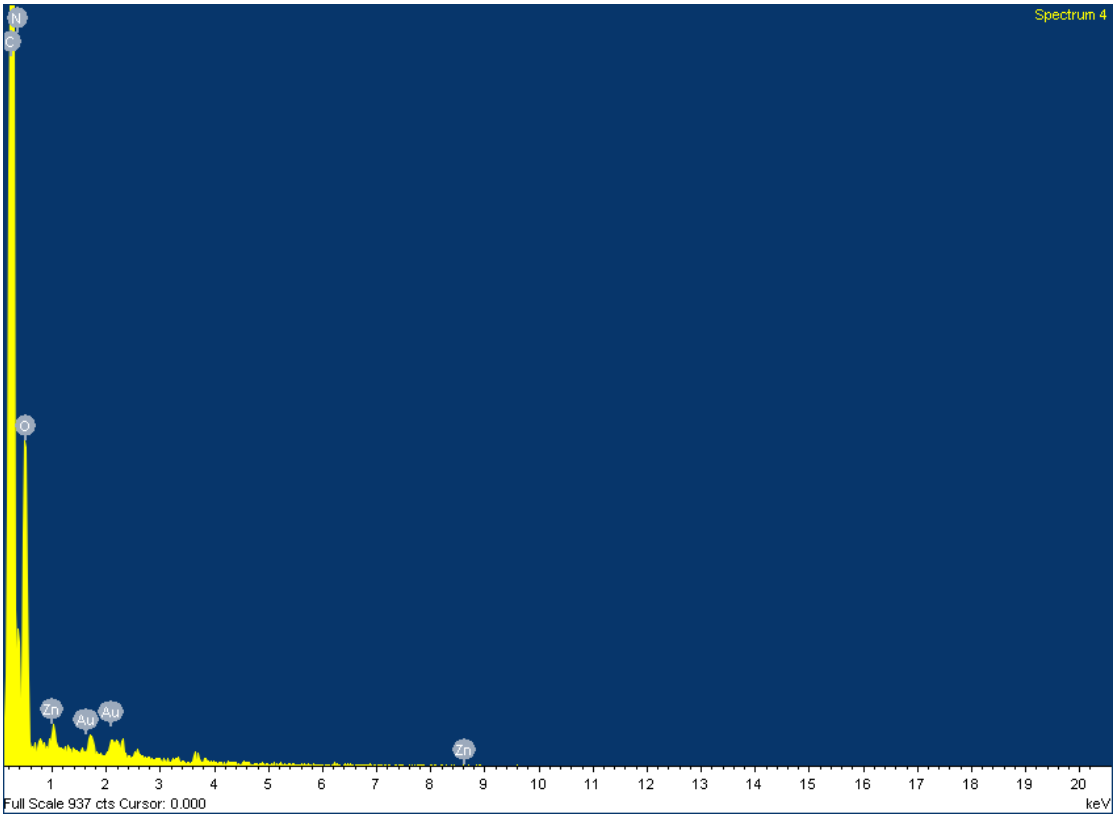

Figure 4.4. EDX spectrum corresponding to SEM image in Figure 4.3c. Contains a small amount of zinc and is likely amorphous 2-methylimidazole formed during sonication.

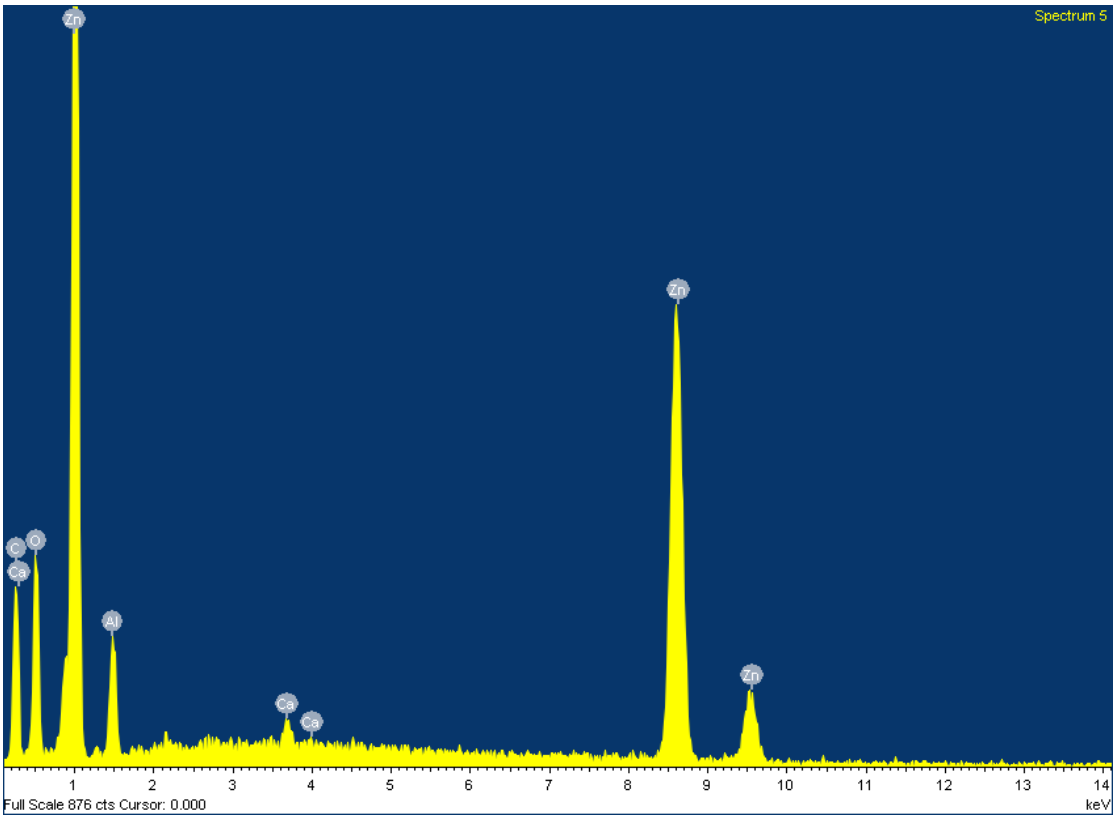

Figure 4.5. EDX spectrum corresponding to Figure 4.3d. Structure shows a considerable increase in zinc and oxygen content.

Combining the observations of SEM and DLS, these results support the occurrence of a sonication-induced Ostwald ripening-like mechanism involving preferential dissolution of smaller ZIF-8 particles and recrystallization and growth of larger ZIF-8 particles.[9] During ultrasonication, cavitation from sonic waves creates localized areas wherein the pressure and temperature are significantly different than that of the surrounding medium, known as "hot spots".[10,11] It is likely that these cavitational effects from ultrasonication lead to the dissolution of the ZIF-8 constituents at the particle surfaces. This is followed by diffusion of the dissolved species and rapid recrystallization on the other particles. Since the smaller particles have a lower thermodynamic stability and a higher surface-to-volume ratio,[12] the ripening process leads to the slow

disappearance of small particles and the rapid growth of large particles to minimize the surface free energy, thereby leading to an increase in the average particle size and a shift from a narrow to a bimodal PSD (Figure 4.6).

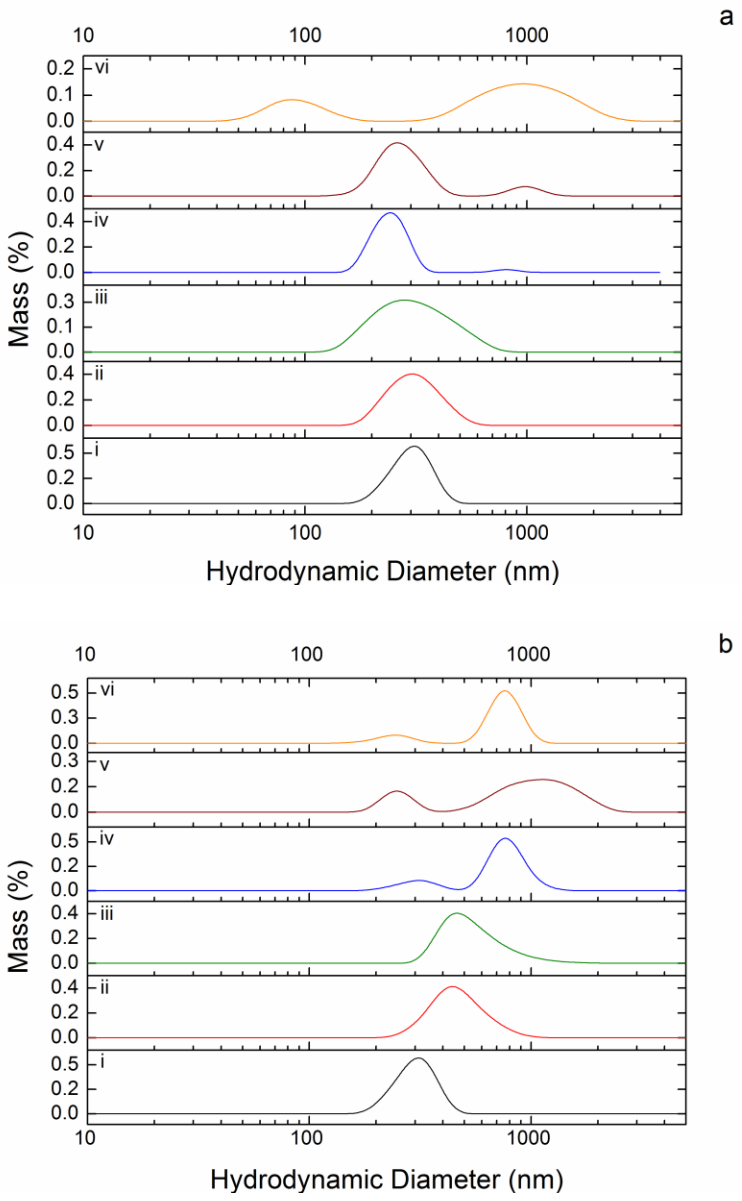

Figure 4.6. Evolution of ZIF-8 particle size distribution in 1 $g \cdot L^{-1}$ (**a**) and 20 $g \cdot L^{-1}$ (**b**) suspensions during sonication, showing the shifts as well as broadening of the size distribution: i) 0 min sonication; ii) 0.5 min; iii) 1 min; iv) 2 min; v) 5 min; vi) 10 min. The appearance of a bimodal distribution is indicative of a non-ideal nanoparticle coarsening phenomenon.

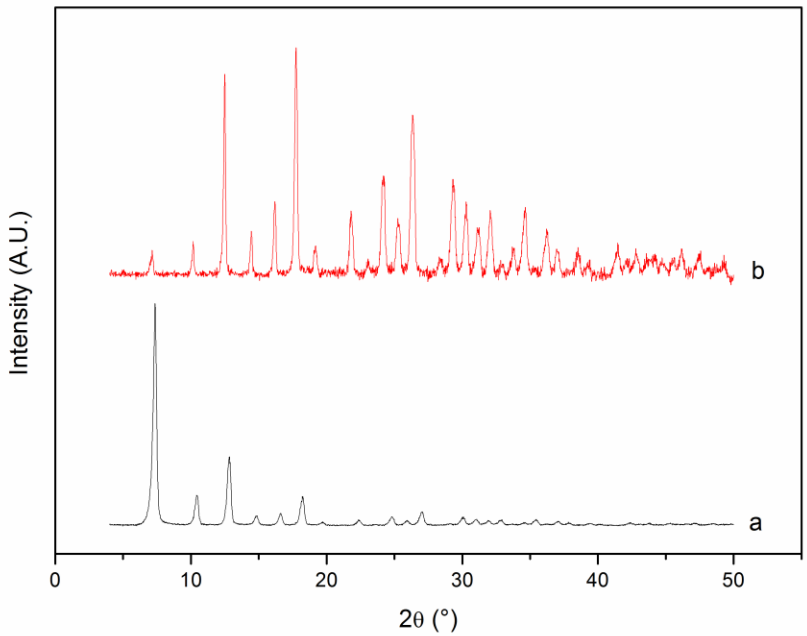

Figure 4.7. Powder XRD pattern of as-made ZIF-8 (**a**) compared with ZIF-8 solvothermally treated in THF at 373 K (**b**).

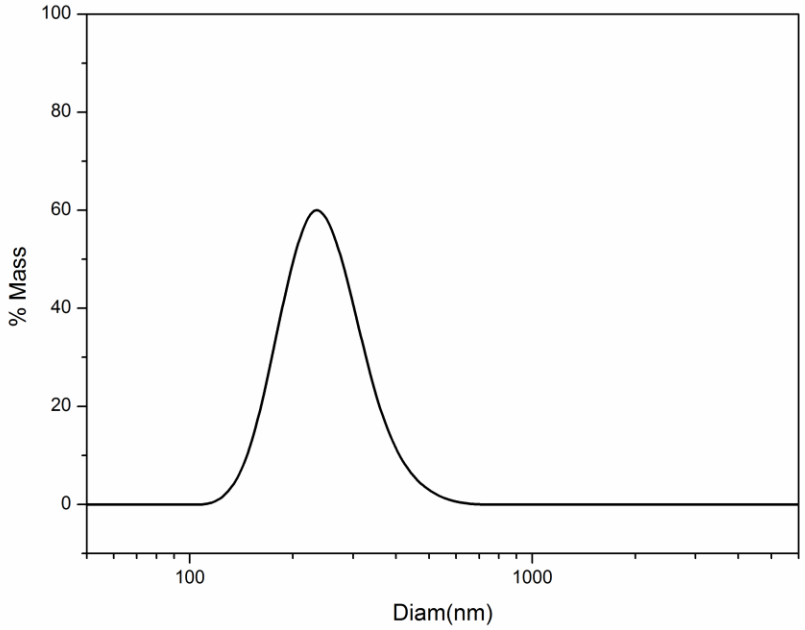

Figure 4.8. Particle size distribution of solvothermally treated ZIF-8.

Because the PSD becomes bimodal, it is important to deconvolute the two distributions to analyze the growth kinetics.[13] If the ripening process is limited by diffusion of the solute from the small particles to the large particles, then the radius (r) of the large particles should grow with time (t) at a rate given by $r \sim Kt^{1/3}$ according to LSW theory.[14,15] In Figure 4.9, r is plotted as a function of $t^{1/3}$. The radius, r, is calculated by integrating the area of each particle size distribution obtained from the curves shown in Figure 4.6. The initial lack of particle growth could be interpreted as an "induction" period, which may be necessary to gain a critical disparity in particle sizes before there are any noticeable ripening effects using DLS. After this induction period, there are large enough particle populations above and below the critical radius for Ostwald ripening to occur.[16] However, it is important to note that under sonication conditions two assumptions of LSW theory are possibly not satisfied, resulting in the observed non-ideal coarsening behavior. The particles are likely colliding from Brownian motion and from cavitation in the sonicated solution; therefore, the particles are not fixed in space and are experiencing interparticle interactions, both of which are not accounted for by LSW theory.

The size of the dissolving smaller particles is also shown in Figure 4.9 for both dispersions, revealing an overall decrease in the smaller particle size with sonication time. This confirms the slow disappearance of the smaller particle population, an effect of Ostwald ripening-like mechanisms. In both dispersions, the larger particles show primarily an increasing particle size with time; however, in the 20 $g \cdot L^{-1}$ dispersion the larger particle size actually shows an apparent decrease at long sonication times. This

leads to the hypothesis that elastic stress effects may play a role in the particle ripening (see Figure 4.10 and discussion). It has been shown that a large increase in elastic stress in "soft" particles leads to their breakage into smaller particles to minimize the energy of the system.[8] This may also be accompanied by a morphological change; for instance, spherical nanoparticles can become cuboidal as the ratio of the interfacial energy to the elastic energy decreases.[17] Because the 20 g·L^{-1} dispersion ripens at a faster rate than the 1 g·L^{-1} suspension, this ratio would decrease more rapidly in the former case, leading to particles breaking to reduce the elastic stress and also leading to formation of different morphologies seen in SEM.

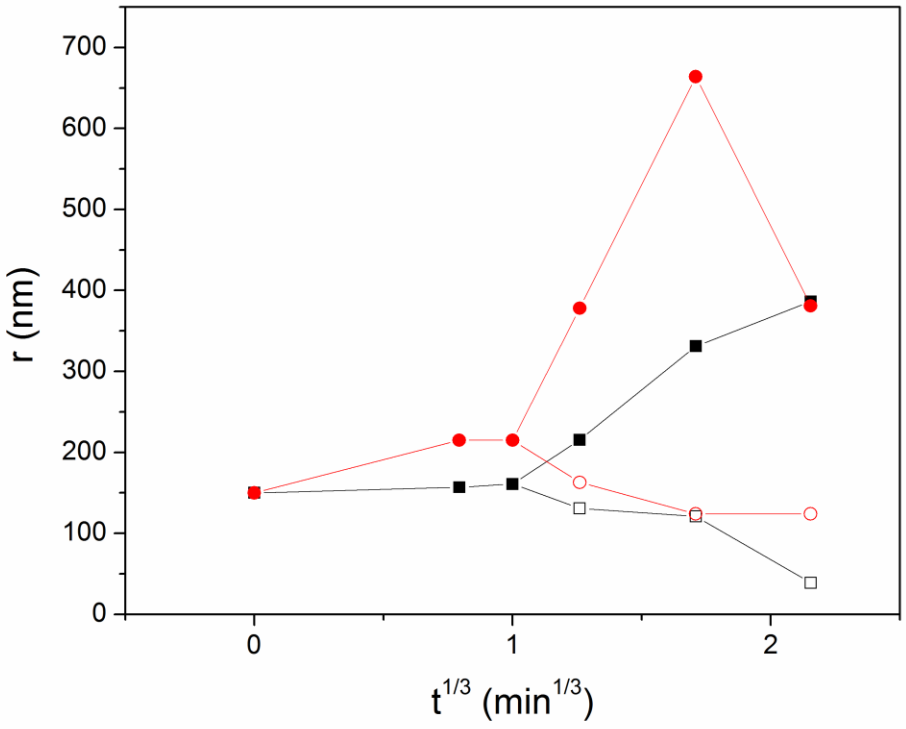

Figure 4.9. Ostwald ripening of ZIF-8 suspensions: *r* as a function of sonication time, $t^{1/3}$. Squares: 1 g·L^{-1}; Circles: 20 g·L^{-1}; Closed symbols: growing particles; Open symbols: shrinking particles.

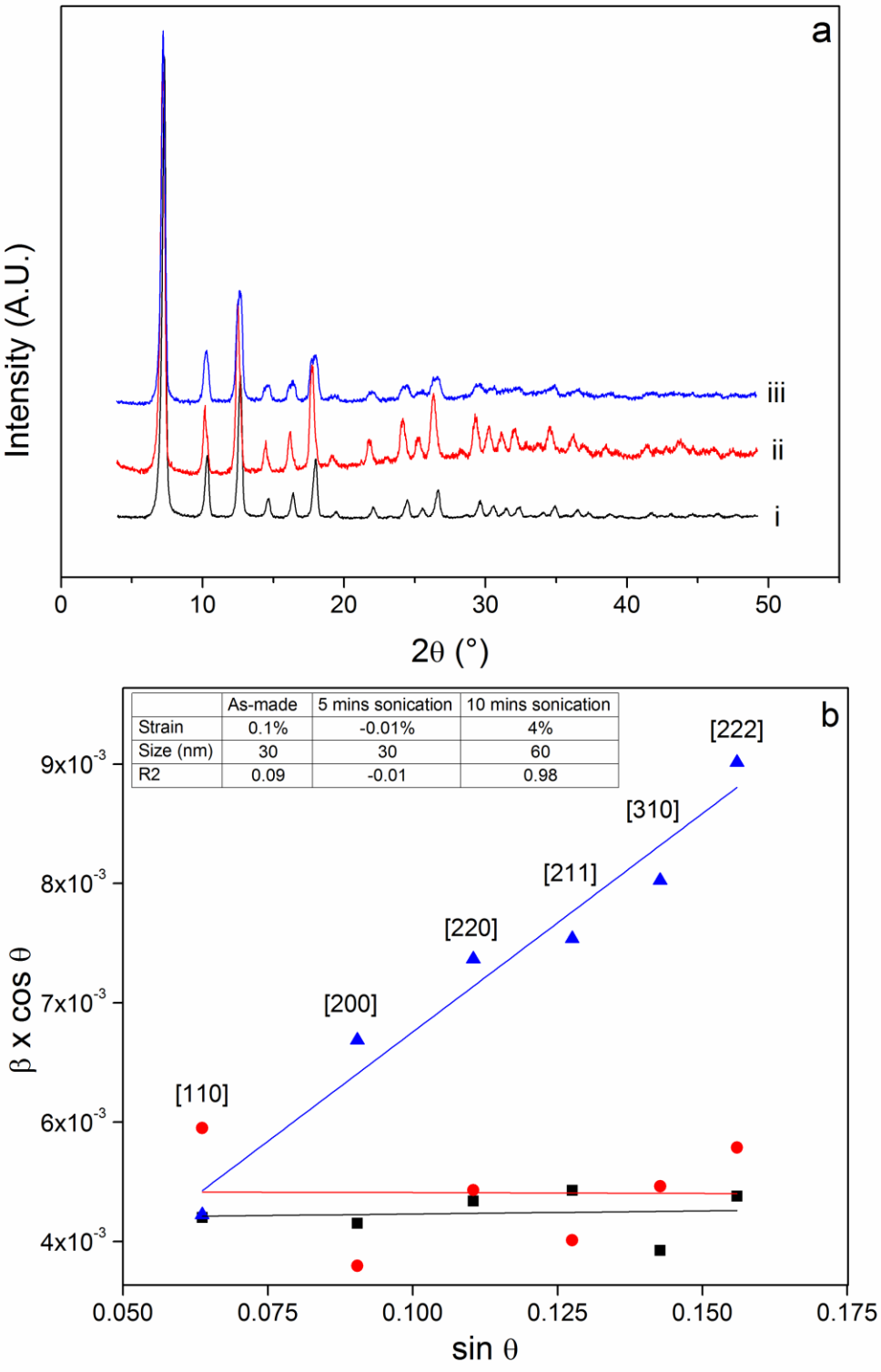

Figure 4.10. Powder XRD patterns (**a**) and Williamson-Hall plots (**b**) of as-made ZIF-8 (i, black squares), ZIF-8 sonicated for 5 min (ii, red circles), and ZIF-8 sonicated for 10 min (iii, blue triangles).

Powder XRD patterns of the sonicated samples (20 $g \cdot L^{-1}$ concentration) are shown in Figure 4.10a. Although the low-angle region of the XRD patterns indicates that the long-range topology of the ZIF-8 framework is preserved, the XRD peaks of the sonicated samples are both shifted as well as broadened. Because XRD peaks at higher 2θ (lower *d*-spacing) disappeared with longer sonication time, this indicates the framework became more locally disordered. These observations suggest that the ZIF-8 nanoparticles maintain long-range crystallinity, but may have a greater degree of static disorder (*e.g.*, rotational orientation of the imidazolate linkers). The crystallite domain size and crystal strain as a result of sonication can be estimated respectively from the intercept and the slope of a Williamson-Hall plot, as shown in Figure 4.10b and Equation 4.1:[18]

$$\beta \cos\theta = \eta \sin\theta + \frac{K\lambda}{L} \tag{4.1}$$

where β is the full-width half-maximum (FWHM) of the diffraction peak, θ is the diffraction angle, K is a constant equal to 0.9, λ is the X-ray wavelength, η is the crystalline strain, and L is the crystallite size. The FWHM of a set of low-angle peaks was determined by fitting the data to a Cauchy-Lorentz peak shape. The as-made ZIF-8 and ZIF-8 sonicated for 5 minutes both show a negligible slope, indicating that the crystal lattice is not significantly strained even after 5 minutes of intense sonication. However at 10 minutes of sonication, there is a clear development of lattice strain (~4%), as well as an increase in crystallite domain size consistent with significant Ostwald ripening and formation of larger crystallites (see inset Table in Figure 4.10b). The lattice strain

developed at 10 min of sonication correlates well with the behavior observed in Figure 4.9. As a large elastic stress develops in the particles, they begin to break apart and/or form different morphologies (both shown in Figures 4.2b and 4.2c) to reduce the overall energy of the system. The synchrotron X-ray PDF patterns (Figure 4.11) also corroborate the observations from powder XRD patterns of maintenance of the crystal structure. The distributions of short-range atomic distances (<1 nm) in sonicated and as-made ZIF-8 are essentially identical, thereby indicating that sonication does not cause localized defects (such as missing metal centers or organic linkers) in the bulk structure. Although there are slight changes in the PDFs at 3.26 and 8.33 Å, this is not indicative of significant differences between the materials, since the changes do not appear to be a function of sonication time.

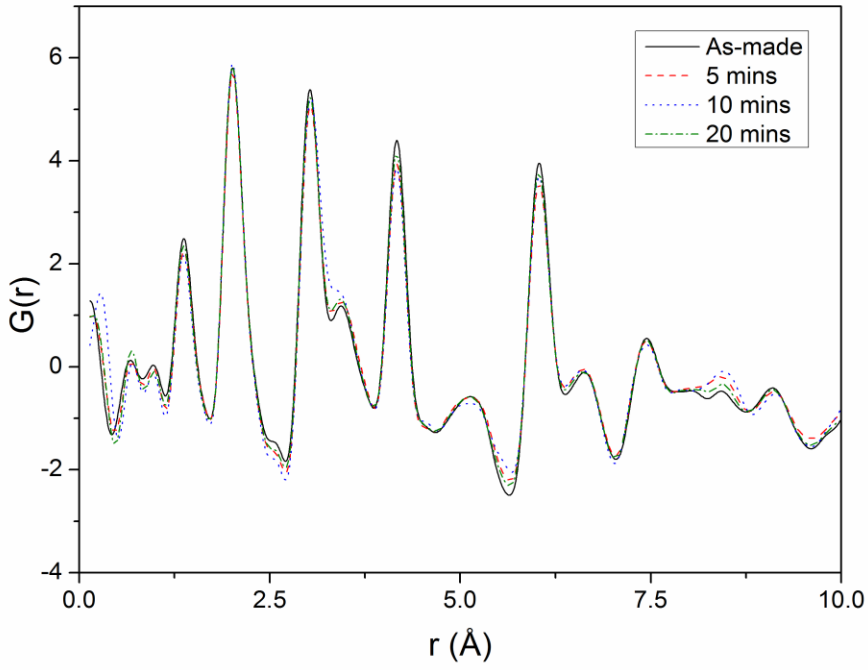

Figure 4.11. Synchrotron X-ray pair distribution functions of sonicated and as-made ZIF-8. Solid line: as-made ZIF-8; Dashed line: ZIF-8 sonicated for 5 min; Dotted line: sonicated for 10 min; Dashed-Dotted line: sonicated for 20 min.

Nitrogen physisorption isotherms of as-made and sonicated ZIF-8 are shown in Figure 4.12. The calculated BET surface area, Langmuir surface area, and t-plot micropore volume are shown in Table 4.1. Because ZIF-8 has an adsorption inflection at $P/P_0 \sim 5x10^{-3}$, selection of the range for BET and Langmuir surface area calculations were done by consistency criteria established previously.[19] There was a noticeable decrease (~10%) in the micropore volume and Langmuir surface area after sonication, although the BET surface area did no change significantly.

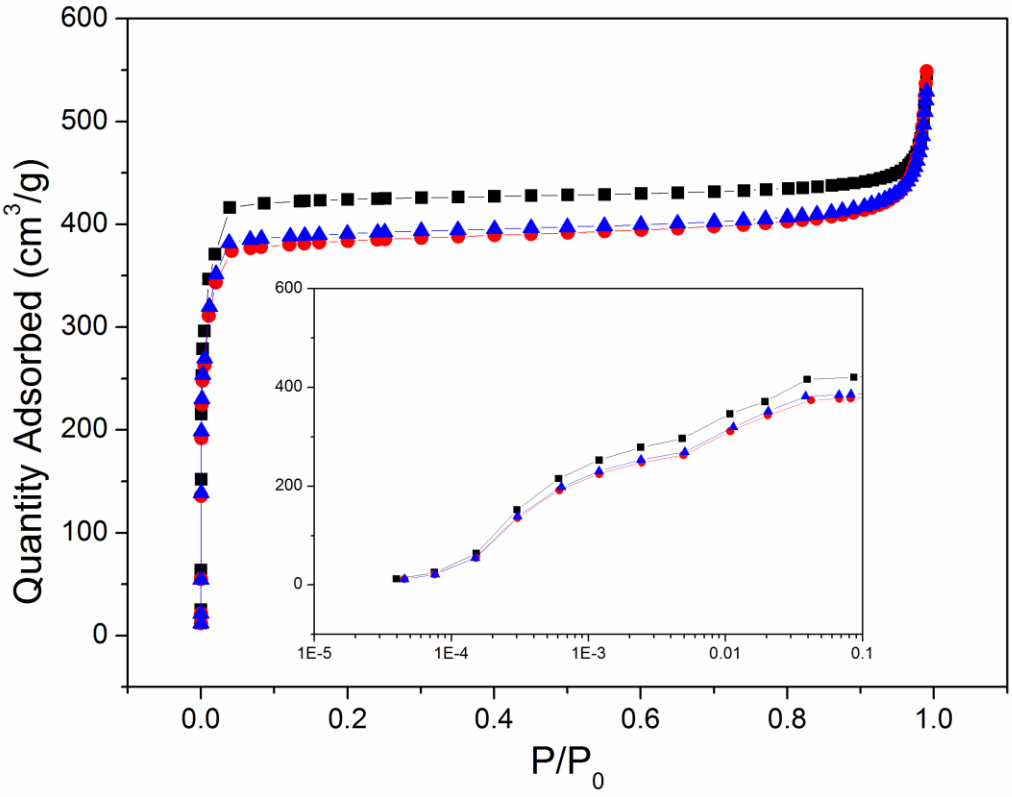

Figure 4.12. Nitrogen physisorption isotherms at 77 K. Squares: as-made ZIF-8; Circles: ZIF-8 sonicated for 5 min; Triangles: ZIF-8 sonicated for 10 min.

Table 4.1. Surface area and micropore volume of ZIF-8 based on N_2 physisorption isotherms at 77 K, showing decreases in both Langmuir surface area and t-plot micropore volume.

Sonication time (mins)	BET SA ($m^2 \cdot g^{-1}$)	Langmuir SA ($m^2 \cdot g^{-1}$)	t-plot micropore volume ($cm^3 \cdot g^{-1}$)
0	1700 ± 60	1870 ± 50	0.64 ± 0.03
5	1650 ± 60	1720 ± 50	0.56 ± 0.03
10	1710 ± 60	1740 ± 50	0.58 ± 0.03

FTIR and FT-Raman spectra (Figure 4.13) were used to further examine the chemical bonding changes in the material. After sonication for 5-10 min, an additional vibrational band appeared in the FTIR spectra at 480 cm^{-1} and the vibration at 3400 cm^{-1} increased in intensity relative to other vibrations in the framework. These vibrations correspond to ν(Zn-O) and ν(-OH), respectively.[20] EDX analysis of sonicated ZIF-8 nanoparticles (Figure 4.4 and 4.5) indicates that these particles can have significantly higher oxygen content than as-made ZIF-8. Interestingly, there were no changes in the FT-Raman spectra after sonicating for 10 min. Since the appearance of Raman-active phonons in ZnO is strongly related to the inherent symmetry of the crystalline wurtzite structure and the wurtzite structure generally has different morphology than ZIF-8, these oxygen-rich domains can be attributed to surface hydroxyl (Zn-OH) groups.[21,22]

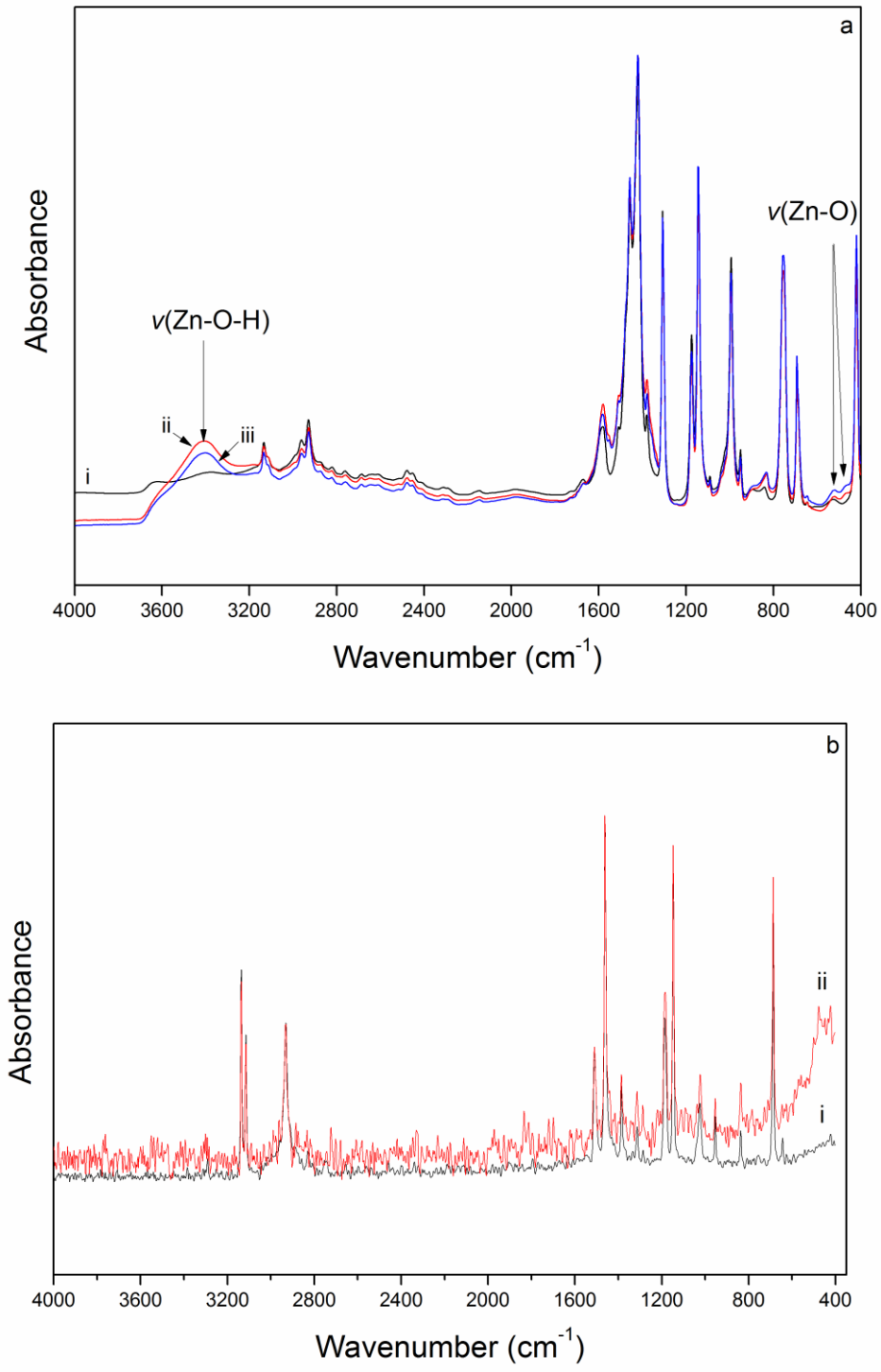

Figure 4.13. FTIR (**a**) and FT-Raman (**b**) spectra of ZIF-8 before and after sonication. FTIR labels: i) as-made ZIF-8; ii) ZIF-8 sonicated for 5 min; iii) ZIF-8 sonicated for 10 min. FT-Raman labels: i) as-made ZIF-8; ii) ZIF-8 sonicated for 5 min.

Overall, the characterization results are consistent with the conclusion that the bulk structure of ZIF-8 remains essentially intact after sonication and even after the non-ideal nanoparticle coarsening, albeit with a somewhat higher degree of static disorder shown by XRD. While the bulk of the resulting ZIF-8 particles may retain a structure close to that of the as-made ZIF-8 crystals, these observations indicate that the outer regions and surfaces of the sonicated particles likely contain more localized defects. The reduction in Langmuir surface area and micropore volume are also consistent with an increased frequency of defects (*e.g.*, Zn-OH bonds occurring at the particle surface) and pore blockages created during rapid recrystallization of ZIF-8 nanoparticles upon sonication. This may alter the rate of molecular diffusion into the crystal if the micropores on the surface are partially blocked, resulting in ZIF-8 composite membrane permeation behavior that cannot be predicted from the structure of the as-made ZIF-8 material or from permeation data collected from as-made ZIF-8 membranes.[23]

4.3.2 ZIF-8/Matrimid® Composite Membranes

Composite membranes were prepared by the solution-casting technique. Permeation measurements were performed on membranes containing 0, 10, and 25 wt% of ZIF-8 and subjected to two different sonication methods (direct and indirect) for dispersing the ZIF-8 particles prior to membrane casting. Different sonication conditions were used to illustrate the large differences in ultrasound energy intensity between direct and indirect sonication and to show the required processing conditions to fabricate defect-free composite membranes. The power output per unit area was 156 $W \cdot cm^{-2}$ for direct sonication and 3.78 $W \cdot cm^{-2}$ for indirect sonication.[24] Cross-sections of membranes

prepared by both sonication methods are shown in Figure 4.14. While the dispersion of nanoparticles in the polymer matrix varies, Figures 4.14a and 4.14b show no large agglomerates when direct sonication was used. Overall, the ZIF-8 particles showed good adhesion to the polymer with some evidence of non-ideal coarsening occurring during membrane fabrication.

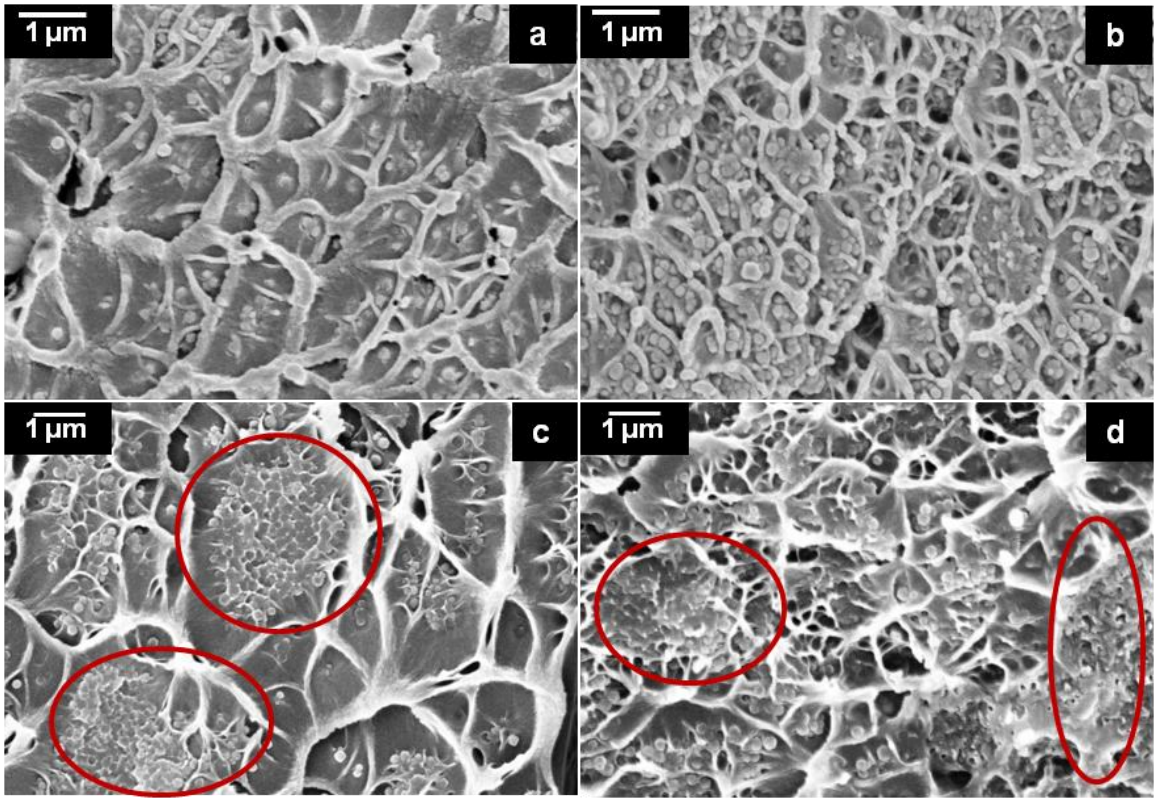

Figure 4.14. SEM images of cross sections of ZIF-8/Matrimid® composite membranes prepared by direct (**a**, **b**) and indirect (**c**, **d**) sonication: (**a**, **c**) 10 wt% loading; (**b**, **d**) 25 wt% loading.

FTIR measurements of as-made films indicated that there was a small shift for the symmetric imide carbonyl group vibration of the polymer (Figure 4.15) in the composite membranes when compared to the pure polymer membrane. This suggests that the carbonyl groups of the polymer interact with the organic linkers on the surface of the

ZIF-8 nanoparticles. Upon annealing at 523 K, the imide carbonyl group vibration (~1775 cm^{-1}) is similar for the composite films while the pure Matrimid® film still shows a higher carbonyl frequency (~1780 cm^{-1}). Additionally, the broadening of the carbonyl band in the composite membranes (FWHM ~20 cm^{-1}) is noticeably larger than in pure Matrimid® (~10 cm^{-1}). These observations indicate that the composite membrane carbonyl groups are in different, more widely distributed electronic environments than the pure polymer and may be interacting with the surface of ZIF-8 nanoparticles.

The annealed films were analyzed by DSC to determine shifts in the glass transition temperature (T_g). In Figure 4.16, there is a clear, upward shift in T_g from 583 K to 593 K. This shift does not appear to be a strong function of the loading of ZIF-8 as the T_g does not change greatly with loading of ZIF-8. Previously, it was shown that only a single T_g was observable in ZIF-8/poly-(ethersulfone) composite membranes, which showed no apparent T_g shift.[25] Considering the more electronegative nature of the carbonyl versus the sulfonyl functional groups, it is hypothesized that the shifts seen in both FTIR and DSC are due to a change in the conjugation of the carbonyl functional groups at the ZIF-8 surface, interacting with terminal imidazolate groups.

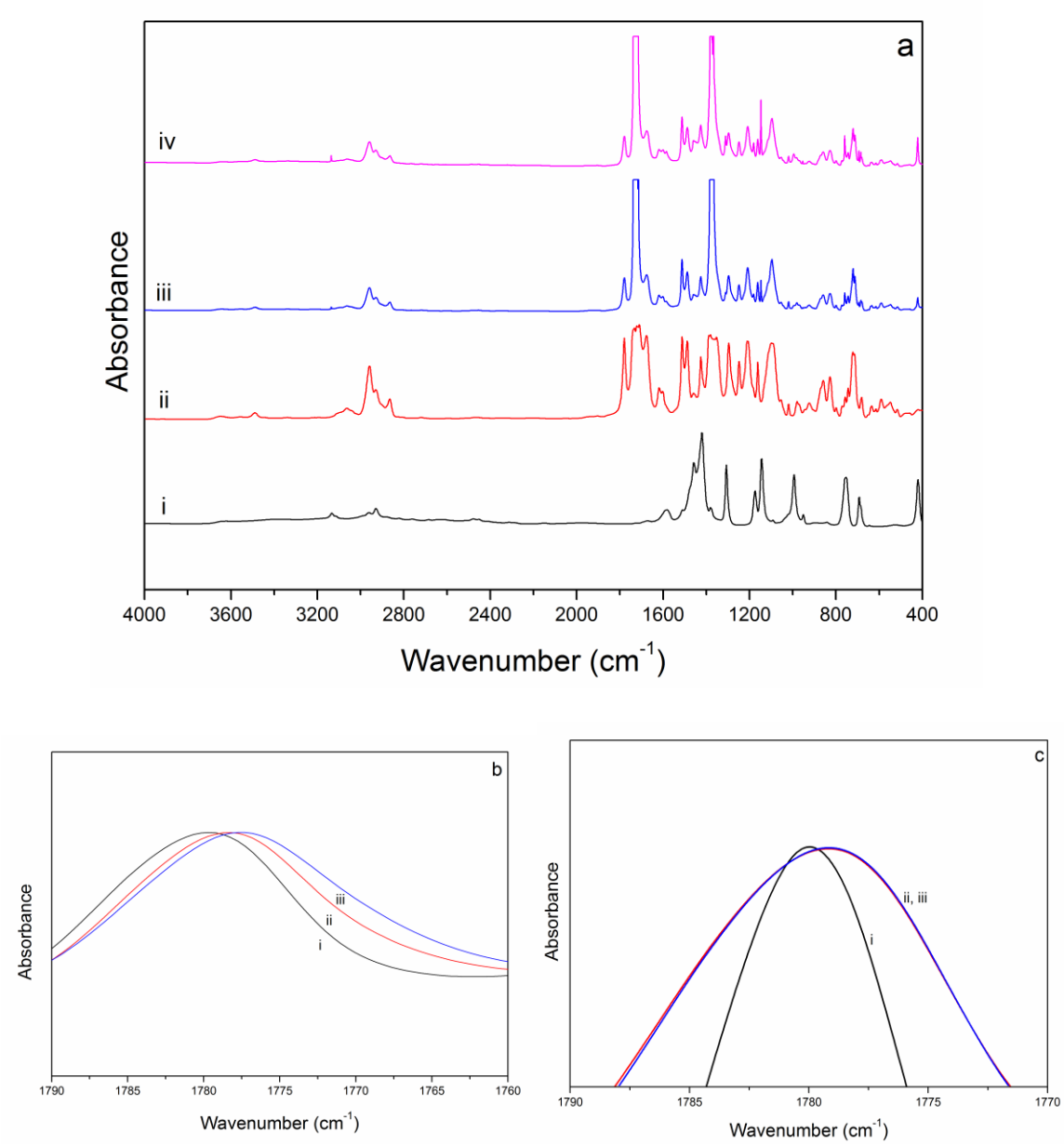

Figure 4.15. FTIR spectra (**a**) of ZIF-8 and composite membranes at different loadings: i) as-made ZIF-8; ii) Pure Matrimid®; iii) 10 wt% ZIF-8/Matrimid® composite; iv) 25 wt% ZIF-8/Matrimid® composite. Zooming in at 1780 cm^{-1} shows a shift to lower wavenumber before (**b**) and after annealing (**c**), indicating the imide carbonyl group is interacting with the ZIF-8 surface: i) Pure Matrimid®; ii) 10 wt% ZIF-8/Matrimid®; iii) 25 wt% ZIF-8/Matrimid®.

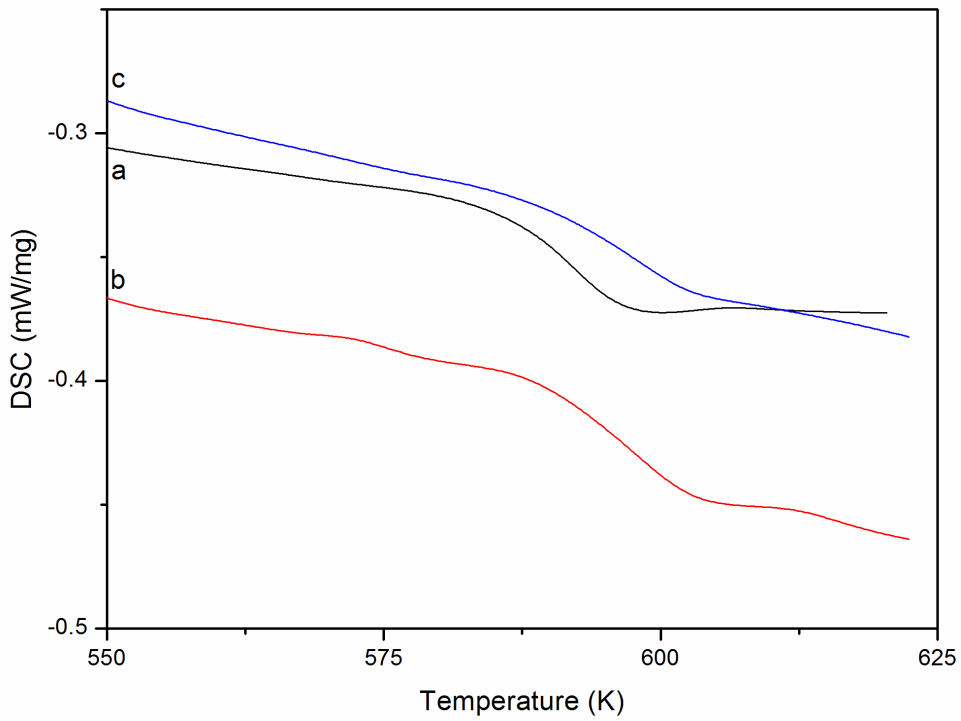

Figure 4.16. DSC curves of the second heating cycle for (**a**) Pure Matrimid®, (**b**) 10 wt% ZIF-8/Matrimid®, and (**c**) 25 wt% ZIF-8/Matrimid®.

Cross-sections of membranes prepared by indirect sonication are shown in Figures 4.14c and 4.14d. There was no change in the particle size, polydispersity, or morphology in comparison to the as-made ZIF-8. Because of its much smaller power density, the indirect sonication method does not provide enough energy to fully break apart nanoparticle aggregates or cause nanoparticle coarsening. Although the ZIF-8 particles still showed good adhesion with the polymer, the nanoparticles in the matrix were in large aggregates, ranging up to several micrometers in size (emphasized with red circles in Figures 4.14c and 4.14d). Poor dispersion typically creates paths for unselective transport of gases between the particles during permeation, resulting in a large increase in permeability and a decrease in selectivity.[26] Conversely, the use of the direct sonication method allowed successful dispersion of the ZIF-8 nanoparticles in the polymer solution,

but also lead to significant changes in the particle size distribution (coarsening) and the quality of the ZIF-8 crystals at the end of the sonication procedure.

Table 4.2. Permeation data from composites membranes prepared by different sonication methods.

Wt %	Composite Membrane Prepared by Direct Sonication			Composite Membrane Prepared by Indirect Sonication		
	CO_2 Permeability (Barrer)	CH_4 Permeability (Barrer)	Ideal CO_2/CH_4 Selectivity	CO_2 Permeability (Barrer)	CH_4 Permeability (Barrer)	Ideal CO_2/CH_4 Selectivity
0	10.7 ± 0.2	0.32 ± 0.01	34 ± 1	10.7 ± 0.2	0.32 ± 0.01	34 ± 1
10	13.2 ± 0.2	0.37 ± 0.01	36 ± 1	21.9 ± 0.3	0.71 ± 0.03	31 ± 2
25	23.2 ± 0.9	0.59 ± 0.02	39 ± 2	47 ± 2	1.5 ± 0.2	32 ± 5

The results of pure gas permeation measurements of the composite membranes are shown in Figure 4.17. Table 4.2 lists the values plotted in Figure 4.17. The error reported represents the standard deviation of the average permeability obtained for each membrane reported. The CO_2/CH_4 gas pair separation was considered due to previous studies showing pure ZIF-8 membranes exhibit poor separation performance for this gas pair. Membranes prepared with direct sonication show a large increase in the permeability of CO_2 as well as a modest increase in ideal gas selectivity compared to the pure polymer film. On the other hand, the use of indirect sonication results in membranes with poor performance, in particular a drop in the selectivity and very high CO_2 permeability even at low ZIF-8 loadings. These characteristics are due to unselective transport through the void spaces in the regions occupied by aggregates of ZIF-8 nanoparticles. The permeation data for composite membranes prepared with direct

sonication exhibit characteristics of a generally defect-free microstructure. Furthermore, the data show a clear and consistent trend in enhancement of membrane performance as a function of ZIF-8 loading. Such a set of permeation data can be analyzed in terms of the Maxwell model (see Equation 2.7), which can be used to estimate the permeation properties of the ZIF-8 filler particles from composite membrane data.[27–30] This analysis leads to a CO_2 permeability of 300 Barrer and CO_2/CH_4 ideal selectivity of 85 for ZIF-8, based on fitting the experimental data from Figure 4.17.

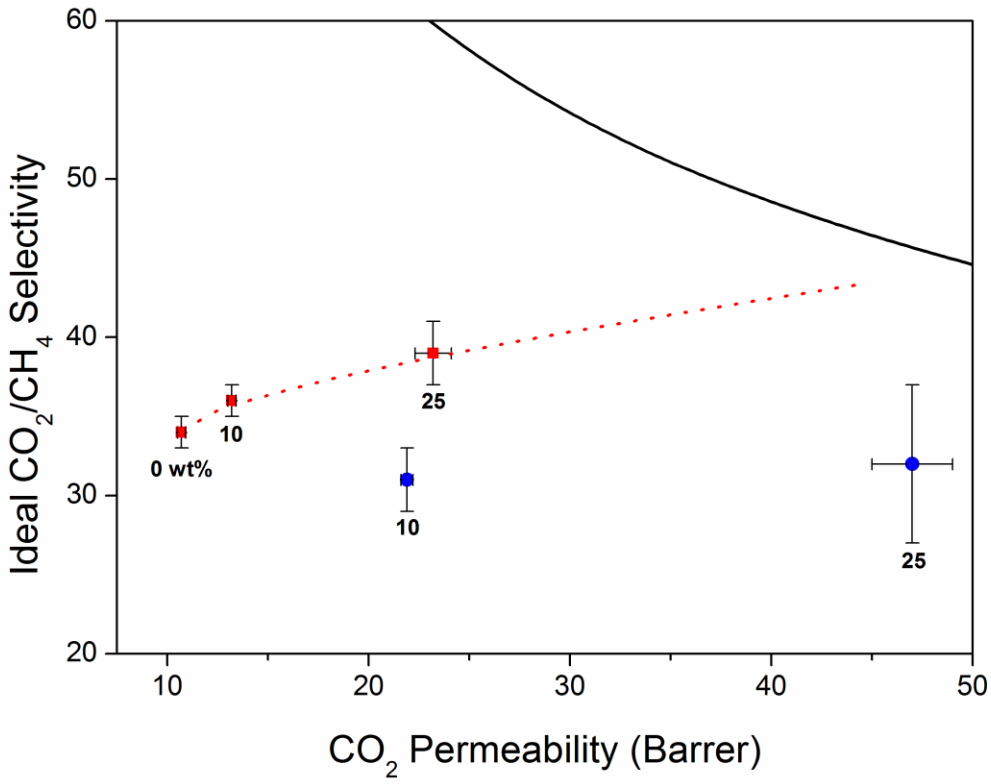

Figure 4.17. Permeation properties at 308 K of ZIF-8/Matrimid® composite membranes, prepared using either direct or indirect sonication. The wt% loadings of ZIF-8 in the membrane are indicated. The Maxwell model is used to predict the membrane performance up to 50 wt% ZIF-8 loading. Squares: direct sonication; Circles: indirect sonication; Solid line: Upper Bound; Dotted line: Maxwell model predictions.

The permeability and selectivity values estimated here reflect the properties of the ZIF-8 material actually constituting the filler in the membranes. These cannot be considered to be the same as those of the as-made ZIF-8 material. Indeed, it is not clear if there is a single "definitive" set of permeation properties of ZIF-8 materials in their practically applied form since the findings from this Chapter indicate clearly that MOFs such as ZIF-8 can be significantly altered by commonly used membrane processing conditions. There is also evidence that many MOFs possess flexible frameworks capable of adsorption and diffusion of molecules larger than the nominal crystallographic pore size.[31–35] It has also been shown that the ZIF-8 framework is much less rigid in comparison with other ZIF materials.[36] With these considerations, it is reasonable that composite membranes containing ZIF-8 may show quite different gas separation performance than pure ZIF-8 membranes due to alterations in the structure of the ZIF material during different processing conditions. A recent study showed that ZIF-8 enhanced the performance of Ultem® hollow-fiber membranes for CO_2/N_2 separation, whereas other studies have shown ZIF-8 to have poor separation performance.[37,38] With the sonication-induced structural changes, adsorption of polymer to the surface of the ZIF-8 crystals, and subsequent annealing at high temperatures, the effective pore size and flexibility of ZIF-8 could be reduced to provide the separation enhancement observed in ZIF-8 composite membranes presented in this Chapter. Finally, the Maxwell model is also used (Figure 4.17) to extrapolate composite membrane performance up to a hypothetical 50 wt% ZIF-8/Matrimid® membrane. Although the present membranes show an increase in separation performance, the present combination of ZIF-8 and Matrimid® is not predicted to allow the fabrication of composite membranes that reach the "upper

bound" of pure polymer membrane separation performance; therefore, other polymers can be selected as matrix materials for ZIF-8 if desired.[39,40] In addition, it may be beneficial to examine the predicted process calculations using permeation data when utilizing ZIF-8 or other filler materials in polymeric membranes and how the required membrane area and product recovery are affected by inclusion of these materials.[41–43]

4.4 Conclusions

High-intensity ultrasonication with a sonication horn is shown to induce a non-ideal coarsening on ZIF-8 nanoparticles in THF. Although there are significant changes in the particle morphology, there are only minor losses in crystallinity and microporosity as concluded from powder XRD, PDF analysis and nitrogen physisorption. From FTIR and EDX data, an increase in Zn-OH groups is observed, most likely due to surface defects created during the ripening process. Light scattering measurements show a clear trend in the coarsening of nanoparticles, and ultrasonication eventually creates a bimodal particle size distribution with long sonication times. The subsequent behavior of the bimodal distribution is affected by the sonication time and the concentration of nanoparticles in solution as well as the development of elastic stresses in the growing nanoparticles. Composite films prepared with both direct and indirect sonication show apparent good adhesion between the polymer and ZIF-8 phases; however, films fabricated using indirect sonication exhibit severe agglomeration of nanoparticles while direct sonication produced coarsened nanoparticles with variable dispersion. Permeation measurements reveal that direct sonication produces an effective composite membrane system whose properties are enhanced over the pure polymer material, and show a full

consistency with the Maxwell model. The latter fact also enables a reliable estimation of the permeation properties of the ZIF-8 particles existing in the composite membranes, and they are shown to be quite different from those obtained using measurements of ZIF-8 crystals, pure ZIF-8 membranes, or computational predictions.

4.5 References

(1) Jung, D.-W.; Yang, D.-A.; Kim, J.; Kim, J.; Ahn, W.-S. *Dalton Trans.* **2010**, *39*, 2883–2887.

(2) Wiebcke, M.; Cravillon, J.; Münzer, S.; Lohmeier, S.-J.; Feldhoff, A.; Huber, K. *Chem. Mater.* **2009**, *21*, 1410–1412.

(3) Chupas, P. J.; Qiu, X.; Hanson, J. C.; Lee, P. L.; Grey, C. P.; Billinge, S. J. L. *J. Appl. Cryst.* **2003**, *36*, 1342–1347.

(4) Chupas, P. J.; Chapman, K. W.; Lee, P. L. *J. Appl. Cryst.* **2007**, *40*, 463–470.

(5) Hammersley, A. P.; Svensson, S. O.; Hanfland, M.; Fitch, A. N.; Häusermann, D. *High Pressure Res.* **1996**, *14*, 235–248.

(6) Qiu, X.; Thompson, J. W.; Billinge, S. J. L. *J. Appl. Cryst.* **2004**, *37*, 678.

(7) O'Brien, K.; Koros, W.; Barbari, T.; Sanders, E. *J. Membr. Sci.* **1986**, *29*, 229–238.

(8) Voorhees, P. W. *Annu. Rev. Mater. Sci.* **1992**, *22*, 197–215.

(9) Wong, E. M.; Bonevich, J. E.; Searson, P. C. *J. Phys. Chem. B* **1998**, *102*, 7770–7775.

(10) Suslick, K. S.; Doktycz, S. J.; Flint, E. B. *Ultrasonics* **1990**, *28*, 280–90.

(11) Thompson, L. H.; Doraiswamy, L. K. *Ind. Eng. Chem. Res.* **1999**, *38*, 1215–1249.

(12) Voorhees, P. W. *J. Stat. Phys.* **1985**, *38*, 231–252.

(13) Schoeman, B. J. *Zeolites* **1997**, *18*, 97–105.

(14) Lifshitz, I. M.; Slyozov, V. *J. Phys. Chem. Solids* **1961**, *19*, 35–50.

(15) Wagner, C. *Z. Elektrochem.* **1961**, *65*, 581–591.

(16) Finsy, R. *Langmuir* **2004**, *20*, 2975–2976.

(17) Li, X.; Thornton, K.; Nie, Q.; Voorhees, P. W.; Lowengrub, J. S. *Acta Mater.* **2004**, *52*, 5829–5843.

(18) Williamson, G.; Hall, W. *Acta Metall. Mater.* **1953**, *1*, 22–31.

(19) Walton, K. S.; Snurr, R. Q. *J. Am. Chem. Soc.* **2007**, *129*, 8552–8556.

(20) Zhang, G.; Shen, X.; Yang, Y. *J. Phys. Chem. C* **2011**, *115*, 7145–7152.

(21) Zhu, M.; Venna, S. R.; Jasinski, J. B.; Carreon, M. A. *Chem. Mater.* **2011**, *23*, 3590–3592.

(22) Xu, X. L.; Lau, S. P.; Tay, B. K. *Thin Solid Films* **2001**, *398-399*, 244–249.

(23) Sholl, D. S. *Nature Chem.* **2011**, *3*, 429–30.

(24) Mason, T. J.; Lorimer, J. P.; Bates, D. M. *Ultrasonics* **1992**, *30*, 40–42.

(25) Diaz, K.; Garrido, L.; Lopex-Gonzalez, M.; Del Castillo, L. F.; Riande, E. *Macromolecules* **2010**, *43*, 316–325.

(26) Hillock, A. M. W.; Miller, S. J.; Koros, W. J. *J. Membr. Sci.* **2008**, *314*, 193–199.

(27) Mahajan, R.; Koros, W. J. *Ind. Eng. Chem. Res.* **2000**, *39*, 2692–2696.

(28) Mahajan, R.; Koros, W. J. *Polym. Eng. Sci.* **2002**, *42*, 1420–1431.

(29) Vu, D. Q.; Koros, W. J.; Miller, S. J. *J. Membr. Sci.* **2003**, *211*, 335–348.

(30) Hashemifard, S. A.; Ismail, A. F.; Matsuura, T. *J. Membr. Sci.* **2010**, *347*, 53–61.

(31) Li, K.; Olson, D. H. D. H.; Seidel, J.; Emge, T. J. T. J.; Gong, H.; Zeng, H.; Li, J. *J. Am. Chem. Soc.* **2009**, *131*, 10368–10369.

(32) Fairen-Jimenez, D.; Moggach, S. A.; Wharmby, M. T.; Wright, P. A.; Parsons, S.; Düren, T. *J. Am. Chem. Soc.* **2011**, *133*, 8900–8902.

(33) Stavitski, E.; Pidko, E. A.; Couck, S.; Remy, T.; Hensen, E. J. M.; Weckhuysen, B. M.; Denayer, J.; Gascon, J.; Kapteijn, F. *Langmuir* **2011**, *27*, 3970–3976.

(34) Zhang, C.; Dai, Y.; Johnson, J. R.; Karvan, O.; Koros, W. J. *J. Membr. Sci.* **2011**, *389*, 34–42.

(35) Zhang, C.; Lively, R. P.; Zhang, K.; Johnson, J. R.; Karvan, O.; Koros, W. J. *J. Phys. Chem. Lett.* **2012**, *3*, 2130–2134.

(36) Tan, J. C.; Bennett, T. D.; Cheetham, A. K. *Proc. Nat. Acad. Sci.* **2010**, *107*, 9938–9943.

(37) Dai, Y.; Johnson, J. R.; Karvan, O.; Sholl, D. S.; Koros, W. J. *J. Membr. Sci.* **2012**, *401-402*, 76–82.

(38) Song, Q.; Nataraj, S. K.; Roussenova, M. V.; Tan, J. C.; Hughes, D. J.; Li, W.; Bourgoin, P.; Alam, M. A.; Cheetham, A. K.; Al-Muhtaseb, S. A.; Sivaniah, E. *Energy Environ. Sci.* **2012**, *5*, 8359–8369.

(39) Robeson, L. *J. Membr. Sci.* **1991**, *62*, 165–185.

(40) Sridhar, S.; Smitha, B.; Aminabhavi, T. M. *Sep. Purif. Rev.* **2007**, *36*, 113–174.

(41) Sengupta, A.; Sirkar, K. K. In *Membrane Separations Technology: Principles and Applications*; Noble, R. D.; Stern, S. A., Eds.; Elsevier B.V.: Amsterdam, The Netherlands, 1995; pp. 499–552.

(42) Baker, R. W.; Lokhandwala, K. *Ind. Eng. Chem. Res.* **2008**, *47*, 2109–2121.

(43) Baker, R. W. *Membrane Technology and Applications*; McGraw-Hill: New York, 2000.

CHAPTER 5

Gas Adsorption Properties and Application of Mixed-Linker Zeolitic Imidazolate Frameworks for Acid Gas Separations

5.1 Introduction

Framework modification of porous materials has considerable potential to enable tuning of the material properties in order to increase performance in a variety of applications such as separations, catalysis, and chemical sensors.[1–4] In particular, improving material performance for separations is highly desirable to reduce the overall process energy requirements. Typically, the two material properties in porous materials that determine separation performance are pore size (kinetic separation) and adsorption selectivity (thermodynamic effect).[5] The different ZIF topologies possess a variety of pore sizes and surface properties.[6–8] ZIFs have been studied for CO_2 adsorption and membrane-based separations by both experiments and computations.[9–15] Although these materials normally have high CO_2 capacity, the adsorption selectivity for typical gas pairs of interest (*e.g.*, CO_2/CH_4) tends to be low and comparable with commercially available adsorbent materials such as BPL carbon.[13,16] Practically, increasing the adsorption selectivity would greatly increase the potential for commercialization. Currently, very few ZIF materials (*e.g.*, ZIF-78) have shown significant CO_2/CH_4 (or CO_2/N_2) adsorption selectivities of 10 (50) or more.[9] Some large pore MOF structures exhibit higher CO_2 affinity and selectivity for these gas pairs; however, these materials typically have open metal centers that are susceptible to performance degradation from steam exposure and

poison from trace contaminants, which adversely affect CO_2 capacity. [1,17–21] Conversely, ZIFs have relatively high thermal and chemical stability that permits modification of the surface properties and have the added benefit of small pore apertures that are promising for kinetic gas separations, which further improves separation performance.[22]

Several techniques have been employed for modifying surface properties of MOF materials to improve CO_2 affinity and separation properties, including postsynthetic modification (PSM) and postsynthetic exchange (PSE) of the linker and metal center. Postsynthetic modification (PSM) involves reaction of a small molecule with a functional group on the organic linker of the MOF.[23,24] In the first report of ZIF-90 postsynthetic modification, the aldehyde moiety on the organic linker was modified with ethanolamine, producing an imine with a pendant alcohol functionality near 100% conversion; however, due to the small pore size of ZIF-90, this treatment eliminated the porosity, as determined through N_2 physisorption at 77 K.[25] Alternatively, PSM of the metal center is possible, provided that the metal center has an open coordination site; however, ZIF materials contain tetrahedrally coordinated Zn^{2+} metal centers that are not open metal sites.[8,17,26] Another way to modify surface properties is by postsynthetic exchange (PSE) of the organic linkers or metal centers by heating the MOF material in a solvent containing a different linker or metal ion that exchanges into the material while maintaining the crystal structure.[27] Recently, the linker of ZIF-71 (4,5-dichloroimidazole) was successfully subjected to PSE with a linker that is not otherwise found in ZIF structures (4-bromoimidazole).[28] ZIF-8 has also been subjected to PSE, replacing the framework

linkers (2-methylimidazole) with imidazole. This produced a material with 85% substituted linkers while maintaining the ZIF-8 crystal structure.[29]

However, the above postsynthetic techniques do not allow control over the amount of sites that are functionalized without consideration of the reaction conditions. In Chapter 3, the linker composition of ZIF materials was shown to be controllable *in situ* (during synthesis) without altering the crystal structure. Both the linkers of ZIF-8 and ZIF-90, ZIF-7 and ZIF-8, or ZIF-8 and 2-aminobenzimidazole were incorporated in the same framework during the ZIF synthesis, while maintaining the ZIF-8 crystal structure. By this synthetic method, the surface functionalities in these ZIF materials can be better controlled, and improvement in gas separations may be realized without severely altering the pore volume of the material. In this Chapter, *in situ* linker substitution in ZIF-8 with two different linkers is performed to introduce two different functionalities in the material without changing the crystal structure. A linker not found in other ZIF materials (2-aminobenzimidazole) is incorporated into the ZIF-8 structure, with good control over the linker substitution stoichiometry, as shown in Chapter 3. Although this linker contains a primary amine functional group, the substituting linker has little effect on the CO_2 adsorption affinity even at high substitution loadings, due to the aromaticity of the linker which reduces the basicity of the primary amine. Subsequently, a mixed-linker ZIF containing an aldehyde functionality, termed ZIF-8-90-(50), can undergo PSM without detrimental loss of pore volume and produces a ZIF material with high CO_2/CH_4 adsorption selectivity.

5.2 Experimental Methods

5.2.1 Materials

Sodium formate (99%, $NaCO_2H$), 2-methylimidazole (98%, 2-MeIM), $Zn(NO_3)_2 \cdot 6H_2O$ (99%), 2-aminobenzimidazole (97%, 2-amBzIM), and carboxaldehyde-2-imidazole (99%, OHC-IM) were obtained from Alfa Aesar. Hydrogen peroxide (H_2O_2, 30 wt% in H_2O), aqueous ammonia (10 wt% NH_3 in H_2O), methanol (MeOH) and dimethylformamide (DMF) were obtained from BDH. Ethylenediamine (99%, en) and methanolic ammonia (2.0 M NH_3 in MeOH) were obtained from Sigma-Aldrich. All chemicals were used as received without further purification.

5.2.2. Synthesis of ZIF-8-ambz Hybrids

The ZIF-8-ambz-(*x*) materials used in this chapter were synthesized in the same manner as those from Chapter 3. Details on the synthesis can be found in Section 3.2.4.

5.2.3. Synthesis of ZIF-90 and ZIF-8-90-(50) Hybrids

Synthesis of ZIF-8-90-(50) is a scaled-up reaction of the procedure described in Section 3.2.2. A solution was prepared containing 12.6 mmol OHC-IM, 87.4 mmol 2-MeIM, and 100 mmol of NaCO2H in 250 mL MeOH. To fully dissolve all the OHC-IM, this solution was heated to 323 K in a sealed polyethylene bottle for 2 hrs. A separate solution was then prepared with 25 mmol $Zn(NO_3)_2 \cdot 6H_2O$ in 250 mL deionized H_2O. After the imidazole solution had cooled to room temperature, the Zn salt solution was added and allowed to stir for 1 hr. The solution was centrifuged at 10,000 rpm for 5 min,

and the precipitate was washed with MeOH after pouring off the supernatant. This was repeated again, and then the precipitate was recovered by vacuum filtration. The recovered product was dried in an oven at 358 K. The yield was approximately 20% based on Zn. ZIF-90 was synthesized exactly as described in Section 3.2.2.

5.2.4. Functionalization Study of ZIF-90 and ZIF-8-90-(50).

To test the stability of ZIF-90 for functionalization, several probes were used. To test the oxidation of the aldehyde linker, ZIF-90 was reacted for 24 hrs with 10 g solution of hydrogen peroxide at two concentrations (1 wt% and 30 wt%) in water. Three conditions were used: (1) reaction at 323 K and 30 wt% H_2O_2/H_2O; (2) reaction at room temperature and 30 wt% H_2O_2/H_2O; and (3) reaction at room temperature and 1 wt% H_2O_2/H_2O. After reaction, the powder sample was recovered by vacuum filtration and washed with MeOH. The powder sample remained white following the reaction. To test the reactivity of the aldehyde with amines, ZIF-90 samples were reacted for 24 hrs with 10 g ammonia solutions in both water and methanol under the following conditions at room temperature: (1) 10 wt% NH_3/H_2O; (2) 1 wt% NH_3/H_2O; and (3) 0.4M NH_3/MeOH. After reaction, the powder sample was recovered by vacuum filtration and washed with MeOH. The powder sample turned a distinct yellow color following reaction with ammonia.

The ZIF-8-90-(50) samples were functionalized with ethylenediamine to form ZIF-en samples. A dispersion of 0.2 g ZIF-8-90-(50) was prepared in 25 mL MeOH. Then, at room temperature, 1 mL ethylenediamine was added to the dispersion. Sealed in

a Teflon cup, the ZIF dispersion was heated to 353 K and stirred for 24 hrs. After cooling to room temperature, the powder was washed with MeOH and recovered by vacuum filtration. The powder sample turned from white to yellow after reaction.

5.2.5. Characterization Methods

The ZIF materials were analyzed by powder X-ray diffraction (XRD) using an X'Pert Pro PANalytical X-ray Diffractometer. Diffraction measurements were done from 3.5-50° 2θ using an X'celerator detector. Nitrogen physisorption measurements were done on a Micromeritics ASAP 2020 surface area analyzer at 77 K. ZIF-8-90-(50) and ZIF-en samples were degassed at 423 K under vacuum for 12 hrs, and ZIF-90 and ZIF-COOH samples were degassed at 473 K. The BET surface area and t-plot micropore volume methods were used to analyze the relative surface properties of each sample. Fourier-transform infrared (FTIR) and Fourier-transform Raman (FT-Raman) spectroscopy were performed on ZIF-8-90-(50) and ZIF-en samples. The powder samples were prepared in KBr pellets for FTIR spectroscopy and then analyzed on a Bruker Vertex 80v FTIR Analyzer from 4000-400 cm^{-1}. For FT-Raman, powder samples were packed tightly in NMR tubes and analyzed on a Bruker RAM II FT-Raman Analyzer from 4000-400 cm^{-1}. To determine the linker composition in the framework, all samples were analyzed with solution ^{1}H nuclear magnetic resonance (NMR) spectroscopy on a Mercury Vx 400 MHz spectrometer after digesting samples using d_4-acetic acid (CD_3CO_2D). Solid state (SS) ^{13}C cross polarization-magic angle spinning (CP-MAS) NMR was performed on a Bruker 300 MHz spectrometer, using a spinning rate of 10 kHz with a 4 mm rotor and collecting a minimum of 5,000 scans. ZIF decomposition stability

was tested on a Netzsch STA-409-PG thermogravimetric analyzer (TGA). Powder samples were heated from room temperature to 1173 K with a ramp rate of 10 $K \cdot min^{-1}$ in a diluted air stream (25% air/75% N_2).

5.2.6. Adsorption Measurements

Adsorption measurements for CO_2 and CH_4 were carried out in a custom-built, constant-volume apparatus.[30] Samples were tested at temperatures of 308, 328, and 348 K to provide data at multiple temperatures for the calculation of heats of adsorption for each gas and sample. Pressure ranges tested were typically from 0-1000 kPa. Samples were degassed at 373 K under vacuum for at least 12 hrs before testing. Ultra-high purity CH_4 (99.999%) and bone-dry CO_2 (99.999%) were used in all adsorption measurements.

5.2.7. Adsorption Analysis

Isotherms obtained from adsorption measurements were fit to a Toth isotherm to describe the heterogeneous surface resulting from the mixed-linker structure:[31,32]

$$q_i = \frac{q_{sat} b_i p}{\left[1 + \left(b_i p\right)^{t_i}\right]^{1/t_i}} \tag{5.1}$$

where q_i is the capacity for adsorbing component i at pressure, p, q_{sat} is the saturation capacity, b_i is the affinity constant of component i, and t_i is the heterogeneity parameter. When t_i is equal to 1, this equation becomes the Langmuir isotherm model. The change in

the affinity constant, b_i, the heterogeneity parameter, t_i, and the saturation capacity, q_{sat}, with temperature can be described with the following:[33]

$$b_i = b_{i,0} \exp\left[\frac{-\Delta H}{RT_0}\left(\frac{T_0}{T} - 1\right)\right] \tag{5.2}$$

$$t_i = t_0 + \alpha\left(1 - \frac{T_0}{T}\right) \tag{5.3}$$

$$q_{sat,i} = q_{sat,0} \exp\left[\chi\left(1 - \frac{T}{T_0}\right)\right] \tag{5.4}$$

where $b_{i,0}$ is the pre-exponential affinity constant, $-\Delta H$ is the heat of adsorption at zero adsorbate loading, T is the absolute temperature, T_0 is the reference temperature (308 K), α and t_0 are parameters used for thermal variation in the heterogeneity parameter, t_i, and $q_{sat,0}$ and χ represent changes in saturation capacity for each adsorbent with temperature. Isotherms at different temperatures for a single gas were fit to the Toth isotherm by maximizing the coefficient of determination (R^2) for all data simultaneously using OriginPro 8.5.

The ZIF materials were analyzed with ideal adsorbed solution theory (IAST) assuming a gas mixture of 25% CO_2/75% CH_4.[32,34,35] To perform the analysis, a

thermodynamic criterion must be satisfied: the spreading pressures of each component are equal to each other ($\pi_i = \pi_j$), where π is the spreading pressure calculated as:

$$\pi_i = \frac{RT}{A}\int_0^{p_i^0} \frac{q_i}{p}\,dp \tag{5.5}$$

Using Equation 5.1, the spreading pressure of component *i* can be expressed in terms of isotherm parameters:

$$\frac{\pi_i A}{RT} = \int_0^{p_i^0} \frac{q_{sat,i} b_i}{\left[1+\left(b_i p\right)^{t_i}\right]^{1/t_i}}\,dp \tag{5.6}$$

Here, p_i^0 is obtained from the expression:

$$y_i p = x_i p_i^0 \tag{5.7}$$

where y_i is the gas phase mole fraction, p is the absolute pressure, x_i is the adsorbed phase mole fraction and p_i^0 is the gas-phase pressure corresponding to adsorbed-phase spreading pressure π for the adsorption of pure component *i*.[34] The adsorption selectivity ($\alpha_{1,2}$) for a specific gas pair can be calculated as:

$$\alpha_{1,2} = \frac{\left(x_1 / y_1 \right)}{\left(x_2 / y_2 \right)} \tag{5.8}$$

and the capacity at p and T can be calculated by

$$\frac{1}{q} = \frac{x_1}{q\left(p_1^0 \right)} + \frac{x_2}{q\left(p_2^0 \right)} \tag{5.9}$$

and

$$q_i = x_i q \tag{5.10}$$

To solve for x_i and calculate selectivity and capacity, Equations 5.6-7 were solved iteratively.

Breakthrough curves are convenient for assessing performance of adsorbents for different adsorption applications.[35,36] Modeling of adsorbents for breakthrough curve analysis normally involves very simple assumptions in order to rapidly assess potential materials: (1) isothermal conditions; and (2) negligible pressure drop along the fixed bed (constant pressure). Using these assumptions, the following equation applies for a packed bed adsorbing column (see Figure 5.1):

$$\frac{1}{RT}\frac{\partial p_i}{\partial t} = -\frac{1}{RT}\frac{\partial (up_i)}{\partial z} - \frac{(1-\varepsilon)}{\varepsilon}\rho\frac{\partial \bar{q}_i}{\partial t} \tag{5.11}$$

where p_i is the partial pressure of component *i*, u is the superficial velocity, ε is the bed voidage, ρ is the framework density of the adsorbent, and z and t represent the length of the adsorbent column and the time. If it is assumed that the equilibrium of the adsorbent is instantaneous ($\bar{q} = q$), then the following governing equations apply:

$$\frac{1}{RT}\frac{\partial p_i}{\partial t} = -\frac{1}{RT}\frac{\partial (up_i)}{\partial z} - \frac{(1-\varepsilon)}{\varepsilon}\rho\frac{\partial q_i}{\partial t} \tag{5.12}$$

$$\frac{P}{RT}\frac{\partial u}{\partial z} + \frac{(1-\varepsilon)}{\varepsilon}\rho\left[\frac{\partial q_1}{\partial t} + \frac{\partial q_2}{\partial t}\right] = 0 \tag{5.13}$$

and using the chain rule, the $\frac{\partial q_i}{\partial t}$ terms can be converted to the following:

$$\frac{\partial q_i}{\partial t} = \frac{dq_i}{dp_i}\frac{\partial p_i}{\partial t} \tag{5.14}$$

Since one of the assumptions made is constant pressure and a binary system of CO_2/CH_4 will only be considered, Equations 5.12 and 5.13 can be converted to be expressed in terms of mole fraction, *y*, rather than partial pressure:[35]

$$\frac{\partial u}{\partial z} = -\frac{(1-\varepsilon)}{\varepsilon}\frac{\rho RT}{P}\left[\frac{dq_1}{dy} + \frac{dq_2}{dy}\right]\frac{\partial y}{\partial t} \tag{5.15}$$

$$\frac{\partial y}{\partial t} = -\frac{u}{\left[1 + \frac{(1-\varepsilon)}{\varepsilon}\frac{\rho RT}{P}\left\{(1-y)\frac{dq_1}{dy} + y\frac{dq_2}{dy}\right\}\right]}\frac{\partial y}{\partial z} \tag{5.16}$$

Utilizing scaling arguments, the following terms were used to make these equations useful to compare adsorbents without specifying dimensions for an adsorber column:

$$t = \left(\frac{L}{u_0}\varepsilon\right)\tau \tag{5.17}$$

$$z = Lz^* \tag{5.18}$$

$$u = u_0 u^* \tag{5.19}$$

and substituting Equations 5.17-5.19 into Equations 5.15 and 5.16 yields the following partial differential equations:

$$\frac{\partial y}{\partial \tau} = -\frac{\varepsilon u^*}{\left[1 + \frac{(1-\varepsilon)}{\varepsilon}\frac{\rho RT}{P}\left\{(1-y)\frac{dq_1}{dy} + y\frac{dq_2}{dy}\right\}\right]}\frac{\partial y}{\partial z^*} \tag{5.20}$$

$$\frac{\partial u^*}{\partial z^*} = -\frac{(1-\varepsilon)}{\varepsilon^2}\frac{\rho RT}{P}\left[\frac{dq_1}{dy} + \frac{dq_2}{dy}\right]\frac{\partial y}{\partial \tau} \tag{5.21}$$

As IAST is important to use for predicting multicomponent adsorption, an algorithm was developed that first calculated the quantity adsorbed, q_i, of each component at the adsorption pressure, P, then a polynomial was fit to relate q_i to y, and using the derivative, the PDEs in Equations 5.20 and 5.21 were solved using Matlab code with the length of the column discretized into 100 slices.

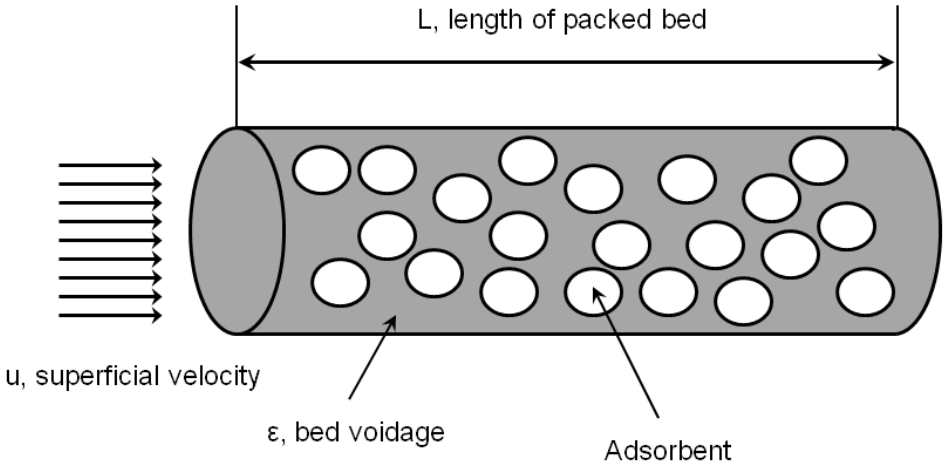

Figure 5.1. Schematic diagram of an ideal packed bed adsorber.

5.3. Results and Discussion

5.3.1 Adsorption Properties of ZIF-8-ambz Hybrids

CO_2 and CH_4 adsorption measurements were used to assess the changes in surface properties for the mixed-linker ZIFs containing 2-amBzIM, compared to ZIF-8. For comparison, the heats of adsorption at zero adsorbate loading for ZIF-8 are calculated to

be -15.6 kJ mol^{-1} and -12.3 kJ mol^{-1} for CO_2 and CH_4, respectively (Table 5.2).[11,13] Framework densities were calculated assuming no change in the unit cell volume of ZIF compared to ZIF-8, and these values are shown in Table 5.1 for each sample presented in this Chapter. Figure 5.2 shows the CO_2 and CH_4 adsorption data and fits of the Toth isotherm for the ZIF-8-ambz-(14) material. The capacities reported in this figure are presented in units of mmol cm^{-3}, instead of the more typical mmol g^{-1}. Because the mass adsorption capacity of MOFs can often be misleading due to low bulk or framework densities, the adsorption units used in this Chapter reflect the material capacity and performance more accurately.[37]

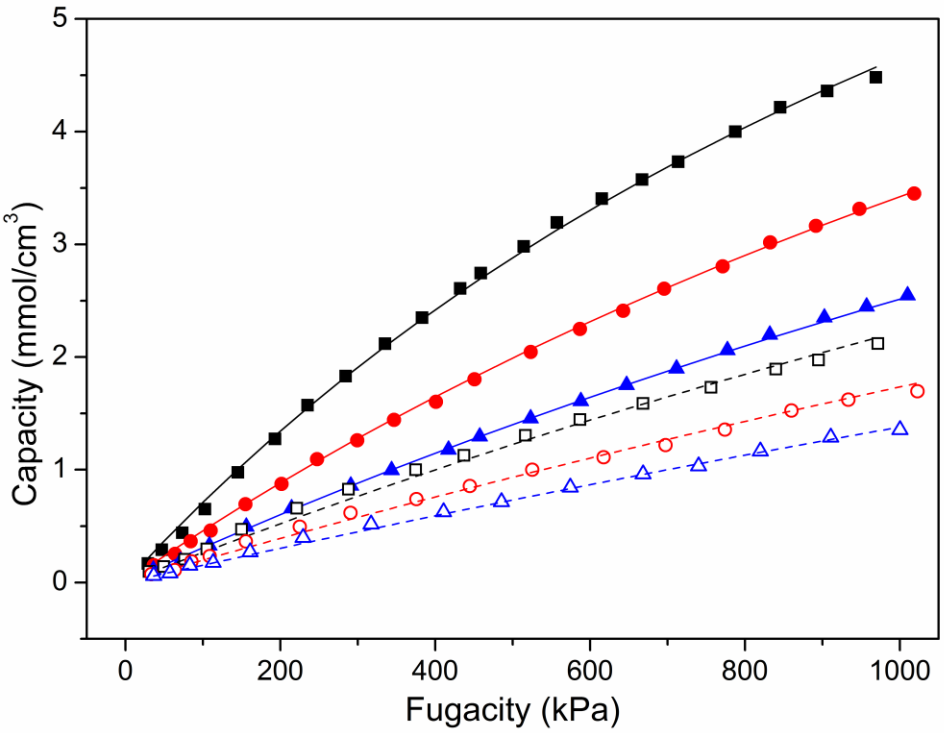

Figure 5.2. CO_2 and CH_4 adsorption isotherms for ZIF-8-ambz-(14). Open symbols denote CH_4 adsorption, closed symbols CO_2. Squares: T = 308 K; circles: T = 328 K; triangles: T = 348 K.

Table 5.1. Linker substitution and framework density of ZIF adsorbent materials.

Sample	Linker Substitution (mol %)[a]	Framework Density ($g \cdot cm^{-3}$)[b]
ZIF-8-ambz-(14)	14	0.983
ZIF-8-ambz-(24)	24	1.024
ZIF-8-ambz-(47)	47	1.120
ZIF-8-90-(50)	48	0.983
ZIF-en	27[c]	1.048

[a] Calculated from solution ^{1}H NMR, balance is 2-MeIM

[b]Calculated from assuming no change in unit cell volume

[c]Total substitution = 22% en-IM + 5% OHC-IM

When comparing the initial slope of the adsorption isotherms of the ZIF-8-ambz-(14) material to those of ZIF-8, it is clear that there is not a significant change in the affinity for CO_2 or CH_4 at this substitution level of 2-amBzIM. Although the substituting linker contains a primary amine functional group, the basicity of this amine is greatly affected by the fused aromatic ring of the imidazolate and benzyl groups.[38] From the isotherm fit, the heats of adsorption were found to be -19.4 kJ mol^{-1} and -12.5 kJ mol^{-1} for CO_2 and CH_4, respectively. The heat of adsorption for CH_4 is almost identical with that of ZIF-8. It has been shown by both simulations and neutron scattering measurements that CH_4 adsorbs in the 6-membered ring (MR) of ZIF-8 at lower pressures, interacting directly with the C=C bond on the 2-MeIM linker.[39,40] Because 2-amBzIM has similar adsorption sites, it is not surprising that no change in the heat of adsorption of CH_4 was seen in ZIF-8-ambz-(*x*) materials compared with ZIF-8. An increase of about 4 kJ mol^{-1} in the heat of adsorption for CO_2 in the ZIF-8-ambz-(*x*) material relative to ZIF-8 is also consistent with the introduction of a more polar functional group than the methyl group

on the ZIF-8 linker; however, this does not greatly affect the overall affinity for CO_2 in this sample.[13,38]

As Figures 5.3a and 5.3b show, with increasing substitution of 2-amBzIM in the ZIF framework, there is an overall increase in the affinity for CO_2 without much change in the affinity for CH_4 (see also Table 5.3). There is a concomitant increase in the heat of adsorption for CO_2. Table 5.2 summarizes the heats of adsorption obtained for each material. With increasing fraction of 2-amBzIM, the heats of CO_2 adsorption show a monotonic increase, consistent with the increasing binding energy due to the polar functional groups.[13] Although ZIF-8-ambz-(14) and ZIF-8-ambz-(24) showed excellent fits to a Langmuir isotherm ($t_i = 1$), the Toth isotherm provided the best overall fit for the ZIF-8-ambz-(47) material (Table 5.3). It is likely that the high substitution obtained in this sample causes significant heterogeneity in the internal surface of the ZIF. Interestingly, although N_2 physisorption showed complete loss of micropore volume at 77 K in Chapter 3, ZIF-8-ambz-(47) adsorbed both CO_2 and CH_4 at ambient temperatures. This shows these materials can have significant "breathing" and "flexibility" effects that allow molecular adsorption and diffusion even when containing bulky benzimidazolate-type linkers.[41,42] Although no gate-opening phenomena is observed from N_2 physisorption, there is clearly some freedom for the linkers to rotate or vibrate to allow adsorption of larger molecules at ambient temperatures, similar to behavior observed in ZIF-8.[43]

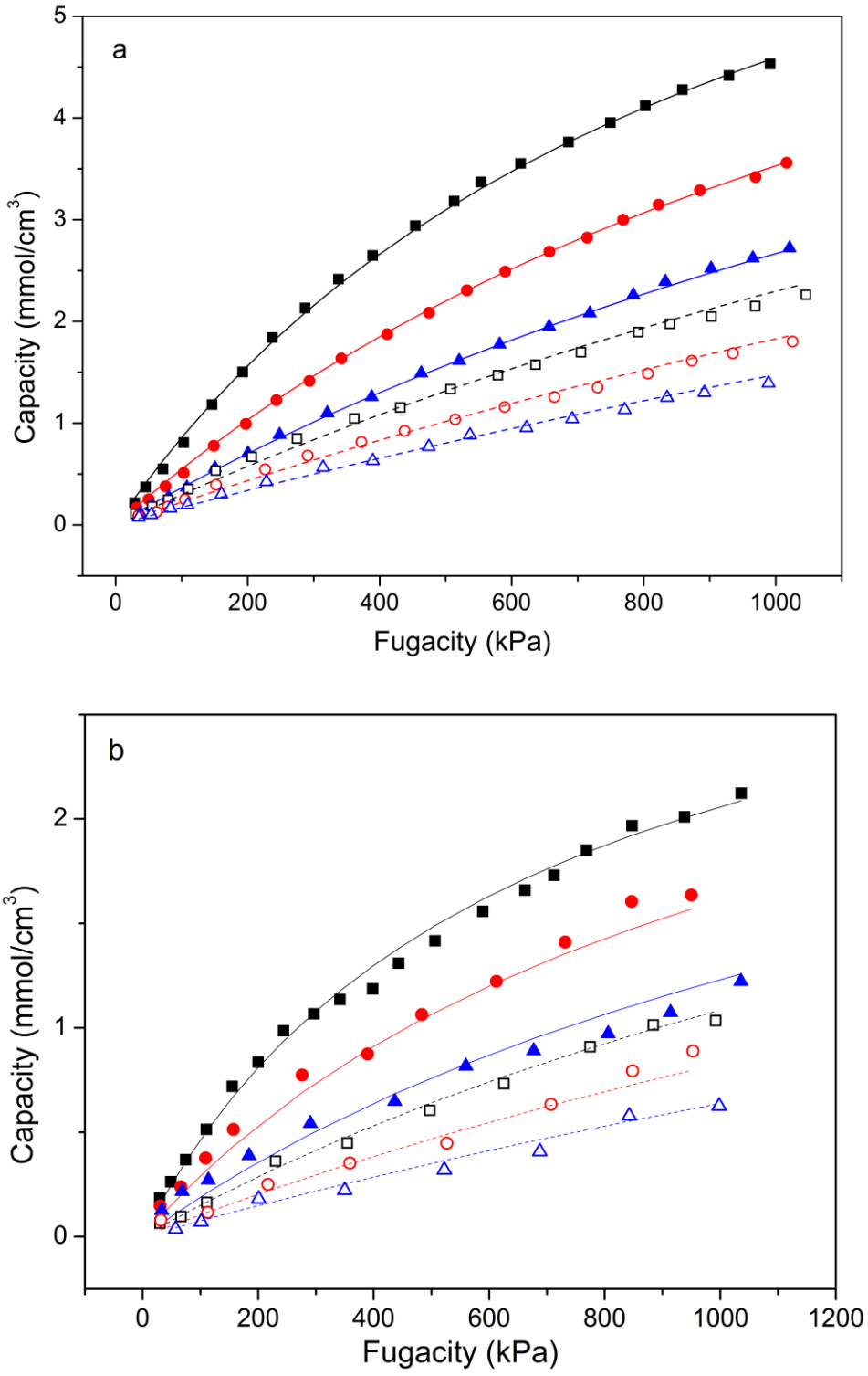

Figure 5.3. CO_2 and CH_4 adsorption isotherms for (**a**) ZIF-8-ambz-(24) and (**b**) ZIF-8-ambz-47. Open symbols denote CH_4 adsorption, closed symbols CO_2. Squares: T = 308 K; circles: T = 328 K; triangles: T = 348 K.

Table 5.2. Heats of adsorption for CO_2 and CH_4 obtained from Langmuir and Toth isotherm fits, Henry's law constants of ZIF materials and ideal selectivity of CO_2/CH_4.

Sample	$-\Delta H$ (kJ·mol^{-1})		K (cm^3 (STP)·cm^{-3}·adsorbent kPa^{-1})[a]		α
	CO_2	CH_4	CO_2	CH_4	(ideal)
ZIF-8[13]	15.6	12.3	0.119	0.050	2.4
ZIF-8-ambz-(14)	19.4	12.5	0.184	0.067	2.8
ZIF-8-ambz-(24)	20.4	12.4	0.235	0.075	3.1
ZIF-8-ambz-(47)	22.1	15.6	0.134	0.038	3.5
ZIF-8-90-(50)	25.6	20.0	0.393	0.070	5.6
ZIF-en	33.9	26.2	0.981	0.075	13.1

[a]Henry's constants were predicted by (q_{sat}·b)

Table 5.2 shows the Henry's constants obtained from isotherm fits and the ideal selectivity, as well as data from ZIF-8 as a standard to compare the CO_2/CH_4 selectivity. Because there is significant reduction in the total adsorption capacity in the ZIF-8-ambz-(47) sample, the Henry's constant decreases, but there is an overall increase in selectivity as the 2-amBzIM fraction increases. Considering that these materials also have a shrinking pore size with increasing 2-amBzIM fraction, it is likely the overall transport selectivity of these materials is higher than that of ZIF-8, and hence, the materials may be useful for membrane-based CO_2 separations.[5]

5.3.2. Postsynthetic Modification of ZIF-90 and ZIF-8-90-(50) Hybrid

Postsynthetic modification was used on ZIF-90 to investigate functionalization stability in the presence of reagents that form different functional groups. Shown in Figure 5.4, it was hypothesized that ZIF-90 may form either carboxylic acid or imine functional groups when reacted with either H_2O_2 or NH_3, respectively. Figure 5.5a shows

powder XRD patterns of ZIF-90 reacted with H_2O_2 at three different conditions. In all conditions, there is a significant change in the overall crystal structure, and there is no longer an appearance of the *I-43m* crystal structure. Nitrogen physisorption shown in Figure 5.5b reveals there to be a complete loss in micropore volume upon transformation to this new crystal structure. Since there is formation of a carboxylic acid in an aqueous solution, there are likely to be free protons in solution. ZIF materials can be very susceptible to materials degradation or changes in acidic conditions due to the basic imidazolate linkers accepting protons in solution, and there is likely a new crystal formation due to the protonation of the imidazolate linkers during the reaction with H_2O_2. Although Amrouche *et al.*[13] showed that ZIF-COOH structures could have very high affinity for CO_2 by using molecular simulations, it may not be practical to pursue synthesized ZIF materials with acidic groups due to the instability shown in Figure 5.5.

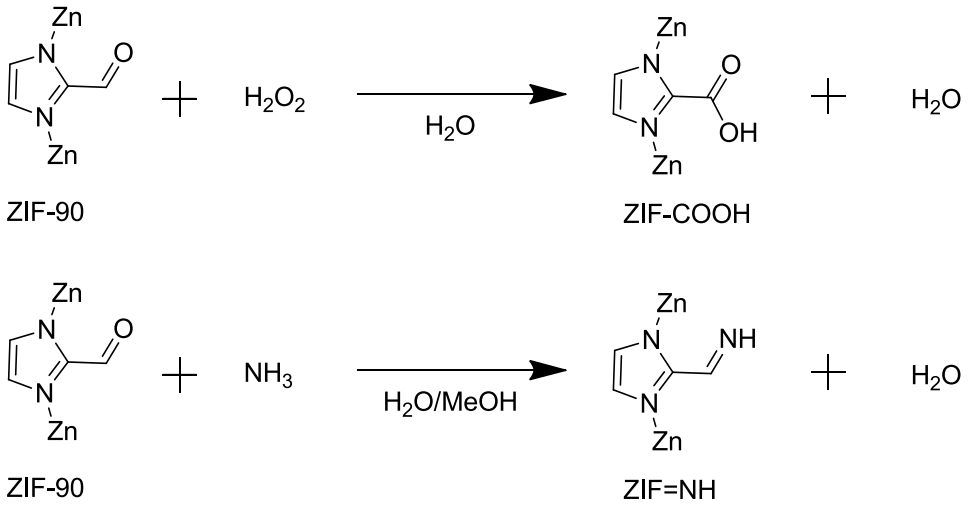

Figure 5.4. Reaction of ZIF-90 with H_2O_2 and NH_3 to form new functional groups.

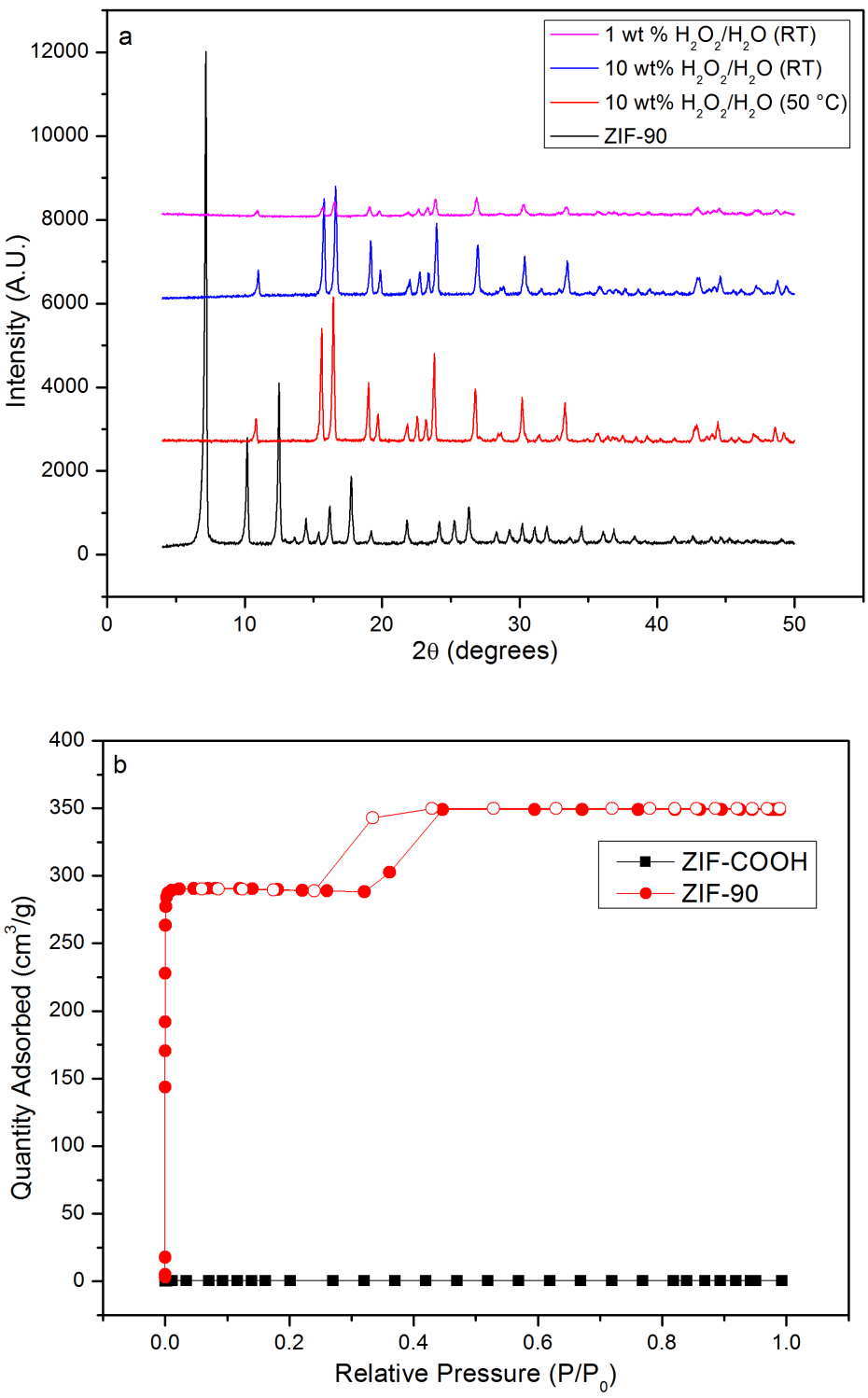

Figure 5.5. (**a**) Powder XRD patterns and (**b**) N_2 physisorption of ZIF-90 treated with H_2O_2 in aqueous solutions.

ZIF-90 was also tested under basic conditions using NH_3 in either water or methanol. Since the imine reaction forms water, it is likely that there will be little conversion of the aldehyde to the imine when water is the solvent; however, methanol has a similar pKa to water, making it weakly acidic and a reasonable solvent and catalyst for the reaction.[44] Figure 5.6a shows powder XRD patterns of ZIF-90 samples treated with NH_3 solutions at three conditions. From Figures 5.5a and 5.6a, it is obvious that ZIF-90 is not a stable structure under either oxidative or basic reaction conditions, except when the base forms a mild pH as in the case of the 1 wt% NH_3/H_2O solution. FTIR spectra in Figure 5.5b show the appearance of a shoulder next to the ν(C=O) following treatment in the 1 wt% NH_3/H_2O solution that is indicative of ν(C=N) vibrations; however, due to the low stability shown in both Figures 5.5a and 5.6a, using pure ZIF-90 may not be suitable for designing ZIF materials with more polar functional groups than the aldehyde and for using in CO_2/CH_4 separations. In addition, the FTIR spectra in Figure 5.6b shows that ZIF-90 still maintains a larger amount of aldehyde functional groups following reaction with NH_3 and using a different solvent than water and different amine molecules may yield higher conversion to the imine group as a result if the structural stability can be maintained.

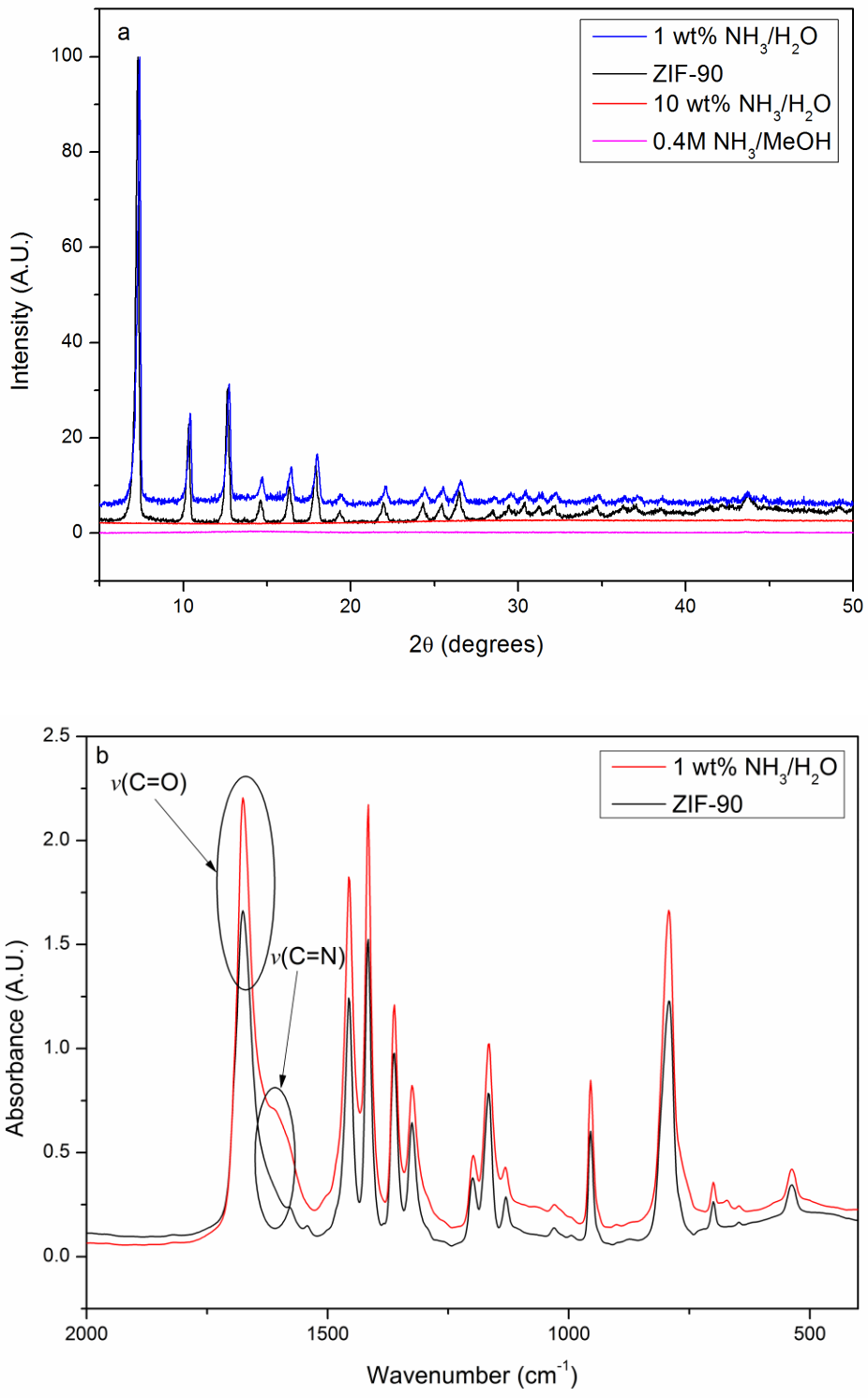

Figure 5.6. (**a**) Powder XRD and (**b**) FTIR spectra of ZIF-90 subjected to imine formation reactions at different conditions.

Due to previous PSM attempts on ZIF materials showing a detrimental loss of micropore volume after functionalization and the poor chemical stability of ZIF-90 when subjected to treatment with H_2O_2 or NH_3,[25] the mixed-linker synthetic strategy, presented in Chapter 3, allows control over the amount of reactive sites and may be able to prevent a total loss of pore volume or crystal structure while still providing active sites for functionalization.[45] Figure 5.7 shows the strategy for producing a ZIF material with a primary amine far enough removed from the aromatic ring of the organic linker to have useful basicity for CO_2-based separations.

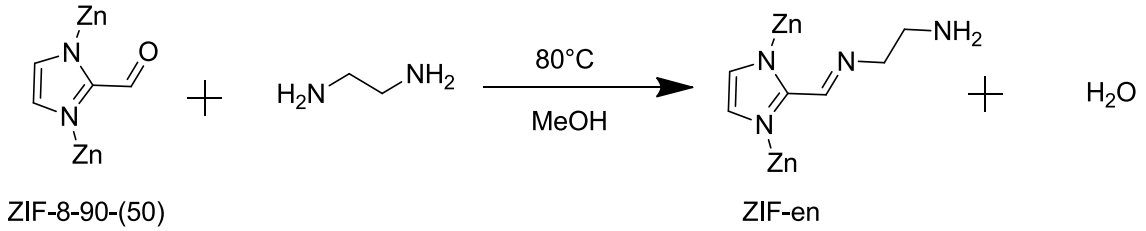

Figure 5.7. Reaction of carbonyl moiety in ZIF-8-90-(50) with ethylenediamine to form ZIF-en.

Figure 5.8 shows FTIR and FT-Raman spectra of ZIF-8-90-(50) and the modified material, ZIF-en. Several FTIR bands that show significant changes are highlighted in Figure 5.8a. Although the bands in the N-H stretching region (3600-3200 cm^{-1}) are broad, there is an appearance of two symmetric bands and one asymmetric band after functionalization, indicating the $–NH_2$ moiety in ZIF-en. In the carbonyl region (1700-1600 cm^{-1}), there is a disappearance of the band from the aldehyde and an appearance of a band in the imine region, suggesting that the aldehyde is converted to an imine by reacting with ethylenediamine; however, there can be an appearance of –N-H bending in the same region, making it necessary to also examine the FT-Raman spectra of ZIF-en.

FT-Raman spectra (Figure 5.8b) confirm the disappearance of the ν(C=O) at 1700 cm^{-1} and the appearance of the ν(C=N) band at 1650 cm^{-1}; however, a weaker ν(C=O) band is still present in ZIF-en, indicating that not all carbonyl groups were reacted.

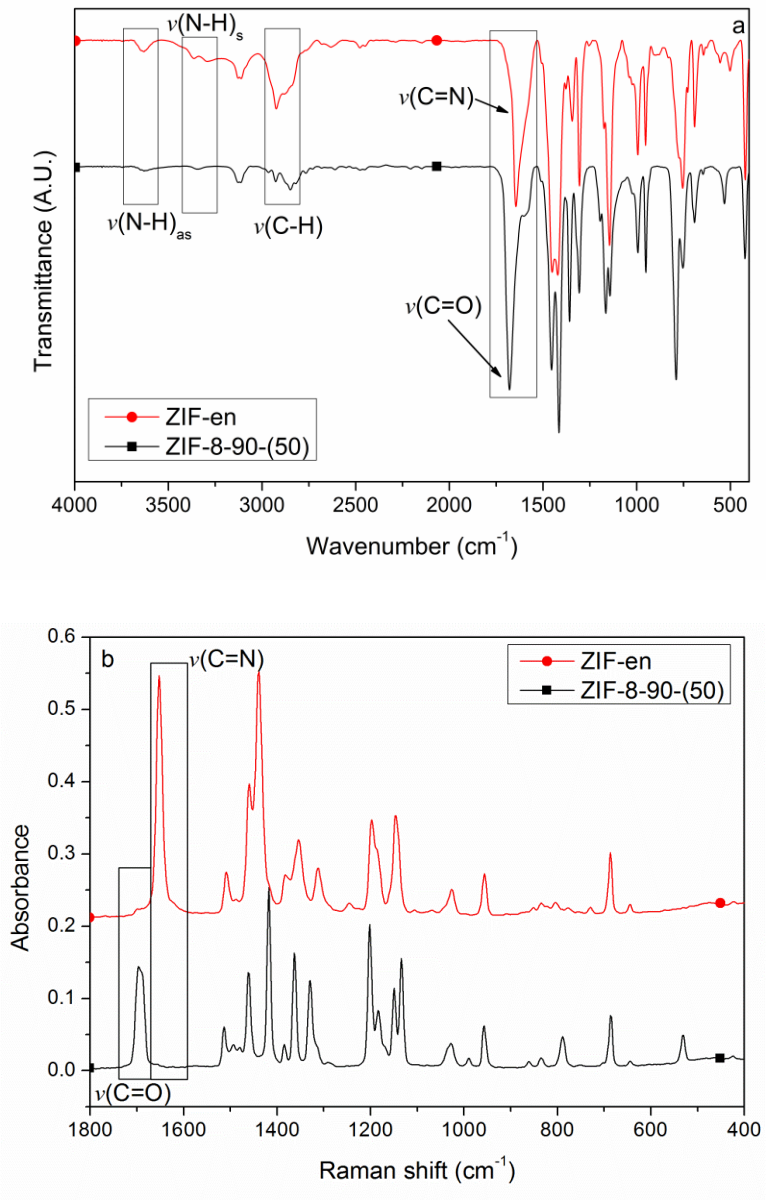

Figure 5.8. (**a**) FTIR and (**b**) FT-Raman spectra of ZIF-8-90-(50) (squares) and ZIF-en (circles), showing appearance of broad N-H bands (IR), C-H bands (IR) and a shift in the band in the 1700-1600 cm^{-1} region (IR and Raman).

NMR spectroscopy was used to identify the functional groups in the ZIF framework and also to determine if there is any "cross-linking" caused by reaction of $-NH_2$ groups of ethylenediamine with nearby OHC-IM linkers. Solution ^1H NMR spectra of the deuterated acid-digested ZIF materials are shown in Figure 5.9a. The chemical shift associated with the aldehyde ($\delta \sim 9.9$ ppm) nearly disappears after PSM, and there is an appearance of a peak associated with an imine bonded to an aromatic ring ($\delta \sim 8.5$ ppm). Taken together, these chemical shifts show a combined linker substitution of 27% (5% OHC-IM and 22% en) after functionalization compared with 48% substitution prior to functionalization. This indicates 46% loss of total OHC-IM linker during PSM, with 81% of the remaining OHC-IM linkers in ZIF-en converted to the functionalized amine linker. However, the TGA mass loss curves (Figure 5.10) of these materials show no significant changes in the total inorganic content (Zn). This indicates that there is some overall loss of ZIF particles during functionalization, but not the selective etching of a linker. It should also be noted that the overall yield of ZIF following functionalization was approximately 60% of the starting ZIF mass, and the filtered reactant solution maintained a yellow color after removal of powder. Therefore, the change in the relative fractions of the different linkers in ZIF-en, compared to ZIF-8-90-(50), is best explained as being due to some dissolution of the ZIF material during PSM. The linkers dissolved in solution can then undergo PSE with the ZIF material, changing the overall linker ratios in the final material. It has already been shown that ZIF materials can easily dissolve in certain solvents and even recrystallize upon cooling.[28] When the integrated area of the imine chemical shift ($\delta \sim 8.5$ ppm) was compared to the methylene groups ($\delta \sim 4.2$, 3.5

ppm), a ratio of 1:2 was calculated, suggesting no cross-linking of OHC-IM linkers by ethylenediamine molecules.

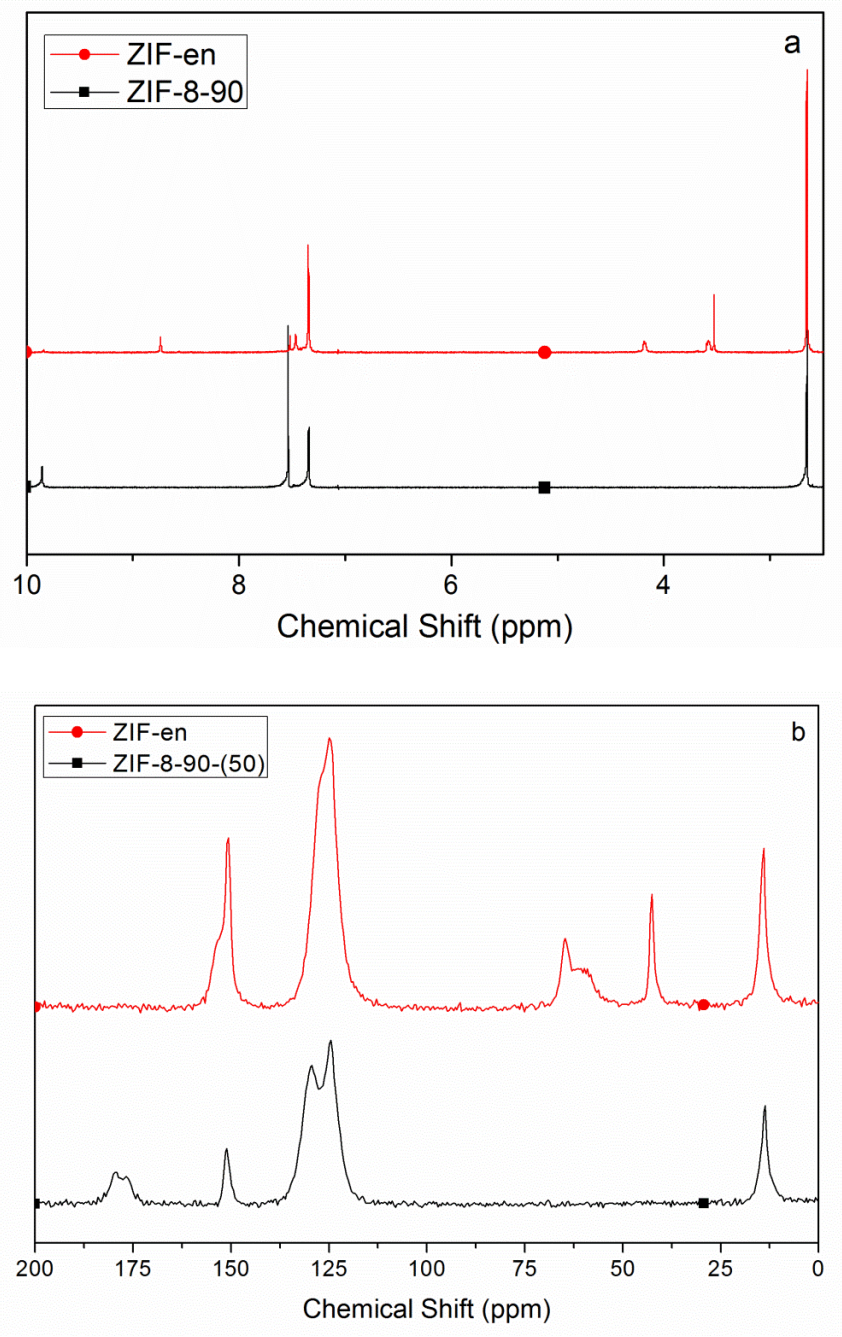

Figure 5.9. (**a**) Solution ^{1}H NMR and (**b**) SS ^{13}C CP-MAS NMR spectra of ZIF-8-90-(50) (squares) and ZIF-en (circles).

In the case of SS ^{13}C CP-MAS NMR spectra (Figure 5.9b), there was no appearance of an aldehyde peak in the region of δ ~ 170-180 ppm following functionalization likely due to low concentration in the framework. Two methylene (–CH_2) peaks appear at δ ~ 55-70 ppm and 42 ppm and may be associated with the ethyl linker between the imine and amine functional groups in ZIF-en. Previously, the peak associated with imine formation in ZIF-90 was attributed to a chemical shift of 60 ppm, meaning the broad peak at δ ~ 55-70 ppm is the methylene –CH_2 bonded to imine nitrogen.[25] Therefore, the other peak at 42 ppm is a resonance of the methylene –CH_2 bonded to the primary amine nitrogen group. The shoulder at 150 ppm is likely associated with C=N bond formation from the imine.[25] Overall, the NMR spectra suggest a high conversion of the aldehyde groups of ZIF-8-90-(50) to imine groups in ZIF-en, and there is no evidence of cross-linking of nearby linkers by ethylenediamine.

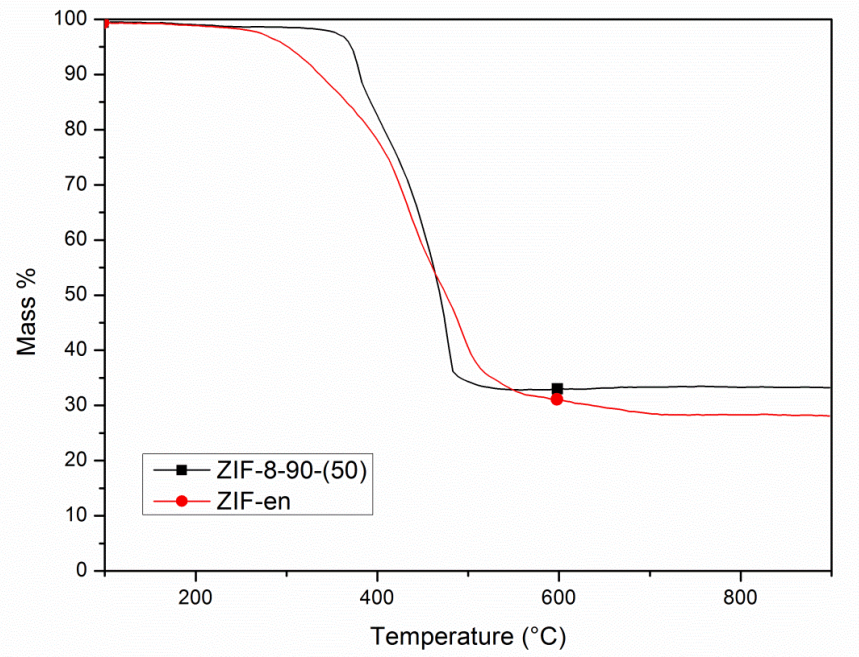

Figure 5.10. TGA mass loss curves of ZIF-8-90-(50) and ZIF-en.

Although there are changes in the relative fractions of the two linkers following PSM, both powder XRD and N_2 physisorption (Figure 5.11) show preservation of the ZIF crystal structure and significant retention of micropore volume compared with previous attempts of PSM of ZIF-90. From *t*-plot micropore volume calculations, a loss of 52% of the pore volume was observed after functionalizing the ZIF material. Considering that previous efforts to functionalize the internal carbonyl groups of ZIF-90 led to near-complete loss of micropore volume or complete degradation of the crystal structure,[25] these characterization results are encouraging. They indicate that ZIF-en still allows gas diffusion through the pores and has good adsorption properties – both of which make it potentially useful for gas separation applications. The preservation of the crystal structure is also encouraging that the mixed-linker synthesis strategy offers a method of changing the functional group in ZIF materials without significant alterations or destruction of the crystal structure. Overall, the mixed-linker synthesis to produce a ZIF-8-90 material followed by PSM with ethylenediamine is a promising example of utilizing these materials for different applications.

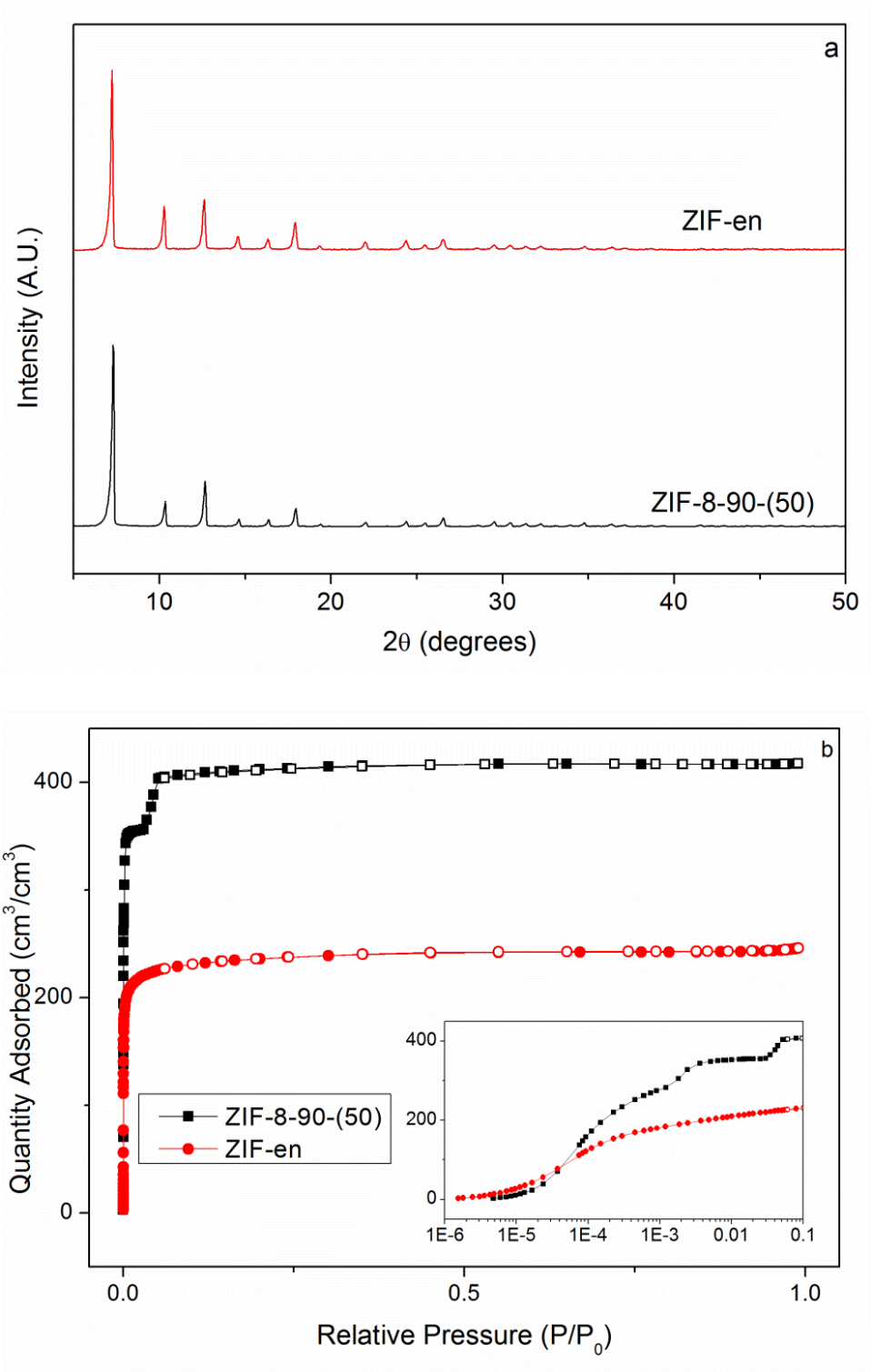

Figure 5.11. (**a**) Powder XRD patterns of ZIF-8-90-(50) and ZIF-en showing maintenance of crystal structure after functionalization; and (**b**) N_2 physisorption isotherms of these materials with no detrimental loss of micropore volume following functionalization.

Figures 5.12a and 5.12b show CO_2 and CH_4 adsorption properties of ZIF-8-90-(50) and ZIF-en, respectively. As seen in Table 5.2, the heats of adsorption for both CO_2 and CH_4 increased after PSM of ZIF-8-90-(50). The heat of adsorption values obtained for ZIF-en are close to typical values for the commercial CO_2 adsorbent zeolite 13X; however, the affinity constants for ZIF-en are much lower than 13X (compare Tables 5.3 with Ref. 33).[33] Unlike zeolite 13X, ZIF-en likely does not have high affinity for H_2O, which significantly affects separation performance in 13X. There is significant enhancement of CO_2 affinity for ZIF-en when compared to ZIF-8-90-(50) or previously published data on ZIF-8.[13] In addition, even though there is a 52% reduction in micropore volume in ZIF-en, the CO_2 capacity does not decrease greatly based on the Toth isotherm fit shown in Table 5.3. When comparing the Henry's law constants of ZIF-8-90-(50) and ZIF-en, the ideal selectivity is found to increase from 5.6 to 13 after PSM, the latter being nearly 6 times higher than that of BPL carbon or ZIF-8.[13,16] Overall, the functionalization of ZIF-8-90-(50) with ethylenediamine leads to a promising enhancement in the affinity of CO_2 over CH_4.

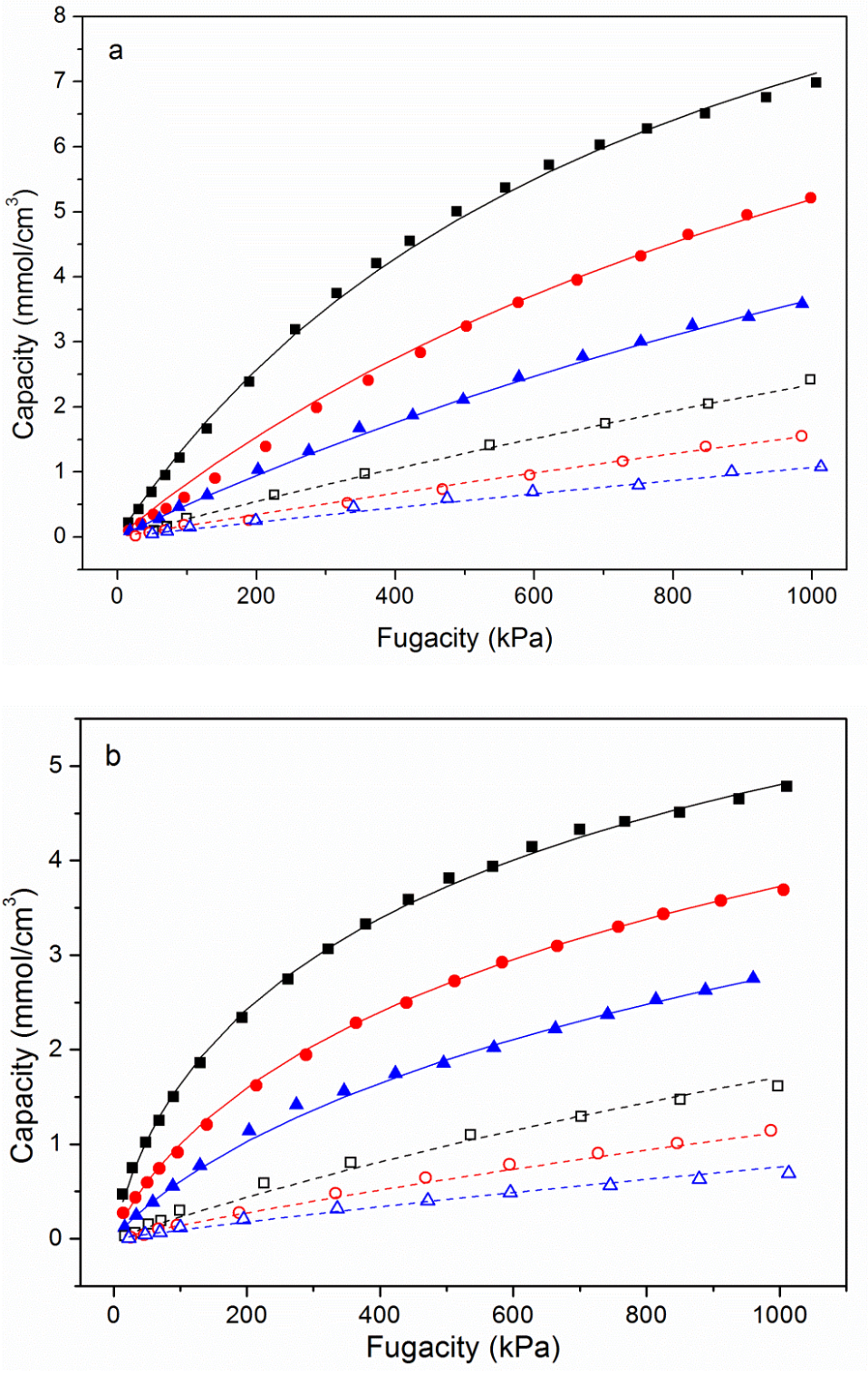

Figure 5.12. CO_2 and CH_4 adsorption isotherms of (**a**) ZIF-8-90-(50) and (**b**) ZIF-en. There are substantial increases in CO_2 adsorption affinity after functionalization. Open symbols denote CH_4 adsorption, closed symbols CO_2. Squares: T = 308 K; circles: T = 328 K; triangles: T = 348 K.

Table 5.3. Isotherm parameters obtained from global fits for CO_2 and CH_4: q_{sat}, saturation capacity; b_0, affinity constant at T_{ref}, $-\Delta H$, heat of adsorption; t_0, heterogeneity parameter of T_{ref}; α and χ, thermal changes for heterogeneity parameter and saturation capacity, respectively.

Sample	CO_2						
	q_{sat} ($mmol \cdot cm^{-3}$)	b_0 (kPa^{-1})	$-\Delta H$ ($kJ \cdot mol^{-1}$)	t_0	α	χ	R^2
ZIF-8-ambz-(14)	12.2	6.18E-04	19.37	1	0	0	0.999
ZIF-8-ambz-(24)	9.0	1.07E-03	20.40	1	0	0	0.999
ZIF-8-ambz-(47)	3.5	1.57E-03	22.1	0.942	-0.085	0	0.989
ZIF-8-90-(50)	12.7	1.27E-03	25.6	1	0	0	0.998
ZIF-en	9.7	4.15E-03	33.9	0.539	0.347	0	0.999

Sample	CH_4						
	q_{sat} ($mmol \cdot cm^{-3}$)	b_0 (kPa^{-1})	$-\Delta H$ ($kJ \cdot mol^{-1}$)	t_0	α	χ	R^2
ZIF-8-ambz-(14)	12.2	2.23E-04	12.5	1	0	0	0.996
ZIF-8-ambz-(24)	9.0	3.43E-04	12.4	1	0	0	0.996
ZIF-8-ambz-(47)	3.5	4.47E-04	15.6	1	0	0	0.960
ZIF-8-90-(50)	12.7	2.26E-04	20.0	1	0	0	0.991
ZIF-en	9.7	4.01E-04	26.2	0.546	1.77	1.9	0.992

5.3.3. IAST, Breakthrough Curve, and PSA Analysis

Ideal adsorbed solution theory is useful for assessing an adsorbent's performance in multicomponent systems.[5,34] Figure 5.13a shows the adsorption selectivity from IAST calculations for the adsorbents considered in this Chapter. The single-component

adsorption parameters required for the IAST predictions are obtained from the experimental data. Although mixed-linker ZIFs may have heterogeneous surfaces, thereby potentially decreasing the accuracy of IAST predictions, it is still useful as a tool for initial assessment of adsorption characteristics.[46,47] Additionally, it has been shown that if the chosen single-component adsorption model fits the experimental data well, then IAST provides good predictions of mixed gas adsorption.[48] Overall, the materials studied here show improvement over ZIF-8 and BPL carbon for CO_2/CH_4 selectivity. Considering the difficulty and expensive linkers required to make ZIFs with selectivities comparable to ZIF-en (*e.g.*, ZIF-78), it may be more prudent to alter ZIF adsorption and gas separation properties by a mixed-linker and/or PSM route rather than using more expensive linkers if the materials are to be considered for practical replacements of commercially available materials (BPL carbon). Interestingly, ZIF-en shows an asymptotic behavior for selectivity at low pressures. The mixed gas adsorption capacity for this sample is shown in Figure 5.13b. Like other amine-modified adsorbents, ZIF-en may have high heats of adsorption (and thus selectivity) at low partial pressures of CO_2.[17,49]

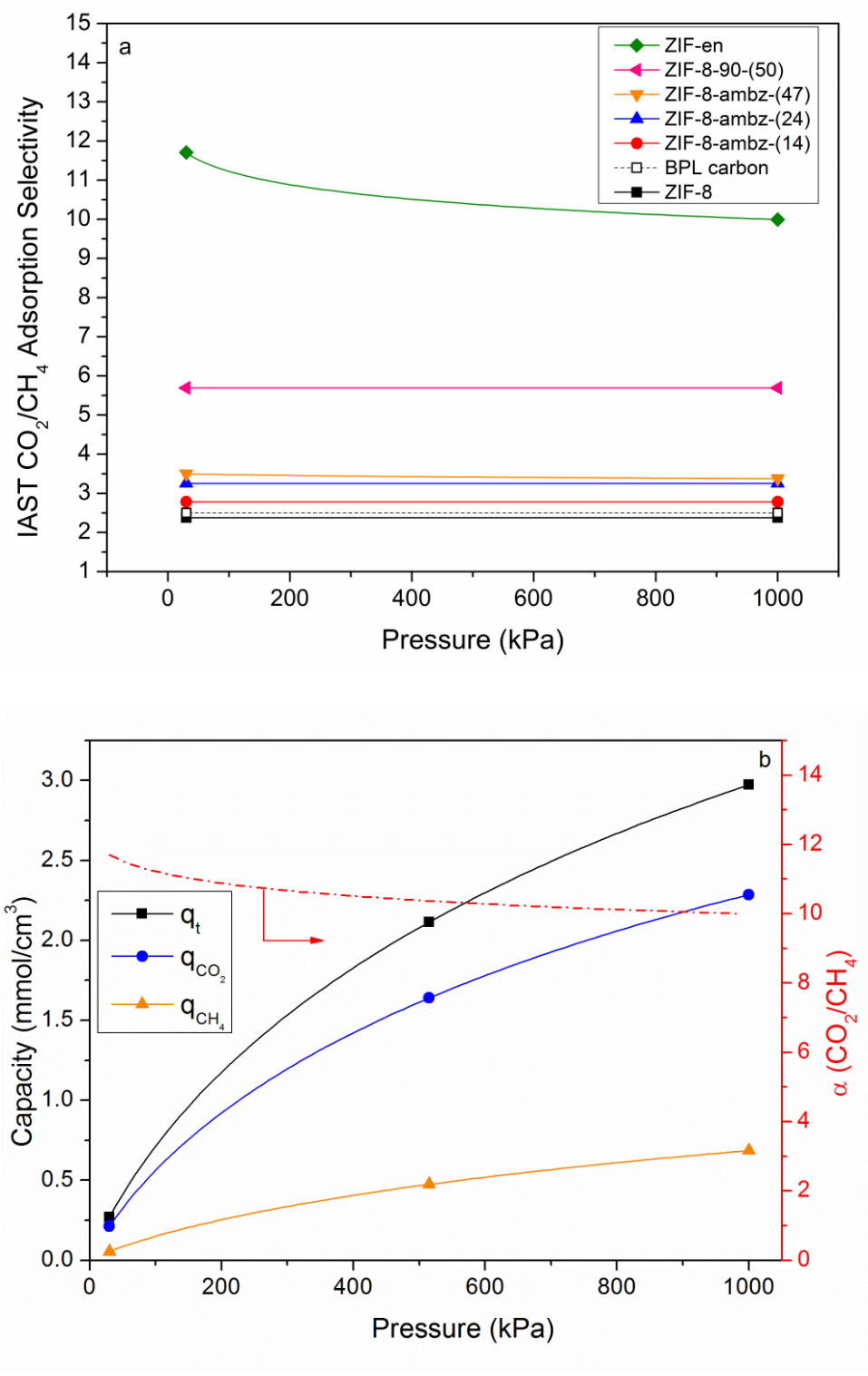

Figure 5.13. IAST calculations of the selective CO_2 adsorption performance of ZIF materials assuming 25% CO_2/75% CH_4 gas phase mixture.

Breakthrough curve analysis is useful to compare different adsorbents under the same conditions. Krishna and Long[36] proposed that analyzing both the breakthrough time and the capacity adsorbed in a simulated packed bed adsorber would aid in PSA and TSA process design for choosing an adsorbent. Breakthrough analysis described in Section 5.2.7 was used to compare the adsorbents presented in this Chapter. Figure 5.14 shows the simulated breakthrough curves, using the assumptions discussed in Section 5.2.7, with a simulated gas feed of 50:50 CO_2:CH_4 at 1000 kPa and bed voidage of 0.4. Interestingly, ZIF-8-90-(50) has a longer calculated dimensionless breakthrough time than ZIF-en. This is likely related to the larger saturation capacity of ZIF-8-90-(50) compared to ZIF-en at the adsorption pressure; however, the sharpness of the breakthrough curve, sometimes expressed as the length of unused bed (LUB), shows that ZIF-en has higher overall selectivity than ZIF-8-90-(50), which is manifested in the IAST calculations.

Other feed conditions were examined to gain understanding of how each adsorbent is affected by different mole fractions of CO_2. In Figure 5.15, the dimensionless breakthrough time, determined by the outlet mole fraction of CO_2 being 2%, is plotted as a function of feed mole fraction of CO_2 at constant feed pressure of 1000 kPa. The increase in breakthrough time observed with all the adsorbents with decreasing CO_2 feed fraction is related to longer time to reach the equilibrated capacity when less CO_2 is present in the feed stream. Because ZIF-en has an asymptotic selectivity behavior, the increase in breakthrough time observed in Figure 5.15 may be related to a higher selectivity at lower concentrations of CO_2 in the feed gas. The breakthrough

simulations overall indicate that feed conditions can largely dictate the expected behavior of an adsorbent, showing that at lower CO_2 feed concentrations ZIF-en has a larger breakthrough time than ZIF-8-90-(50). This observation is important since typical natural gas wells contain CO_2 in mole fractions of 0.1 or less.

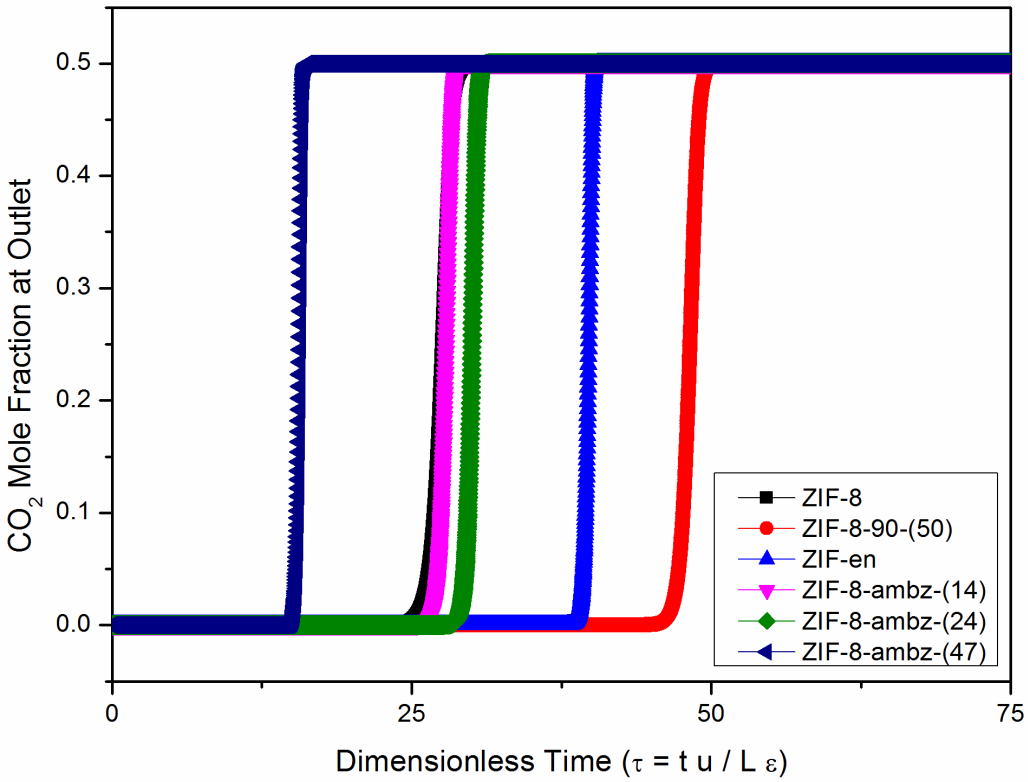

Figure 5.14. Breakthrough curve simulations of different adsorbents for a CO_2/CH_4 feed mixture of 50:50 at 1000 kPa. ZIF-8 and ZIF-8-ambz-(14) closely overlap.

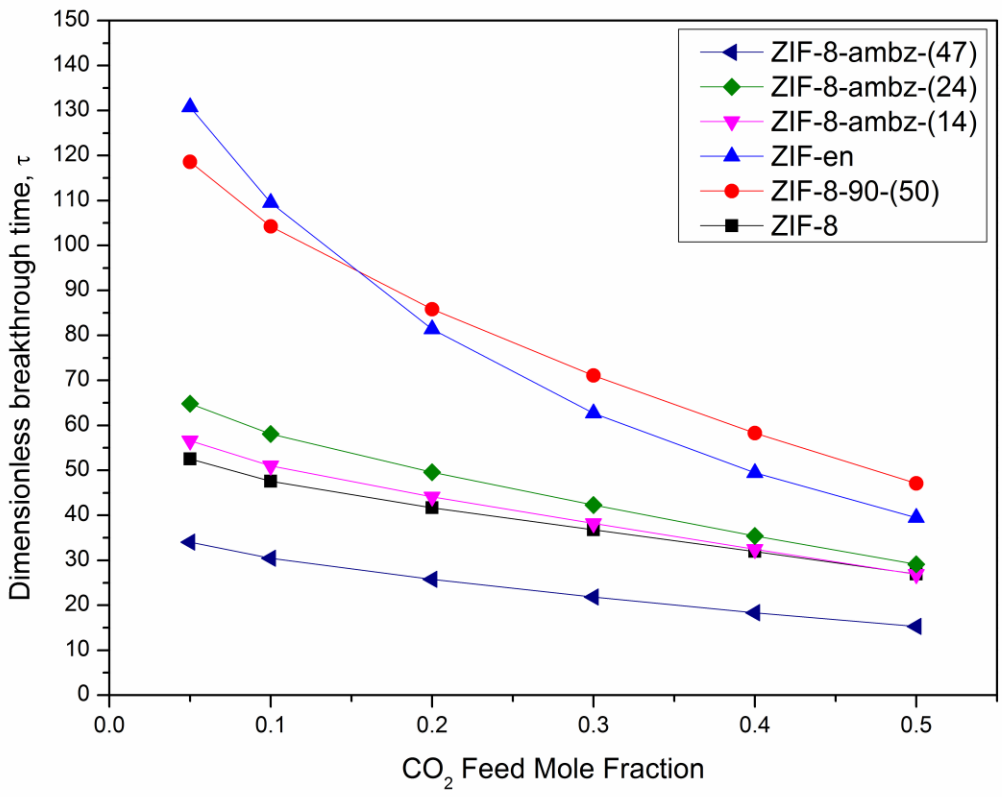

Figure 5.15. Dimensionless breakthrough time related to incoming CO_2 mole fraction of feed gas for a fixed bed adsorber.

Krishna and Long proposed that an adsorbent can be screened based on the dimensionless breakthrough time and the *total* amount of CO_2 adsorbed in a column that is free of adsorbate prior to adsorption;[36] however, this implies that the adsorbent is fully regenerated between adsorption cycles. In practice, this is typically not done, and instead, the pressure and/or temperature of the adsorber column is changed to provoke a change in the equilibrium capacity.[35] To illustrate why a full regeneration may not be desirable, breakthrough curves for the desorption of ZIF-8, ZIF-8-90-(50) and ZIF-en were calculated and are shown in Figure 5.16, assuming the adsorbent is regenerated by purging the adsorption column at 100 kPa with the product stream, nearly pure CH_4, with the initial conditions having a 50:50 CO_2:CH_4 mixture. Even with ZIF-8 as the adsorbent,

the time to purge CO_2 from the adsorption column is 3 times larger than the time to adsorb CO_2. This is not surprising, considering that adsorption of CO_2 in all these adsorbents is favorable, making the desorption unfavorable.[35] It is also important to note that desorption under these conditions appears to mainly be dictated by adsorption selectivity and not capacity. This is correlated by ZIF-en showing the longest desorption time, even though the breakthrough curves for adsorption in Figure 5.14 indicate that ZIF-8-90-(50) would have the longest breakthrough curve under the feed conditions of a 50:50 CO_2:CH_4 feed stream. With these desorption curves in mind, in order to provide a proper assessment of an adsorbent's performance, along with using the dimensionless breakthrough time and *total* adsorption capacity at the feed pressure, other parameters should be consider, such as the working capacity – the capacity difference between the adsorption step and the desorption step.[50] In addition, the amount of CH_4 recovered is an important parameter to consider since increasing loss of CH_4 will relate directly to less product recovered during the separation process.

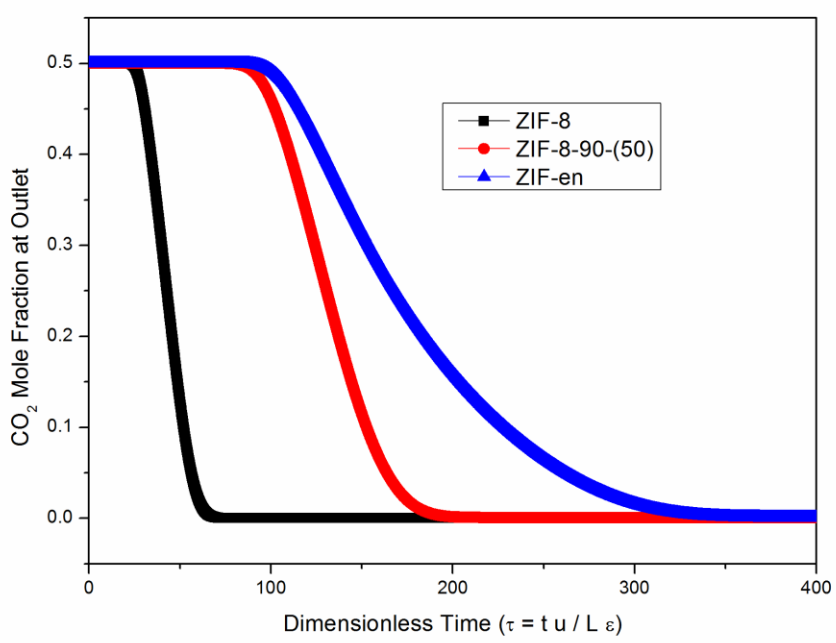

Figure 5.16. Breakthrough curve simulations for purging adsorbents with product gas of 99.95% CH_4.

Table 5.4 shows the dimensionless breakthrough time, the total CO_2 capacity at the adsorption pressure (1000 kPa), the working capacity of CO_2 between the adsorption and desorption pressure (100 kPa), the ideal CH_4 recovery, determined by assuming CH_4 lost in the PSA process is only the working capacity of the adsorbent and one bed volume of the adsorber, and the adsorbent selectivity for a CO_2:CH_4 feed with a 50:50 mixture. Although the adsorption selectivity and CH_4 recovery increases for the adsorbents containing 2-aminobenzimidazole, there is not much incentive to consider these materials for *equilibrium adsorption*-based separations due to a decrease in both the total CO_2 capacity and the working CO_2 capacity when compared with ZIF-8. The use of either ZIF-8-90-(50) and ZIF-en does provide some benefit by increasing both the breakthrough time and adsorption selectivity while still maintaining a modest CO_2 working capacity. If the CH_4 recovery is not of great importance, then it may be more beneficial to use an

adsorbent such as ZIF-8-90-(50) due to longer breakthrough time, larger working CO_2 capacity compared to ZIF-en, and no requirements for postsynthetic modification of the ZIF material. However, if there is a desire to consider the CH_4 recovery, then ZIF-en offers excellent operating parameters, considering the higher selectivity and sharper breakthrough curve behavior compared to the other adsorbents in this Chapter. In addition, optimization of the PSM of ZIF-8-90-(50) to make an amine-functionalized material with high loadings of aliphatic amines may greatly improve the comparison to its parent material, ZIF-8-90-(50).

Table 5.4. Parameters to consider for screening adsorbents for different applications.

Adsorbent	τ_{break}	N_{CO2}^{ads} ($mmol \cdot cm^{-3}$)	ΔN_{CO2} ($mmol \cdot cm^{-3}$)	Ideal CH_4 Recovery (%)	α^{ads}
ZIF-8	23.6	6.80	4.35	42	2.60
ZIF-8-ambz-(14)	25.6	2.65	2.29	45	2.77
ZIF-8-ambz-(24)	28.0	2.82	2.37	49	3.12
ZIF-8-ambz-(47)	14.8	1.31	1.06	43	3.40
ZIF-8-90-(50)	45.1	4.61	3.86	62	5.62
ZIF-en	38.3	3.52	2.50	64	9.98

Overall, the breakthrough simulations shown here illustrate the need to assess more than just the breakthrough time and *total* amount of target gas adsorbed in an adsorption column. Many parameters need to be considered before deciding on an adsorbent for a target application. In addition, actual breakthrough experiments should be considered before a narrowed selection of materials is made. For example, although Mg-

MOF-74 has been predicted to be one of the better adsorbent materials for adsorption applications,[36,51] experimental breakthrough curves with a series of M-MOF-74 samples have shown there to be complex and dispersive breakthrough behavior depending on the metal center selected for the material for CO_2/CH_4 separations, indicating non-ideal behavior of the adsorbent under real conditions.[52]

5.4 Conclusions

Two different strategies for improving CO_2 selectivity and tuning the surface properties of ZIF materials have been demonstrated: (i) the use of amine-containing imidazolate linkers to substitute for ZIF-8 linkers during synthesis and prepare an amine-containing mixed-linker ZIF; and (ii) postsynthetic modification of carbonyl groups in a mixed-linker ZIF-8-90 material using ethylenediamine molecules. The two routes yield different adsorption properties as assessed by single-component measurements and binary IAST predictions and breakthrough curve simulations, with the route utilizing PSM leading to a more CO_2 selective material compared to ZIF-8 or BPL carbon. In addition, these ZIF materials were compared using breakthrough curve simulations to assess the performance for a fixed bed adsorption process. The simulations and analysis demonstrated that there is a complicated, and not straightforward, method for choosing the right adsorbent, but ZIF-8-90-(50) and ZIF-en samples showed the best overall predicted performance for an equilibrium-based adsorption process. Although the present work is focused on the CO_2/CH_4 gas pair, it is also likely the above materials would have much higher CO_2/N_2 selectivity when compared to ZIF-8 and other commercially available adsorbents, since N_2 typically has lower affinity in adsorbents compared to

CH_4, due to lower polarizability.[5] Equally important, because these materials all maintain the same *I-43m* cubic crystal topology and have a reduced pore volume and micropore distribution in comparison to ZIF-8, the kinetic separation performance of these materials may show improvement over ZIF-8, and these new materials may provide a novel route for CO_2/CH_4 or CO_2/N_2 separations using pure ZIF membranes or polymer/ZIF composite membranes, of which the latter will be explored in Chapter 6.[5,53–55]

5.5 References

(1) Sumida, K.; Rogow, D. L.; Mason, J. A.; McDonald, T. M.; Bloch, E. D.; Herm, Z. R.; Bae, T.-H.; Long, J. R. *Chem. Rev*. **2012**, *112*, 724–781.

(2) Li, J.-R.; Sculley, J.; Zhou, H.-C. *Chem. Rev*. **2012**, *112*, 869–932.

(3) Corma, A.; Garcia, H.; Llabrés i Xamena, F. X. *Chem. Rev*. **2010**, *110*, 4606–4655.

(4) Kreno, L. E.; Leong, K.; Farha, O. K.; Allendorf, M.; Van Duyne, R. P.; Hupp, J. T. *Chem. Rev*. **2012**, *112*, 1105–1125.

(5) Keskin, S.; Van Heest, T. M.; Sholl, D. S. *ChemSusChem* **2010**, *3*, 879–891.

(6) Banerjee, R.; Phan, A.; Wang, B.; Knobler, C. B.; Furukawa, H.; O'Keeffe, M.; Yaghi, O. M. *Science* **2008**, *319*, 939–943.

(7) Wang, B.; Côté, A. P.; Furukawa, H.; O'Keeffe, M.; Yaghi, O. M. *Nature* **2008**, *453*, 207–211.

(8) Phan, A.; Doonan, C. J.; Uribe-Romo, F. J.; Knobler, C. B.; O'Keeffe, M.; Yaghi, O. M.; O'Keeffe, M. *Acc. Chem. Res.* **2010**, *43*, 58–67.

(9) Banerjee, R.; Furukawa, H.; Britt, D.; Knobler, C.; Keeffe, M. O.; Yaghi, O. M.; O'Keeffe, M. *J. Am. Chem. Soc.* **2009**, *131*, 3875–3877.

(10) Morris, W.; Leung, B.; Furukawa, H.; Yaghi, O. K.; He, N.; Hayashi, H.; Houndonougbo, Y.; Asta, M.; Laird, B. B.; Yaghi, O. M. *J. Am. Chem. Soc.* **2010**, *132*, 11006–11008.

(11) Pérez-Pellitero, J.; Amrouche, H.; Siperstein, F. R.; Pirngruber, G.; Nieto-Draghi, C.; Chaplais, G.; Simon-Masseron, A.; Bazer-Bachi, D.; Peralta, D.; Bats, N. *Chem. Eur. J.* **2010**, *16*, 1560–1571.

(12) Aguado, S.; Bergeret, G.; Titus, M. P.; Moizan, V.; Nieto-Draghi, C.; Bats, N.; Farrusseng, D. *New J. Chem.* **2011**, *35*, 546–550.

(13) Amrouche, H.; Aguado, S.; Pérez-Pellitero, J.; Chizallet, C.; Siperstein, F.; Farrusseng, D.; Bats, N.; Nieto-Draghi, C. *J. Phys. Chem. C* **2011**, *115*, 16425–16432.

(14) Liu, J.; Keskin, S.; Sholl, D. S.; Johnson, J. K. *J. Phys. Chem. C* **2011**, *115*, 12560–12566.

(15) Atci, E.; Keskin, S. *Ind. Eng. Chem. Res.* **2012**, *51*, 3091–3100.

(16) Sircar, S.; Golden, T. C.; Rao, M. B. *Carbon* **1996**, *34*, 1–12.

(17) Choi, S.; Watanabe, T.; Bae, T.-H.; Sholl, D. S.; Jones, C. W. *J. Phys. Chem. Lett.* **2012**, *3*, 1136–1141.

(18) McDonald, T. M.; Lee, W. R.; Mason, J. A.; Wiers, B. M.; Hong, C. S.; Long, J. R. *J. Am. Chem. Soc.* **2012**, *134*, 7056–7065.

(19) Pirngruber, G. D.; Hamon, L.; Bourrelly, S.; Llewellyn, P. L.; Lenoir, E.; Guillerm, V.; Serre, C.; Devic, T. *ChemSusChem* **2012**, *5*, 762–776.

(20) Liu, J.; Benin, A. I.; Furtado, A. M. B.; Jakubczak, P.; Willis, R. R.; LeVan, M. D. *Langmuir* **2011**, *27*, 11451–11456.

(21) Yu, K.; Kiesling, K.; Schmidt, J. R. *J. Phys. Chem. C* **2012**, *116*, 20480–20488.

(22) Park, K. S.; Ni, Z.; Côté, A. P.; Choi, J. Y.; Huang, R.; Uribe-Romo, F. J.; Chae, H. K.; O'Keeffe, M.; Yaghi, O. M. *Proc. Nat. Acad. Sci.* **2006**, *103*, 10186–10191.

(23) Wang, Z.; Cohen, S. M. *Chem. Soc. Rev*. **2009**, *38*, 1315–1329.

(24) Tanabe, K. K.; Cohen, S. M. *Chem. Soc. Rev*. **2011**, *40*, 498–519.

(25) Morris, W.; Doonan, C. J.; Furukawa, H.; Banerjee, R.; Yaghi, O. M. *J. Am. Chem. Soc.* **2008**, *130*, 12626–12627.

(26) Demessence, A.; D'Alessandro, D. M.; Foo, M. L.; Long, J. R. *J. Am. Chem. Soc.* **2009**, *131*, 8784–8786.

(27) Kim, M.; Cahill, J. F.; Su, Y.; Prather, K. A.; Cohen, S. M. *Chem. Sci.* **2012**, *3*, 126–130.

(28) Kim, M.; Cahill, J. F.; Fei, H.; Prather, K. A.; Cohen, S. M. *J. Am. Chem. Soc.* **2012**, *134*, 18082–18088.

(29) Karagiaridi, O.; Lalonde, M. B.; Bury, W.; Sarjeant, A. A.; Farha, O. K.; Hupp, J. T. *J. Am. Chem. Soc.* **2012**, *134*, 18790–18796.

(30) Koros, W. J.; Paul, D. R. *J. Polym. Sci. Polym. Phys. Ed.* **1976**, *14*, 1903–1907.

(31) Toth, J. *Acta. Chim. Acad. Sci. Hungar.* **1971**, *69*, 311–328.

(32) Do, D. D. *Adsorption Analysis: Equilibrium and Kinetics*; Imperial College Press, 1998.

(33) Cavenati, S.; Grande, C. A.; Rodrigues, A. E. *J. Chem. Eng. Data* **2004**, *49*, 1095–1101.

(34) Myers, A. L.; Prausnitz, J. M. *AIChE J.* **1965**, *11*, 121–127.

(35) Ruthven, D. M. *Principles of Adsorption and Adsorption Processes*; John Wiley & Sons, Inc., 1984.

(36) Krishna, R.; Long, J. R. *J. Phys. Chem. C* **2011**, *115*, 12941–12950.

(37) Bae, T.-H.; Hudson, M. R.; Mason, J. A.; Queen, W. L.; Dutton, J. J.; Sumida, K.; Micklash, K. J.; Kaye, S. S.; Brown, C. M.; Long, J. R. *Energy Environ. Sci.* **2013**, *6*, 128–138.

(38) Stavitski, E.; Pidko, E. A.; Couck, S.; Remy, T.; Hensen, E. J. M.; Weckhuysen, B. M.; Denayer, J.; Gascon, J.; Kapteijn, F. *Langmuir* **2011**, *27*, 3970–3976.

(39) Fairen-Jimenez, D.; Galvelis, R.; Torrisi, A.; Gellan, A. D.; Wharmby, M. T.; Wright, P. A.; Mellot-Draznieks, C.; Düren, T. *Dalton Trans.* **2012**, *41*, 10752–10762.

(40) Wu, H.; Zhou, W.; Yildirim, T. *J. Phys. Chem. C* **2009**, *113*, 3029–3035.

(41) Haldoupis, E.; Watanabe, T.; Nair, S.; Sholl, D. S. *ChemPhysChem* **2012**, *13*, 3449–3452.

(42) Fairen-Jimenez, D.; Moggach, S. A.; Wharmby, M. T.; Wright, P. A.; Parsons, S.; Düren, T. *J. Am. Chem. Soc.* **2011**, *133*, 8900–8902.

(43) Zhang, C.; Lively, R. P.; Zhang, K.; Johnson, J. R.; Karvan, O.; Koros, W. J. *J. Phys. Chem. Lett.* **2012**, *3*, 2130–2134.

(44) Abdel-Magid, A. F.; Carson, K. G.; Harris, B. D.; Maryanoff, C. A.; Shah, R. D. *J. Org. Chem.* **1996**, *61*, 3849–3862.

(45) Jiang, H.-L.; Feng, D.; Liu, T.-F.; Li, J.-R.; Zhou, H.-C. *J. Am. Chem. Soc.* **2012**, *134*, 14690–14693.

(46) Sircar, S. *Ind. Eng. Chem. Res.* **1991**, *30*, 1032–1039.

(47) Sircar, S. *AIChE Journal* **1995**, *41*, 1135–1145.

(48) Richter, E.; Schütz, W.; Myers, A. L. *Chem. Eng. Sci.* **1989**, *44*, 1609–1616.

(49) Choi, S.; Drese, J. H.; Eisenberger, P. M.; Jones, C. W. *Environ. Sci. Technol.* **2011**, *45*, 2420–2427.

(50) Bae, Y.-S.; Snurr, R. Q. *Angew. Chem. Int. Ed.* **2011**, *50*, 11586–11596.

(51) Herm, Z. R.; Krishna, R.; Long, J. R. *Micropor. Mesopor. Mater.* **2012**, *151*, 481–487.

(52) García, E. J.; Mowat, J. P. S.; Wright, P. A.; Perez-Pellitero, J.; Jallut, C.; Pirngruber, G. D. *J. Phys. Chem. C* **2012**, *116*, 26636–26648.

(53) Zornoza, B.; Tellez, C.; Coronas, J.; Gascon, J.; Kapteijn, F. *Micropor. Mesopor. Mater.* **2013**, *166*, 67–78.

(54) Gascon, J.; Kapteijn, F.; Zornoza, B.; Sebastián, V.; Casado, C.; Coronas, J. *Chem. Mater.* **2012**, *24*, 2829–2844.

(55) Keskin, S.; Sholl, D. S. *Ind. Eng. Chem. Res.* **2009**, *48*, 914–922.

CHAPTER 6

Fabrication and Performance of Zeolitic Imidazolate Framework-Based Mixed-Matrix Membranes for Acid Gas Separations

6.1 Introduction

Mixed-matrix membranes (MMMs) are a promising membrane technology for gas and liquid separations due to combining the ease of processability from the polymer matrix and the improved molecular sieving properties from the filler phase.[1–3] In addition, MMMs can be a promising platform for testing the gas separation properties of nanoporous materials prior to developing fabrication techniques for pure nanoporous membranes.[4–7] As shown in Chapter 2 and recent review articles, there are currently few studies that convincingly and comprehensively show the utility of metal-organic frameworks (MOFs) to improve CO_2-based gas separation properties in comparison to pure polymeric membranes.[1,8–12] In particular, often the previous works do not utilize materials that closely match the permeation properties of the polymer, making assessment of the composite membranes difficult.[13–15] In Chapter 4, the need to closely study the fabrication steps for preparing MMMs was demonstrated. The use of high-intensity ultrasonication resulted in well-dispersed zeolitic imidazole framework (ZIF) materials in a Matrimid® polymer matrix, but characterization of the sonicated ZIF-8 revealed changes in the textual and particle properties that may affect the gas transport through the crystal structure;[16] therefore, fabrication steps of MMMs should be carefully considered in analyzing the gas separation properties of ZIF and other MOF materials.

In this Chapter, ZIF materials are synthesized utilizing synthesis techniques described in preceding Chapters. Control over the pore size distribution and the linker composition of different ZIFs is shown to alter the effective permeability and diffusivity properties of composite membranes based on single gas permeation experiments. To prevent nanoparticle coarsening during membrane fabrication, a different solvent is chosen from that used in Chapter 4, and mixed-matrix membranes are prepared containing similar weight percentages of each ZIF. Single gas permeation experiments reveal considerable differences in effective permeability and diffusivity properties of composite membranes, and overall, both the linker functionality and composition are shown to have significant effects on the permeability of CO_2 and CH_4 in the ZIF composite membranes. Mixed gas permeation experiments demonstrate that although there is some enhancement in ideal permselectivity in single gas permeation experiments, there is still little enhancement in the permselectivity of composite membranes compared to the pure Matrimid® polymer at high operating pressures. However, high pressure mixed gas permeation shows stabilization of CH_4 permeability when mixed-linker ZIF materials are used as the filler phase, an indication that there is enhancement in plasticization resistance in the composite membranes. Process calculations of a simulated hollow fiber membrane module are performed to demonstrate that although there are improvements in both permeability and selectivity in some ZIF composite membranes, the major benefit of including these filler materials in composite membranes is significant reduction of membrane area for a desired feed flow rate and product purity due to large increases in effective permeability.

6.2 Experimental Methods

6.2.1 Materials

Sodium formate (99%, $NaCO_2H$), $Zn(NO_3)_2 \cdot 6H_2O$ (99%), 2-methylimidazole (99%, 2-MeIM), 2-aminobenzimidazole (97%, 2-amBzIM), benzimidazole (BzIM), and chloroform (HPLC grade, $CHCl_3$) were obtained from Alfa Aesar. Dimethylformamide (99%, DMF) and methanol (99%, MeOH) were obtained from BDH. Matrimid® 5128 was obtained from Ciba. All materials were used without further purification.

6.2.2 Synthesis of ZIF-8

ZIF-8 was synthesized using a scaled-up procedure reported in Chapter 4. In one solution, 80 mmol 2-MeIM was dissolved in 200 mL MeOH. In a separate solution, 20 mmol $Zn(NO_3)_2 \cdot 6H_2O$ was dissolved in 200 mL MeOH. After stirring separately for 5 min, the Zn salt solution was poured into the 2-MeIM solution, and after 5 min of mixing, a milky white precipitate formed, an indication of crystal formation. The combined mixture was allowed to stir for 1 hr. The precipitate solution was then centrifuged at 10,000 rpm for 5 mins. The supernatant was removed, and the precipitate was washed with MeOH. This procedure was repeated 3 times, and then the product was collected by vacuum filtration and dried at 358 K. The yield for the ZIF-8 product was approximately 25% based on Zn added to the solution.

6.2.3 Synthesis of ZIF-8-ambz Hybrids

ZIF-8-ambz-(15) and ZIF-8-ambz-(30) hybrid samples were synthesized using the procedure reported in Chapter 3. First, 2 mmol (8 mmol) of 2-amBzIM, 18 mmol (12 mmol) 2-MeIM, and 5 mmol $NaCO_2H$ were dissolved in 50 mL deionized (DI) H_2O by heating the solution to 348 K for 2 hrs to form the imidazole solution for ZIF-8-ambz-(14) (or ZIF-8-ambz-(30)). A separate solution containing 5 mmol $Zn(NO_3)_2 \cdot 6H_2O$ was prepared with 50 mL DMF. After the imidazole solution cooled to room temperature, the Zn salt solution was added, and a precipitate formed almost immediately. The solution was allowed to react for 1 hr before centrifugation at 10,000 rpm for 10 mins. The supernatant was removed, and the precipitate was washed with MeOH. This procedure was repeated 3 times, and then the product was recovered by vacuum filtration and dried at 358 K. The yield of ZIF-8-ambz-(*x*) hybrids was approximately 30-40% based on Zn added to the solution.

6.2.4 Synthesis of ZIF-7-8-(20) Hybrid

ZIF-7-8-(20) was synthesized by a scaled-up procedure similar to what is reported in Chapter 3. A solution of 8.4 mmol BzIM, 111.6 mmol 2-MeIM, and 120 mmol $NaCO_2H$ was prepared in 300 mL MeOH. A separate solution of 30 mmol $Zn(NO_3)_2 \cdot 6H_2O$ was prepared in 300 mL DMF. Once both solutions were clear, the Zn salt solution was poured into the imidazole solution. The combined mixture was then placed in an oven in a sealed polyethylene bottle and allowed to stir for 24 hrs at 323 K. After cooling to room temperature, the milky solution was centrifuged at 10,000 rpm for 5 min. The supernatant was removed, and the precipitate was washed with MeOH. This

washing procedure was repeated 3 times, and then the product was recovered by vacuum filtration and dried at 358 K. The yield of ZIF-7-8-(20) was approximately 10% based on Zn added to the solution.

6.2.5 Mixed-Matrix Membrane Fabrication

Mixed-matrix membranes were prepared by first dispersing ZIF samples in a solvent, and then after addition of polymer, films were prepared using the solution-casting technique.[17] In a typical film preparation procedure, 0.15 g ZIF sample was sonicated in 5 mL $CHCl_3$, using a sonication bath with a sonication intensity of 3.8 $W \cdot cm^{-2}$. Once particles appeared well-dispersed after approximately 1-2 hrs of sonication, 0.2 g Matrimid® 5128 (chemical structure shown in Figure 4.1) was added and allowed to dissolve while sonicating in the sonication bath. The addition of Matrimid® acts as a primer to cover the ZIF surface with polymer to help promote adhesion to the polymeric phase and to prevent aggregation during film preparation.[18] Once the polymer was fully dissolved, the primed ZIF dispersion was sonicated using an ultrasonication horn with a sonication intensity of 156 $W \cdot cm^{-2}$. In order to prevent solvent evaporation, primed ZIF dispersions were sonicated with the horn in 30 sec intervals, and this procedure was repeated twice. The primed dispersion was then sonicated in the bath again for 1 hr. The primed ZIF dispersion was sonicated with the horn for two more 30 sec intervals and then poured over the remaining balance of Matrimid® to obtain the desired ratio of ZIF to polymer (0.15:0.85 w/w). The membrane dope solution was allowed to tumble overnight on a roller. A glove bag was prepared with $N_2/CHCl_3$ atmosphere, and using a casting knife of 200 μm, a film was manually

cast and allowed to vitrify overnight. All films were roughly 30-50 μm in thickness, measured using a micrometer, and films were annealed at 498 K for 24 hrs under vacuum.

6.2.6 Characterization Methods

The ZIF materials were analyzed by powder X-ray diffraction (XRD) using an X'Pert Pro PANalytical X-ray Diffractometer. Diffraction measurements were done from 3.5-50° 2θ using an X'celerator detector. Nitrogen physisorption measurements were done on a Micromeritics ASAP 2020 surface area analyzer at 77 K. All samples were degassed at 523 K for 18 hrs prior to physisorption measurements. The BET surface area and t-plot micropore volume methods were used to analyze the relative surface properties of each sample. Horváth-Kawazoe pore size distributions were used to compare the relative changes in pore size distributions between the different ZIF samples. The methodology for this analysis was covered in Chapter 3. To determine the linker composition in the ZIF framework, all samples were analyzed with solution ^{1}H nuclear magnetic resonance (NMR) spectroscopy on a Mercury Vx 400 MHz spectrometer after digesting samples using d_4-acetic acid (CD_3CO_2D). SEM imaging of ZIF particles was done on a Zeiss Leo 1550 scanning electron microscope (SEM). Samples were coated with gold by sputtering under vacuum, and images were taken with an accelerating voltage of 10 kV. Mixed-matrix membrane films were characterized using Fourier-transform Infrared (FTIR) spectroscopy and scanning electron microscopy (SEM). FTIR measurements were done in transmission mode on a Bruker Vertex 80v FTIR analyzer from 4000-400 cm^{-1}. SEM imaging was done on a Zeiss LEO 1550 SEM. Membrane

microscopy samples were prepared by submerging films in liquid nitrogen and fracturing the film to examine the cross section of the mixed-matrix membrane. Samples were coated by sputtering gold under vacuum, and images were taken with an accelerating voltage of 10 kV.

6.2.7 Gas Permeation Measurements

Permeation measurements were performed using a constant volume permeation cell described in earlier work.[19] A small area of the film was cut out from a larger membrane film, and using aluminum tape, a mask was prepared with approximately 1 cm in diameter of exposed membrane area. At least two areas of a film and two separate films were tested for each membrane reported for single gas measurements. The membrane area edges were sealed using Duralco 4525 high temperature epoxy obtained from Cortronics and allowed to set overnight before sealing the permeation cell. After insertion of the film into the permeation cell, the film was degassed at 308 K for at least 24 hours before each permeation test. Leak tests were done before each permeation experiment, ranging from 10^{-8}-10^{-7} kPa·sec^{-1}. Subsequent permeation tests following the first test were performed after degassing both sides of the film under vacuum for 12-24 hours and testing the leak rate again. Single gas permeation experiments were performed at 308 K with 345 kPa of upstream pressure of either CO_2 or CH_4. Measurements started once upstream gas was introduced to the cell and the downstream was evacuated ($<10^{-3}$ kPa. Permeability of CO_2 and CH_4 were calculated by the following:

$$P = \left(\frac{dp}{dt}\right)\frac{V_d l}{RTA_m \Delta f} \tag{6.1}$$

where $\frac{dp}{dt}$ is the pressure rise rate, V_d is the volume of the permeate side of the membrane, l is the thickness of the membrane, R is the ideal gas constant, T is the absolute temperature, A_m is the measured area of the exposed membrane, and Δf is the fugacity difference of the feed and permeate sides of the membrane.

Time lag measurements were performed by analyzing the time for gas to permeate through the film. By this method, the approximate time to reach the permeation flux steady-state and the apparent diffusion coefficient of the film can be calculated by the following:[10]

$$D_{app} = \frac{l^2}{6\theta} \tag{6.2}$$

where D_{app} is the effective diffusion coefficient of the membrane, l is the membrane thickness measured by a micrometer, and θ is the measured time lag of the membrane film. The approximate time to reach steady-state can be estimated by allowing each permeation measurement to take at least 4-6 θ, but in most cases, 10 θ was used for each measurement. Although fillers have been shown to affect the measured time lag in mixed-matrix membranes, this typically only occurs if the fillers strongly adsorb the gas that is being tested.[20,21] From Chapter 5, it has been shown that the primary amine on the

2-amBzIM substituting linker does not greatly influence the overall CO_2 affinity in these mixed-linker ZIF materials, making Equation 6.2 a reasonable approximation for the apparent diffusion rate through a mixed-matrix membrane film.

Mixed gas permeation experiments were performed on a constant volume apparatus with a feed mole fraction of 50:50 CO_2:CH_4. Prior to mixed gas testing, each membrane was tested for single gas permeation to confirm if there were noticeable differences in performance between mixed gas-tested films and single gas-tested films. Films for mixed gas testing had areas approximately 2.5 times larger compared to single gas-tested films to obtain a representative performance of each membrane sample tested for mixed gas. The retenate flow rate was set to approximately 100 times the downstream gas flux in the permeate side of the apparatus. Pressures tested for each film were approximately 690, 1380, 2760, and 4140 kPa of total feed pressure. To confirm that at each pressure point the membrane was at steady state, films were allow to equilibrate over a 12 hr period, which was well-beyond the time required to reach steady-state permeation as estimated by the pure gas time-lag measurements. Additionally, permeability was measured 1-3 hr after the steady-state time had been reached to confirm equilibrium. The composition of gas in the permeate side was determined by using a Bruker Daltronics Varian 450 gas chromatograph (GC) with a thermal conductivity detector and He reference gas. At each pressure point, at least 3-6 GC injections were done to obtain an average of the permeate composition, and at least two injections at different times were performed to check that each film was at steady state. The permeate composition was used to calculate the separation factor:

$$SF = \frac{\left(y_{CO_2} / y_{CH_4} \right)_{perm}}{\left(y_{CO_2} / y_{CH_4} \right)_{feed}} \tag{6.3}$$

where y_i is the mole fraction of component i in the feed or permeate side. Permeability values were calculated by the molar flux across the membrane and the gas composition on the permeate side obtained from GC measurements, and mixed gas permselectivity is the ratio of the CO_2 and CH_4 permeability values:

$$\alpha = \frac{P_{CO_2}}{P_{CH_4}} \tag{6.4}$$

where P_i is the permeability of component i. It should be noted that as the feed pressure is reduced to low pressures the mixed gas permselectivity will appear to be the same as the separation factor due to low differences in driving force for a 50:50 CO_2:CH_4 feed mixture.

6.2.8 Process Calculations

To compare the effects of adding ZIFs to mixed-matrix membranes, process calculations were done using the permeation data obtained for each mixed-matrix membrane sample. A single hollow fiber membrane module was modeled using a VBA macro program in Microsoft Excel that has been developed by the Koros Research

Group, assuming counter-current flow with a shell side feed.[22] The permeance of the hollow fiber module was predicted by assuming the selective skin layer of the membrane to be 500 nm in thickness, and permeance can then be predicted by:

$$Permeance = \left(\frac{Permeability}{l} \right) \tag{6.5}$$

By this prediction, the required membrane area and resulting CH_4 recovery to obtain a 98 mol% CH_4 product stream was calculated as a function of feed pressure, assuming a 50:50 CO_2:CH_4 feed stream of 1 $m^3 \cdot hr^{-1}$ volumetric flow rate. This methodology is similar to the procedures used by other researchers to compare performance of different membrane materials.[23] In addition, the product stream was varied from 90-98 mol% CH_4 to understand the relative changes in required membrane area and CH_4 recovery for each membrane sample.

6.3 Results and Discussion

6.3.1 ZIF Synthesis and Characterization

Different ZIF samples were synthesized to understand the relative changes in effective permeability and diffusivity in mixed-matrix membranes. Figure 6.1 shows the ^1H NMR spectra of each sample prepared, following degassing at 523 K. The NMR peaks have been assigned, and the calculated linker substitutions for the samples are: 100 mol% 2-MeIM in ZIF-8 sample; 20 mol% BzIM/80 mol% 2-MeIM in ZIF-7-8-(20) sample; 15 mol% 2-amBzIM/85 mol% 2-MeIM in ZIF-8-ambz-(15) sample; and 30

mol% 2-amBzIM/70 mol% 2-MeIM in ZIF-8-ambz-(30) sample. The substitutions chosen for this Chapter represent two hypotheses: (1) the organic functionality in small pore ZIFs affects the overall transport through the ZIF crystal based on differences in effective flexibility at ambient temperatures;[24] and (2) increasing the amount of substitution of bulky organic linkers in the ZIF sample, while maintaining the same ZIF crystal structure, increases the overall gas transport permselectivity for CO_2/CH_4. Figure 6.2 shows the powder XRD patterns of each sample compared with the simulated ZIF-8 structure, using Mercury. In all cases, even at the higher 2-amBzIM substitution, the cubic *I-43m* ZIF-8 structure is maintained, as demonstrated in Chapter 3; however, there appears to be some differences in peak positions and peak broadening related to framework substitutions in the ZIF crystal structure.

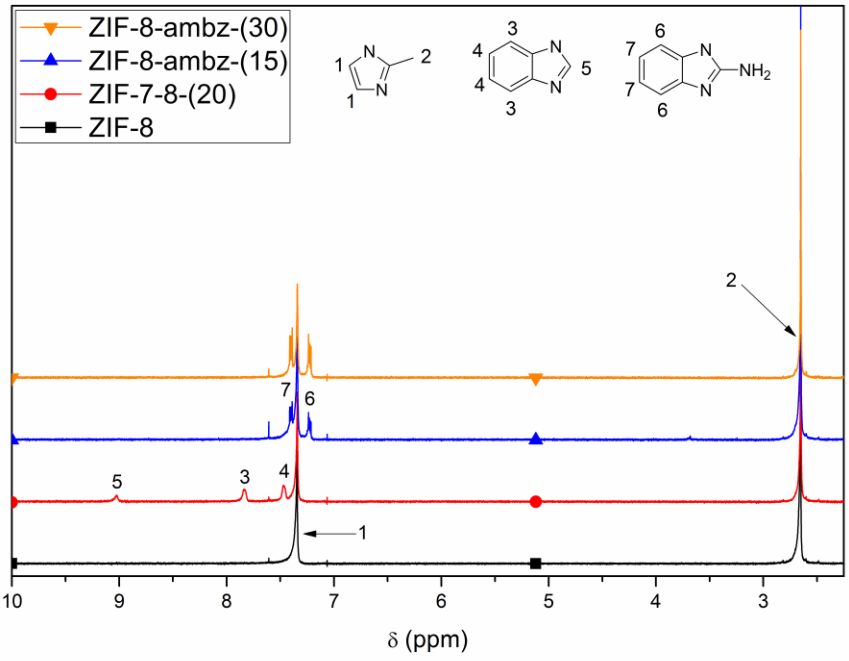

Figure 6.1. Solution ^{1}H NMR of ZIF samples prepared for mixed-matrix membrane fabrication.

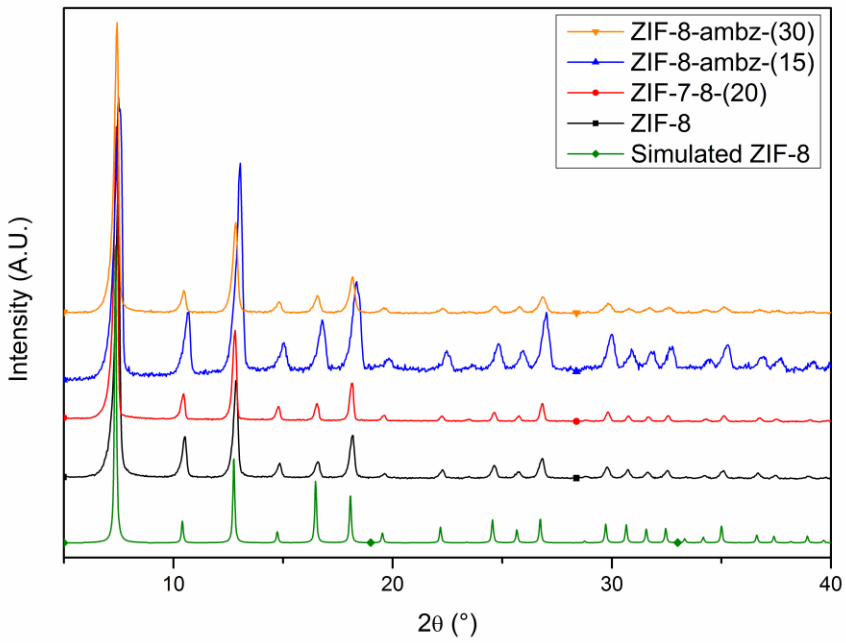

Figure 6.2. Powder XRD patterns of ZIF samples prepared for mixed-matrix membrane fabrication and compared with simulated ZIF-8 structure.

Figure 6.3 shows high-resolution, low-pressure N_2 physisorption isotherms of the ZIF samples used in mixed-matrix membrane preparation. As the ZIF-8 crystal structure changes in linker substitution, there is a decrease in both the BET surface area and t-plot micropore volume (Table 6.1). Using the methodology from Chapter 3, the H-K pore size distributions (PSD) of each sample were calculated and are shown in Figure 6.4. Interestingly, ZIF-7-8-(20) and ZIF-8-ambz-(15) have the same PSDs, making comparison of permeation data crucial to understanding the effects of organic functionality on bridging organic linkers in small pore ZIFs. Additionally, as the substitution of 2-amBzIM is increased, the PSD has a shift to smaller pore widths, indicating more difficult diffusion pathways for larger gas molecules, such as CH_4.

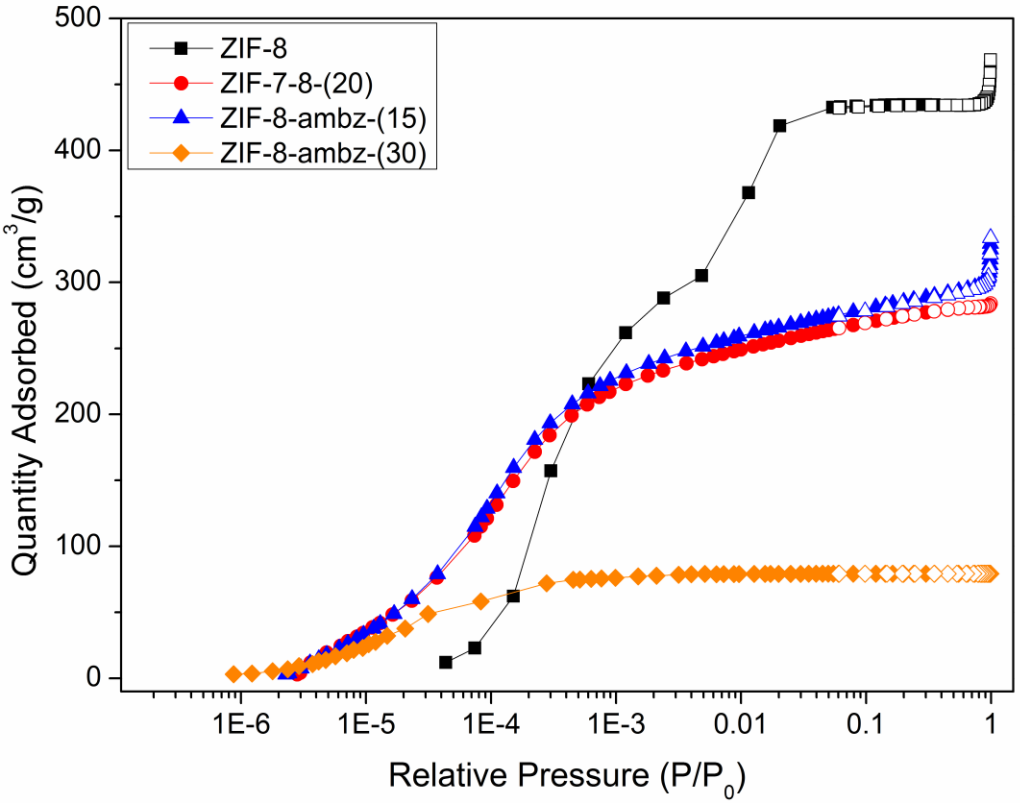

Figure. 6.3. Nitrogen physisorption of ZIF samples, showing decrease in surface area and micropore volume as ZIF composition changes.

Table 6.1. Linker substitution amounts, framework density, BET surface area and t-plot micropore volume of ZIF samples used in mixed-matrix membrane films.

Sample	Linker Substitution (mol%)	Framework Density ($g \cdot cm^{-3}$)	BET Surface Area ($m^2 \cdot g^{-1}$)	t-plot micropore volume ($cm^3 \cdot g^{-1}$)
ZIF-8	0	0.925	1860	0.671
ZIF-7-8-(20)	20	0.983	1100	0.389
ZIF-8-ambz-(15)	15	0.987	1150	0.399
ZIF-8-ambz-(30)	30	1.049	350	0.122

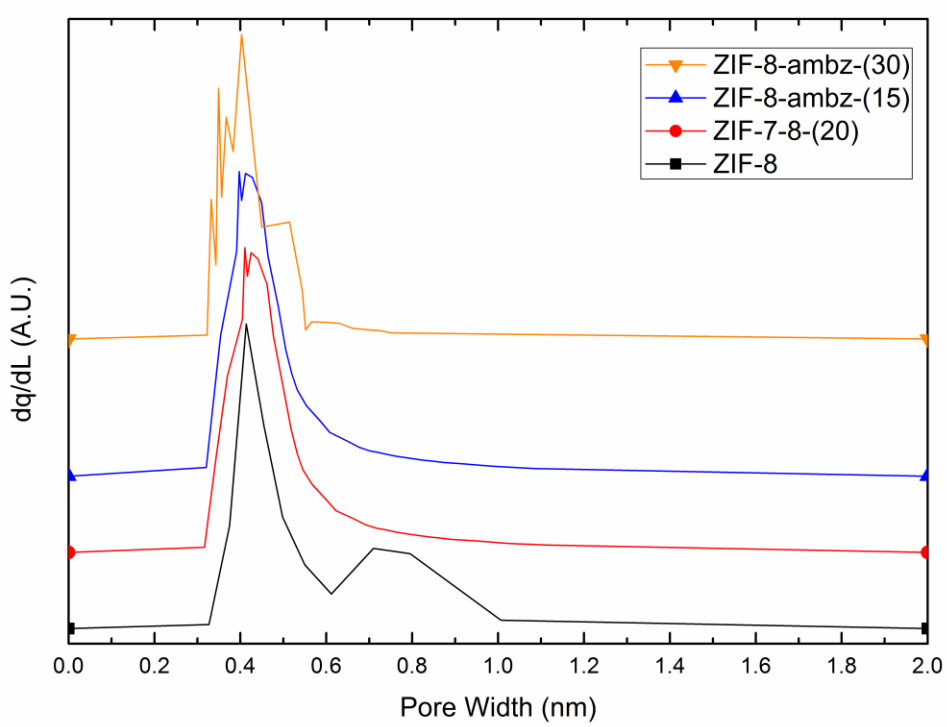

Figure 6.4. Horváth-Kawazoe pore size distributions of ZIF samples. As BzIM or 2-amBzIM is added to ZIF framework, there is a shift in PSD to a smaller pore width.

6.3.2 Mixed-Matrix Membrane Performance

SEM images of ZIF particles and MMM film cross sections shown in Figures 6.5 and 6.6 demonstrate good adhesion to the Matrimid® polymeric matrix and adequate dispersion throughout the film. It is important to note that without the priming step described previously there was inadequate dispersion and adhesion of ZIF particles throughout the polymeric matrix; therefore, it is recommended with further MMM studies utilizing ZIF materials to use a polymeric priming step to obtain well-dispersed particles. Unlike the SEM images shown in Chapter 4, the ZIF particles do not exhibit any significant changes in particle size or morphology following membrane fabrication. It is

likely that the solvent chosen for this study, $CHCl_3$, does not provide sufficient solubility of the ZIF framework to cause any nanoparticle coarsening.

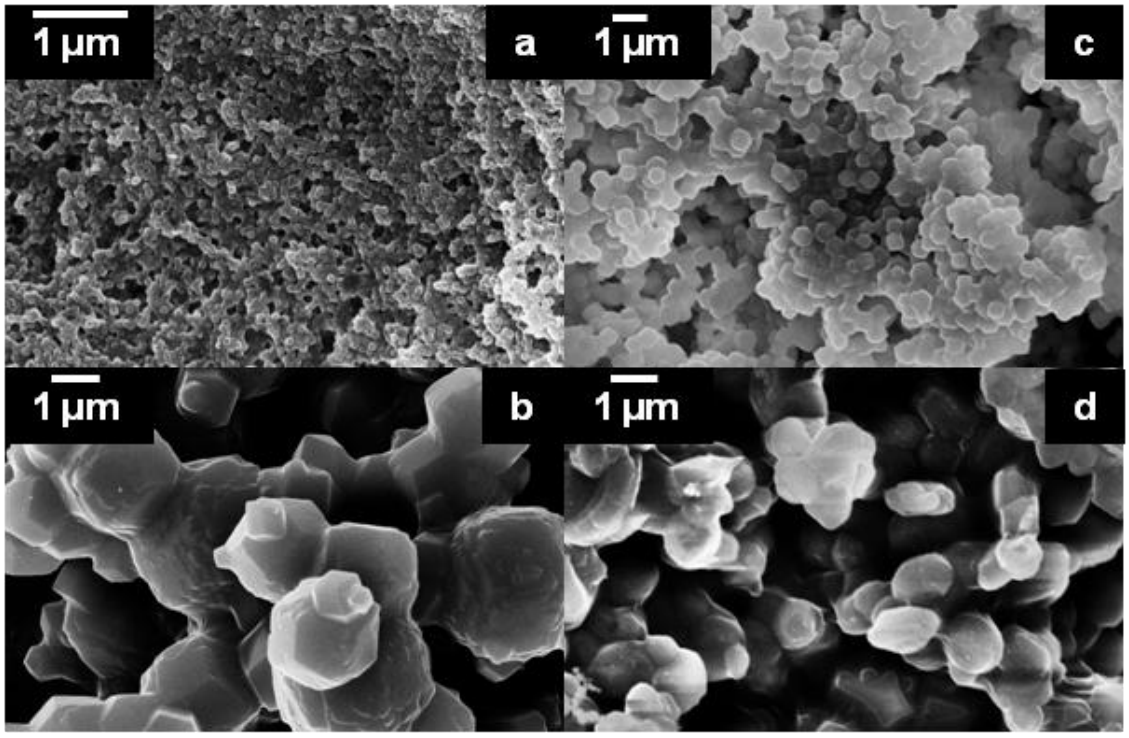

Figure 6.5. SEM images of ZIF particles prior to membrane fabrication: (**a**) ZIF-8; (**b**) ZIF-7-8-(20); (**c**) ZIF-8-ambz-(15); (**d**) ZIF-8-ambz-(30).

FTIR spectra of annealed films in Figure 6.7 show vibrations typical for Matrimid® with both symmetric and asymmetric vibrations for the imide group in the polymer backbone at approximately 1700 cm^{-1}. Unlike the FTIR spectra in Chapter 4, there is no apparent shift in the imide vibrations when ZIFs are added to the polymeric film. This may be due to the lower annealing conditions chosen for the set of films in this Chapter compared with Chapter 4. In addition, there are significant differences in the membrane fabrication steps for these films, including a different casting solvent and sonication procedure. The presence of ZIF materials is evident in the FTIR spectra due to

ν(Z-N) at 450 cm^{-1} and to ν(C-H) at 3150 cm^{-1} corresponding to the imidazolate ring. The ν(-N-H) band that appears at 3400 cm^{-1} in the ZIF-8-ambz-(x) samples is due to the presence of the primary amine functional group in the mixed-linker ZIFs.

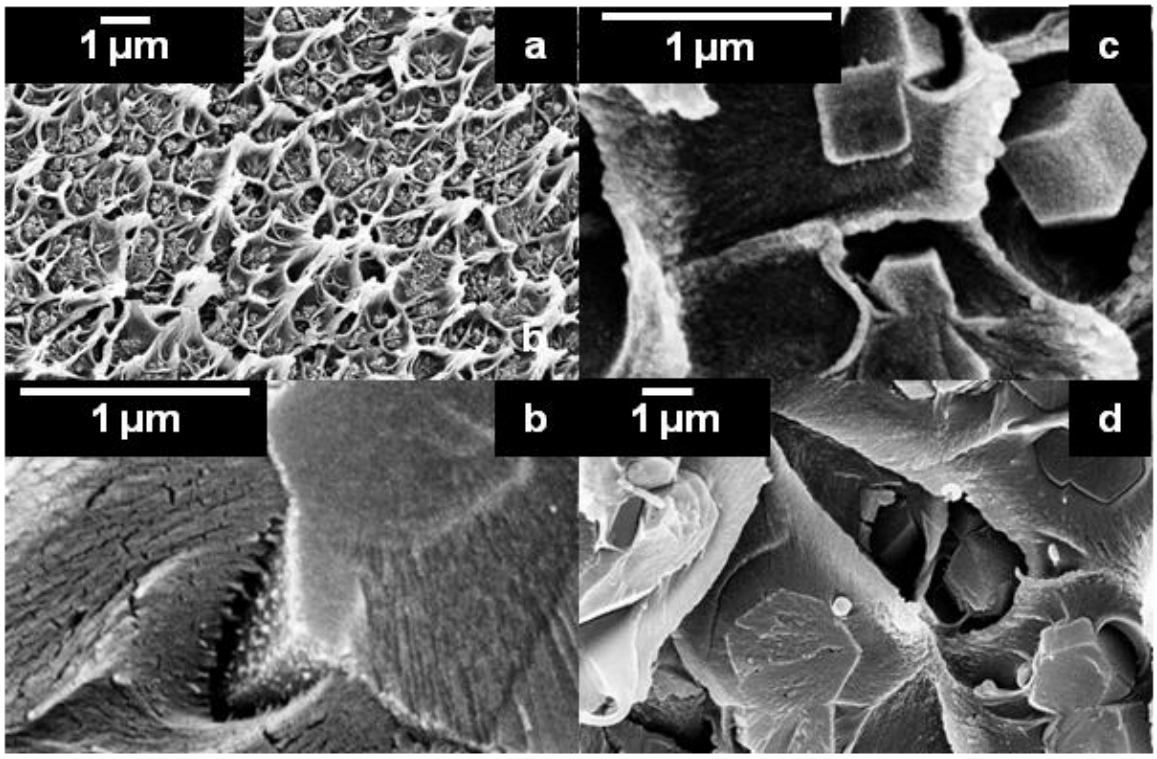

Figure 6.6. SEM images of 15 wt% ZIF/Matrimid films fabricated, using priming and solution casting techniques: (**a**) ZIF-8; (**b**) ZIF-7-8-(20); (**c**) ZIF-8-ambz-(15); (**d**) ZIF-8-ambz-(30).

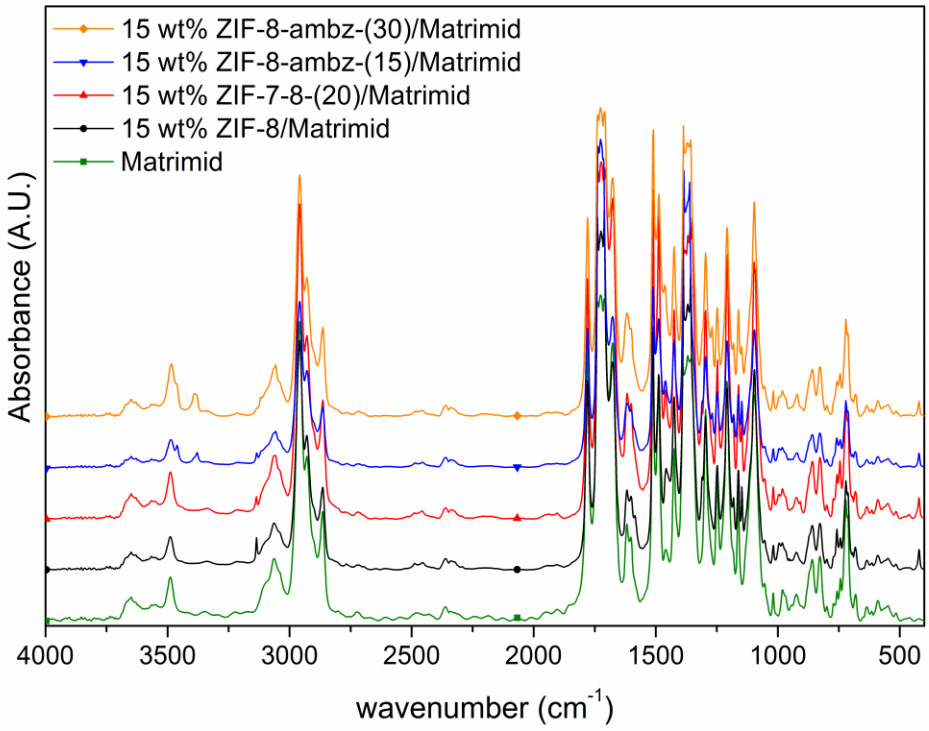

Figure 6.7. FTIR spectra of annealed ZIF/Matrimid films, showing presence of ZIF with ν(Z-N) at 450 cm^{-1} and no shift or broadening of the imide vibration.

Permeation results for pure Matrimid® and ZIF/Matrimid® membranes are shown in Figure 6.8. As expected from previous studies,[14,25] when ZIF-8 is used as the filler phase in a highly-selective, glassy polymeric matrix, without the occurrence of nanoparticle coarsening as seen in Chapter 4, there is no change or a slight decrease in the ideal selectivity and a large increase in the effective permeability of the membrane. These permeation characteristics for ZIF-8 are due to low selective transport of CO_2 and CH_4 in the ZIF crystal, resulting in a polymer-filler mismatch in terms of permeability.[26] To compare the effect of functional groups in small pore ZIFs, ZIF-7-8-(20) and ZIF-8-ambz-(15), which have similar micropore volume and PSD, are used with the same weight percentage and fabrication steps. As Figure 6.8 shows, there is a slight increase in ideal permselectivity when ZIF-7-8-(20) is used as the filler phase and a decrease in the

effective CO_2 permeability, compared with the ZIF-8/Matrimid® films; however, when ZIF-8-ambz-(15) is used as the filler phase, there is a further increase in CO_2/CH_4 ideal permselectivity compared to the pure polymer, the ZIF-8/Matrimid® membrane, and the ZIF-7-8-(20)/Matrimid® membrane samples. Additionally, there is a significant reduction in CO_2 permeability compared to the ZIF-8/Matrimid® membrane. Because the ZIF-8 unit cell has eight open pore windows and the amount of substitution for 2-amBzIM in the sample is roughly more than 1/7 of total linkers in the framework, there may be substantial intermolecular interaction between the 2-amBzIM linkers, possibly *via* hydrogen bonding, that could change the effective flexibility of the ZIF pore window in comparison to ZIF-8 or ZIF-7-8-(20), thus altering the diffusion pathway through the ZIF crystal.[24,27] Other mixed-matrix membrane studies using both an amine-functionalized and unfunctionalized MOF fillers have shown substantial differences in CO_2 and CH_4 permeation characteristics between membrane samples, likely due to structural changes in the MOF filler and not due to the pendant amine enhancing separation performance based on affinity for CO_2.[12,21]

As the effective substitution of 2-amBzIM is further increased, there is a concurrent increase in ideal permselectivity with a slight decrease in the effective CO_2 permeability compared to ZIF-8-ambz-(15)/Matrimid®. It is likely that at the studied linker loadings there is not significant hindrance of CO_2 diffusion as the substitution of 2-amBzIM increases; however, when the mixed-linker ZIF/Matrimid® membranes are compared, there are apparent differences in the CO_2 permeability when BzIM or 2-amBzIM is used in the mixed-linker ZIF structure. Regardless, the permeation results

suggest that the mixed-linker ZIF approach does provide enhancement in CO_2/CH_4 selectivity for a ZIF-8-type structure, and that this approach may be useful for tuning not just the CO_2/CH_4 gas separation properties, but other molecular separations, in different ZIF materials.[26,28,29]

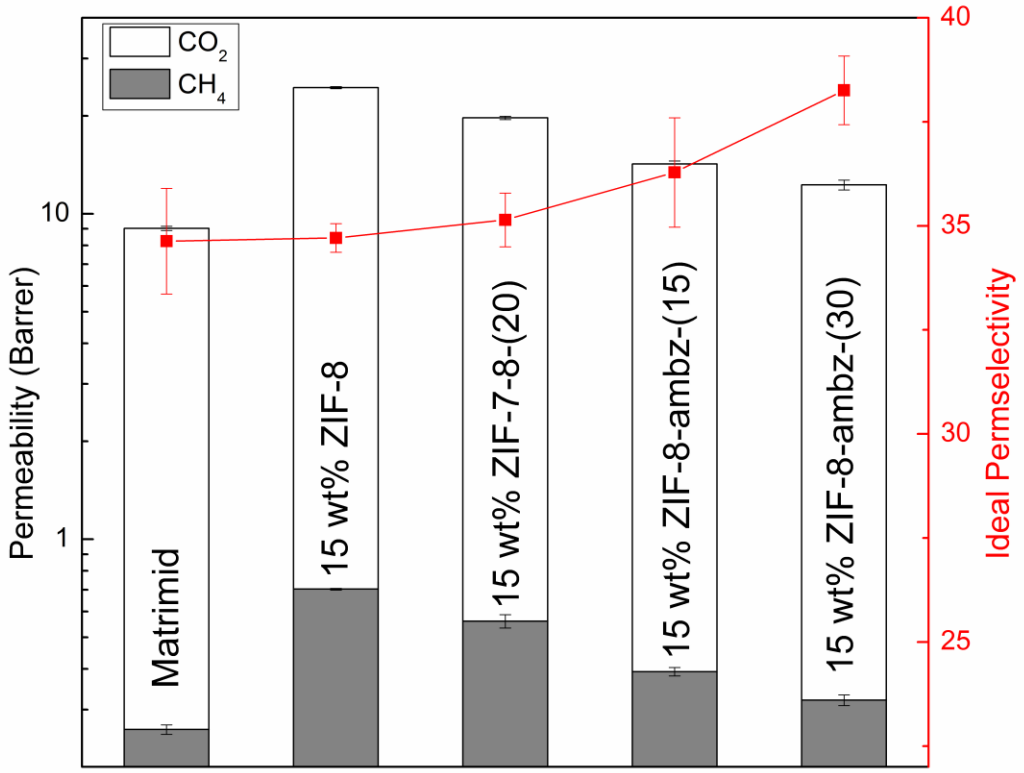

Figure 6.8. Single gas permeation results of ZIF/Matrimid membranes at 345 kPa and 308 K. There is an increase in ideal selectivity when there is a substitution in the ZIF-8 framework for a bulkier organic linker.

Diffusion coefficients of each film were calculated using the time lag method and are shown in Table 6.2. When the diffusion coefficients are compared with the permeability values obtained for each membrane, it is apparent that the ideal permselectivity increase observed for the mixed-linker ZIFs is related to an increase in

diffusion selectivity, and the decrease in CO_2 permeability is linked to a decrease in diffusivity. This implies that substitution of 2-MeIM for a bulkier organic linker, such as BzIM or 2-amBzIM, enhances the effective transport selectivity for CO_2/CH_4. This may also enhance other gas pair separations for these mixed-linker ZIFs; for instance, ZIF-8 has been shown to have low C_2H_4/C_2H_6 kinetic selectivity,[30,31] but careful substitution with a bulky linker may improve the diffusion selectivity without severe hindrance of diffusion for C_2H_4. It should be noted that at the highest linker substitution in the ZIF-8 framework, ZIF-8-ambz-(30), the diffusion coefficient is close to the Matrimid® diffusion coefficient. If there is any further increase in substitution, there may be a substantial drop in diffusion for CO_2, resulting in a "plugged-sieve" type behavior for mixed-matrix membranes.

Table 6.2. Diffusion coefficients of Matrimid® and ZIF/Matrimid® films, determined by the time lag method. Error of each sample is shown in parentheses.

Sample	CO_2 Diffusivity (10^{-9} $cm^2 \cdot sec^{-1}$)	CH_4 Diffusivity (10^{-9} $cm^2 \cdot sec^{-1}$)	Diffusion Selectivity
Matrimid®	8 (2)	0.8 (0.2)	11 (1)
15 wt% ZIF-8/Matrimid®	25 (2)	2.3 (0.2)	10 (1)
15 wt% ZIF-7-8-(20)/Matrimid®	18 (2)	1.5 (0.1)	11 (1)
15 wt% ZIF-8-ambz-(15)/Matrimid®	10.6 (0.7)	0.86 (0.04)	12 (1)
15 wt% ZIF-8-ambz-(30)/Matrimid®	8.8 (0.5)	0.67 (0.05)	13 (1)

Mixed gas permeation isotherms can reveal behavior of membranes under realistic feed conditions for natural gas purification.[32] Often, single gas permeation can be misleading when determining permselectivity due to competitive sorption and diffusion

affecting the overall separation performance in a pure polymer matrix as well as CO_2 plasticization decreasing the permselectivity at high operating pressures.[33,34] Separation factor values of membrane samples determined from mixed gas permeation experiments are shown in Figure 6.9. As previous studies have shown,[23] the ideal permselectivity of pure Matrimid® is often lower than the mixed gas separation factor and permselectivity, which is evident when comparing Figures 6.8 and 6.9 for pure Matrimid®. The composite membranes show interesting behavior as the partial pressure of CO_2 is increased in the feed. The separation factor is close to or even less than pure Matrimid® below the expected plasticization pressure; however, above the plasticization pressure, the ZIF-8-ambz-(30) composite membrane shows higher separation factor than pure Matrimid®. Additionally, the other composite membranes show a constant separation factor as the partial pressure of CO_2 is increased by 700 kPa above the plasticization pressure. This indicates that the presence of mixed-linker ZIFs in the polymeric matrix suppresses the plasticization effect that is typically expected in glassy polymeric membranes.[35]

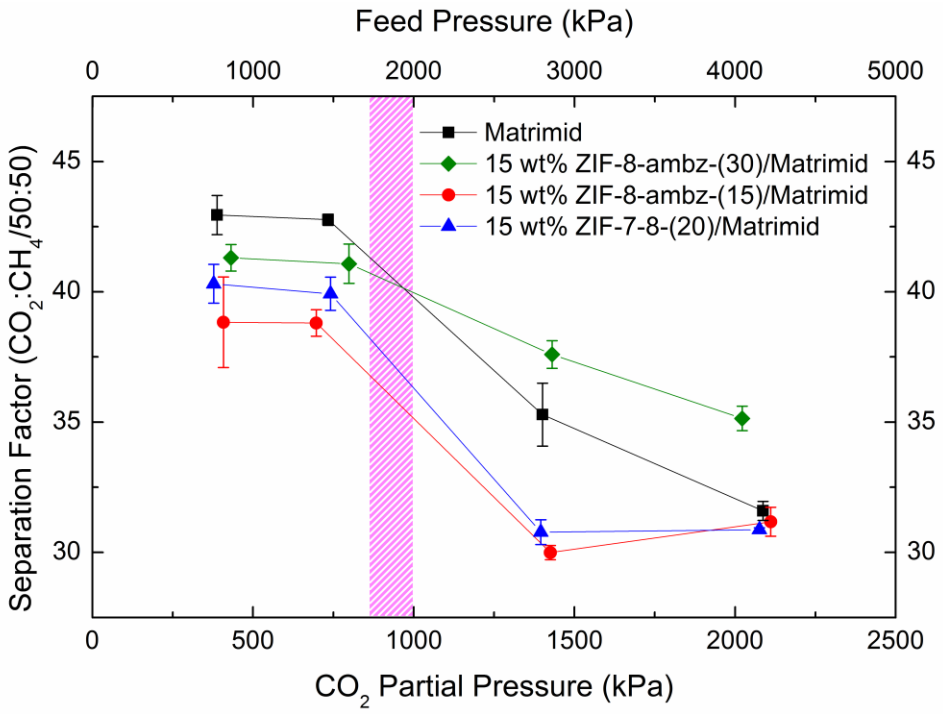

Figure 6.9. Separation factor of mixed-matrix membranes with increasing feed and CO_2 partial pressure. Error bars represent variance in measured GC injections. Shaded area represents typical plasticization pressure for Matrimid®.

The CO_2 and CH_4 permeability values, shown in Figure 6.10, reveal that at the highest pressure tested the CH_4 permeability is stabilized in the composite membranes while the CO_2 permeability continues to decrease, similar to the behavior in pure Matrimid®. The near-constant CO_2 permeability at high CO_2 partial pressure is a result of saturated sorption sites in the surrounding polymeric matrix as the feed pressure increases.[36,37] The stabilized CH_4 permeability suggests that the observed improvement in separation factor found in the composite membranes is caused by suppression of plasticization when the ZIF is used as a filler in Matrimid®. As the surrounding polymeric matrix continues to swell due to an increase in the partial pressure of CO_2, resulting in increased CH_4 permeability around the ZIF as seen in pure Matrimid®, the ZIF crystals

may exhibit some hindrance in CH_4 transport with increasing pressure, giving the apparent enhancement in plasticization resistance. Chmelik et al.[38] have explored the transport diffusion properties of ZIF-8 in pure gases and mixtures of CO_2 and CH_4, measured by IR microscopy. The authors found that without the presence of CO_2 the diffusion coefficient of CH_4 increased considerably with loading (analogous to increasing feed pressure). When mixtures of CO_2 and CH_4 in different concentrations is present in the ZIF-8 crystal, the CH_4 diffusivity did not exhibit this same increase with adsorbate loading and showed an apparent hindrance in diffusion due to the presence of CO_2. Molecular simulations revealed that CO_2 adsorption sites occur near the pore window of ZIF-8, and this adsorption behavior slows the transport of CH_4 in gas mixtures as the adsorbate loading increases. Hindering diffusion effects have also been shown with other nanoporous materials, such as zeolite DDR, using molecular simulations.[39] It is likely that use of bulky organic linkers in the ZIF framework, while maintaining a ZIF-8-like structure, results in further hindrance of CH_4 diffusion as the loading of CO_2 inside the ZIF crystal increases with feed pressure. This increased hindrance would result in apparent CH_4 permeability and permselectivity stabilization (Figure 6.11) with increasing partial pressure of CO_2 if the mixed-linker ZIFs have higher permselectivity than the parent ZIF-8 material.

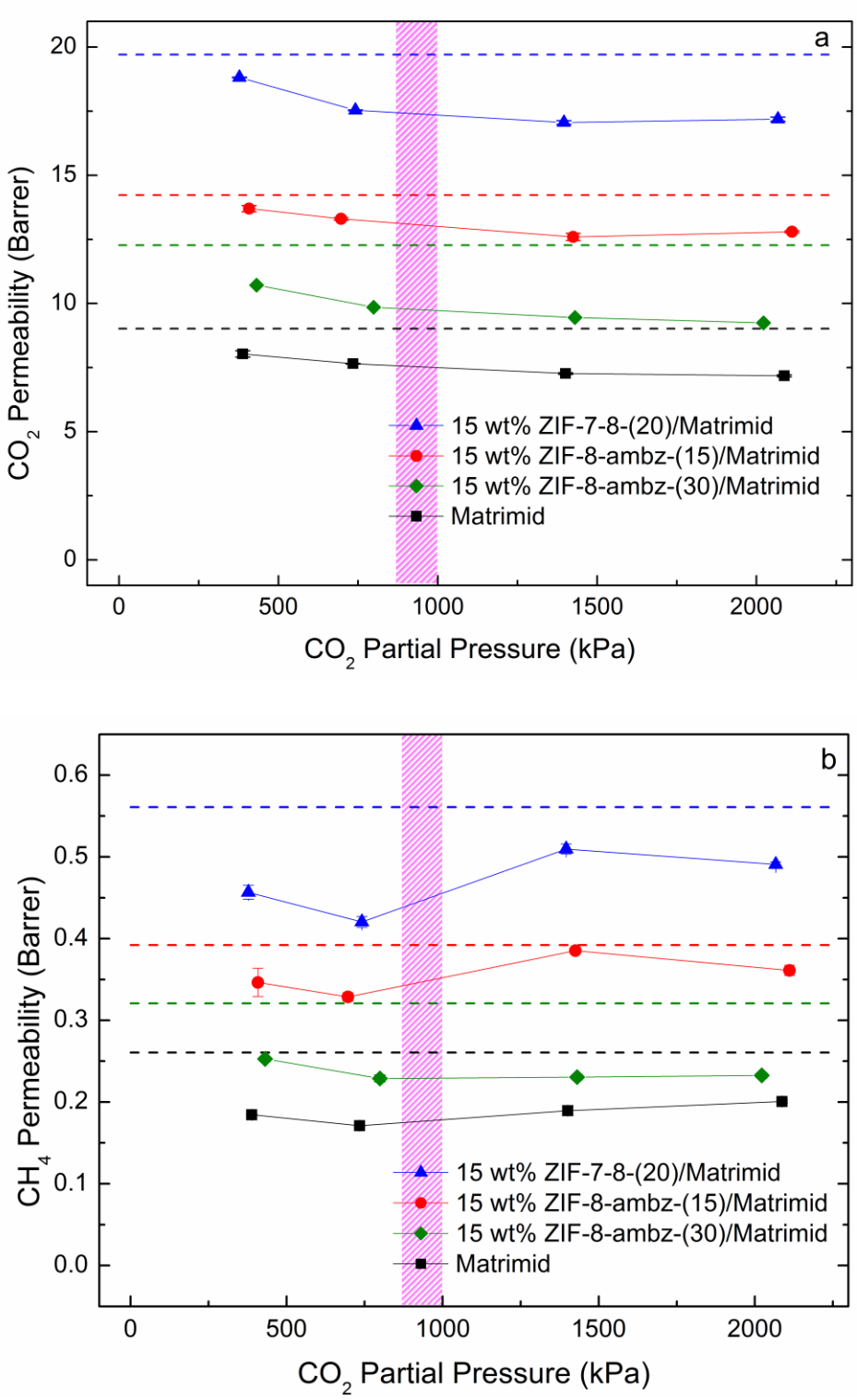

Figure 6.10. Permeability of CO_2 (a) and CH_4 (b) calculated from mixed-gas permeation, normalized by fugacity driving force. Dashed lines represent permeability values from pure gas measurements. Shaded area represents typical plasticization pressure for Matrimid®.

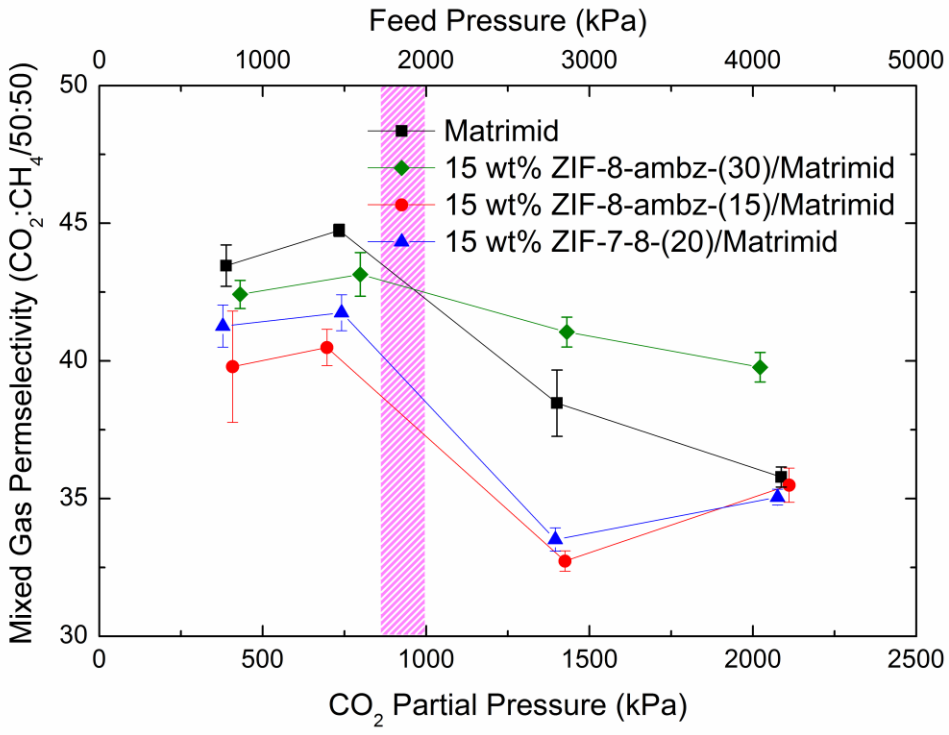

Figure 6.11. Mixed gas permselectivity of membrane samples with increasing feed and CO_2 partial pressure. Error bars represent variance in GC injection measurements. Shaded area represents typical plasticization pressure for Matrimid®.

These mixed gas results shows that the mixed-linker ZIFs have mixed gas permselectivity comparable to Matrimid® at lower feed pressures, but as the CO_2 partial pressure increases, the mixed gas permselectivity inside the ZIF crystal shows improvement and even suppresses transport of CH_4 through the ZIF crystal, resulting in an effective stabilization of CH_4 permeability in the composite membranes. Increasing either the weight loading of ZIF in the polymer or increasing the molar ratio of the substituting bulky organic linkers in the ZIF framework may further improve the permselectivity and separation performance of the composite membrane; however, as

diffusivity measurements showed, there may exist an "upper limit" in the linker substitution to maintain highly permeable ZIF materials. More importantly, these results are the first to examine permeation behavior of dense-film mixed-matrix membranes above the CO_2 plasticization pressure of the surrounding polymeric matrix and at CO_2 partial pressures that are relevant for industrial gas separations.[32] Although there is increased polymeric chain mobility associated with CO_2-induced swelling and plasticization,[35] there is no degradation of the polymer/ZIF interface that results in large changes in the CH_4 permeability or separation factor for CO_2/CH_4.

6.3.3 Hollow Fiber Membrane Process Simulations

Hollow fiber membrane simulations are useful for comparing different membranes without determining proper hollow fiber spinning and fabrication techniques, and these simulations can help screen different filler materials without the need of testing each filler sample.[40,41] Furthermore, it has already been shown that the membrane properties of mixed-matrix dense film membranes containing ZIF-8 are transferrable to hollow fiber membranes with suitable spinning and fabrication.[42] Table 6.3 shows the permeance values assumed for each membrane studied, calculated by assuming a 500 nm selective skin layer and using the mixed gas permeability values of CO_2 and CH_4 calculated from mixed gas testing. Because Matrimid® shows a decrease in selectivity as the CO_2 feed pressure increases in mixed gas streams, it is important to consider anticipated separation performance under conditions more closely related to industrially relevant separations.[32] The dimensions of the hollow fiber module and the conditions

assumed for the fiber module are shown in Table 6.4 and represent typical commercial hollow fiber module properties.[32]

Table 6.3. Hollow fiber membrane permeance values assumed for process calculations, based on a 500 nm selective skin layer.

Sample	CO_2 Permeance (GPU)				CH_4 Permeance (GPU)			
	690 kPa	1380 kPa	2760 kPa	4140 kPa	690 kPa	1380 kPa	2760 kPa	4140 kPa
Matrimid	16.0	15.3	14.5	14.4	0.37	0.34	0.38	0.40
ZIF-7-8-(20)/Matrimid	37.6	35.1	34.1	34.4	0.91	0.84	1.02	0.98
ZIF-8-ambz-(15)/Matrimid	27.4	26.6	25.2	25.6	0.69	0.66	0.77	0.72
ZIF-8-ambz-(30)/Matrimid	21.4	19.7	18.9	18.5	0.51	0.46	0.46	0.47

Table 6.4. Hollow fiber membrane module dimensions and parameters.

Hollow Fiber Module Properties	
Feed Flow Rate (m^3(STP)·hr^{-1})	1.00
Temperature (K)	308
Fiber Outer Diameter (μm)	300
Fiber Inner Diameter (μm)	150
Active Fiber Length (m)	0.8
Permeate Pressure (kPa)	103
Feed Location	Shell Side
CO_2:CH_4 Feed Composition	50:50 mol%

The first case considered for hollow fiber membrane process simulations was done under the requirement that 98 mol% CH_4 and 2 mol% CO_2 are the product composition based on the feed flow rate of 1 $m^3 \cdot hr^{-1}$. The flow rate chosen for these case

studies represents a base line that can then allow the membrane area to be scaled linearly with increasing feed flow rate.[23] The required membrane area to reach this composition and the total CH_4 recovery are shown in Figure 6.12. Because the separation factor and permselectivity does not change greatly when ZIF materials are added to the polymeric matrix, the major difference in hollow fiber membrane performance between pure Matrimid® and the composite membranes is the predicted area needed to reach the product composition; therefore, if the cost of ZIF materials is the same or less than the polymeric matrix, the inclusion of ZIFs in the membrane module provides a significant cost benefit by reducing the overall area required for CO_2/CH_4 separations. Figure 6.12a also shows a significant reduction in membrane area with increasing feed pressure due to higher effective flux through the hollow fiber module.[23] The approximate membrane area reduction with adding ZIFs to the polymeric matrix is at least 25% and varies based on the feed pressure and the mixed-linker ZIF used in the composite membrane. Because membrane area typically scales linearly with feed flow rate, a 25% reduction of membrane area can be very cost-beneficial as the desired feed flow rate increases.

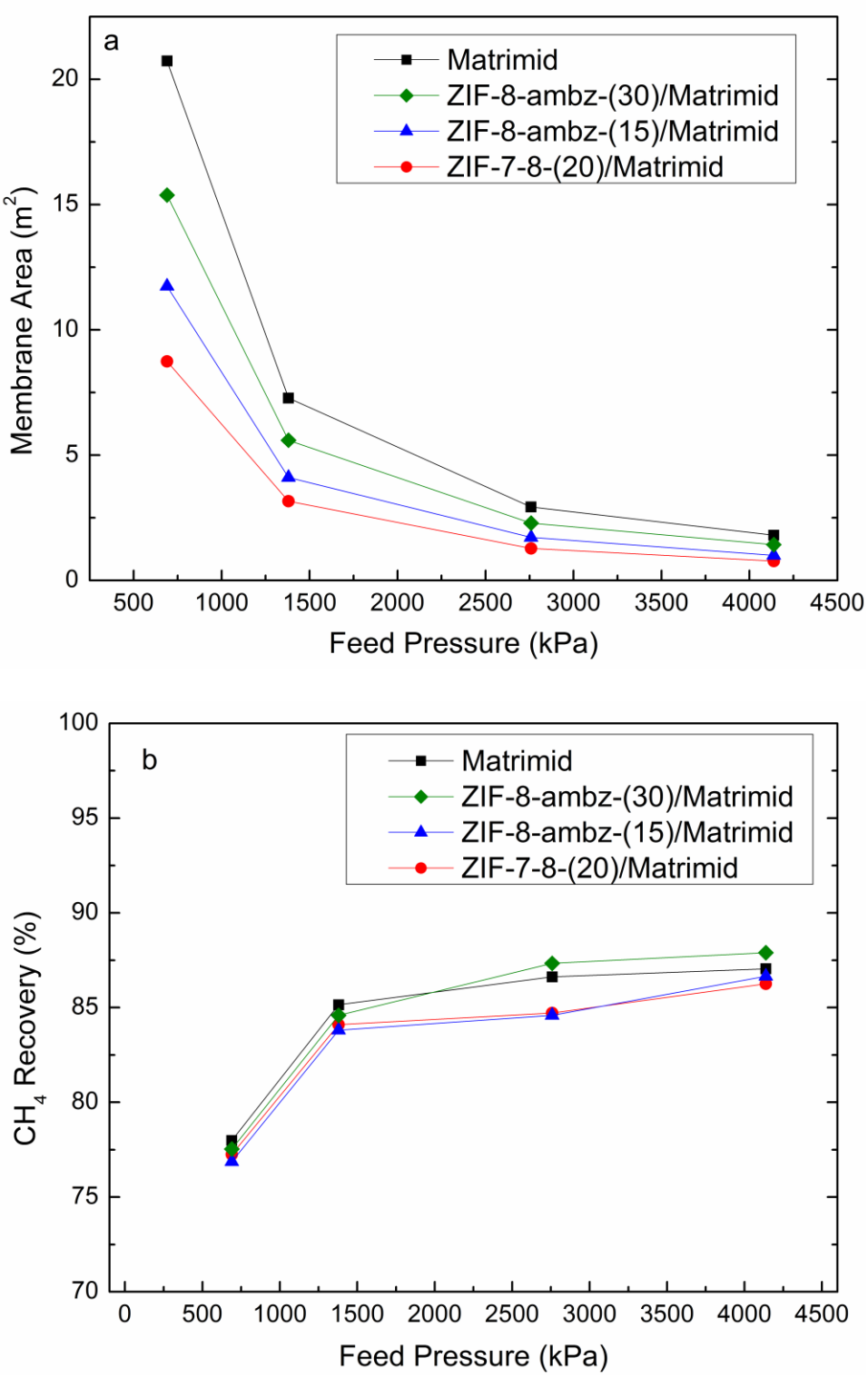

Figure 6.12. Required membrane area (**a**) and CH_4 recovery (**b**) to reach target product composition of 98 mol% CH_4.

The second case considered for process simulations is varying the required product composition with a constant feed pressure of 4200 kPa. The membrane area and CH_4 recovery are shown in Figure 6.13. Again, because the separation performance of all the membranes examined in this Chapter does not change substantially with inclusion of ZIF in the polymer, the CH_4 recovery does not vary greatly between membranes. The benefit of ZIF materials is manifested in the reduction of required membrane area to reach the target CH_4 product composition. To avoid a great loss in CH_4 recovery, it may be beneficial to use these membranes for a "rough cut" of the CO_2/CH_4 feed stream that can then be further purified by other separation techniques. For instance, if a product composition of 8 mol% CO_2 is desired for transport in pipelines to a gas processing facility,[32] these simulations predict CH_4 recovery of approximately 93% can be achieved with one module. Additionally, it may be possible to increase the overall CH_4 recovery with these mixed-matrix membranes by utilizing higher weight loading of ZIF in the polymer or assuming a smaller selective skin layer can be achieved.[22,43] As these simulations and mixed gas experiments have shown, inclusion of mixed-linker ZIFs can reduce the required membrane area to perform natural gas purification. It may be possible to use mixed-linker syntheses on smaller pore ZIF materials (*e.g.*, ZIF-11) to further enhance the observed separation performance in ZIF-containing mixed-matrix membranes without significantly altering the diffusion of CO_2 inside the ZIF crystal.

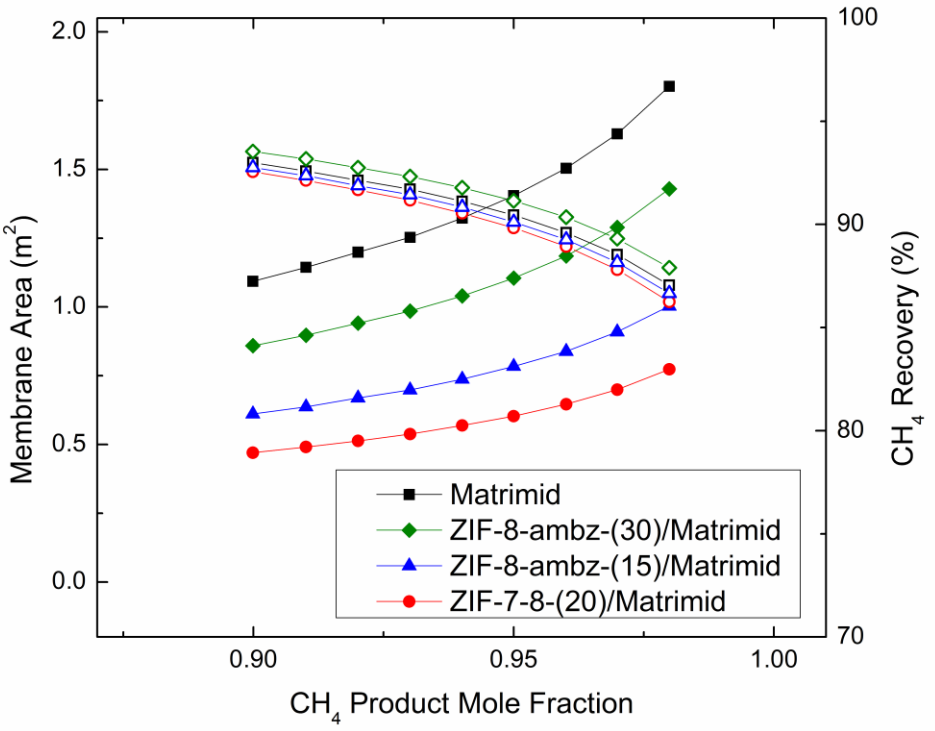

Figure 6.13. Required membrane area and CH_4 recovery as a function of target CH_4 composition in the product stream. Closed symbols: membrane area; open symbols: CH_4 recovery.

6.4 Conclusions

The work in this Chapter has shown that by controlling the organic linker composition in ZIF materials the apparent diffusion and permeability of gases can be controlled in mixed-matrix membranes. This ultimately results in improved separation properties, as shown by single and mixed gas CO_2/CH_4 permeation, for mixed-matrix membranes containing mixed-linker ZIFs. High pressure mixed gas permeation has shown that ZIF materials have unusual permeation behavior that results in effective stabilization of permselectivity with increasing pressure by suppressing the transport of CH_4 in the composite membrane. Hollow fiber membrane process simulations revealed that the largest benefit of including ZIF materials in mixed-matrix membranes is

reduction of membrane area for a target gas separation and feed conditions. These simulations are promising for mixed-linker ZIFs, and now hollow fiber membranes containing these materials are the next step in investigating the effective separation properties of mixed-linker ZIF materials.

6.5 References

(1) Zornoza, B.; Tellez, C.; Coronas, J.; Gascon, J.; Kapteijn, F. *Micropor. Mesopor. Mater.* **2013**, *166*, 67–78.

(2) Tanh Jeazet, H. B.; Staudt, C.; Janiak, C. *Dalton Trans.* **2012**, *41*, 14003–14027.

(3) Zhang, Y.; Sunarso, J.; Liu, S.; Wang, R. *Int. J. Greenh. Gas Con.* **2013**, *12*, 84–107.

(4) Jang, K.-S.; Kim, H.-J.; Johnson, J. R.; Kim, W.; Koros, W. J.; Jones, C. W.; Nair, S. *Chem. Mater.* **2011**, *23*, 3025–3028.

(5) Brown, A. J.; Johnson, J. R.; Lydon, M. E.; Koros, W. J.; Jones, C. W.; Nair, S. *Angew. Chem. Int. Ed.* **2012**, *51*, 10615–10618.

(6) Venna, S. R.; Carreon, M. A. *J. Am. Chem. Soc.* **2010**, *132*, 76–8.

(7) Bux, H.; Liang, F.; Li, Y.; Cravillon, J.; Wiebcke, M.; Caro, J. *J. Am. Chem. Soc.* **2009**, *131*, 16000–16001.

(8) Zornoza, B.; Martinez-Joaristi, A.; Serra-Crespo, P.; Tellez, C.; Coronas, J.; Gascon, J.; Kapteijn, F. *Chem. Commun.* **2011**, *47*, 9522–9524.

(9) Bae, T.-H.; Lee, J. S.; Qiu, W.; Koros, W. J.; Jones, C. W.; Nair, S. *Angew. Chem. Int. Ed.* **2010**, *122*, 9863–9866.

(10) Adams, R.; Carson, C.; Ward, J.; Tannenbaum, R.; Koros, W. *Micropor. Mesopor. Mater.* **2010**, *131*, 13–20.

(11) Basu, S.; Cano-Odena, A.; Vankelecom, I. F. J. *Sep. Purif. Technol.* **2011**, *81*, 31–40.

(12) Nik, O. G.; Chen, X. Y.; Kaliaguine, S. *J. Membr. Sci.* **2012**, *413-414*, 48–61.

(13) Car, A.; Stropnik, C.; Peinemann, K.-V. *Desalination* **2006**, *200*, 424–426.

(14) Zornoza, B.; Seoane, B.; Zamaro, J. M.; Téllez, C.; Coronas, J. *ChemPhysChem* **2011**, *12*, 2781–2785.

(15) Hu, J.; Cai, H.; Ren, H.; Wei, Y.; Xu, Z.; Liu, H.; Hu, Y. *Ind. Eng. Chem. Res.* **2010**, *49*, 12605–12612.

(16) Sholl, D. S. *Nature Chem.* **2011**, *3*, 429–30.

(17) Chung, T.-S.; Jiang, L. Y.; Li, Y.; Kulprathipanja, S. *Prog. Polym. Sci.* **2007**, *32*, 483–507.

(18) Vu, D. Q.; Koros, W. J.; Miller, S. J. *J. Membr. Sci.* **2003**, *211*, 311–334.

(19) O'Brien, K.; Koros, W.; Barbari, T.; Sanders, E. *J. Membr. Sci.* **1986**, *29*, 229–238.

(20) Paul, D. R.; Kemp, D. R. *J. Polym. Sci. Polym. Symp.* **1973**, *41*, 79–93.

(21) Chen, X. Y.; Vinh-Thang, H.; Rodrigue, D.; Kaliaguine, S. *Ind. Eng. Chem. Res.* **2012**, *51*, 6895–6906.

(22) Coker, D.T.; Freeman, B.D.; Fleming, G.K. *AIChE J.* **1998**, *44*, 1289-1302.

(23) Bos, A.; Pünt, I. G. M.; Wessling, M.; Strathmann, H. *Sep. Purif. Technol.* **1998**, *14*, 27–39.

(24) Haldoupis, E.; Watanabe, T.; Nair, S.; Sholl, D. S. *ChemPhysChem* **2012**, *13*, 3449–3452.

(25) Song, Q.; Nataraj, S. K.; Roussenova, M. V.; Tan, J. C.; Hughes, D. J.; Li, W.; Bourgoin, P.; Alam, M. A.; Cheetham, A. K.; Al-Muhtaseb, S. A.; Sivaniah, E. *Energy Environ. Sci.* **2012**, *5*, 8359–8369.

(26) Zhang, C.; Lively, R. P.; Zhang, K.; Johnson, J. R.; Karvan, O.; Koros, W. J. *J. Phys. Chem. Lett.* **2012**, *3*, 2130–2134.

(27) Stavitski, E.; Pidko, E. A.; Couck, S.; Remy, T.; Hensen, E. J. M.; Weckhuysen, B. M.; Denayer, J.; Gascon, J.; Kapteijn, F. *Langmuir* **2011**, *27*, 3970–3976.

(28) Zhang, C.; Dai, Y.; Johnson, J. R.; Karvan, O.; Koros, W. J. *J. Membr. Sci.* **2011**, *389*, 34–42.

(29) Yilmaz, G.; Keskin, S. *Ind. Eng. Chem. Res.* **2012**, *51*, 14218–14228.

(30) Bux, H.; Chmelik, C.; Van Baten, J. M.; Krishna, R.; Caro, J. *Adv. Mater.* **2010**, *22*, 4741–4743.

(31) Bux, H.; Chmelik, C.; Krishna, R.; Caro, J. *J. Membr. Sci.* **2010**, *369*, 284–289.

(32) Baker, R. W.; Lokhandwala, K. *Ind. Eng. Chem. Res.* **2008**, *47*, 2109–2121.

(33) Donohue, M. D.; Minhas, B. S.; Lee, S. Y. *J. Membr. Sci.* **1989**, *42*, 197–214.

(34) Staudt-Bickel, C.; Koros, W. J. *J. Membr. Sci.* **1999**, *155*, 145–154.

(35) Ismail, A. F.; Lorna, W. *Sep. Purif. Technol.* **2002**, *27*, 173–194.

(36) Koros, W. J.; Chern, R. T.; Stannett, V.; Hopfenberg, H. B. *J. Polym. Sci. Polym. Phys. Ed.* **1981**, *19*, 1513–1530.

(37) Kamaruddin, H. D.; Koros, W. J. *J. Membr. Sci.* **1997**, *135*, 147–159.

(38) Chmelik, C.; Van Baten, J.; Krishna, R. *J. Membr. Sci.* **2012**, *397-398*, 87–91.

(39) Jee, S. E.; Sholl, D. S. *J. Am. Chem. Soc.* **2009**, *131*, 7896–904.

(40) Chern, R. T.; Koros, W. J.; Fedkiw, P. S. *Ind. Eng. Chem. Process Des. Dev.* **1985**, *24*, 1015–1022.

(41) Thundyil, M. J.; Koros, W. J. *J. Membr. Sci.* **1997**, *125*, 275–291.

(42) Dai, Y.; Johnson, J. R.; Karvan, O.; Sholl, D. S.; Koros, W. J. *J. Membr. Sci.* **2012**, *401-402*, 76–82.

(43) Baker, R. W. *Membrane Technology and Applications*; McGraw-Hill: New York, 2000.

CHAPTER 7

Summary and Outlook

7.1 Summary

The focus of this thesis has been to examine the possible synthesis and fabrication methods necessary to engineer materials useful for acid gas separations by either adsorption or membrane separations. The main theme has been the synthesis of zeolitic imidazolate frameworks with controlled organic linker compositions that alter the adsorption and diffusion properties. These mixed-linker ZIFs showed promising results for improving the CO_2/CH_4 gas separation properties in a ZIF-8-like structure, but may also extend to other gas pairs such as olefin/paraffin separations. Fabrication of mixed-matrix membranes has shown a number of interesting results. In particular, depending on the solvent and dispersion techniques, there are significant differences in the effective permeability properties of the composite membrane. Mixed-linker ZIFs used to fabricate mixed-matrix membranes demonstrated an improvement in the overall separation properties compared to the parent ZIF material, ZIF-8, and permeation experiments demonstrated this improvement to be linked to enhancing the diffusion selectivity by substitution in the ZIF framework with a bulky organic linker.

7.1.1 Synthesis and Characterization of Mixed-Linker Zeolitic Imidazolate Frameworks

In Chapter 3, a synthesis method was presented that allowed the control of organic linkers in a ZIF material without severely altering the apparent crystal structure.

This synthesis method, termed as non-solvent induced crystallization, has shown to be applicable to a number of different crystal structures and organic linkers with examples of synthesizing materials containing: (1) 2-methylimidazole; (2) carboxaldehyde-2-imidazole; (3) benzimidazole; and (4) 2-aminobenzimidazole. These results were promising that this may be a general synthesis technique which could be applied to different ZIF crystal structures, or even different MOF structures.

Nitrogen physisorption was used as the primary characterization method for analyzing these mixed-linker ZIF materials. For ZIFs containing 2-methylimidazole and carboxaldehyde-2-imidazole, the N_2 physisorption isotherms showed a great deal of control over where the gate-opening pressure in the ZIF structure occurred along the isotherm. When bulkier organic linkers were used in the mixed-linker ZIF synthesis, such as benzimidazole and 2-aminobenzimidazole, the isotherms revealed that there was no evidence of gate-opening as the loading of the bulky linkers increased in the ZIF material while maintaining the ZIF-8 crystal structure. In addition to analyzing the isotherms, a methodology for using Horváth-Kawazoe equations in these mixed-linker ZIFs was proposed, and the subsequent pore size distributions of the bulky linker-substituted ZIF materials showed the appearance of a secondary pore size that was smaller than the primary pore size distribution. Due to the current understanding of how flexibility affects transport in these ZIF materials, it is likely that the bulky linkers preventing the gate-opening from occurring will affect the molecular diffusion in the ZIF crystal and improve the gas separation performance for CO_2/CH_4.

Other characterization showed consistent trends between different techniques. TEM images did not reveal different crystal phases by analyzing the crystal size distribution and morphology, and the crystals obtained from this synthesis technique showed particle size distributions useful for mixed-matrix membrane fabrication. TGA analysis showed that incorporation of different organic linkers would lead to thermal stability changes, but did not significantly reduce the overall stability that the parent ZIF materials exhibited or show evidence of two separate decomposition temperatures to indicate different crystal phase formation.

7.1.2 Processing Condition Effects on Zeolitic Imidazolate Framework Materials during Mixed-Matrix Membrane Fabrication

In Chapter 4, the effects of ultrasonication were investigated to understand the stability of ZIF materials using fabrication techniques typically employed for making mixed-matrix membranes. Different sonication times, dispersion concentrations, and sonication power were examined to know changes in ZIF-8 related to its structure, its adsorption properties and its particle size and morphology. Additionally, mixed-matrix membranes were fabricated using different sonication intensity and tested with CO_2/CH_4 permeation experiments to understand changes in membrane performance related to membrane fabrication methods.

High-intensity ultrasonication utilizing a sonication horn showed that there are significant alterations in the ZIF-8 particle size and morphology following ultrasonication. SEM images and dynamic light scattering measurements showed the

particle size of ZIF-8 increased with increasing sonication time, but when the ZIF nanoparticles were solvothermally treated in the same organic solvent, there was no apparent change in particle size or morphology. These results indicated that ultrasonication causes a non-ideal nanoparticle coarsening that may be related to Ostwald ripening effects caused by rapid dissolution and recrystallization in the chosen organic solvent, tetrahydrofuran.

Characterization of ZIF-8 nanoparticles following ultrasonication showed maintenance of the crystal structure with some evidence from Williamson-Hall analysis that there is an increase in the crystallite size and strain related to the coarsening phenomenon. Nitrogen physisorption showed some reduction in Langmuir surface area and t-plot micropore volume that may correlate to changes in the diffusion pathways inside the ZIF-8 crystals. Lastly, X-ray synchrotron measurements and Pair Distribution Function analysis revealed the local atomic structure of the ZIF-8 nanoparticles did not change significantly following ultrasonication.

Mixed-matrix membranes fabricated from different sonication intensities revealed that the composite membrane transport of CO_2 and CH_4 can be very dependent on the fabrication steps. Importantly, membranes prepared with high-intensity ultrasonication showed membrane performance consistent with expected mixed-matrix membranes as the weight loading of ZIF-8 increased. The membranes showed both an increase in the selectivity and permeability for the gas pairs considered while membranes prepared with low-intensity ultrasonication exhibited poor separation performance in comparison to the

pure Matrimid® polymer. SEM images revealed this to be related to the poor dispersion of ZIF-8 nanoparticles in the surrounding polymeric matrix. Several characterization techniques of the membranes prepared with high-intensity ultrasonication showed good adhesion and interaction with the polymeric matrix as indicated by changes in FTIR spectra and glass transition temperature measurements using differential scanning calorimetry.

7.1.3 Gas Adsorption Properties and Application of Mixed-Linker Zeolitic Imidazolate Frameworks for Acid Gas Separations

Chapter 5 was the investigation of how mixed-linker ZIFs affect the CO_2 and CH_4 adsorption properties and how these properties are related to an ideal adsorption process by utilizing thermodynamic and chemical engineering relations to simulate a packed bed adsorption column. Different mixed-linker ZIF materials were fabricated, and the CO_2 and CH_4 isotherms were measured to obtain Henry's constants, isotherm parameters and heats of adsorption. Ideal adsorbed solution theory was used to calculate the adsorption behavior in gas mixtures containing different concentrations of CO_2 and CH_4, and a packed bed adsorption column was simulated to obtain the breakthrough characteristics of each adsorbent as well as the CH_4 recovery for a typical adsorption cycle.

Incorporation of 2-aminobenzimidazole in mixed-linker ZIFs revealed that there was only a small enhancement for CO_2 affinity compared to a pure ZIF-8 material and was best explained by reduction of basicity of the primary amine group from the aromatic ring fused with the imidazolate linker. However, there was an observable increase in

adsorption selectivity based on the calculated Henry's constants and a concomitant increase in the CO_2 heat of adsorption compared to ZIF-8. These results indicate that mixed-linker ZIFs containing 2-aminobenzimdiazole may not be necessarily useful for equilibrium-based separation techniques, but kinetic-based separations (either an adsorption column or membrane) may show significant improvement in separation enhancement compared to ZIF-8, considering the degree of control for incorporating the substitution linker into the ZIF-8 framework.

Modification of a pure ZIF-90 structure revealed low chemical stability and susceptibility to postsynthetic modification to enhance or change the adsorption properties. Synthesis of a mixed-linker ZIF material containing the ZIF-90 linker showed excellent chemical stability when reacted with ethylenediamine to form a ZIF material containing a primary amine functional group not affected by an aromatic ring. CO_2 adsorption experiments revealed significant enhancement of Henry's constant and heat of adsorption while showing little change in the CH_4 adsorption properties. The ideal adsorption selectivity of this functionalized material showed the highest CO_2/CH_4 adsorption selectivity in a ZIF material.

Breakthrough simulations were used to assess the performance of each adsorbent by using several simplifying assumptions. Overall, the results showed that use of mixed-linker ZIFs as adsorbents significantly increased the breakthrough time, and this was shown to occur over different feed compositions based on constant feed pressure. Additionally, CH_4 recovery, based on loss of CH_4 adsorbed and CH_4 in the adsorption

column at a certain breakthrough time, increased substantially with the use of mixed-linker ZIFs. These simulations indicated that in a limiting case ZIFs that incorporate more polar functional groups than ZIF-8 will outperform the parent material for an adsorption process. More detailed simulations, taking into account mass and heat transfer resistances, may reveal even more enhancement in separation performance when utilizing mixed-linker ZIF materials.

7.1.4 Fabrication and Performance of Zeolitic Imidazolate Framework-Based Mixed-Matrix Membranes for Acid Gas Separations

In Chapter 6, the effects of mixed-linker ZIFs on the permeability and separation performance of mixed-matrix membranes was studied to understand how functional groups in small pore ZIFs and how increasing substitution in mixed-linker ZIFs changes the transport properties without changing the overall crystal structure. ZIF materials were synthesized with controlled pore size distributions and incorporated into mixed-matrix membranes by typical fabrication techniques. Both single gas and mixed gas permeation experiments revealed changes in the separation properties when compared to the pure polymeric membrane performance. Mixed gas permeation experiments were used to simulate a hollow fiber membrane module containing different ZIF materials in the selective skin layer. These process simulations demonstrated that the primary benefit of incorporating ZIF materials was the significant reduction of membrane surface area required to obtain different separation product targets.

Synthesis of mixed-linker ZIFs with controlled organic linker compositions showed an associated control in pore size distribution, determined from N_2 physisorption experiments and Horváth-Kawazoe pore size distribution analysis. Fabrication and characterization of membranes containing different ZIF materials showed there to be adequate dispersion of ZIF particles in the polymeric matrix and excellent adhesion to the surrounding polymeric phase. SEM images revealed there to be no relative changes in particle size and morphology following fabrication, and this was attributed to using different fabrication conditions to avoid nanoparticle coarsening during membrane preparation.

Single gas permeation experiments showed a decrease in effective permeability in mixed-matrix membranes as the linker composition changed in either organic functionality or molar loading. Comparison of permeability and diffusivity values between mixed-linker ZIFs containing benzimidazole and 2-aminobenzimidazole with similar pore size distributions revealed a relative decrease when a primary amine functional group was used, and this may be related to changes in localized flexibility in the ZIF framework. Increasing the loading of 2-aminobenzimidazole in the ZIF framework without altering the crystal structure showed a slight decrease in the CO_2 diffusivity inside the membrane and a significant reduction in the CH_4 diffusivity, lowering below the intrinsic polymeric diffusivity. This was likely due to the amount of 2-aminobenzimidazole linkers blocking the effective transport of CH_4 inside the ZIF crystal.

Mixed gas permeation revealed unusual permeation behavior when mixed-linker ZIFs were used in mixed-matrix membranes. In all samples, the effective CO_2 permeability increased at high pressures, above the plasticization pressure, while the effective CH_4 permeability remained constant above the plasticization pressure. This may likely be related to the hindering diffusion effects that have been observed previously for ZIF-8. Hollow fiber membrane simulations using the mixed gas permeation data showed that the largest benefit of utilizing ZIFs in a polymeric matrix was significant reduction in required membrane area to obtain a desired CH_4 product purity at various feed pressures. Calculation of CH_4 recovery at a constant feed pressure revealed there to be no difference between the pure polymeric membrane and membranes containing mixed-linker ZIF materials.

7.2 Future Work

7.2.1 Mixed-Linker and Mixed-Metal Strategies for Zeolitic Imidazolate Frameworks

The work presented in this thesis offers multiple avenues for future research in the science and engineering of metal-organic frameworks for gas separations. As Chapter 3 demonstrated, the mixed-linker synthesis strategy can be used to make materials with different organic functional groups and different crystal structures. To probe if materials could be synthesized that do not have the SOD topology, a brief study, shown in Appendix A, shows that ZIF-11, a ZIF material with a zeolite RHO topology, could be synthesized using the non-solvent induced crystallization technique in a similar manner as ZIF-8, ZIF-90 and ZIF-7. Therefore, it may be possible to apply the same synthesis

techniques demonstrated in this thesis to other ZIF materials besides the ZIF-8 crystal structure or SOD topology.[1]

While amine and carbonyl groups are the only functional groups investigated in this thesis for changing the separation properties in ZIFs, it should be possible to include other functional groups of interest into the ZIF structure. As this thesis has shown, the effect of different functional groups may change the ZIF framework flexibility, affecting adsorption and molecular diffusion of gas molecules through the crystal structure. Introduction of different functional groups may also change the ZIF flexibility to enhance separation properties. Additionally, it may also be possible to "open up" ZIF-8 by introducing imidazole linkers with no functional groups. This has been demonstrated previously by using postsynthetic exchange techniques;[2] therefore, by introducing the imidazole in the synthesis stage, a more uniform distribution of linkers could be realized. By "opening up" ZIF-8, changes in diffusion coefficients of larger gas molecules may make an imidazole-substituted ZIF-8 material attractive for larger hydrocarbon separations, such as n-butane/iso-butane molecular separations.[3] Though zinc has been used exclusively in this thesis, it is possible to use other transition metals to fabricate ZIF materials.[1,4,5] By introducing different metal groups, ZIF materials can have many different properties, including adsorption, diffusion, and even catalytic properties.[6,7] It may be possible to introduce different metal salts in controlled quantities besides zinc to change the overall properties. Overall, the synthesis techniques may be generally applied to different ZIF structures to tailor the desired properties of the crystal to the target molecular separation.

7.2.2 Asymmetric Hollow Fiber Membranes with Zeolitic Imidazolate Frameworks

All membranes studied in this thesis are fabricated into dense film membranes to study the fundamental permeability properties of the composite membranes. In order to be applied to industrially relevant separations, these membranes must be fabricated into membranes with much higher surface area packing per volume, and hollow fiber membranes are an ideal platform for mixed-matrix membranes.

There already exist some examples of MOFs and ZIFs incorporated into polymeric membranes in hollow fiber membrane form.[8–10] It is likely that the mixed-linker ZIF strategy presented in this thesis can be easily scaled up to synthesize enough materials for hollow fiber membrane fabrication. As Chapter 6 demonstrated, the main benefit of including ZIF materials in a polymeric matrix will be significant reduction for the target CH_4 purity and feed flow rate. These simulations may predict the actual behavior in the hollow fiber membrane, assuming that fabrication of ZIF-containing hollow fiber membranes does not greatly affect the porosity and crystal structure of the filler ZIF material.

7.3 References

(1) Park, K. S.; Ni, Z.; Côté, A. P.; Choi, J. Y.; Huang, R.; Uribe-Romo, F. J.; Chae, H. K.; O'Keeffe, M.; Yaghi, O. M. *Proc. Nat. Acad. Sci.* **2006**, *103*, 10186–10191.

(2) Karagiaridi, O.; Lalonde, M. B.; Bury, W.; Sarjeant, A. A.; Farha, O. K.; Hupp, J. T. *J. Am. Chem. Soc.* **2012**, *134*, 18790–18796.

(3) Zhang, C.; Lively, R. P.; Zhang, K.; Johnson, J. R.; Karvan, O.; Koros, W. J. *J. Phys. Chem. Lett.* **2012**, *3*, 2130–2134.

(4) Wang, F.; Shu, Y.-B.; Bu, X.; Zhang, J. *Chem. Eur. J.* **2012**, *18*, 11876–11879.

(5) Fei, H.; Cahill, J. F.; Prather, K. A.; Cohen, S. M. *Inorg. Chem.* **2013**, *52*, 4011–4016.

(6) Li, J.-R.; Sculley, J.; Zhou, H.-C. *Chem. Rev.* **2012**, *112*, 869–932.

(7) Corma, A.; Garcia, H.; Llabrés i Xamena, F. X. *Chem. Rev.* **2010**, *110*, 4606–4655.

(8) Basu, S.; Cano-Odena, A.; Vankelecom, I. F. J. *J. Membr. Sci.* **2010**, *362*, 478–487.

(9) Basu, S.; Cano-Odena, A.; Vankelecom, I. F. J. *Sep. Purif. Technol.* **2011**, *81*, 31–40.

(10) Dai, Y.; Johnson, J. R.; Karvan, O.; Sholl, D. S.; Koros, W. J. *J. Membr. Sci.* **2012**, *401-402,* 76–82.

APPENDIX A

Room-Temperature Synthesis and CO_2/CH_4 Adsorption Properties of Zeolitic Imidazolate Framework-11

A.1 Introduction

In the preceding Chapters, only one crystal structure, ZIF-8, was closely examined for preparing mixed-linker zeolitic imidazolate frameworks for acid gas separations. There are many other ZIF topologies that exist, and in particular, ZIF-11 is of interest for CO_2/CH_4 and CO_2/N_2 separations due to its small pore channel.[1–3] Figure A.1 compares the ZIF topologies of ZIF-8 and ZIF-11. The challenge of studying ZIF-11 so far has been synthesizing the material without the presence of other crystalline phases. Seoane et al. have shown that traditional solvothermal techniques for making ZIF-11 result in a non-porous ZIF phase as a secondary crystal phase.[4] By sonochemical synthesis, the authors obtained a pure ZIF-11 phase after 12 hrs following an initial ZIF-7 phase formation; however, by this technique, the authors only obtained ZIF-11 in very small quantities (1.1-7.5 mg) and low yields (0.4-2.9%).[4]

The work presented in this thesis has shown that utilization of the non-solvent induced crystallization (NSIC) technique can provide a unique route to crystallizing materials that would normally require solvothermal techniques (*e.g.* ZIF-7). The goal of this Appendix is to demonstrate that NSIC techniques can be applied to other crystal structures other than the ZIF sodalite topology. In addition, because ZIF-11 has an interesting pore structure and crystal topology, it would be useful to obtain gas adsorption properties relevant to possible target separations. CO_2 and CH_4 adsorption measurements

were performed at 308, 328 and 348 K to obtained heats of adsorption and Henry's constants.

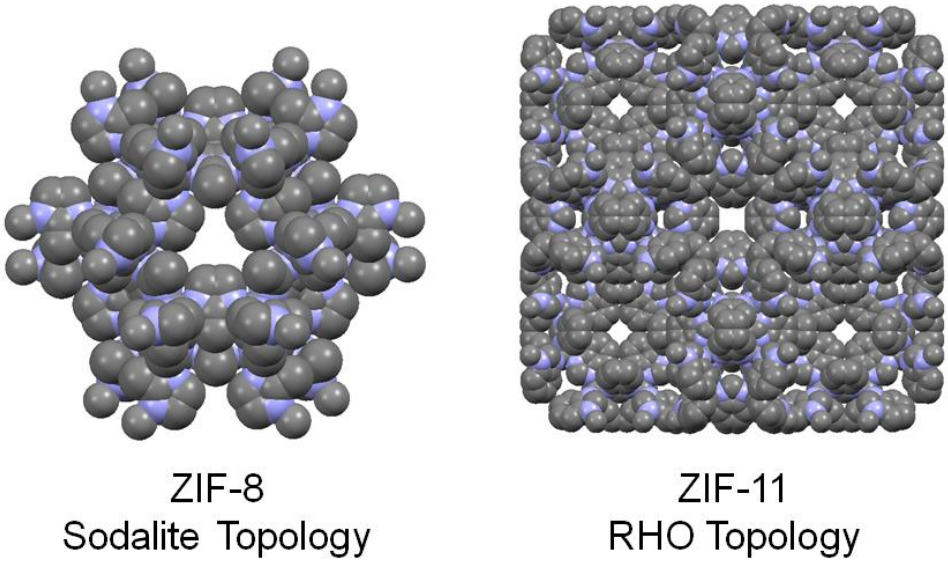

Figure A.1. Comparison of ZIF-8 and ZIF-11 topologies, with 1x1x1 unit cell displayed. ZIF-8 has one open pore window constructed from a 6-membered ring. ZIF-11 has two open pore windows constructed from a 6-membered ring and a 8-membered ring.

A.2 Experimental Methods

A.2.1 Materials

N,N-diethylformamide (DEF, 99%) and formamide (99%) were obtained from Alfa Aesar. $Zn(NO_3)_2 \cdot 6H_2O$ (98%) and benzimidazole (BzIM, 99%) were obtained from Sigma Aldrich. Methanol (MeOH, 99%) and N,N-dimethylformamide (DMF, 99%) were obtained from BDH. All chemicals were used as-is without further purification.

A.2.2 Synthesis of ZIF-11

To understand the effects of different synthesis preparation steps, Table A.1 shows the different conditions examined to precipitate ZIF-11 using NSIC. In general, 5

mmol $Zn(NO_3)_2 \cdot 6H_2O$ and 20 mmol BzIM was dissolved in 50 mL DEF, formamide or DMF and aged for 0-24 hrs at room temperature or 328 K. After cooling to room temperature, a non-solvent (MeOH or deionized H_2O) was added to the solution and left stirring for 1-24 hrs. A white precipitate formed, and the precipitate was separated from the solution by centrifugation at 10,000 rpm for 5 mins. The precipitate was washed with MeOH, and this process was repeated twice. In general, the product recovered resulted in yields of 0.3-0.4 g (10-15% based on Zn).

Table A.1. Synthesis conditions to test necessary crystallization conditions to prepare ZIF-11.

Experiment	Aging Time (hrs)	Aging Temp. (K)	Solvent	Non-Solvent	Volumetric Ratio (S:NS)
1	0	RT	Formamide	MeOH	1:1
2	0	RT	DMF	MeOH	1:1
3	0	RT	DEF	MeOH	1:1
4	2	RT	DEF	MeOH	1:1
5	24	RT	DEF	MeOH	1:1
6	2	328	DEF	MeOH	1:1
7	24	RT	DEF	MeOH	1:0.2
8	24	RT	DEF	H_2O	1:1

A.2.3. Gas Adsorption Measurements of ZIF-11

Adsorption measurements for CO_2 and CH_4 were carried out in a custom-built adsorption apparatus.[5] Samples were tested at temperatures of 308, 328, and 348 K. Pressure ranges tested were typically 0-1500 kPa. ZIF-11 samples were first degassed in a vacuum oven at 523 K for 24 hrs to remove any occluded solvent molecules in the framework. After insertion into the adsorption cell, samples were degassed again at 393

K for 12 hrs prior to each adsorption measurement. Ultra-high purity CH_4 (99.999%) and bone-dry CO_2 (99.999%) were used in all adsorption measurements.

A.3. Results and Discussion

A.3.1. Crystallization of ZIF-11

Previous synthesis procedures for crystallizing ZIF-11 required the use of DEF as the solvent.[1,4] To test if this solvent is required, the first several syntheses attempted were without the use of DEF. It was found (see Figure A.2) that without DEF only a non-porous, dense ZIF phase or ZIF-7 precipitated when formamide or N,N-dimethylformamide were used, respectively, as determined by powder XRD. This suggests that DEF allows some preferred precursor and nuclei formation that promote the growth of ZIF-11 over other phases; however, crystallization of ZIF-11 also occurred with the precipitation of the non-porous, dense ZIF phase.

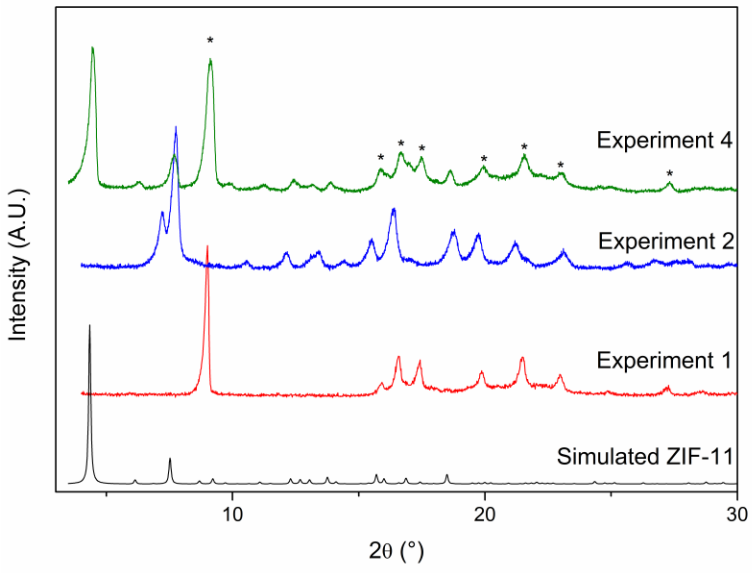

Figure A.2. Powder XRD patterns of synthesis experiments, showing dependence of ZIF crystal phase formation on the solvent used. Asterisks represent peaks of undesired dense ZIF phase.

Effects of aging the precursor solution with varying time and temperature is shown in Figure A.3. As the aging time increased, the intensity of the peaks associated with the non-porous ZIF phase decreased relative to the ZIF-11 XRD peaks, indicating suppression of formation of the dense ZIF phase. Interestingly, if the precursor solution was aged at higher temperatures, the XRD peaks associated with ZIF-11 nearly disappeared. This indicates that increased aging temperatures may promote the crystallization of more dense ZIF phases using the NSIC technique. This may be related to more energetically-favorable conditions to form a more thermodynamically-stable ZIF structure;[6,7] therefore, other methods of promoting ZIF-11 crystallization were pursued.

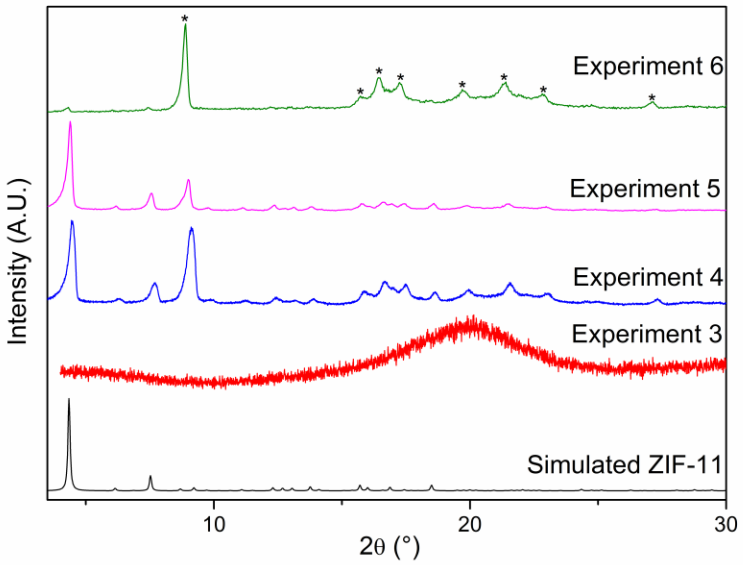

Figure A.3. Powder XRD patterns, demonstrating suppression of the dense ZIF phase with increased aging time. Asterisks represent peaks of undesired dense ZIF phase.

The last synthesis conditions tested were varying either the non-solvent volumetric ratio compared to the solvent or changing the non-solvent to DI water. When less non-solvent was used to precipitate a ZIF structure, powder XRD showed favorable formation of the dense ZIF phase. Therefore, either more non-solvent should be used to

rapidly promote formation of ZIF-11 or an entirely different non-solvent should be chosen. When DI water was used, there is only formation of ZIF-11. As shown in Figure A.4, when compared to the simulated ZIF-11 pattern, there is only evidence of the desired crystal phase, ZIF-11, and no X-ray peaks to indicate formation of the undesired dense ZIF structure. These series of crystallization experiments help show that NSIC is a technique that can be applied generally to other ZIF crystal structures and may be useful as a higher yield, easy-to-scale synthesis technique compared to solvothermal or sonochemical synthesis techniques. Because ZIF-11 has small pores, powder XRD patterns of degassed ZIF-11 were also measured to understand if there is any structural degradation or alteration during degassing at 523 K. Figure A.5 shows maintenance of the ZIF-11 phase following the degassing step. This suggests that, unlike ZIF-7, ZIF-11 does not undergo structural changes once the solvent is removed from its pores.[8]

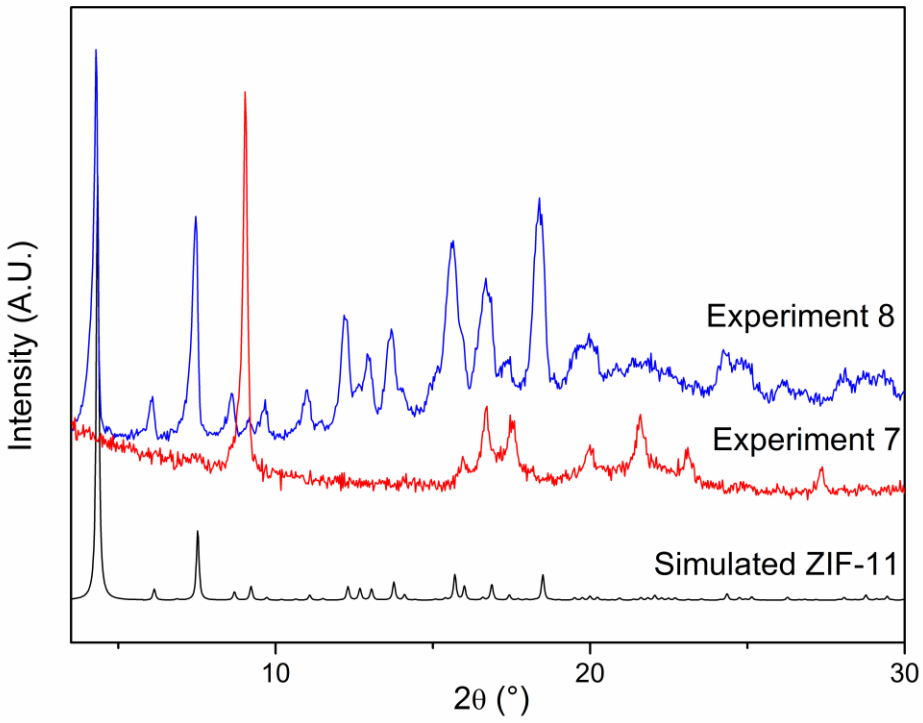

Figure A.4. Powder XRD patterns of ZIF samples prepared with different non-solvent compositions, showing that H_2O as a non-solvent produces the desired ZIF-11 phase.

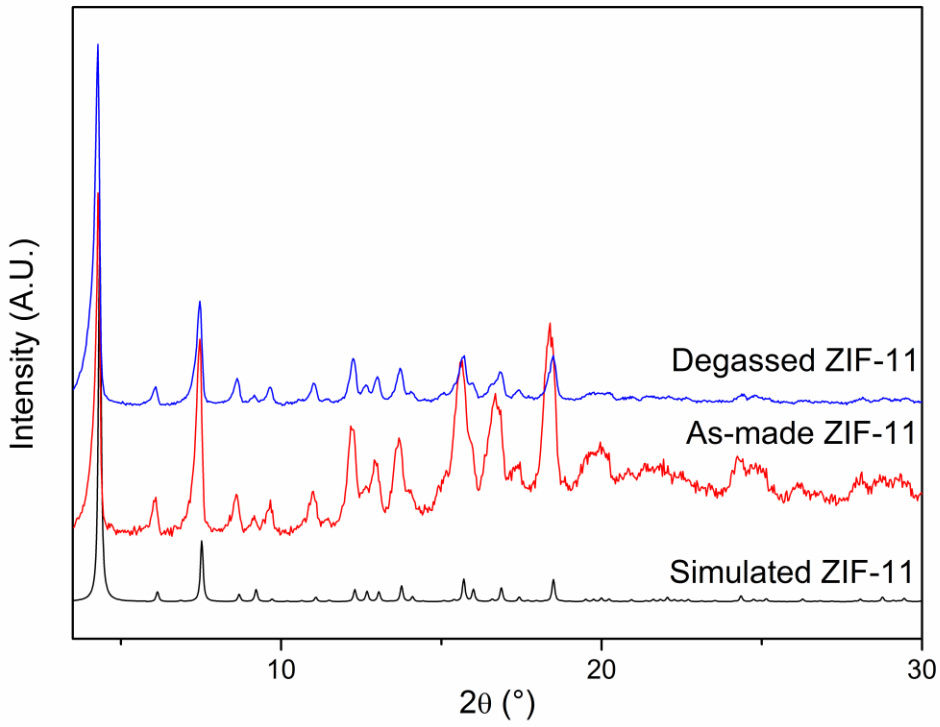

Figure A.5. Powder XRD patterns of as-made and degassed ZIF-11 samples, demonstrating maintenance of the crystal structure after high-temperature degassing to remove occluded solvent molecules.

A.3.2 Adsorption Properties of ZIF-11

CO_2 and CH_4 adsorption measurements were performed at multiple temperatures to obtain both the Henry's constants of each gas and the isosteric heats of adsorption, calculated by the virial isotherm equation.[9,10] Figure A.6 shows the CO_2 and CH_4 adsorption isotherms of ZIF-11 measured at 308, 328 and 348 K. Like other ZIF materials with non-polar organic linkers, ZIF-11 does not exhibit much apparent adsorption affinity for CO_2 over CH_4.[11] In the low pressure, linear region of the isotherms (see Figure A.7), the Henry's constants were calculated by finding the slope of the isotherm. Based on the Henry's constants of CO_2 and CH_4, ZIF-11 has an ideal adsorption selectivity of 2.9 for CO_2/CH_4, approximately 16% larger compared to ZIF-8 (Table 5.2).

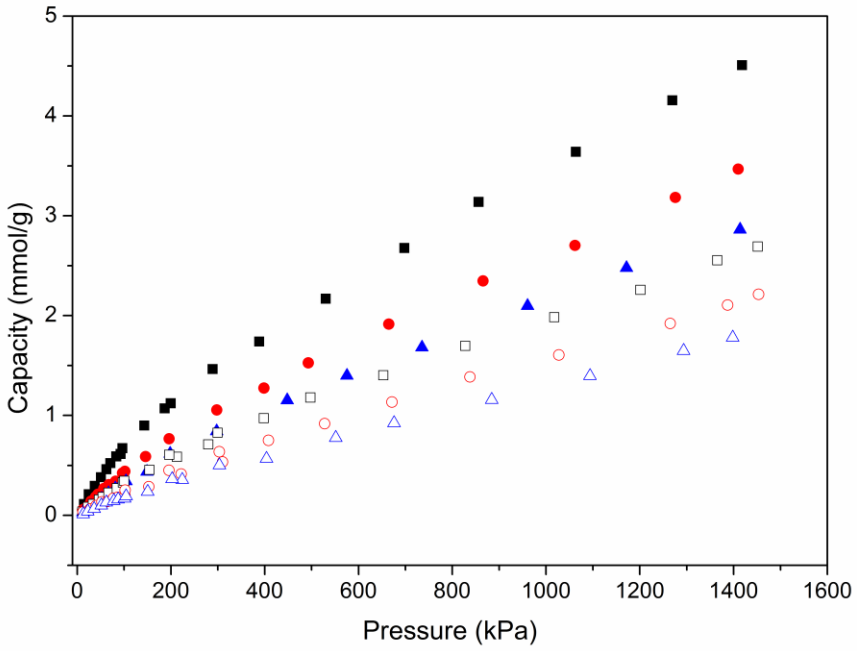

Figure A.6. CO_2 and CH_4 adsorption isotherms of ZIF-11. Open symbols are CH_4; closed symbols are CO_2. Squares: T = 308 K; circles: T = 328 K; triangles: T = 348 K.

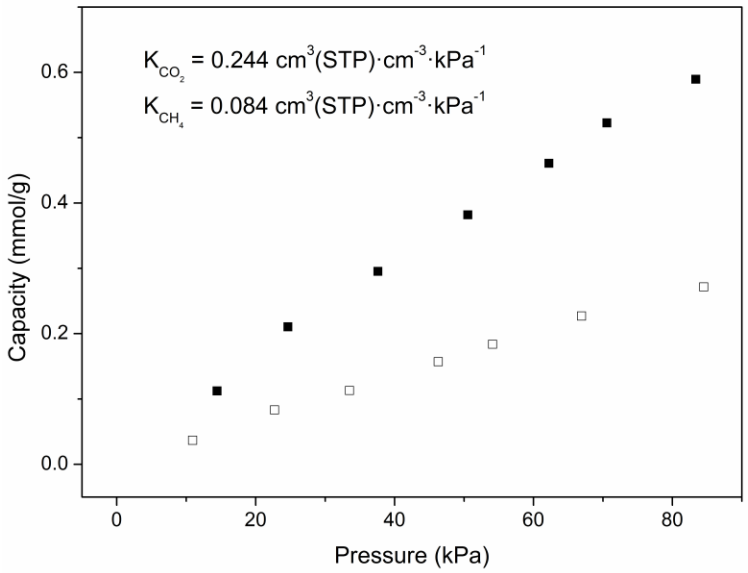

Figure A.7. Low pressure, linear region of CO_2 and CH_4 isotherms. Open symbols are CH_4; closed symbols are CO_2.

Previous studies on ZIF-11 with experiments and simulations have shown CO_2 isosteric heats of adsorption to be 22-18 kJ/mol with the isosteric heat of adsorption decreasing with increasing capacity of adsorbate.[12] Utilizing the virial isotherm equation, the isosteric heats of adsorption for CO_2 and CH_4 were calculated and are shown in Figure A.7. The values obtained for CO_2 match well with previous studies, indicating complete removal of solvent during degassing.[12] Interestingly, the CH_4 heat of adsorption is considerably higher when compared to ZIF-8 (18 kJ/mol for ZIF-11; 12 kJ/mol for ZIF-8).[13,14] This suggests more favorable adsorption sites for CH_4 in ZIF-11 and may be related to the high H_2 affinity in ZIF-11 compared to ZIF-8 that has been demonstrated with molecular simulations previously.[15]

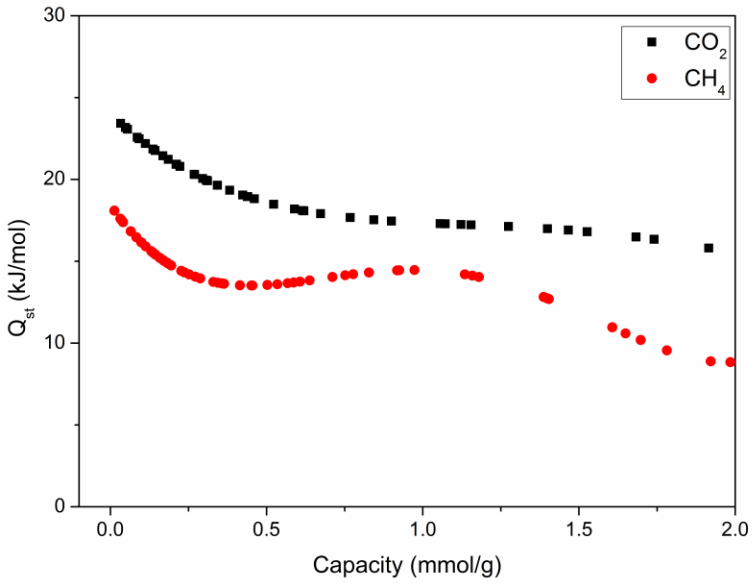

Figure A.7. Isosteric heats of adsorption determined from the virial isotherm equation. CO_2 heats of adsorption match well with previous experimental studies.

A.4 Conclusions

This synthesis and adsorption study has shown that NSIC is a synthesis technique that can be applied to other crystal systems, even crystal structures that are considerably

more complex than simpler, cubic structures such as ZIF-8. In particular, ZIF-11 was successfully synthesized without the need for solvothermal techniques, and other ZIF structures may be synthesized in a similar manner; however, as the results have shown, determining proper crystallization parameters is necessary for successful synthesis of the desired crystal structure. CO_2 and CH_4 adsorption properties show that ZIF-11 is not very selective based on equilibrium separation techniques for the CO_2/CH_4 gas pair. However, molecular simulations suggest that ZIF-11, and possible hybrid ZIF structures, would be very selective utilizing kinetic or transport-based separation technologies.[3]

A.5 References

(1) Park, K. S.; Ni, Z.; Côté, A. P.; Choi, J. Y.; Huang, R.; Uribe-Romo, F. J.; Chae, H. K.; O'Keeffe, M.; Yaghi, O. M. *Proc. Nat. Acad. Sci.* **2006**, *103*, 10186–10191.

(2) Phan, A.; Doonan, C. J.; Uribe-Romo, F. J.; Knobler, C. B.; O'Keeffe, M.; Yaghi, O. M.; O'Keeffe, M. *Acc. Chem. Res.* **2010**, *43*, 58–67.

(3) Yilmaz, G.; Keskin, S. *Ind. Eng. Chem. Res.* **2012**, *51*, 14218–14228.

(4) Seoane, B.; Zamaro, J. M.; Tellez, C.; Coronas, J. *CrystEngComm* **2012**, *14*, 3103–3107.

(5) Koros, W. J.; Paul, D. R. *J. Polym. Sci. Polym. Phys. Ed.* **1976**, *14*, 1903–1907.

(6) Lewis, D. W.; Ruiz-Salvador, A. R.; Gómez, A.; Rodriguez-Albelo, L. M.; Coudert, F.-X.; Slater, B.; Cheetham, A. K.; Mellot-Draznieks, C. *CrystEngComm* **2009**, *11*, 2272–2276.

(7) Baburin, I. A.; Leoni, S. *J. Mater. Chem.* **2012**, *22*, 10152–10154.

(8) Aguado, S.; Bergeret, G.; Titus, M. P.; Moizan, V.; Nieto-Draghi, C.; Bats, N.; Farrusseng, D. *New J. Chem.* **2011**, *35*, 546–550.

(9) Demessence, A.; D'Alessandro, D. M.; Foo, M. L.; Long, J. R. *J. Am. Chem. Soc.* **2009**, *131*, 8784–8786.

(10) Ruthven, D. M. *Principles of Adsorption and Adsorption Processes*; John Wiley & Sons, Inc., 1984.

(11) Amrouche, H.; Aguado, S.; Pérez-Pellitero, J.; Chizallet, C.; Siperstein, F.; Farrusseng, D.; Bats, N.; Nieto-Draghi, C. *J. Phys. Chem. C* **2011**, *115*, 16425–16432.

(12) Morris, W.; He, N.; Ray, K. G.; Klonowski, P.; Furukawa, H.; Daniels, I. N.; Houndonougbo, Y. A.; Asta, M.; Yaghi, O. M.; Laird, B. B. *J. Phys. Chem. C* **2012**, *116*, 24084–24090.

(13) Pérez-Pellitero, J.; Amrouche, H.; Siperstein, F. R.; Pirngruber, G.; Nieto-Draghi, C.; Chaplais, G.; Simon-Masseron, A.; Bazer-Bachi, D.; Peralta, D.; Bats, N. *Chem. Eur. J.* **2010**, *16*, 1560–1571.

(14) Fairen-Jimenez, D.; Galvelis, R.; Torrisi, A.; Gellan, A. D.; Wharmby, M. T.; Wright, P. A.; Mellot-Draznieks, C.; Düren, T. *Dalton Trans.* **2012**, *41*, 10752–10762.

(15) Assfour, B.; Leoni, S.; Seifert, G. *J. Phys. Chem. C* **2010**, *114*, 13381–13384.

APPENDIX B

Matlab Code for Horváth-Kawazoe Pore Size Distributions

```
clear all;

%Author: Joshua A. Thompson
%e-mail: thompson.josh.a@gmail.com
%Date last updated: 05-22-2012

%The following is code developed to calculate pore size distributions
in
%microporous materials using a slit-shaped geometry using HK equations,
%both original and modified.

%See the following publication for comparison of the two models for
different pore
%geometries: S.U. Rege, R.T. Yang, "Corrected Horvath-Kawazoe Equations
for
%Pore-Size Distributions," AICHE Journal, 46(4), 2000, 734-750. NOTE:
There
%are several typos in the equation derivations.

%To remain in the micropore range, do not enter data that goes over
P/P0 =
%0.05. Quantity adsorbed units are suggested, but are not necessary;
the
%code will work with whatever units.

%All other units are specified. If they are in different units, the
code
%will not work.

%Insert Relative Pressure (P/P0)

RP = [];

%Insert Quantity Adsorbed (cm3/g) corresponding to RP and also the
maximum
%QA value from isotherm OR maximum QA determined from Langmuir equation

QA = [];

QAmax = ;

%Enter thermodynamic parameters for Horvath-Kawazoe equations

%For adsorbent
d1 = 7.01; %diamter of adsorbent (d); units [=] Angstroms
```

```
alpha1 = 11.59e-24; %polarizability of adsorbent (alpha); units [=]
cm^3
chi1 = 6.90e-29; %susceptibility of adsorbent (chi); units [=] cm^3
rho1 = 4.51e15; %surface density of adsorbent (rho); units [=]
molecule/cm^2

%For adsorbate
d2 = 3.00; %diameter of adsorbate (d); units [=] Angstroms
alpha2 = 1.46e-24; %polarizability of adsorbate(alpha); units [=] cm^3
chi2 = 2.00e-29; %susceptiblity of adsorbate (chi); units [=] cm^3
rho2 = 6.71e14; %surface density of adsorbent (rho); units [=]
molecule/cm^2

%Cheng-Yang Correction -- HK Model assumes Henry's law for adsorption.
%CY-correction will account for LANGMUIR behavior. 0 = no; 1 = yes.

CYcorr = 0;

%Modified HK Equations -- There are some inconsistencies in the
original
%assumptions for the derivation of the HK equations. 0 = no; %1 = yes.

MHK = 0;

%Constants
me = 9.11e-31; %mass of an electron; units [=] kg
c = 3.00e8; %speed of light; units [=] m/s
R = 1.986; %Ideal Gas constant; units [=] cal/mol/K
T = 77.3; %Temperature of Experiment; units [=] K

%Dispersion Constants

A1 = 6 * me * c^2 * alpha1 * alpha2 / (alpha1/chi1 + alpha2/chi2);
%Dispersion between adsorbent and adsorbate; units [=] J/mol/cm^6
A2 = 3 * me * c^2 * alpha2 * chi2 / 2; %Dispersion between adsorbate
and adsorbate; units [=] J/mol/cm^6

%Diameter constants

d01 = (d1 + d2) / 2; %units [=] Angstroms
d02 = d2; %units [=] Angstroms
sigma1 = (2/5)^(1/6) * d01; %Minimum Distance at zero energy between
adsorbent and adsorbate; units [=] Angstroms
sigma2 = (2/5)^(1/6) * d02; %Minimum Distance at zero energy between
adsorbate and adsorbate; units [=] Angstroms

%Energy Term for HK Slit Model based on Relative Pressure

dimension = length(RP); %Dimension length of Relative Pressure vector
Etot = zeros(dimension,1); %Generation of Experimental Energy Term
Vector

for i = 1:dimension
    if CYcorr == 0
```

```
        Etot(i) = R * T / 1000 * log(RP(i));
    else
        Etot(i) = R * T / 1000 * log(RP(i)) + R * T / 1000 * (1-
1/(QA(i) / QAmax)*log(1/(1-(QA(i) / QAmax))));
    end
end

%Vector generation for length, L

Lopt = zeros(dimension,1);
Ll = d1 + d2; %Lower limit of L
Lu = d1 + d2 + 17; %Upper limit of L
length = 10000;
deltaL = (Lu - Ll)/length;
Lv = zeros(length,1);

for j = 1:length+1
    Lv(j) = Ll + (j - 1)*deltaL;
end

%Fitting and least-squares parameters

RMSE = 1000*ones(dimension,1);
Emodel = zeros(dimension,1);
sqrt = zeros(dimension,1);
Eplot = zeros(dimension,1); %Used to compare experimental and modeled
data

%HK Equation calculations

for l = 1:dimension %Loop to determine both Lopt and Eplot
   for k = 1:length+1
        sqrt(l) = 0;
        if MHK == 0
            Emodel(l) = 2.39 * 0.0001 * 6.022 * 10^23 * (rho1*A1 +
rho2*A2) / sigma1^4 / (Lv(k) - 2*d01) * (10^10 / 100)^4 *
(sigma1^4/3/(Lv(k) - d01)^3 - sigma1^10/9/(Lv(k) - d01)^9 -
sigma1^4/3/d01^3 + sigma1^10/9/d01^9); %HK Equation to a slit-shaped
pore
        else
            M = (Lv(k) - d1) / d2;
            E1 = rho1 * A1 / 2 / sigma1^4 * (10^10 / 100)^4 * (-1 *
(sigma1 / d01)^4 + 1 * (sigma1 / d01)^10 - 1 * (sigma1 / (Lv(k) -
d01))^4 + 1 * (sigma1 / (Lv(k) - d01)^10));
            E2 = rho1 * A1 / 2 / sigma1^4 * (10^10 / 100)^4 * (-1 *
(sigma1 / d01)^4 + 1 * (sigma1 / d01)^10) + rho2 * A2 / 2 / sigma2^4 *
(10^10 / 100)^4 * (-1 * (sigma2 / d02)^4 + 1 * (sigma2 / d02)^10);
            E3 = 2 * rho2 * A2 / 2 / sigma2^4 * (10^10 / 100)^4 * (-1 *
(sigma2 / d02)^4 + 1 * (sigma2 / d02)^10);
            if M < 2
                Emodel(l) = 2.39 * 0.0001 * 6.022 * 10^23 * E1;
            else
                Emodel(l) = 2.39 * 0.0001 * 6.022 * 10^23 * (2 * E2 +
(M - 2) * E3) / M;
            end
```

```
        end
        sqrt(l) = sqrt(l) + (Emodel(l) - Etot(l))^2;
        if Emodel(l) < Etot(l) %Condition set to not overshoot Lopt
            if sqrt(l) < RMSE(l)
                RMSE(l) = sqrt(l);
                Lopt(l) = Lv(k);
                Eplot(l) = Emodel(l);
            end
        end
   end
end

d = Lopt - d1; %Slit pore width
dqdL = zeros(dimension,1); %Differential volume

for m = 1:dimension
    if d(m) < d2 %If the slit width is less than the adsorbate size
        d(m) = 0; %Make the slit equal to 0
        dqdL(m) = 0; %Make differential volume equal to 0
    elseif m - 1 == 0 %If the initial point is some actual value
        dqdL(m) = QA(m)/d(m); %Extrapolate to 0
    elseif d(m) < d(m-1) %When using CY correction, there is sometimes
decreasing L as RP increase due to coverage approaching 1.
        d(m) = max(d) + 1;
        dqdL(m) = 0;
    else
        dqdL(m) = (QA(m) - QA(m - 1))/(d(m) - d(m - 1));
    end
end

%Differential volume plot
figure;
plot(d,dqdL,'b');
xlabel({'Slit Width (Angstroms)'},'FontSize',14);
ylabel({'dq/dL (cm3/g/Angstrom)'},'FontSize',14);

%Write data to Excel (or ASC) file

user_entry = input('Enter 1 to write data to an Excel file. Enter 0 to
cancel.  ');
if user_entry == 1
    user_entry = input('Specify desired file name:  ', 's');
    filename = user_entry;
    xlswrite(filename,[d, dqdL]);
end

clc;
d
dqdL
```

APPENDIX C

Matlab Code for Ideal Adsorbed Solution Theory

```
%=========================================================================
==%
%   The following is a program to perform Ideal Adsorbed Solution
Theory
%   calculations by using either Henry's law, Langmuir or Toth isotherm
%   parameters. This method is useful for predicting binary
%   adsorption mixtures and calculating adsorption selecitivities. For
%   references on these calculations and isotherms and how they are
useful,
%   see the following:
%
%   1) A.L. Myers, J.M. Prausnitz, AIChE J., 11 (1965), 121
%   2) D.M. Ruthven, Molecular Sieves, 7 (2008), 1-43
%=========================================================================
==%
%   Author: Joshua A. Thompson
%   email: thompson.josh.a@gmail.com
%   Date: 07-05-2012
%   Last Date Modified: 07-17-2012
%=========================================================================
==%

clear all
%=========================================================================
==%
%Isotherm Parameters
%Component 1 = CO2; Component 2 = CH4.

iso = 2;        % This determines which isotherm model to use. 1 =
Henry's Law; 2 = Langmuir; 3 = Toth.
qmax1 = 135.3;  % Saturation capacity of component 1
b1 = 0.119;  % Affinity constant of component 1
n1 = 1;     % Toth heterogeneous parameter of component 1
qmax2 = 120.2;  % Saturation capacity of component 2
b2 = 0.178;  % Affinity constant of component 2
n2 = 1;    % Toth heterogenenous parameter of component 2
rho = 1.019;    % Density of adsorbent
%=========================================================================
==%

%Thermodynamic data

Temp = 273.15 + 35; % Input temperature in degrees Celsius, K
R = 8.314;          % Ideal gas constant, J/mol/K
pmin = 1;          % Minimum pressure isotherm data was taken, kPa
pmax = 1000;        % Maximum pressure isotherm data was taken, kPa

%=========================================================================
==%
```

```
y1 = (0.01:0.01:0.99);      % Gas phase mole fraction of component 1
y1c = 0.5;                  % Constant gas phase mole fraction
x1 = (0.0001:0.0001:0.9999);% Adsorbed phase mole fraction of component
1
sp1 = zeros(length(y1),1);  % Spreading pressure of component 1
sp2 = zeros(length(y1),1);  % Spreading pressure of component 2
x = zeros(length(y1),1);    % Adsorbed phase mole fraction of IAST
sol'n
y = zeros(length(y1),1);    % Gas phase mole fraction of IAST sol'n
int = 100;                  % Number of intervals for 2nd set of
calculations
delp = (pmax-pmin)/int;     % Delta p step
p = (pmin:delp:pmax);       % Array of pressure for 2nd set of
calculations
alpha = zeros(length(p),1); % Array of selectivity -- 2nd
sp1c = zeros(length(p),1);  % Array of spreading pressure for component
1 -- 2nd
sp2c = zeros(length(p),1);  % Array of spreading pressure for component
2 -- 2nd
xc = zeros(length(p),1);    % Array of adsorbed phase mole fraction --
2nd
yc = zeros(length(p),1);    % Array of gas phase mole fraction -- 2nd
pc = zeros(length(p),1);    % Array of pressure output

%=========================================================================
==%
%       Iterations to determine best fit of x1 vector
%
%    The following will provide a y vs. x curve by specifying pmax.
%
%=========================================================================
==%

for i = 1:length(y1)
   SSE = 1000;
   sp11 = 0;
   sp22 = 0;
   for j = 1:length(x1)
       if iso == 1
           sp11 = rho*R*Temp*pmax*b1*y1(i)/x1(j);
           sp22 = rho*R*Temp*pmax*b2*(1-y1(i))/(1-x1(j));
           diff = (sp11 - sp22)^2;
           if diff < SSE
               SSE = diff;
               x(i) = x1(j);
               y(i) = y1(i);
               sp1(i) = sp11;
               sp2(i) = sp22;
           end
       elseif iso == 2
           sp11 = rho*R*Temp*qmax1*log(1 + b1*y1(i)*pmax/x1(j));
           sp22 = rho*R*Temp*qmax2*log(1 + b2*(1 - y1(i))*pmax/(1 -
x1(j)));
           diff = (sp11 - sp22)^2;
           if diff < SSE
```

```
                SSE = diff;
                x(i) = x1(j);
                y(i) = y1(i);
                sp1(i) = sp11;
                sp2(i) = sp22;
            end
        elseif iso == 3
            sp11 =
rho*R*Temp*qmax1*quad(@(x)toth(x,b1,n1),0,y1(i)*pmax/x1(j));
            sp22 = rho*R*Temp*qmax2*quad(@(x)toth(x,b2,n2),0,(1-
y1(i))*pmax/(1-x1(j)));
            diff = (sp11 - sp22)^2;
            if diff < SSE
                SSE = diff;
                x(i) = x1(j);
                y(i) = y1(i);
                sp1(i) = sp11;
                sp2(i) = sp22;
            end
        end
    end
end

%=========================================================================
===%
%           Iterations to determine best fit of x1 vector
%
%  The following will provide a P(total) vs. Selectivity
(x1/x2)/(y1/y2)  %
%=========================================================================
===%

for i = 1:length(p)
    SSE = 1000;
    sp11 = 0;
    sp22 = 0;
    for j = 1:length(x1)
        if iso == 1
            sp11 = rho*R*Temp*p(i)*b1*y1c/x1(j);
            sp22 = rho*R*Temp*p(i)*b2*(1-y1c)/(1-x1(j));
            diff = (sp11 - sp22)^2;
            if diff < SSE
                SSE = diff;
                xc(i) = x1(j);
                yc(i) = y1c;
                pc(i) = p(i);
                alpha(i) = (x1(j)/(1-x1(j)))/(y1c/(1-y1c));
                sp1c(i) = sp11;
                sp2c(i) = sp22;
            end
        elseif iso == 2
            sp11 = rho*R*Temp*qmax1*log(1 + b1*y1c*p(i)/x1(j));
            sp22 = rho*R*Temp*qmax2*log(1 + b2*(1 - y1c)*p(i)/(1 -
x1(j)));
            diff = (sp11 - sp22)^2;
            if diff < SSE
```

```
                SSE = diff;
                xc(i) = x1(j);
                yc(i) = y1c;
                pc(i) = p(i);
                alpha(i) = (x1(j)/(1-x1(j)))/(y1c/(1-y1c));
                sp1c(i) = sp11;
                sp2c(i) = sp22;
            end
        elseif iso == 3
            sp11 =
rho*R*Temp*qmax1*quad(@(x)toth(x,b1,n1),0,y1c*p(i)/x1(j));
            sp22 = rho*R*Temp*qmax2*quad(@(x)toth(x,b2,n2),0,(1-
y1c)*p(i)/(1-x1(j)));
            diff = (sp11 - sp22)^2;
            if diff < SSE
                SSE = diff;
                xc(i) = x1(j);
                yc(i) = y1c;
                pc(i) = p(i);
                alpha(i) = (x1(j)/(1-x1(j)))/(y1c/(1-y1c));
                sp1c(i) = sp11;
                sp2c(i) = sp22;
            end
        end
    end
end

figure;
plot(y,x,'-b');
xlabel('Gas phase mole fraction');
ylabel('Adsorbed phase mole fraction');
title(['Plot of gase phase vs. adsorbed phase mole fraction at '
num2str(pmax) ' kPa']);

figure;
plot(p,alpha,'-r');
xlabel('Absolute pressure (kPa)');
ylabel('IAST Selectivity');
title('Plot of pressure vs. IAST selectivity');



clc;
```

APPENDIX D

Matlab Code for Breakthrough Curve Simulations

```
%=========================================================================
===%
%   The following is a program that simulates breakthrough curves for
%   adsorbent beds based on physicochemical properties of an adsorbent
%   powder. The program was adopted based on the methodology from the
%   following reference:
%
%   R. Krishna, J.R. Long. "Screening Metal-Organic Frameworks by
Analysis
%   of Transient Breakthrough of Gas Mixtures in a Fixed Bed Adsorber."
J.
%   Phys. Chem. C, 2011, 115, 12941-12950.
%
%   D.M. Ruthven. "Principles of Adsorption and Adsorption Processes."
%   Chapter 8.
%
%=========================================================================
===%
%   Author: Joshua A. Thompson
%   Date Created: Jan. 28, 2013
%   Last Date Modified: Jan. 28, 2013
%   e-mail: thompson.josh.a@gmail.com
%=========================================================================
===%
clear all
%=========================================================================
===%

%   Isotherm Parameters

components = 2; %Number of components
qmax = zeros(components,1); %Saturation loading of each component
qmax(1) = 12.7; %mol/kg
qmax(2) = 12.7; %mol/kg
%qmax(3) = x.xxx; %mol/kg, Remove % and copy if more than 2 components
bi = zeros(components,1);
bi(1) = 0.00127; %kPa^-1
bi(2) = 0.000226; %kPa^-1
%bi(3) = x.xxx; %kPa^-1, Remove % and copy if more than 2 components
rho = 1; %kg/L, Framework density
%=========================================================================
===%

%Thermodynamic data

Temp = 273.15 + 35; % Input temperature in degrees Celsius, K
R = 8.314;          % Ideal gas constant, kPa*L/mol/K
p0 = 1000;          % Starting total pressure, kPa
y0 = zeros(components,1); % Starting mole fraction
y0(1) = 0.05;        %Component 1
```

```
y0(2) = 0.95;         %Component 2
%y0(3) = 0.5;        %Component 3, Remove % and copy if more than 2
components
eps = 0.4;           %Bed voidage
u0 = 1.0;             %Velocity, m/sec

%=========================================================================
==%

%Discretization and initialization

delz = 0.01; %Discretized bed length, bed is normalized to 0-1
zmax = 1.0; %Dimensionless bed length
m = zmax/delz; %Number of points
z = zeros(1,m+1); %Zeroed z matrix
delt = 0.01; %Discretized time scale, time is normalized to velocity
and bed
tmax = 200; %Max breakthrough time, dimensionless time
n = tmax/delt;  %Number of points
t = zeros(n+1,1); %Zeroed t matrix
p1 = zeros(n+1,m+1); %Matrix for pressure 1
p2 = zeros(n+1,m+1); %Matrix for pressure 2
%p3 = zeros(n+1,m+1); %Matrix for pressure 3
py1 = zeros(n+1,m+1); %Matrix for pressure 1
py2 = zeros(n+1,m+1); %Matrix for pressure 2
%p3 = zeros(n+1,m+1); %Matrix for pressure 3
p1store = zeros(1,m+1); %Storage matrix
p2store = zeros(1,m+1); %Storage matrix
ustore = zeros(1,m+1); %Storage matrix
y1 = zeros(n+1,m+1); %Matrix for mole fraction 1
y2 = zeros(n+1,m+1); %Matrix for mole fraction 2
u = zeros(n+1,m+1); %Matrix for superficial velocity
q1 = zeros(n+1,m+1); %Matrix for adsorbed gas 1
q2 = zeros(n+1,m+1); %Matrix for adsorbed gas 2
%q3 = zeros(n+1,m+1); %Matrix for adsorbed gas 3
for i = 1:m+1 %Initial conditions
        p1(1,i) = 0;
        p2(1,i) = 0;
        py1(1,i) = 0;
        py2(1,i) = 0;
        y1(1,i) = 0;
        y2(1,i) = 0;
        u(1,i) = 0;
        %p3(1,i) = 0;
end
for j = 2:n+1 %Boundary conditions
        p1(j,1) = y0(1)*p0;
        p2(j,1) = y0(2)*p0;
        py1(j,1) = y0(1)*p0;
        py2(j,1) = y0(2)*p0;
        y1(j,1) = y0(1);
        y2(j,1) = y0(2);
        u(j,1) = 1;
        %p3(j,1) = y0(3);
end
for i = 1:m
```

```
    z(i+1) = z(i) + delz;
end
for i = 1:n
    t(i+1) = t(i) + delt;
end
%=========================================================================
===%

%PDE Solver


for j = 2:m+1

    for i = 1:n
            p0 = 1000;
            %dq1dy =
qmax(1)*bi(1)*p0*(1+bi(2)*p0)/(1+y1(i,j)*p0*(bi(1)-bi(2))+bi(2)*p0)^2;
%Langmuir isotherm
            %dq2dy = -
qmax(2)*bi(2)*p0*(1+bi(1)*p0)/(1+y1(i,j)*p0*(bi(1)-bi(2))+bi(2)*p0)^2;
%Langmuir isotherm
            dq1dy = -1.1892*y1(i,j)^5+4.373*y1(i,j)^4-
7.2572*y1(i,j)^3+7.6065*y1(i,j)^2-6.04*y1(i,j)+3.6737; %IAST
            dq2dy = 0.5556*y1(i,j)^5-2.1645*y1(i,j)^4+3.7656*y1(i,j)^3-
4.05*y1(i,j)^2+3.2202*y1(i,j)-1.9423; %IAST
            func1 = 1+(1-eps)/eps*rho*R*Temp/p0*((1-
y1(i,j))*dq1dy+y1(i,j)*dq2dy);
            func2 = -(1-eps)/eps^2*rho*R*Temp/p0*(dq1dy+dq2dy);
            u11 = u(i,j-1) + delz*func2*u(i,j-1)*eps/func1*(y1(i,j)-
y1(i,j-1))/delz;
            y11 = y1(i,j)-delt*u11*eps/func1*(y1(i,j)-y1(i,j-1))/delz;
            y22 = (1-y11);
            yt = y11 + y22;
            if u11 == 0
                p0 = 0;
            else
                p0 = 1000;
            end
            y1(i+1,j) = y11;
            y2(i+1,j) = y22;
            u(i,j) = u11;
            py1(i+1,j) = y11*p0;
            py2(i+1,j) = y22*p0;
            if j == m+1
                if y11 <= 0.02
                    tbreak = t(i+1);
                    p1store = py1(i+1,:);
                    p2store = py2(i+1,:);
                    ustore = u(i,:);
                end
                if y11/y0(1) <= 0.5
                    tstoich = t(i+1);
                end
            end
    end
end
```

```
figure;
plot(z,p1store,z,p2store);
figure;
plot(z,ustore);

tbreak
LUB = (1-tbreak/tstoich)
```